Mechanism of the flexible micro-tube plasma and the influence of a metallic target by temporally and spatially resolved spectroscopy and potential measurements in contrast to a corona discharge

Zur Erlangung des akademischen Grades eines

Dr.rer.nat

von der Fakultät Bio- und Chemieingenieurwesen
der Technischen Universität Dortmund
genehmigte Dissertation

vorgelegt von

M.Sc. Hao Song

aus

Xiaogan, Hubei, China

Tag der mündlichen Prüfung: 22.01.2026

1. Gutachter: Prof. Dr. Oliver Kayser

2. Gutachter: PD Dr. Joachim Franzke

Dortmund 2026

Zusammenfassung

Diese Arbeit untersucht den Entladungsmechanismus typischer flexibler mikro-Tuben Plasmen (FμTP), den Einfluss benachbarter Ziele, die zugrunde liegenden Ionisierungsprozesse sowie die charakteristischen Merkmale, die FμTP von der Koronaentladung unterscheiden. Ziel ist es, die Wechselwirkungen zwischen elektrostatischem Potenzial, dem zeitlichen und räumlichen Verhalten der Plasmaentwicklung und der analytischen Leistungsfähigkeit zu verstehen.

Zur Unterscheidung von Edelgas-Ionen und angeregten Spezies wurde eine neue Datenverarbeitungsmethode entwickelt. Mithilfe raum-zeitlich aufgelöster optischer Emissionsmessungen konnten die primären Anregungs- und Ionisierungsprozesse in *He*-FμTP und *Ar*-FμTP identifiziert werden. Gleichzeitig wurde der bislang unterschätzte Einfluss eines benachbarten Leiters auf die Plasmadynamik nachgewiesen. In diesem Zusammenhang werden die optischen Evolutionseigenschaften von FμTPs mit drei unterschiedlichen Polaritäten vor einem metallischen Ziel systematisch unter variierenden Abständen untersucht.

Aufgrund ähnlicher Entladungsgeometrien wird das FμTP häufig fälschlicherweise als Wechselstrom-Koronaentladung betrachtet. Zur Korrektur dieses Missverständnisses umfasst die vorliegende Studie eine optische Charakterisierung von Gleichstrom- und Wechselstrom-Koronaentladungen. Darüber hinaus werden die elektrostatischen Potenziale im Umfeld von Koronaentladungen und FμTPs analysiert und miteinander verglichen. Ergänzend werden verschiedene Gleichspannungs-Bias in die Ansteuerspannung des FμTP integriert, das mit einem Massenspektrometer (MS) gekoppelt ist, um die Auswirkungen auf die analytische Leistung zu bewerten.

Die kombinierte Analyse umfasst optische Emissionsspektren, das Ringpotenzial um die Plasmaregion, die Zündung des Diagnoseplasmas sowie die Signalintensität im MS – jeweils für Koronaentladungen und FμTP. Die zentrale Rolle der Kapillare im FμTP wird hervorgehoben: Sie steuert die Plasmabewegung, verstärkt den Restladungseffekt und isoliert die Sekundärelektronenemission. Diese Eigenschaften machen FμTP zu einer eigenständigen Technologie mit klaren Vorteilen.

Auf Basis dieser Experimente wird das FμTP neu definiert – nicht lediglich als Koronaentladung, sondern als geführte Plasmasäule bzw. Plasmajet mit breitem Anwendungspotenzial. Indirekte Hinweise deuten darauf hin, dass FμTP als Ionisierungsquelle effizienter und schonender sein könnte als herkömmliche Koronaentladungen. Diese Erkenntnisse vertiefen das Verständnis der Ionisierungsmechanismen und liefern wertvolle Impulse für die wissenschaftliche Forschung und die ingenieurtechnische Nutzung der Plasmatechnologie.

Abstract

This work studies the discharge mechanism of typical flexible micro-tube plasma (FμTP), the influence of proximal targets, specific ionisation mechanisms, and the main features distinguishing FμTP from corona discharge. This study aims to clarify the interrelationship between electrostatic potential, plasma evolution behaviours, and analytical performance.

For distinguishing noble gas ions from excited species, a new data processing method has been proposed. The primary excitation and ionisation processes for *He*-FμTP and *Ar*-FμTP are identified through spatiotemporal optical emission measurements. Concurrently, the underestimated impact of an adjacent conductor was demonstrated. Accordingly, the optical evolution characteristics of three polarity FμTPs in front of a metallic target are investigated.

Given the similar configuration, FμTP is frequently regarded as merely an AC-corona discharge. To address this misconception, this research executed optical characterisation of DC- and AC-corona discharges. Electrostatic potentials around corona discharges and FμTPs are also explored and contrasted. Furthermore, various DC biases are introduced into the driven voltages of FμTP coupled to mass spectrometer (MS) to assess analytical performance.

A combined analysis of optical emission spectra, ring potential, diagnosis plasma ignition, and MS signal height is presented for both corona discharge and FμTP. The key role of capillary in FμTP is highlighted: guiding plasma propagation, amplifying the residual charge effect, and isolating secondary electron emission. These characteristics make FμTP to be a standalone technology with clear advantages.

Based on these experiments, FμTP is redefined – not only as a corona discharge, but also as a guided plasma column and even a plasma jet with broad application prospects. Evidence obtained indirectly implies that FμTP has the potential to be more efficient and softer than conventional corona discharge as an ionisation source. These insights enhance the understanding of ionisation mechanisms and provide a valuable reference for both scientific research and engineering applications of plasma technology.

Table of Contents

Symbols and abbreviations

Symbols

Symbol	Unit	Description
C	F	Capacitance
d	cm	Distance from the separation of electrodes
E	$V \cdot m^{-1}$	Electric field
h	J·s	Planck constant
p	Torr	Gas pressure
R	Ω	Resistance
t	ms, μs, ns	Time
ν	Hz	Frequency
x	mm	Spatial coordinate
λ	nm	Wavelength
ε_0	$C \cdot V^{-1} \cdot m^{-1}$	Electric permittivity of vacuum
ε′	-	Dielectric constant
ε″	-	Dielectric loss factor
ε_r	-	Relative dielectric constant
σ	$S \cdot m^{-1}$	Electrical conductivity
σ	$C \cdot m^{-2}$	Surface charge density
tanδ	-	Dielectric loss tangent angle
τ	s, ms, μs, ns	Characteristic time/time constant

Abbreviations

Abbreviation	Description
A^+	Ionised state of A
A^{**}	Upper excited states of A
A^*	Lower excited states of A
A^M	Metastable states of A
AC	Alternating Current
APCI	Atmospheric Pressure Chemical Ionisation
Ar	Argon
a.u.	Arbitrary Units
CCD	Charge-Coupled Device
CI	Chemical Ionisation
DC	Direct Current
DBD	Dielectric Barrier Discharge
DBDI	Dielectric Barrier Discharge Ionisation
CAP	Cold Atmospheric Plasma
eV	Electron volt
ESI	Electrospray Ionisation
FμTP	Flexible micro-Tube Plasma
FNS	First Negative System
FPS	First Positive System
He	Helium
HV	High Voltage
ICCD	Intensified Charge-Coupled Device
ID	Inner diameter
iLTP	inverse Low Temperature Probe
IMS	Ion Mobility Spectrometry
kHz	Kilohertz
kV	Kilovolt
LTP	Low Temperature Probe

Continued on the next page

– continued from previous page

Abbreviations	**Description**
m/z	Mass-to-charge ratio
MS	Mass Spectrometry
N	Negative-biassed voltage
NIR	Near-Infrared
NP	Bipolar voltage
OD	Outer diameter
OES	Optical Emission Spectroscopy
P	Positive-biassed voltage
p-FWHM	position-Full Width at Half Maximum
POEPS	Plasma Optical Emission Phoresis Spectroscopy
ppm	Parts per million
sccm	Standard cubic centimetres per minute
SPS	Second Positive System
UV	Ultraviolet
V_{pp}	Peak-to-peak voltage

CHAPTER 1

Introduction

1.1 Motivation

Ionisation source is an essential part for analytical technology, such as in mass spectrometry (MS) and ion mobility spectrometry (IMS). In addition to classical electrospray ionisation (ESI) [1, 2], ultraviolet (UV) ionisation lamps and beta-radiation electron emitters [3], plasma-based ionisation sources have attracted increasing attention in recent years [4-6]. This can be attributed to their ability to operate under ambient conditions, while offering efficient ionisation for a wide range of analytes. Among them, flexible micro-tube plasma (FμTP) and atmospheric pressure chemical ionisation (APCI) represent two typical cold plasma configurations with distinct discharge characteristics and ionisation behaviours. APCI, based on corona discharge, is well established for its simplicity and stability. It often suffers from limited discharge volume, strong electric field localisation, and potential fragmentation of analytes. In contrast, FμTP, which features a confined capillary structure and dielectric guidance, provides extended plasma propagation, reduced energy density, and more controllable ionisation environments.

Due to flexibility and miniaturisation features, FμTP is gaining growing attention as a novel soft ionisation source [7-22]. It has been proved to be a dielectric guided discharge running by charged particles attached on the inner wall of the capillary, but the indeed responsible particles are still not confirmed. Recent research has proved that plasma initiated in argon (*Ar*) is a good alternative to play a role of a soft ionisation source in the field of analytical chemistry. For further optimisation, the specific discharge mechanisms of FμTP with helium (*He*) and *Ar* as discharge gases in the same configuration are essential to investigate and clarify.

In terms of application, we noticed that bringing a conducting object in the vicinity of the plasma has a non-negligible impact on the plasma evolution. Since the performance of a plasma is entirely determined by its discharge properties, this nearby conductor may significantly affect the final application, particularly in instances where it is employed as an ionisation source and coupled with MS. It is therefore imperative that such interference mechanisms are explored and identified in order to enhance controllability. To regulate plasma behaviour, efforts must be made to comprehensively study the effect of conductor on plasma evolution in specific situations.

At first glance, FμTP and corona discharge seem equal, but in fact a great difference is reported regarding discharge behaviour [9, 10, 23-29]. Corona discharge seems to be only a local field discharge that occurs near the tip of an electrode with a small radius of curvature. However, there are few publications on the optical differences between positive and negative DC-corona discharges, let alone AC-corona discharges. In contrast, FμTP is more like a discharge that starts as a corona discharge from the electrode tip but is capable of forming a long plasma column along the capillary.

Therefore, a systematic comparison between corona discharge and FμTP is essential to elucidate the underlying discharge mechanisms, distinguish their ionisation process, and identify the advantages and limitations of each configuration. In particular, there is an urgent need to survey and compare their individual ionisation mechanisms and analytical capacities in an overall perspective. This study will contribute to a deeper distinction and understanding. In addition, such findings will not only advance the fundamental knowledge of micro-scale plasma discharges but also support the optimisation of plasma-based ionisation sources for analytical applications.

1.2 Scope of this thesis

The present thesis is organised into 6 different chapters. The following **Chapter 2** describes some elementary knowledge about discharge plasma, dielectric characteristics, and optical emission spectra to help to understand the following measured results and discussions. To identify the key particles responsible for plasma development, **Chapter 3** deals with the kinetics of excitation and ionisation processes in a *He*- and *Ar*-FμTP, as well as the effect of additional propane for *Ar*-FμTP, the comparison between these two plasmas is also included. To improve the controllability of applications, **Chapter 4** is devoted to investigating the interference mechanisms involved in a metallic target to the FμTPs driven by three polarity voltages, and a possible explanation is proposed, taking into account the varying target distance. In order to better understand and also compare with FμTP, the specifics of the discharge behaviours of DC- and AC-corona discharge are represented in **Chapter 5**. Then, to distinguish them from each other, a combined comparison of discharge features, electrostatic potential, and analytical abilities between corona discharge and FμTP is performed in **Chapter 6**. Finally, based on these experiments and discussions, **Chapter 7** concludes the findings of these results and possible continuing research directions in the future.

CHAPTER 2

Fundamentals

In the scope of this thesis, the discharge features and analytical efficiency of FμTP are characterised and compared to corona discharge. This chapter begins with a brief overview of the basic knowledge about electrical breakdown and plasma generation. As one of the most used plasma-based ionisation sources, the properties of corona discharge are introduced. In particular, as a plasma-based ionisation source, the physical configuration and properties of the component material of FμTP are revealed. Then, the dielectric polarisation characteristics and the charge accumulation mechanisms are addressed. These two physical processes are crucial for distinguishing FμTP from corona discharge. As one of the main used plasma diagnostic means, OES can be categorised into different groups based on their mechanisms. Subsequently, the different principles and advantages of these two methods are introduced separately.

2.1 Plasma-based ionisation source

2.1.1 Electrical breakdown and plasma generation

Plasma has been classified as the fourth state of matter and is defined as an ionised gas capable of conducting electricity [30-34]. It forms when a neutral gas becomes partially ionised, producing a substantial population of charged species, such as ions and electrons. Because of these charges, plasmas exhibit high electrical conductivity and their behaviour is strongly governed by electric potentials. Despite being composed of unbound positive and negative particles, a plasma remains approximately quasi-neutral on macroscopic scales. Charged species continuously interact through the electromagnetic fields they generate, resulting in collective phenomena that differ markedly from the behaviour of individual particles [35]. Consequently, both microscopic particle dynamics and macroscopic plasma motion are highly sensitive to externally applied fields [36].

Plasma can be generated by various artificial methods, all of which share the fundamental requirement of inducing local electrical breakdown. For example, it can be achieved by subjecting a neutral gas, such as air, to a strong electrical field. In the event that an electrical discharge occurs at atmospheric pressure, the resultant plasma is designated as atmospheric pressure plasma [37]. Typical atmospheric pressure discharge phenomena include lightning, arc discharge, corona discharge, atmospheric pressure glow discharge [38] and dielectric barrier discharge (DBD), etc. In circumstances where a sufficiently high voltage is applied to an electrode encased within a gaseous environment, the local electric field can reach a threshold at which the charge density in the gas rises abruptly by many magnitudes. This causes the gas to become conductive and its resistance to drop greatly [39]. This stage is called "electrical breakdown", which is a local process. In other words, once the applied voltage is above the threshold value, the nearby gas is stressed and effectively transforms from an insulator to a conductor as ionisation progresses. For a conductor immersed in a homogeneous gas, it initiates once the local electric field surpasses the dielectric strength of the gas. Because conductors exhibit the strongest surface fields at protrusions, sharp tips, and edges, these regions typically serve as the sites where breakdown first develops.

In instances where the voltage is appropriate, the breakdown may occur only in a particular region. It will give rise to what is termed partial discharge, which is exemplified by the phenomenon of corona discharge. However, once a region has broken down and became conductive, it no longer sustains a voltage drop. In contrast, the complete voltage difference is transferred to the remaining gap. As the effective discharge gap shortens, the same voltage is applied over a reduced distance, further intensifying the local electric field in the remaining gas. This, in turn, induces further breakdown of the adjacent gas. Consequently, the breakdown region rapidly spreads (typically within nanoseconds) along the voltage gradient until a continuous conductive path is established between the electrodes, allowing current flow and initiating an electric arc. Therefore, a gas discharge can be initiated or a plasma can be sustained only when the electrode-applied voltage exceeds the breakdown threshold of the gas.

For a specified gas, the voltage required for breakdown is a function only of the product $p \cdot d$, where p denotes the gas pressure and d represents the distance from the separation of electrodes. This relationship is formally known as the Paschen law [40-42], the corresponding voltage curve versus the product p·d is called the Paschen curve [43]. The Paschen curves for several gases are shown in Figure 2.1. As illustrated, they exhibit a minimum estimated breakdown voltage at approximately $p \cdot d$ = 1~10 Torr·cm [42]. This implies that, as gas pressure increases, a smaller electrode-gap is usually preferred to get a lower practical breakdown voltage. Such voltage reduction benefits plasma-source design by improving operational ease and enhancing flexibility in device configuration. However, the mean free path of a gas molecule (defined as the average distance between consecutive collisions [44]) is inversely related to the gas pressure under fixed thermal conditions.

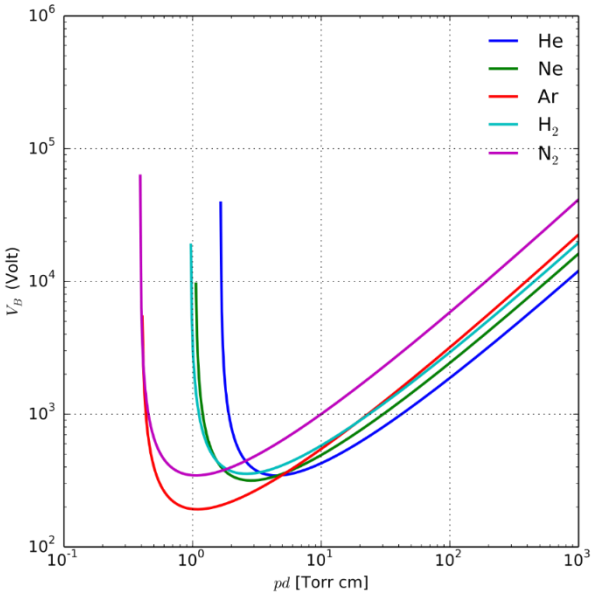

Figure 2.1: Paschen curves obtained for helium, neon, argon, hydrogen, and nitrogen, using the expression for the breakdown voltage (V_B) as a function of product $p \cdot d$ [41].

In the case of atmospheric pressure with a large product $p \cdot d$, an electron will undergo numerous collisions with surrounding gas molecules during its travel process. To ensure ionisation of enough gas molecules for sustaining breakdown, continuous energy (e.g., electric field) input is needed to counteract the recombination of ions and electrons. Due to more collisions taking place in an atmospheric pressure gas, the recombination rates also increase. A higher voltage is therefore also required for electrical breakdown or maintenance of the plasma compared to low-pressure environments. However, collisions dissipate electron energy, hindering their ability to ionise gas molecules. Consequently, a higher applied voltage is required for electrons to acquire sufficient energy for ionisation.

As pressure increases, there are greater electron-impact collisions, improving the efficiency of energy transfer from electrons to gas molecules and ions [42]. In addition, this also tends to drive the system toward thermal equilibrium among electrons, gas molecules, and ions. Nevertheless, energy transfer can be effectively suppressed. DBD is one of the excellent representatives that can produce cold, non-equilibrium plasmas at atmospheric pressure [45-47].

The underlying process of maintaining plasma can be described as a rapid cascade process in which mobile charged particles liberate further charged particles. This is visualised in Figure 2.2. The potential gradient and subsequent electric field accelerate the initial electrons to sufficient velocities to kick the electrons out of the gas molecules upon collision. These seed electrons originate from natural processes like photo-ionisation or radioactive decay. The first impact of an electron on a neutral particle will result in one ion and two electrons. The liberated electrons will in turn be accelerated during their movement process, which will continuously excite and ionise more neutral molecules [48]. This process creates more free electrons and ions in a chain reaction called Townsend discharge [37, 42, 49, 50]. It will induce an exponential increase in electron density until an electron avalanche develops [48, 51, 52], and

an electric arc can occur as a consequence of the electron cascade. The number of charged particles has been reported to increase sharply, reaching millions, only after approximately 20 successive collision events [53].

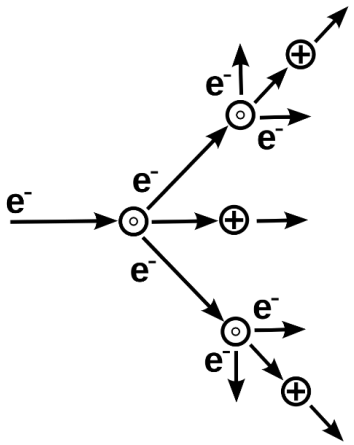

Figure 2.2: Cascade process of the ionisation process. Electrons are "e⁻", neutral molecules are "o", and cations are "+".

Because an electron has a much longer mean free path in a high electric field, it will be accelerated and acquire sufficient kinetic energy to excite or ionise other atoms or molecules (A). In the event that the energy of an electron being lower than the ionisation energy but higher than the excited state of particle A, the particle will be excited to A*. This process is given in Equation 2.1.

$$e^- + A \rightarrow A^* + e^- \tag{2.1}$$

In the event that the energy of an electron exceeds or is equal to the ionisation energy of particle A, ionisation of the particle will occur, forming A^+. During this time, a secondary electron is produced. The ionisation process is expressed in Equation 2.2.

$$e^- + A \rightarrow A^+ + 2e^- \tag{2.2}$$

The newly released electrons are then accelerated, leading to further excitation and ionisation through collisions. Excited species and ions are either rapidly quenched through collisions with neutral gas molecules or relax to lower energy states via photon emission. In the field of plasma physics, radiative decay processes of excited species generally occur on shorter timescales than collisional de-excitation [54], thus making photon emission the dominant relaxation pathway.

The metastable state (A^M) is optically forbidden to decay to the ground state under the selection rules of quantum mechanics, resulting in a significantly extended lifetime [55]. A^M is subject to a loss of energy as a consequence of its collision with other partners. The collisional processes of A^M with a neutral particle (B) are delineated as follows.

$$A^M + B \rightarrow A + B^* \tag{2.3}$$

$$A^M + B \rightarrow A + B^+ + e^- \tag{2.4}$$

If particle B is promoted to an excited state as described in Equation 2.3, the process is referred to as excitation transfer [56]. If particle B is ionised, as shown in Equation 2.4, the process is termed Penning ionisation [57]. Additionally, the quenching of an ion by particle B can proceed via a charge transfer mechanism (see Equation 2.5), in which particle B is ionised.

$$A^+ + B \rightarrow A + B^+ \tag{2.5}$$

The emission processes of excited states and ions will be further discussed in Section 2.3.1.

Cold atmospheric plasma (CAP), such as corona discharge and DBD, can be easily created at atmospheric pressure and room temperature, and possess outstanding chemical and physical properties [30, 42, 49]. These decisive advantages make the technology applicable in numerous fields without the need for vacuum equipment. The employed plasmas are typically characterised as weakly ionised, with only a small fraction of the gas molecules undergoing ionisation. This kind of plasma is also known as cold or non-equilibrium plasmas. They are not in thermodynamic equilibrium because the electron temperature is significantly higher than that of the heavy species (ions and neutrals). This means that only electrons are thermalised and possess a very different Maxwell-Boltzmann velocity distribution from others [58]. Nevertheless, the overall gas temperature remains near ambient conditions [42, 46, 48, 49, 59].

2.1.2 Corona discharge

Although air is usually an excellent insulator, when a high voltage is applied across relatively small gaps, regions of intense electrical field can cause air to be ionised and become partially conductive. At this time, a so-called corona discharge occurs. Corona discharge is often considered as a “single-electrode discharge”, as opposed to the typical “two-electrode discharge” [60, 61]. A corona discharge forms only when one electrode is sufficiently separated from the counter electrode. When the applied voltage is sufficiently high, the air undergoes full electrical breakdown, and the ionised region expands until it bridges to the opposite electrode. Therefore, a low resistance conductive path will be formed that bridges the entire gap, resulting in an electrical spark [42, 49, 62]. This spark will evolve into a continuous discharge called an electric arc if the current is supplied continuously [48, 49]. In fact, corona discharge can also be ignited without counter electrode, but stricter start-up conditions (e.g., much higher voltage) are required.

As one of the classic plasma-based ionisation sources, the commercially available APCI is maturely and extensively used in MS. APCI generally refers specifically to an ionisation technique using a corona discharge driven by a DC voltage. Therefore, the mentioned terms of “APCI” and “DC-corona discharge” are used interchangeably in the following text. In the typical implementation of APCI, a strong electric field is formed between the needle electrode (tip diameter 20~200 µm) and the counter electrode by applying a high DC voltage (usually 2~6 kV) [63]. This will then induce a corona discharge of gas (such

as air) under atmospheric pressure to produce primary ions (e.g., N_2^+, H_3O^+). And these ions in turn ionise the analyte molecules through the so-called "Chemical Ionisation" (CI) process. The consensus is that APCI is realised through direct reactions of reagent gas ions with sample molecules [64], which means that mutual contact between these species is one of the prerequisites.

Recently, corona discharge has been proven to be performed in ambient air also by AC voltage [28, 29, 46, 65-72]. It has already been researched and even tried as an optimised ionisation source coupling to MS [67-71]. It should be noted that positive and negative DC-corona discharges are generated alternatively in AC-corona discharge due to repetitive gas breakdown. It is an undeniable fact that, given the same electrode configuration, an AC-corona discharge seems to be easier to ignite than a DC-corona discharge [67, 68, 71]. The respective remnant space negative charges and positive charges concentrate near the needle tip are suspected to act as key triggers for plasma breakdown during the positive and negative half-phases of an AC-corona discharge, respectively [29, 68, 71, 72].

According to established knowledge, smaller electrodes generate stronger electrical fields, yielding thinner plasmas with fewer electrons, while these electrons possess a higher average kinetic energy compared to those produced by larger electrodes. Consequently, it is easier to ignite corona discharge with a thinner electrode [73]. For ignition of an AC-corona discharge, the electrode must be sufficiently sharp at an appropriate distance using a specific power supply. If the distance is too small, it can easily degenerate into a spark or arc discharge [42]. In addition to corona discharge, FμTP can also produce a CAP in an even more controllable way [7].

2.1.3 Flexible micro-tube plasma

Many plasma-based ionisation sources have been used for soft ionisation applications, such as Dielectric Barrier Discharge Ionisation (DBDI), Low Temperature Probe (LTP) and the inverse LTP (iLTP). Recently, a new plasma-based soft ionisation source has attracted numerous attentions because of its many strengths. It was developed after a series of modifications to DBDI for ensuring safe operation, enhancing ionisation performance, and miniaturising further. It was implemented by altering the electrode configuration, removing the ground electrode, and decreasing the dimensions, particularly the inner diameter of the discharge tube. As a result, a novel robust setup for compact plasma was invented and named as flexible micro-tube plasma (FμTP) [7]. It has been used as a soft ionisation source for the detection of various analytes, and a good ionisation performance was demonstrated [7, 8, 11-22].

The physical configuration of the FμTP ionisation source is illustrated by the schematic diagram in Figure 2.3, the included key components are drawn. A fused silica capillary (inner and outer diameters of 250 μm and 350 μm, respectively) is utilised for the transmission of discharge gas and separation from air as well. A tungsten wire with a diameter of 100 μm is inserted into the capillary and acts as a high voltage (HV) electrode. Importantly, there is no physical counter electrode in this design. The plasma column is generated in the volume between the electrode tip and the capillary exit, which can

even inject into ambient air and form a plasma jet [7]. The length of the discharge volume can be adjusted to meet specific requirements by replacing the terminal capillary of differing lengths with ease and efficiency.

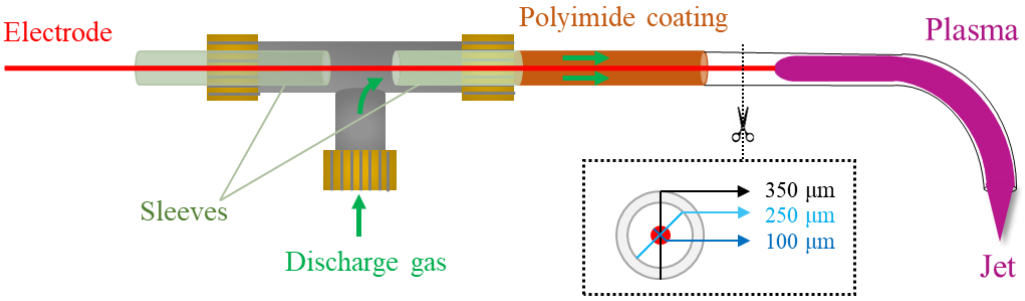

Figure 2.3: Schematic diagram of the FµTP ionisation source to produce a plasma even inject into ambient air. Inset: Sectional view and dimensions of the capillary used in FµTP.

The capillary tube has a thin wall and a polyimide radial coating thickness of 5 µm, allowing a minimum bending radius of 25 mm and high mechanical compatibility [7]. To offer a transparent channel for optical measurements in the following text, the capillary coating in the discharge region has to be stripped off. Usually, it is removed at least 2~3 mm above the length of the discharge volume to make the measurements more accurate. Its flexible and miniaturised design allows for adaptability to a variety of specialised application scenarios (e.g., narrow, obstructed, etc.). It also effectively avoids the risk of direct discharge, ensuring safety and reliability, and is easy to integrate with various instrument platforms [7].

Fused silica is the ideal dielectric material for FµTP due to its unique physicochemical properties. It is a high-purity glass with a single component of silica, with SiO_2 in purity ⩾99.999%, and possesses a high degree of chemical inertness due to the absence of metal impurities (e.g., Na^+, Ca^{2+}). At the same time, the high chemical stability makes it resistant to the erosion of reactive plasma species (e.g., O·, OH·) and prolongs its lifetime. The exceptionally low thermal expansion coefficient (~5.5×10^{-7}/°C) and melting point (>1600 °C) make it withstand to possible localised high temperatures during plasma generation, providing excellent thermal stability. The high dielectric strength (~10^8 V/m) makes it hard to breakdown at high voltages and guarantees the insulating properties of the capillary. The capillary also has excellent optical properties with high transmittance in the range of 180~2500 nm, making it suitable for spectroscopic measurements.

The complex dielectric constant of fused silica, $\varepsilon_r = \varepsilon' - j\varepsilon''$, exhibits two key properties in an AC electric field. First, the dielectric constant ($\varepsilon' \approx 3.8$) reflects a weak polarisability yet still enabling a uniform electric field distribution. Second, the loss factor ($\varepsilon'' \approx 10^{-4}$) and the corresponding tangent of the loss angle ($tan\delta = \varepsilon''/\varepsilon'$) of ~$2.6\times10^{-5}$, which indicates an extremely weak ability to dissipate electric energy [74]. The polarisation process is nearly hysteresis-free, enabling charges to respond instantaneously to the electric field variations. The electric-field energy can be transferred to the gas molecules almost

without loss, promoting plasma development (e.g., electron avalanching) and efficient ionisation. At the same time, low dielectric loss can effectively suppress Joule heat accumulation [75, 76], contributing to stable long-term operation. It is worth mentioning that ceramic materials, despite having a high dielectric constant ($\varepsilon_r \sim 9$), suffer from poor optical transmission, brittleness, and limited flexibility and therefore do not suit FμTP systems.

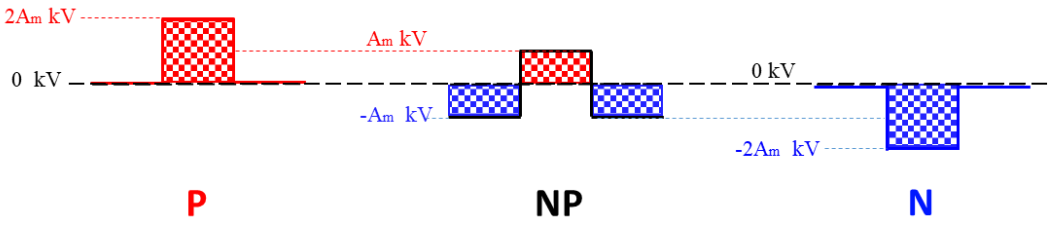

Figure 2.4: Schematic diagram of the three polarity square wave voltages, the black dashed lines represent 0 kV, the left values stand for the corresponding relative amplitudes.

FμTP is usually driven by a square wave voltage, whose polarity can be switched through a specific bias circuit. This is implemented by adding a positive (+A_m kV) or negative (-A_m kV) DC bias voltage to a bipolar voltage that has a peak-to-peak voltage (V_{pp}) of 2A_m kV. Therefore, as shown in Figure 2.4, these three polarity cases are defined as P, NP, and N. In the case of bipolar voltage (NP) typically applied in FμTP, each cycle consists of two distinct half-phases with opposite polarity amplitudes (red blocks represent positive amplitudes and blue blocks represent negative amplitudes). However, only a positive amplitude is applied in a positive-biassed voltage (P) and only a negative amplitude is applied in a negative-biassed voltage (N).

For the P and N cases, the applied amplitudes no longer alternate strictly between positive and negative during each half-cycle. Instead, the amplitudes are doubled in the corresponding half-cycle for these two cases. To avoid confusion, the terms “rising and falling half-phases” are adopted to distinguish the two halves of one cycle. The rising half-phase (red blocks) denotes the half-cycle starting from instant 0, whereas the falling half-phase (blue blocks) denotes the subsequent half-cycle. This unified terminology is used throughout the thesis, including for the NP case without a DC bias.

2.2 Dielectric polarisation and charge accumulation

2.2.1 Dielectric polarisation

Dielectric polarisation is the term given to describe the behaviour of a dielectric (insulating) material when an external electric field is applied, which creates the induced electric dipole moments and polarised charges near the surface of the material. This means that the alignment of charges within a dielectric material, with positive charges aligned along the electric field and negative charges opposing it, leads to a net macroscopic polarisation throughout the material [77]. These charges within the atoms or molecules of the material experience electric forces in opposite directions, causing them to slightly

separate and shift in positions, even though the charges do not move freely like in a conductor. In an AC electric field, the polarisation process of a dielectric such as glass involves the dynamic response of the charge distribution within the material.

There are four principal types of polarisation that can occur in dielectric materials, including electronic, ionic, orientation, and space-charge polarisation. All insulating materials are capable of undergoing electronic polarisation [78], in which the electron cloud (e.g., in a Si-O bond) is elastically displaced by an electric field, forming a transient dipole moment as an essentially instantaneous response [79]. If mobile ions are present, such as Na^+ in soda-lime glass, short-range ion migration under the local electric field gives rise to ionic polarisation [79]. Orientation polarisation occurs in materials containing permanent dipoles. However, because dipole rotation is strongly hindered in solids, this mechanism is generally weak in solids and common in polar liquids or gases [79]. Space-charge polarisation is highly material-dependent and arises when charges accumulate in regions where they are not free to move or where movement is restricted [77].

In an AC electric field, the polarisation response of dielectric materials is strongly frequency dependent, with each polarisation having its own "operating frequency band". The corresponding frequencies and main reasons for this are shown in Table 2.1.

Table 2.1: Polarisation type of dielectric material

Polarisation type	Response frequency range	Main reasons
Electronic Polarisation	Above THz (optical frequency)	The electrons are light in mass and prompt in response
Ionic Polarisation	Up to THz (medium and high frequency)	The ions have a large mass and slow movement
Orientation Polarisation	Up to MHz (low frequency)	The molecules rotate more slowly
Space-Charge Polarisation	Up to kHz (very low frequency)	A large number of carriers must overcome interface resistance and migrate

The polarisation response tends to lag behind the electric field changes, especially at high frequencies. Such hysteresis leads to dielectric losses, i.e., the conversion of partial electrical energy into thermal energy [80]. The ability of different types of polarisation mechanisms to "keep up" with changes in the electric field at different frequencies significantly affects the dielectric constant (ε_r) and the loss tangent ($tan\delta$) of the material [78, 80, 81]. The material ε_r quantifies its ability to polarise in response to an electric field. A high ε_r indicates adequate polarisation, and the material has a strong ability to store

charge or electric field energy [77]. The dielectric loss tangent ($tan\delta$) is also known as the dissipation factor, which reflects the energy loss during the polarisation-depolarisation process [76].

In FμTP, the capillary material of fused silica consists primarily of nonpolar structural units and contains virtually no free-moving ions. Within solid materials, the intermolecular strength strongly restricts its rotation, so even if polar molecules exist, they are unable to rotate and orient. As a consequence, the polarisation process of the capillary is manifested mainly as an electronic polarisation behaviour. In other words, the electron cloud of the Si-O bond is rapidly displaced by the electric field, resulting in a slight deformation and the formation of an instantaneous dipole moment. Its response time is extremely short ($\sim 10^{-16}$ seconds [78, 82]) and causes minimal dielectric losses. This process can completely follow the electric field variations up to the THz range. The result is only a local redistribution of the charge density within the material, while remaining electrically neutral overall. Thus, polarisation does not "charge" the glass, but merely forms an interfacial dipole layer. It should be noted that the polarised charge is not really a "measurable surface charge". This means that polarisation provides only one background field modulation mechanism.

However, the plasma itself contains a large number of charges. When they come into contact with the insulator wall, these charges are adsorbed and cannot move because of the non-conductivity. This then leads to the remainder of a large number of charges at the plasma-dielectric interface, triggering additional surface charge distributions. And these surface charges coupled with the polarised dipole field may lead to local electric field distortion near the insulator, affect the discharge pattern, and so on. In micro-tubes, this effect is particularly pronounced due to the large surface-to-volume ratio. It may either inhibit or enhance the discharge region, affect the subsequent ion energies and reaction pathways. Under AC electric fields, surface charges may be partially neutralised. However, owing to the disparity in mobilities between electrons and ions, asymmetric voltage waveforms and wall adsorption hysteresis, cyclic wall charge build-up and asymmetric modulation may still occur. These effects probably alter the discharge characteristics in the following cycle.

The resistivity of quartz is extremely high (about 10^{16} Ω·cm), making the equivalent resistance (R) very large. So, it is difficult for charges to dissipate through bulk conduction. At the same time, its small relative dielectric constant results in limited overall capacitance (C). The two work together ($\tau = R \cdot C$, further described in Section 2.2.2.1) resulting in long-term retention of charges on the surface (time constants can reach milliseconds to seconds) [49]. If the time constant is much larger than the period of the square wave (20 kHz corresponds to 50 microseconds), the charges cannot be completely dissipated in each half-period, resulting in charge accumulation. If the time constant is in the millisecond range then, over multiple consecutive square wave periods, the charge gradually increases until a steady-state equilibrium is reached. This slow change can be captured by the oscilloscope as a low-frequency fluctuation or DC offset, which will be discussed further in Chapter 6.

In summary, in the 20 kHz AC-driven FμTP system, the fused silica capillary enables efficient coupling of electric field energy into the discharge gas through its low-loss electronic polarisation and high dielectric strength. At the same time, it ensures the flexibility and long-term operational stability of the device. The excellent material properties of fused silica balance insulation strength, energy efficiency, and structural flexibility in FμTP, providing a key foundation for the development of miniaturised and flexible plasma devices. Most importantly, the polarisation and charge accumulation behaviours of the capillary directly regulate the electric field distribution inside the capillary, the gas breakdown process, and the development and propagation of plasma.

2.2.2 Charge accumulation

2.2.2.1 Charge accumulation mechanism

Many publications have indicated that the dielectric surface acts as a reservoir for charges deposited by the discharge, causing a "memory charge effect" on the insulator surface [46, 49, 66, 83-85]. It has been demonstrated and quantified that a "surface charging memory effect" is produced, i.e., that substantial surface charges and the associated electric field persist between discharge pulses [86]. The essence of such effect can be attributed to free charges from plasma striking the insulator surface, these charges cannot penetrate or move away because of the high insulation. Therefore, with discharge evolution, they "stay" or "accumulate" on the surface, forming a true net charge layer. The accumulation and decay of charges on a dielectric surface can usually be analogised to an RC circuit, whose time constant is given by $\tau = R \cdot C$, where R is determined by the resistivity and geometry of the material, and C is determined by the dielectric constant and geometry of the material.

This phenomenon, also known as "surface charge accumulation" [23, 42, 51, 52, 87-94], is entirely a charge injection process and is independent of whether the material is polarised or not. In practical systems, polarisation can modulate the wall electric field distribution, change the conditions under which free charges approach the wall, and affect the charging rate or the stability of space charges [93]. In this manner, polarisation may indirectly alter the charging behaviour, but it is not a prerequisite for charge accumulation. In short, surface charge accumulation does not depend on the polarisation response but on the interactions of free plasma charges with the insulator wall.

If the charged particles generated in plasma were not taken into account, the polarisation charge would fully follow the electric field reversal at the end of each half-phase, resulting in no net charge accumulation on the capillary surface. Although these charged particles produced in plasma do not participate in conventional polarisation, studies have shown that their presence can indirectly affect the polarisation of the dielectric [93, 95-97]. The plasma charges hitting the dielectric surface can inject charge and modify the surface electric field distribution, thus affecting the internal polarisation state. The space charge field within the plasma sheath may superimpose on the applied field, changing the effective field strength in the dielectric, and thus indirectly modulating the polarisation behaviours.

2.2.2.2 The role of the accumulated charge

It has been reported that a primary plasma formed in the ambient air can travel along a dielectric tube and initiate a secondary plasma [26, 98]. Detailed investigations show that the primary plasma disappears before the secondary plasma emerges and that the accumulated charges can form a local electric field that exceeds 2 kV/mm [98]. Therefore, the local electric field induced by the charges on the dielectric surface is declared to be the driving factor for the ignition of the secondary plasma. Similarly, studies of point-to-plane discharges with a dielectric layer blocked in the gap demonstrated that charge accumulation on the dielectric surface significantly facilitates discharge re-ignition over the dielectric layer [99].

Experiments on corona discharge confined within a plastic tube [71] have shown that DC-corona discharge requires higher sustaining voltages than in open configurations. This is attributed to the charging of the inner tube wall, which partially shields the electric field at the needle tip. Additionally, studies on AC-corona discharge demonstrate that the residual space charge in air and the deposited charges on the dielectric surface substantially influence the discharge process [46, 65, 66]. After polarity reversal, these charges strongly enhance the applied electric field, thereby lowering the ignition and self-sustaining voltages and producing more intense discharge reactions in AC-corona discharge compared with DC-corona discharge [67, 68, 71].

A ceramic sampling plate has been found to potentially improve the ion transmission efficiency and improve peak intensities. This was explained by the accumulated charges on the ceramic surface, which distort the electric field around the MS orifice and focus the charged particles into the MS inlet. Enhanced MS signals were observed for several compounds in on-line experiments, and the presence of these charges was also validated by charge measurements and numerical simulations [100]. In addition, an employed floating helix electrode that winds around the surface of the quartz tube has recently been reported to contribute to lower power consumption and longer jet length [85]. This is explained by the effect of enhancing charge accumulation on the dielectric surface surrounding the helix, which subsequently provides a conductive path for the plasma jet.

In a DBD plasma, it is understood that charge deposition on the dielectric surface restricts the current, thereby enabling the operation of non-equilibrium discharges at atmospheric pressure [90]. In addition, the significance of the surface charge and its finite relaxation time in discharge dynamics was also noted [101]. A numerical work shows that the electric field is influenced not only by the volume charge density but also by the surface charge density, which is determined by the distribution of charge carriers that migrate along the insulator surface [89].

In summary, charge accumulation on the dielectric surface can markedly affect discharge dynamics through several mechanisms [23, 42, 49, 85, 87-89, 102]. It can generate a reverse electric field that rapidly counteracts the net field below the breakdown threshold, triggering self-quenching of the discharge. The surface charge distribution also contributes to controlling the discharge uniformity by

suppressing local current concentrations and promoting the formation of multiple micro-discharge channels. Additionally, it helps to optimise energy efficiency by limiting the energy of individual discharges and thereby reducing Joule heat accumulation. These mechanisms provide the key guidance for the design of DBDI: e.g., precise control of the discharge mode (filamentary/uniform) and energy partitioning (dissociation /ionisation) can be achieved by tuning the electrode configuration, dielectric conductivity, and driving voltage characteristics [65, 103-106].

In the case of FμTP, the accumulation of a "quasi-permanent" dielectric surface charge [88] generates an electrostatic field that overlays the AC electric field, forming an equivalent extra potential bias (i.e., "DC component potential" detected in Chapter 6). This extra potential bias can exert a destructive effect on plasma behaviour [23, 42, 46, 52, 65, 66, 85, 87-91, 94, 102]. It distorts the local electric field distribution (e.g., sheath field), thereby disrupting field symmetry and inducing local variations in field direction and strength, which in turn results in deviations in the trajectories of charged particles. This distortion may lead to uneven discharge characteristics, including localised enhancement, suppression, or even extinguishment. Consequently, the electron temperature becomes non-uniform, with regions of excessive energy that may cause over-ionisation or material sputtering. Continuous ion acceleration under the DC field component also intensifies ion bombardment on the capillary walls or electrodes, leading to material damage. Overall, these effects compromise discharge stability, potentially inducing plasma oscillations or mode transitions, and thus reducing operational reliability.

2.2.2.3 Formation of charge clouds

When positive and negative species become unevenly distributed, local charge clouds may form, and associated electric fields can also influence subsequent discharge behaviours [107]. In AC electric fields, electrons are generally more difficult than ions to gather into groups, forming such charge clouds. Overall, charge clouds essentially arise from localised, non-uniform charge distributions, with their formation primarily governed by the characteristics and dynamics of the charge carriers.

Due to their extremely high mobility, which is several orders of magnitude greater than that of positive ions [68, 72, 90, 102], electrons move rapidly under an electric field and tend to distribute uniformly rather than aggregate locally. Their extremely small mass (10^3~10^5 times smaller than ions) also makes them highly susceptible to thermal motion and collisional disturbances, preventing stable remains in one place. In contrast, ions can persist in specific regions because of their much lower mobility. The large mass and inertia of ions also make them hard to accelerate, thus contributing to their stability and allowing them to resist disturbances and maintain localised aggregation. Environmental factors, including collision and diffusion, further affect this process. Electrons are readily consumed through recombination with positive charges or absorption at surfaces. In contrast, ions possess relatively long lifetimes, gradually aggregating to result in localised charge enrichment. Therefore, electrons respond to electric fields quickly, resulting in faster charge neutralisation or redistribution, whereas ions are indeed more prone to gather and maintain charge clouds in specific areas. For example, the familiar

plasma sheath and stream head are actually a direct manifestation of localised ion aggregation [102]. Actually, the charge cloud is a gathering of net space charges, which can significantly modify the local spatial electric field distribution.

Under most ionisation mechanisms, particularly those induced by the impact of electrons on gas molecules or atoms, positive ions are generated directly together with free electrons. Consequently, positive ions are stably produced and are typically abundant under steady-state discharge conditions. In contrast, negative ions are produced primarily by electron capture. For example, oxygen molecules capture electrons to form O_2^-. The principle underlying the effective generation of negative ions is that molecules with a sufficiently high electron affinity are required to facilitate electron attachment [42]. However, the extra electron present in the negative ion is frequently loosely bound, making it susceptible to detachment through collisions with other electrons [108, 109]. Consequently, negative ions are comparatively unstable and the concentration is usually low. For comparison, a summary of the characteristics of primary charged particles in CAP is listed in Table 2.2.

Table 2.2: Charged particle features in CAP

Particles	Mobility	Lifetime	Energy/Stability	Aggregation Trend
Positive ion	low	long	High ionisation energy (>10 eV), relatively slow recombination processes, possesses high stability.	Strong, easily forming a space charge cloud
Negative ion	low	short	Low electron affinity (1–4 eV), easily dissociated by electron impact and therefore possesses low stability.	Weak, making it difficult to form stable charge clouds
Electron	extremely high	extremely short	Fast-moving and prone to loss.	Hardly any, not easily to form charge clouds

The electron temperature in CAP typically ranges from 1 to 10 eV [85], which is sufficient to sustain ionisation, but results in relatively slow recombination processes. Consequently, positive ions exhibit comparatively long lifetimes within the plasma, allowing for local aggregation and the development of space charge zones. In contrast, the electron affinity of most negative ions lies between 1 and 4 eV [110, 111], considerably lower than the ionisation energies of neutrals. Because of their relatively weak binding energies, negative ions are readily detached or dissociated through collisions with energetic electrons or photons. Therefore, they generally exhibit limited stability and short lifetimes, which hinders their ability to maintain significant spatial enrichment. Based on these considerations, it can be concluded that positive ions in CAP are more prone than negative ions to aggregate, form, and sustain spatial charge clouds.

Like that discussed in DBDI [104], the plasma process in FμTP also begins shortly after the initial polarisation of the dielectric material due to the sharp rise of the applied HV. The high potential gradient results in the acceleration of electrons around the HV electrode, which then collide with other species producing excited or ionised particles. The sudden acceleration of electrons also causes a large number of positive ions to remain in the capillary bulk. The positive ion clouds in turn accelerate electrons from the capillary bulk to neutralise their positive charges, which leads to excitation and ionisation waves propagating away from the HV electrode.

2.3 Optical emission spectroscopy

Optical Emission Spectroscopy (OES) is one of the most powerful diagnostic techniques widely used for plasma characterisation, which is based on the phenomenon of light emission from plasma. It is achieved by the detection of photons, which are emitted during the process of the transition of excited particles (atoms, ions, and molecules) relax to lower energy states and recombine radiatively with electrons or ions [49, 51, 59, 112, 113]. OES constitutes a non-invasive technique requiring no insertion of electrodes or probes, thereby causing no interference whatsoever with the discharge process. The implementation of this system only needs an observing window and an optical system. It permits simultaneous observation of multiple emission lines (atomic, ionic, and molecular) to derive species information, whilst enabling rapid response or time-domain recording, rendering it suitable for monitoring dynamic discharge processes. At the same time, its limitations must be considered in the measurements. Fox example, observational bias may arise from potential reabsorption/self-absorption effects. Spatial distribution blurring may occur due to the optical line-of-sight integration effect. Currently, system calibration and absolute intensity measurement present challenges. In order to obtain absolute density, absolute calibration is required (referencing standard light sources, transmittance correction, fibre/lens efficiency correction, etc.) [59, 113, 114].

In the case of FμTP, where the discharge channel is confined within a dielectric capillary and driven under atmospheric pressure, electrical diagnostics can be challenging due to geometrical constraints and capacitive effects. Therefore, OES provides an indispensable tool to investigate the discharge properties and plasma dynamics without disturbance. Depending on the measurement configuration, OES can be divided into two main categories: integrated emission spectra (time- and space-averaged diagnostics for basic identification and intensity analysis) and temporally and spatially resolved emission spectra (dynamic and localised plasma analysis). Together, these complementary approaches enable a comprehensive understanding of the discharge mechanism in FμTP.

2.3.1 Optical emission

In an electric field, free electrons are subjected to acceleration and subsequently collide with surrounding particles. If an electron possesses sufficient energy (exceeding a certain threshold), it may be able to

exciting the particle to a higher energy level. The excited particle then undergoes a radiative transition (spontaneous emission) to de-excite back to a lower energy level, emitting a photon [115]. For excited particles, the emission process can be expressed as Equation 2.6.

$$A^{**} \rightarrow A^{*} + h\nu \tag{2.6}$$

For ions, the recombination radiation is expressed as Equation 2.7.

$$A^{+} + e^{-} \rightarrow A^{(*)n} + h\nu_1 \rightarrow A^{(*)n-1} + h\nu_2 \overset{\cdots}{\rightarrow} A^{*} + h\nu_n \tag{2.7}$$

Here, ν is the frequency, and h is the Planck constant. The energy carried off by the photon is equivalent to the energy difference between two states. For each individual particle, there are a multitude of possible transitions. Each transition is characterised by a specific energy difference. The combination of these transitions results in characteristic radiated wavelengths. These wavelengths collectively constitute the "emission spectrum" of the source.

Thus, OES enables the observation of excited-state populations and physical conditions within the plasma, including electron energy distribution, density, and temperature, etc. [59, 112-114, 116]. This is achieved by collecting the emitted photons and measuring their wavelengths and intensities [112, 113]. The emitted intensity I(λ) at wavelength λ is proportional to the population of the corresponding excited states and the transition probability. This can be expressed as Equation 2.8.

$$\mathrm{I}(\lambda) \propto \mathrm{N_i A_{ij}} h\nu \tag{2.8}$$

where N_i is the population of the upper energy level, $\mathrm{A_{ij}}$ is the Einstein coefficient for spontaneous emission, and $h\nu$ is the photon energy [59]. Typical OES analysis involves the identification of atomic and molecular lines, which are commonly observed in atmospheric pressure plasmas. The relative intensity and shape of these lines provide qualitative information on plasma composition, excitation temperature, and energy transfer processes [116]. It should be noted that the transition of a positive ion (A^{+}) to a high-energy excited state (A^{**}) involves electron capture, is often followed by radiative de-excitation to lower excited states (A^{*}) through near-infrared (NIR) photon emission [117, 118].

2.3.2 Integrated emission spectra

In actual experiments, the first step is usually to obtain the integrated emission spectra (also called steady-state spectra, or average spectra) over a certain period of time or under steady-state conditions. By systematically comparing the integrated spectra under different operating parameters (voltage, gas composition, flow rate, etc.), the discharge mechanism might be inferred from the tendency.

Integrated emission spectra reflect the time- and space-integrated optical emission distribution collected from the entire observation area (or along a line of sight) over a given exposure period. This measurement does not discriminate between individual discharge pulses or spatial regions, thus only providing an overall impression of the average radiative characteristics of all active species under

steady-state or quasi-steady plasma conditions. In practice, the emitted light is collected via an optical fibre and guided to a spectrometer equipped with a diffraction grating and a charge coupled device (CCD) detector. The resulting signal is dispersed to obtain the recorded emission intensity I(λ), which is proportional to the population of excited states and, indirectly, to plasma properties, including electron density and electron temperature [59].

Therefore, integrated emission spectra enable the estimation of key physical parameters, such as the relative density or concentration of species. This is typically achieved by analysing spectral line intensity ratios or by integrating line intensities over the total spectrum or background. They are particularly suitable for identifying active species through their characteristic emission lines, estimating excitation temperatures from line ratios of the same species, and monitoring plasma stability because the spectra provide reproducible signatures of operating conditions. Moreover, by comparing the relative intensities of ionic and neutral emissions, integrated spectra enable evaluation of the energy coupling efficiency between the electric field and plasma species. They also facilitate the investigation of how external parameters affect the population and dynamics of excited species [59, 112-114, 116].

Integrated emission spectra are simple, robust, and easy to implement. It has a high signal-to-noise ratio because of long integration times, which is useful for long-term stability and qualitative diagnostics. However, temporal and spatial averaging often conceals important temporal or spatial differences, such as fast or localised phenomena. It has only limited quantitative accuracy when there is no calibration or modelling. Thus, while integrated emission spectra provide valuable overall insights, they must be complemented by temporally or spatially resolved techniques for full understanding.

2.3.3 Temporally and spatially resolved emission

In the context of the study of discharge mechanisms, although integrated emission spectra offers the overall spectral fingerprint of a plasma, it frequently prove to be an inadequate means of revealing the dynamic evolution and propagation/expansion mechanisms of discharge plasmas [114]. Consequently, temporally-/spatially-resolved emission represents a more refined and information-rich approach.

Temporally and spatially resolved emission measurements capture variations in emission intensity as a function of wavelength, time, and position, yielding the recorded I(λ, t, x). By introducing temporal gating and spatial imaging or fibre scanning, transient processes and spatial structures of plasma can be resolved [52, 112, 114, 119]. The technical implementation involves several approaches [59, 112-114, 116, 119]. Time-resolved measurements record emission over distinct temporal intervals (ns ~ μs scale) using fast-gated detection systems such as an intensified charge coupled device (ICCD) or streak cameras synchronised with the power supply trigger. Spatial-resolved measurements acquire spectra at different positions (e.g., along the radial or axial directions) by employing optical arrangements such as slits, collimators, fibre arrays, or optical imaging systems. In certain cases, both methods are combined, enabling the acquisition of emission spectra at multiple spatial positions over several time segments.

This combined method allows for the construction of two- or three-dimensional distribution maps of emission intensity, thereby providing a comprehensive description of plasma evolution.

Compared with integrated emission spectra, this multidimensional diagnostic approach provides a wealth of diagnostic information on discharge dynamics [52, 59, 112-114, 116, 119]. By comparing the intensity distributions of multiple spectral lines over time and space, it enables the investigation of difference in the spatiotemporal behaviour of various particles and energy levels, revealing excitation, relaxation, recombination and other elementary processes. These dynamics are closely linked to parameters such as electron density, excitation temperature, and local electric field strength, allowing for a direct comparison of how different species respond to transient events. Time-resolved imaging further traces the complete discharge sequence, from breakdown or ionisation wave propagation to glow stabilisation and afterglow relaxation, quantifying the transport and expansion of electrons and excited species populations. By mapping axial and radial emission structures, it allows visualisation of plasma morphology, including excitation and ionisation fronts, glow regions, afterglow zones, etc. It also identifies asymmetries or local perturbations indicative of discharge instabilities.

When combined with electrical diagnostics, the spatiotemporal emission dynamics can be correlated with voltage and current waveforms to elucidate discharge triggering, collision-radiation process and power deposition, etc. Moreover, the measured dataset serves as a valuable input for validating or developing discharge mechanism models. The combination of experimental emission maps with numerical simulations enables estimation of local physical parameters and assessment of the consistency between observation and theory, thereby supporting a comprehensive reconstruction of plasma kinetics, transport, and collision-radiation equilibrium processes.

In short, temporally and spatially resolved emission provides dynamic and localised insight into plasma behaviour, facilitates correlation between optical and electrical diagnostics, and also supports quantitative modelling of discharge kinetics. However, it always requires complex, synchronised instrumentation. In addition, only reduced signal intensity can be obtained due to short gating times. Nonetheless, for FμTP, it remains one of the few non-intrusive techniques to visualise plasma dynamics and understand the discharge mechanisms.

In summary, OES serves as a cornerstone diagnostic for the study of plasma discharges. Integrated emission spectra provide averaged spectral fingerprints useful for qualitative and semi-quantitative plasma characterisation. Temporally and spatially resolved emission reveals the underlying discharge dynamics, transient species evolution, and plasma structure. The combined use of these techniques offers a comprehensive multi-scale understanding of plasma excitation processes and contributes to elucidating the fundamental discharge mechanisms in FμTP systems.

CHAPTER 3

Investigation of the discharge mechanisms in *He*- and *Ar*-FμTPs

When a FμTP is employed as an ionisation source coupled to a mass spectrometer (MS) for analysis, the capillary exit is usually placed in front of the MS inlet. However, detected MS signals are relatively low if the electrode tip is too far away from the outlet of the discharge capillary, such as 30 mm [23, 24]. Therefore, a short discharge distance is typically selected, generally 3 mm in analytical applications, for instance. To clarify the mechanisms behind plasma behaviour under such operation conditions, further investigations of FμTP are urgently needed to be carried out and discussed. In this chapter, the discharge mechanism of FμTP will be investigated in a 3 mm long discharge column, which was defined as the volume from the electrode tip to the capillary outlet.

Both noble gases Helium (*He*) and Argon (*Ar*) can be used as working gas of the plasma-based ionisation sources for analytical applications. The ignition and sustaining voltage of a *He*-plasma is usually lower than that of an *Ar*-plasma, greatly increasing the usability of *He*. Thus, the ionisation mechanism of a *He*-plasma has been widely characterised and accepted. It has long been assumed to be similar to APCI, where N_2^+ as a significant species through Penning ionisation is considered to be directly related to the generation of a protonated water cluster [3]. Considering the relatively low price of *Ar* (10 ~ 35 % of *He*), more and more plasma-based applications switch to *Ar* as discharge gas. Unexpectedly, *Ar*-plasmas can compete with *He*-plasmas and sometimes even get better LOD [120, 121]. However, its ionisation mechanism is still challenging since no N_2^+ can be produced through Penning ionisation in *Ar*-plasma as present in *He*-plasma [122]. Moreover, the physical background of *Ar*-plasma has also not been clarified yet.

In this chapter, the discharge properties of plasmas using not only *He* but also *Ar* as discharge gas will be investigated comprehensively in the same configuration. One of the key elements is the comparison of the discharge behaviours derived from several discharge gases. Another element will show the propagation of plasmas during the falling half-phase and then compare with the rising half-phase. The objective of the present study is to undertake a systematic comparison of *He*- and *Ar*-plasmas, with a view to identifying both the commonalities and the differences between them with regard to the discharge mechanism. Moreover, it offers a reference for further applications of plasma, notably as a soft ionisation source in the field of analytical chemistry. The elucidation of these two plasmas was published in 2024 in the context of this work [25].

3.1 Experimental arrangement

The experimental arrangement used in this chapter is shown in Figure 3.1, where the longitudinal axis of the discharge capillary, the vertical axis of the lens, and the slit of the spectrometer are aligned parallel to each other. The distance between the electrode tip and the end of the capillary is fixed to 3 mm, which is consistent with the actual MS applications in real life [9, 10, 20].

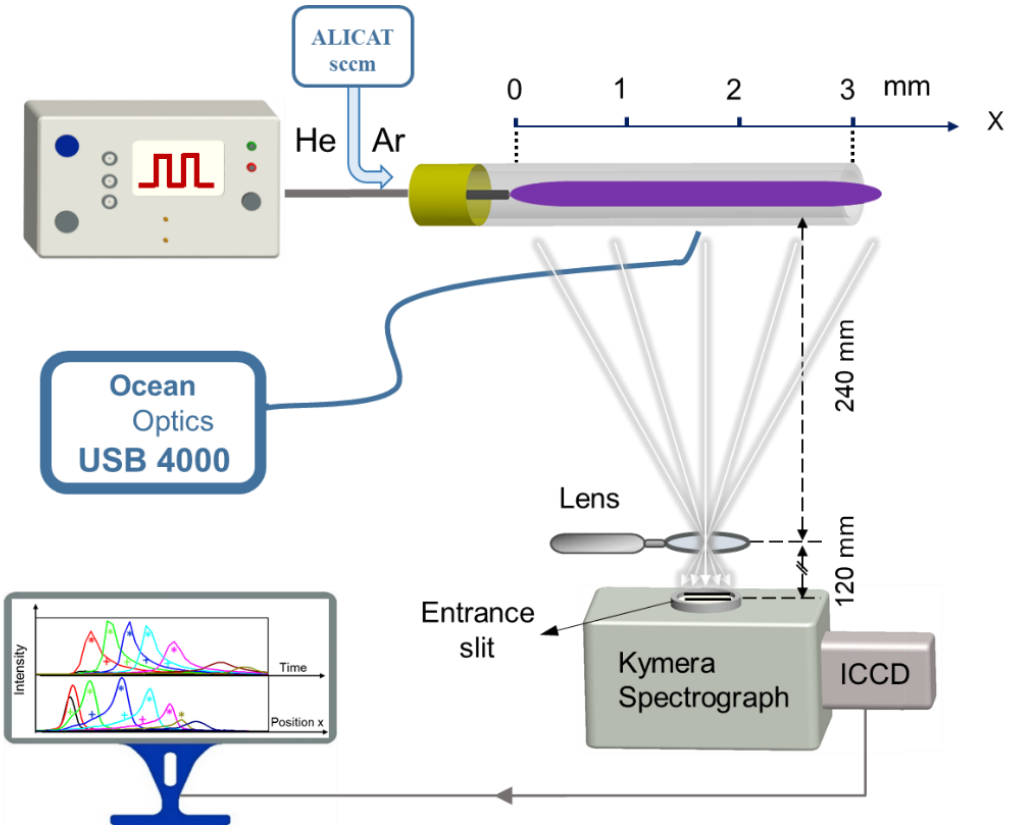

Figure 3.1: Experimental arrangement for the characterisation of plasmas along the discharge capillary.

An USB 4000 spectrometer (Ocean Optics, USA) with a wavelength range of 300 - 900 nm and a resolution of 1.9 nm is used for full spectral information of the reactive species. The optical fibre is installed perpendicular to the discharge capillary axis at a distance of 1 mm. To obtain the spatiotemporal

optical emission information of the plasma, the DH 720 18F-03 ICCD camera (Andor Technology, UK) is utilised. It allows continuous imaging with a minimum time resolution of 5 ns. This camera is connected with a Kymera 193i adaptive focus imaging spectrograph (Andor Technology, UK) to achieve spectral resolution in the range of 200 ~ 900 nm, which achieves both spectrally resolved and spectrally integrated measurements of discharge evolution behaviours. For the time-resolved images, integration on the chip was chosen because light emission in a single exposure is insufficient to obtain clear images, even with a gate width of up to dozens of nanoseconds.

For complete plasma emission imaging, a quartz convex lens with a focal length of 75 mm is placed between the plasma and the entrance slit (set in a width of 200 μm). The object and image distances are about 240 and 120 mm, respectively. A diffraction grating comprising 1200 grooves per millimetre is set to obtain a resolution of 0.21 nm. For achieving an adequate emission intensity and an acceptable acquisition time, the gate and step widths are set differently depending on the specific plasma.

The tungsten electrode is directly connected to a home-built power supply capable of external triggering. The power generator provides a square wave voltage with a sharp rising edge (reach 1.7 kV in 50 ns, maximum V_{pp} of 3.5 kV). In this chapter, the bipolar voltage (NP) with a frequency of 20 kHz and duty cycle of 50:50 is applied to drive the plasma. The synchronous function generator (Musashino, Japan) was utilised to ensure the synchronisation of the ICCD system with the power supply. This was accomplished by employing two simultaneous signals that were used as trigger signals for the two, respectively. The detailed voltages for various plasmas are presented in Table 3.1. Various gaseous mixtures are used as discharge gases in this work, different conditions are then chosen accordingly, which are listed in Table 3.1.

Table 3.1: Experimental conditions used for the study

Plasma type	Propane concentration (ppm)	Applied voltage: V_{pp} (kV)	Gate width (ns)	Step width (ns)	Integration time (ms)
He-FμTP	0	2.5	10	10	20
Ar-FμTP	0	3.0	10	10	20
		2.8	5	5	/
		2.9	5	5	/
Ar-propane-FμTP	2000	2.2	5	5	/
Ar-propane-FμTP	4000	2.2	5	5	/
		2.0	5	5	/

" / " : not applicable

In this section, typical *He* 5.0 and *Ar* 5.0 (both from Westfalen Austria GmbH) were supplied as discharge gas. Since a slightly lower ionisation energy than the metastable state of *Ar* and the cheapness, propane was chosen as an additional impurity to be added to *Ar* as a discharge gas [122-124]. A gas mixture of 10,000 ppm (parts per million) propane in *Ar* was compounded to get any specific concentration from 100 ppm to 10,000 ppm, this is accomplished by combing the gas mixture with *Ar* 5.0 through two gas flow controllers. The gas mixture was prepared in-house through an evacuated gas bottle: Firstly, a specific amount of propane 3.5 (purity 99.95%) was injected into the empty bottle by utilizing an ordinary syringe. Then, the cylinder was filled with *Ar* 5.0 until the pressure reached 5 bar. Thus, an *Ar* gas mixture with 10,000 ppm propane was yielded. The discharge gas with a stable flow rate in total of 50 standard cubic centimetres per minute (sccm) controlled by gas flow controllers (Alicat Scientific) is introduced in a precision of ±0.5%. The mass flow mode is selected because the same amount of gas particle (molar quantity) per unit time can always be supplied in this case, regardless of the particle weight. This is beneficial for the investigation of various plasmas like *He*-, *Ar*- and *Ar*-propane-FμTP.

3.2 Overview of species in *He*- and *Ar*-FμTPs

Integrated spectral measurement of the emission lines for different plasmas can provide a general overview of the species involved within the detection range of the spectrometer. This is the basis for further characterisation of an individual plasma. For this reason, the first measurements of reactive species are obtained using an USB 4000 spectrometer for *He*-FμTP and *Ar*-FμTP and the results are presented in Figure 3.2. The optical fibre of the spectrometer is positioned in the middle of the discharge column (at x = 1.5 mm). The wavelengths of the measured species generated in both plasmas differ from each other.

In case of *He*-FμTP, the emission of the excited hydroxyl band (OH), molecular N_2 (the second positive system SPS (N_2 (C) → N_2 (B)), N_2^+ (the first negative system FNS (N_2^+ (B) → N_2^+ (X)), excited atomic *He* and O species are observed, in which N_2^+ 391 nm is the dominant one. These are expected and consistent with the results presented [24, 26], which means that the spectra measured at the middle of the discharge column are typical spectra of the discharge gas without the interference of ambient air. Since the diffusion of ambient air only takes place in the vicinity of the capillary exit under such conditions with a gas flow of 50 sccm and an inner diameter of 250 μm, interference to the inner part plasma can be neglected. Therefore, these species must result from impurities in the discharge gases itself. For *He* 5.0, its composition consists of 3 ppm H_2O, 2 ppm O_2 and 5 ppm N_2. In *Ar*-FμTP, besides a series of excited *Ar* lines from around 650 to 850 nm as marked in the Figure 3.2 (b), the emissions of excited hydroxyl (OH) and molecular N_2 (SPS) are also observed, which originate from the impurities in *Ar* 5.0 (including 3 ppm H_2O, 2 ppm O_2 and 5 ppm N_2).

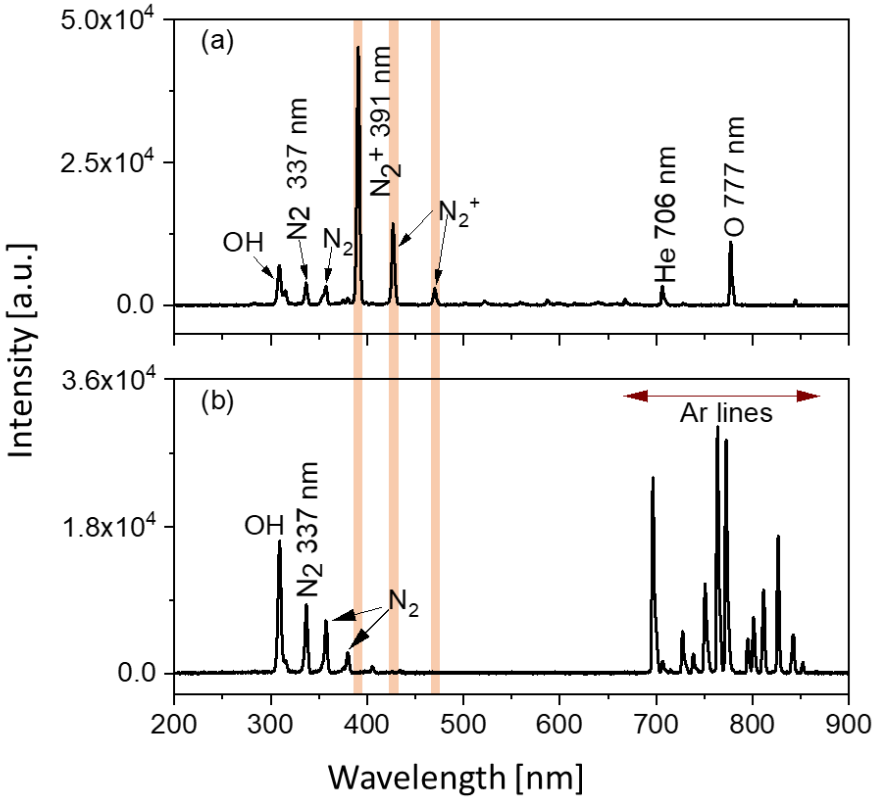

Figure 3.2: The emission spectra of the He- and Ar-plasmas at x = 1.5 mm. (a) He-FμTP, (b) Ar-FμTP. The integration time is 20 ms for both plasmas.

One of the major differences of the emission spectra in these two plasmas is N_2^+ (FNS). In *He*-plasma, FNS are generated due to the collision of the molecular N_2 present in the discharge gas with electrons and *He* metastables (He^M) and the emission intensity of N_2^+ 391 nm is even the highest. The emission intensities of spectral lines are related to the density of excited state particles at the upper energy level. In *Ar*-plasma, no FNS is identified even though an equivalent molecular content of N_2 was involved, meaning that very little or even no N_2^+ (B) is generated. The primary reason for this is suspected to be the significant deficiency in energy of *Ar* metastables (Ar^M) to produce N_2^+ (B).

The optical transition from a metastable state to the ground state is forbidden, and the metastable state can only lose its energy by collision with other partners or with the wall of the capillary. So, they usually have a high population in cold temperature plasmas because of their long lifetimes, which are four to five orders of magnitude higher than almost all other excited states [59, 122, 125]. Therefore, there is a much higher probability for metastable collisions with other molecules and atoms than for collisions of all other excited states. In contrast, other excited states can lose energy by fast spontaneous optical transitions to lower states, or directly to the ground state in the case of resonant transitions [59]. It is evident that, due to their considerably shorter lifetime, these states are unlikely to collide with other species.

The energetic states of these main species are shown in Figure 3.3. The energy level of N_2^+ B $^2\Sigma_u^+$ is lower than that of He^M marked as $M^{S/T}$, which are two types of metastable levels of *He*, a singlet M^S and

a triplet M^T level. The energy level of He^M is high enough to generate the state of N_2^+ B $^2\Sigma_u^+$ by collisions with N_2 in the state of N_2 X $^1\Sigma_g^+$. The Ar^M energy level is lower than that of the N_2^+ B $^2\Sigma_u^+$ state. Therefore, it is not possible to produce the N_2^+ B $^2\Sigma_u^+$ state by the collision of Ar^M with the N_2 X $^1\Sigma_g^+$ state. However, N_2^+ X $^2\Sigma_g^+$ might be possible to be produced by Ar^+. Since the lifetime of Ar^+ is much shorter than that of Ar^M, the corresponding production of N_2^+ X $^2\Sigma_g^+$ is very little.

Similarly, since the energy required for the generation of O 777 nm is at least 15.89 eV (5.15 eV for dissociation of O_2 molecule and 10.74 eV for excitation of O atom), which is higher than the energy of Ar^M, excited O atoms are not likely to be generated in *Ar*-FμTP. It should be pointed out that the emission intensities of the same wavelength obtained from these two plasmas should not be directly compared because of the different experimental conditions used.

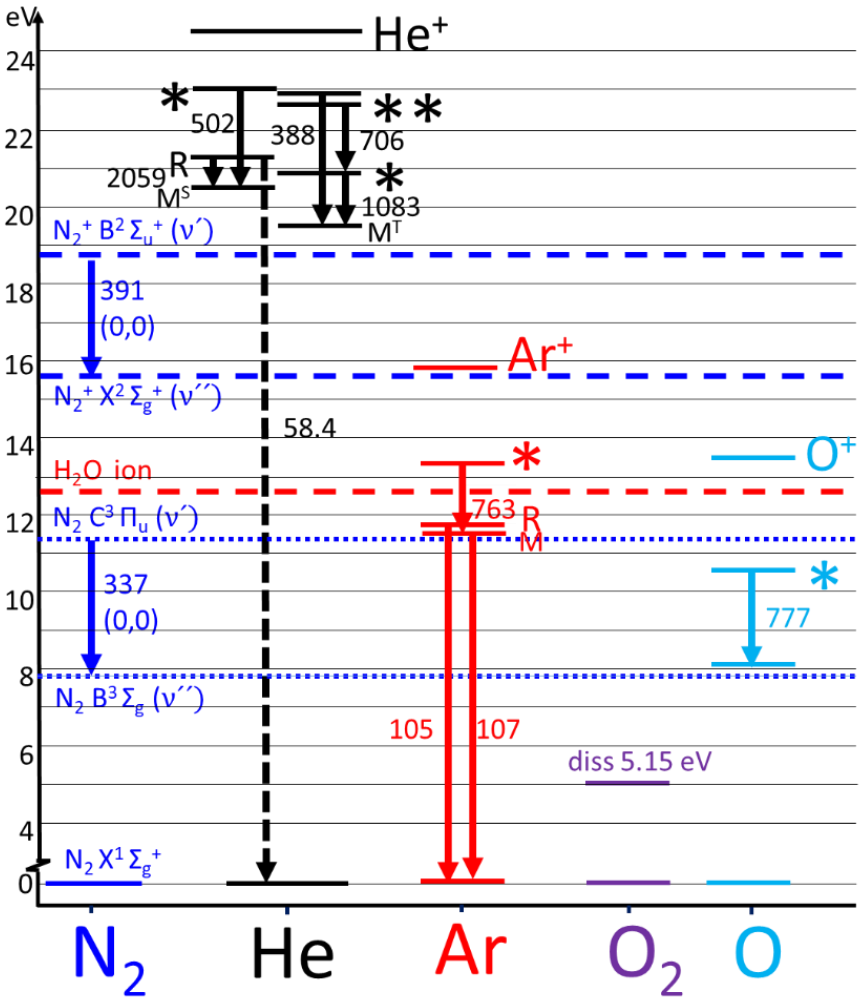

Figure 3.3: Energetic states of N_2 and N_2^+ (dark blue), He (black), Ar (red), propane (green), O_2 (purple) and O (light blue). The schematic shows some selected energy levels and associated optical transitions with their respective wavelengths. The numbers at the transitions are the wavelength in [nm].

3.3 Temporally and spatially resolved plasma emission

3.3.1 Data acquisition and processing

After we know the important reactive species involved in the plasmas used here, the generation and propagation behaviour of the main species within the capillary are also important for further exploration of their discharge mechanisms. The wavelengths of *He* 706 nm, N_2^+ 391 nm, and O 777 nm generated in *He*-FμTP and N_2 337 nm, and *Ar* 763 nm generated in *Ar*-FμTP are chosen as representative of the individual plasma source for the following measurements. The selection of these wavelengths is achieved by changing the central wavelength of the spectrometer using the Andor Solis software. To record these processes, the temporally and spatially resolved plasma emission evolutions were measured by the Kymera Spectrograph with an ICCD camera.

Usually, to give an overall perspective to the whole plasma evolution, the measured data are normally visualised as reference two-dimensional (2D) colour plots. As shown on the left side of Figure 3.4, the emission intensities are displayed in different colours depending on the time and position. However, since only a few colours can be recognised, such plots have a low resolution of the intensity dependent on time and position, thus losing information. It should be noted that the adjacent instants of time and neighbour positions also contribute to the actual intensity to varying degrees. Besides, in instances where multiple peaks emerge at distinct moments at a given position or multiple peaks appear at disparate positions at a particular moment, the relatively smaller ones are always obscured and fail to be recognised.

To shed more light on the importance of contributing states and species, a so called “phoresis plot” is introduced [25]. In this kind of plot, the data is extracted and replotted in two different kinds of 2D curves. The emission intensities are presented separately as a function of time for multiple discrete positions and as a function of position for multiple moments. These processes are performed for all active species referred to in this chapter. It is necessary to point out that the “phoresis plot” in this work is not meant by a traditional technology that separates charged particles based on various mobility in the electric field, but rather a method of signal analysis. The repeated development of excitation and ionisation waves along the capillary is accompanied by the constant production of reactive species. It should be noted that these species are also separated in signals for reasons that will be explained later.

3.3.2 Time dependent behaviour of *He*-FμTP during the rising half-phase

Figure 3.4 shows the temporal and spatial emission of the *He* 706 nm, N_2^+ 391 nm, and O 777 nm lines measured in *He*-FμTP during the rising half-phase. The emission intensities of these three species as a function of time at different positions are shown on the right side of the Figure. The corresponding positions are inserted into sub-plots, where the distance step of 0.5 mm is used. For example, the curve

of 0 mm represents the emission measured at the electrode tip, the curve of 3.5 mm represents the emission obtained at 0.5 mm away from the exit beyond the capillary end.

The emission intensities of *He* 706 nm from the position of 0.5 mm to 2.5 mm are nearly the same with a slight decrease. The shape and the constant time-full width at half maximum (t-FWHM) are stable, which are only shifted in time. When the plasma reaches the capillary end, x = 3 mm at 0.27 μs, the intensity of *He* 706 nm becomes higher than those at lower positions. The emission intensity represents directly the density of the excited He^{**} state, as marked in Figure 3.3 and indirectly the density of He^{*} from which the only transition (1083 nm) to the 2s $^3S_1$ (He^M) state is allowed. Therefore, the emission intensity of *He* 706 nm is an indirect measurement of the density of He^M. It is at least related to the increase part of signal when He^M are populated by a transition from He^{*}. The shape of the decrease part of He^M would be differentiated to the shape of *He* 706 nm due to the significantly longer lifetime of He^M. Unfortunately, the density of He^M cannot be measured directly by the absorption of *He* 1083 nm since the diameter of discharge capillary is too small to align a laser through the capillary perpendicular to the axis of the capillary. Consequently, it is impossible to ascertain its density in both the increasing and decreasing parts of the signal.

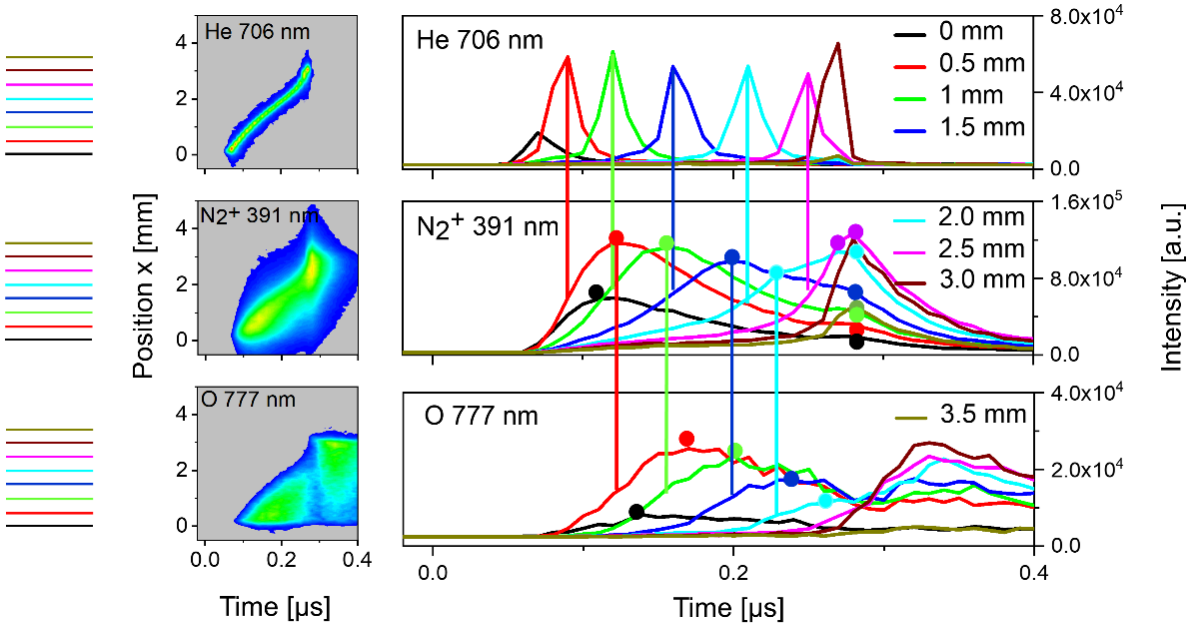

Figure 3.4: Two dimensional colour plots in time and position and the related phoresis plots for the emission intensities as a function of time at different positions during the rising half-phase for He 706 nm, N_2^+ 391 nm and O 777 nm measured in He-FμTP with an applied voltage of 2.5 kV. The lines of different colours on the left represent the process of obtaining values from the corresponding positions over the entire observation time.

The N_2^+ B $^2\Sigma_u^+$ state can be produced by collision of He^M with N_2 in the grounded state (N_2 X $^1\Sigma_g^+$), which is called Penning ionisation. The signal measured at 391 nm is detected due to the transition from N_2^+ B $^2\Sigma_u^+$ to N_2^+ X $^2\Sigma_g^+$, as shown in Figure 3.3. Therefore, information on He^M can be supplemented by measuring and understanding the signal of N_2^+ 391 nm.

Comparing the signals of *He* 706 nm and N_2^+ 391 nm along the capillary, the maximum of N_2^+ 391 nm is later than the maximum of *He* 706 nm at the same position as marked by the vertical colour lines in Figure 3.4. The integrated area under the *He* 706 nm signal leads to the increase part of the N_2^+ 391 nm signal. Once the emission intensity of *He* 706 nm reaches its maximum, the increase rate of N_2^+ 391 nm is also the highest. When the emission intensity of *He* 706 nm starts decreasing, the increase rate of N_2^+ 391 nm starts slowing down gradually until its intensity reaches the maximum which is illustrated by the derivatives of the temporal profiles of N_2^+ 391 nm shown in Figure 3.5. The decrease part of the N_2^+ 391 nm signal is replied to in the slow decline process of the N_2^+ B $^2\Sigma_u^+$ state. As the N_2^+ B $^2\Sigma_u^+$ state is directly related to the signal of He^M, N_2^+ 391 nm can be treated as an indirect indicator for the decrease part of He^M.

The one maximum of the N_2^+ 391 nm signals is shifted in time with respect to the corresponding maxima of *He* 706 nm ($t_{He} < t_{N2+}$), as shown in Figure 3.5. This means that the ions are generated later than the excited neutrals, it is related to the generation mechanisms of these two specific emission signals. When the rising half-phase comes, a positive potential is applied to the electrode and quickly reaches the set voltage ($t_1 > 0$, $x = 0$). In this condition, the electrons will be attracted towards the electrode and accelerated in the electric field. *He* will be excited to He^{**} by the collision of *He* atoms with these energetic electrons. He^{**} will then decay to He^* by emitting 706 nm and further to He^M, resulting in the production of N_2^+ B $^2\Sigma_u^+$ through Penning ionisation.

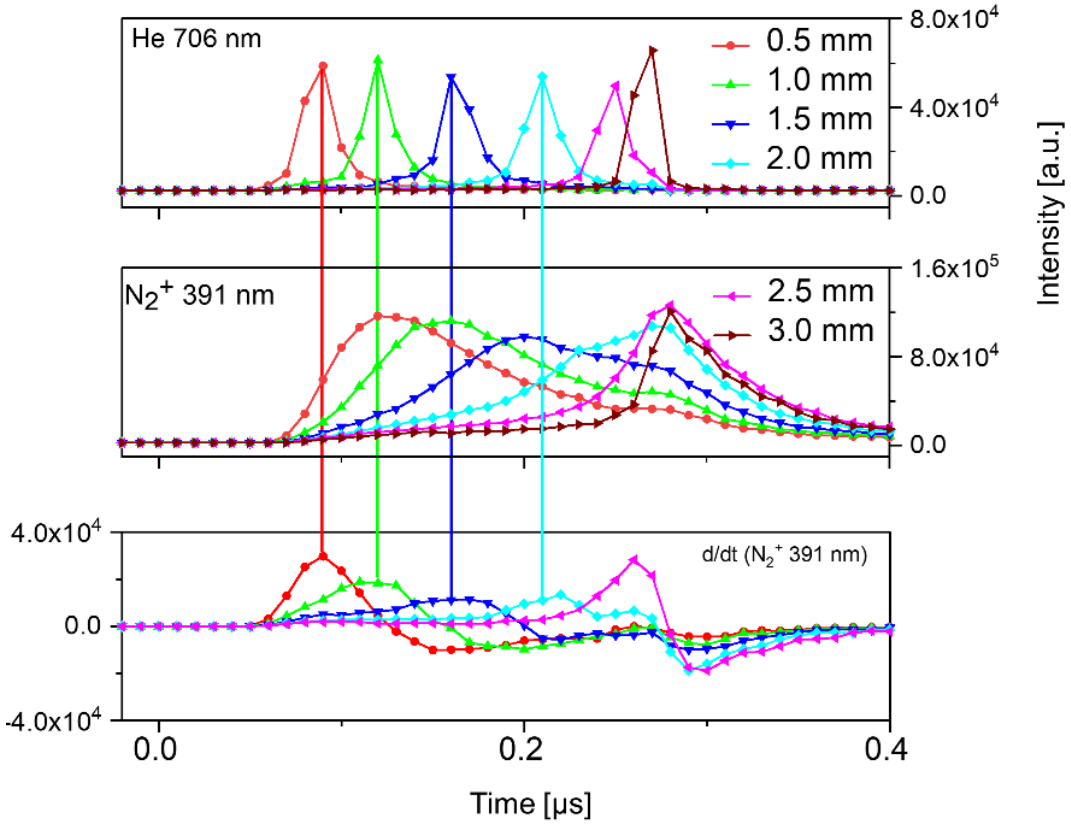

Figure 3.5: Phoresis plots for emission intensities as a function of time at different positions during the rising half-phase for He 706 nm and N_2^+ 391 nm measured in He-FμTP, and d/dt (N_2^+ 391 nm).

At a later moment ($t_2 > t_1$, $x = 0$), N_2^+ creates a new transient potential. The ions creating the local potential will move in the electric field in the time period of $\Delta T = t_2 - t_1$, which will be responsible for the further excitation of He^{**}, He^*, and He^M at the next position ($x_1 > 0$). That new metastable will initiate another new transient potential, causing further development of excited neutrals and ionised species along the capillary. As a result, the excitation and ionisation waves move forward until the potential is not sufficient to sustain the next round of excitation. So, the production of excited neutrals is dependent on the presence of a temporally and spatially limited potential formed by ions in the capillary. This will also be discussed in the next section with regard to the emission intensity as a function of position at different moments.

It is proposed that the stationary plasma visible to human eyes is actually the result of a repetitive development process of excitation and ionisation waves [126-129]. All maxima of N_2^+ 391 nm for each position are indicated by colour dots as shown in the sub-plots of N_2^+ 391 nm in Figure 3.4. Nevertheless, each curve has more than one maximum. If there are two dots, this means that there are two maxima at each position but at different instants of time. The development of the first maximum has been explained above, which is responsible for the propagation of excitation and ionisation waves along the capillary. The second maximum is observed for all positions, which means that there exists another source for the generation of N_2^+ B $^2\Sigma_u^+$, which is different from the one interpreted above.

Since N_2^+ is generated step by step along the capillary, some of them attach to the inner wall of the capillary on their generation journey. After N_2^+ B $^2\Sigma_u^+$ is produced by Penning ionisation, electrons with a remaining energy of approximately 1eV (the energy difference between He^M and N_2^+ B $^2\Sigma_u^+$) are yielded and then can be collected by N_2^+ B $^2\Sigma_u^+$ ions attached on the inner surface. Once the excitation and ionisation waves reach the capillary exit at 0.27 μs, the potential gradient in the discharge column becomes very small thereby resulting in a weakness of the electric field and thus a sharp decrease in the kinetic energy of electrons over the whole capillary. This increases the possibility of detachment and recombination of N_2^+ B $^2\Sigma_u^+$ from the inner wall. These ions decay to the lower state and emit 391 nm at the same time.

Therefore, a possible interpretation for the second maximum of N_2^+ 391 nm observed simultaneously for all positions is the result of the detachment and recombination of N_2^+ B $^2\Sigma_u^+$ attached on the wall. In addition, the closer to the end of the capillary, the stronger is the second maximum of N_2^+ 391 nm. This is because the farther away from the capillary nozzle, the longer time for surface ions to detach and recombinate during plasma propagation, leading to less N_2^+ B $^2\Sigma_u^+$ remaining.

In addition to *He* 706 nm and N_2^+ 391 nm, the emission of O 777 nm is also carried out, which is another indirect indicator of the existence of He^M [105]. As mentioned above, the energy required for the generation of O 777 nm is at least 15.89 eV. The He^M states with 19.8 and 20.9 eV and the N_2^+ B $^2\Sigma_u^+$ state with 18.8 eV have enough energy to perform the aforementioned reactions. Although N_2^+ X $^2\Sigma_g^+$ with 15.6 eV could gain another 0.25 eV energy supply by acceleration in the electric field to meet the

energy difference for these reactions, N_2^+ X $^2\Sigma_g^+$ are easily to be quenched by other collision partners. Therefore, only two collision partners are supposed to be able to contribute to the generation of excited O. One is the neutral He^M and the other is N_2^+ in the N_2^+ B $^2\Sigma_u^+$ state.

The temporal and spatial emission shape of O 777 nm was more similar to the shape of *He* 706 nm rather than N_2^+ 391 nm [24]. However, the energy difference between the N_2^+ B $^2\Sigma_u^+$ state and the energy required for the generation of O 777 nm is lower compared to the He^M states. In order to identify the exact generation mechanism of O 777 nm, an intuitive comparison was done with the help of their related phoresis plots.

As shown in the subplot of O 777 nm in Figure 3.4, the increasing slopes of emission intensity are gentler than those of N_2^+ 391 nm and *He* 706 nm, which could be attributed to a two-step reaction that occurs for the formation of the O*. Nevertheless, the time intervals between the corresponding maxima of O 777 nm marked by colour dots are comparable to the corresponding intervals of N_2^+ 391 nm, but shifted. Furthermore, when the maximum of N_2^+ 391 nm is reached and the generation of N_2^+ B $^2\Sigma_u^+$ is no longer increasing, the increase rate of O 777 nm almost reaches the maximum and starts slowing down, as can be seen from the derivatives of the temporal emission profiles of O 777 nm in Figure 3.6. Such phenomenon is similar to the relationship between *He* 706 nm and N_2^+ 391 nm.

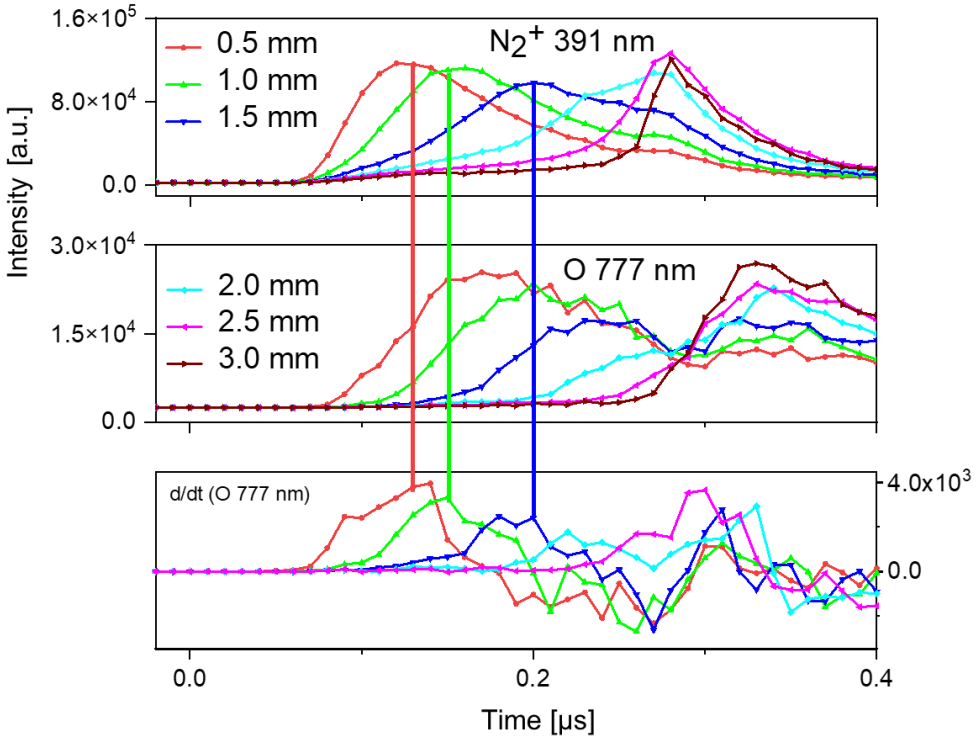

Figure 3.6: Phoresis plots for emission intensities as a function of time at different positions during the rising half-phase for N_2^+ 391 nm and O 777 nm measured in He-FµTP and d/dt (O 777 nm).

A second maximum of O 777 nm along the capillary is also observed, which follows the second maximum of N_2^+ 391 nm. In addition to electrons, O_2 can also be collected by N_2^+ B $^2\Sigma_u^+$ attached on the wall and thus be dissociated and excited to O*. However, such a process is apparently slower than

the recombination of N_2^+ B $^2\Sigma_u^+$ with electrons due to the higher density and mobility of the electrons compared to O_2. Therefore, it can be interpreted that the dissociation of O_2 to O atoms and the subsequent excitation of the O atom to O* seem to be attributed more to the collisions of O_2 with N_2^+ B $^2\Sigma_u^+$ than with He^M in the rising half-phase.

When rescaling the time dependent phoresis plots of *He* 706 nm, the second maximum at the same instant of time can also be observed in Figure 3.7 as marked by a vertical line. This is the same moment when the main peak of *He* 706 nm reaches the end of the capillary at 0.27 µs. Taking into account the interpretation of the second maximum of *He* 706 nm, it is supposed that He^+ is also produced in the plasma and some He^+ are attached to the inner wall of the capillary during plasma propagation along the capillary, just as N_2^+ B $^2\Sigma_u^+$ did. In the event that He^+ collects slow electrons, they are detached from the wall. This supposition is supported by the decay of He^+ to He^{**} through NIR emission, and *He* 706 nm signal responds to the transition from the He^{**} state to the He^* state. Therefore, He^+ can also be measured by the signal of *He* 706 nm.

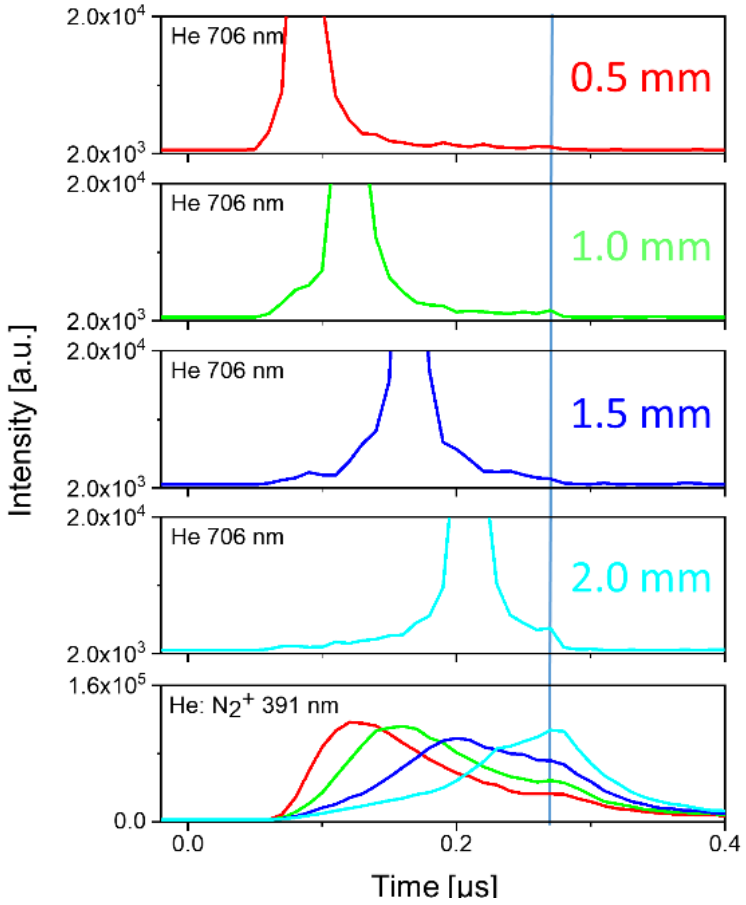

Figure 3.7: Rescaled phoresis plots for emission intensities as a function of time at different positions during the rising half-phase for He 706 nm and N_2^+ 391 nm measured in He-FμTP. The second maximum at t = 0.27 µs (line) is the result of He^+ detached from the wall that is depopulated by NIR emission.

For quantitative comparison, an estimate of the densities of N_2^+ and He^+ in a *He*-FµTP is calculated for the position x = 1.0 mm. Figure 3.8 shows the *He* 706 nm signal on two different scales and the signal of N_2^+ 391 nm at the same position. The peak intensity of He^{**} is read as 60000. Based on the previously described principle that the production of excited neutrals and ionised species is related to the presence of local potential formed by ions in the capillary, the productivity of He^+ also depends on N_2^+ due to the requirement of a strong electric field for electron collision. Therefore, the expected He^+ peak at the time corresponding to the first maximum of N_2^+ 391 nm, as marked by a vertical line, can be directly read off.

According to the peak value of 112122 a.u. for N_2^+, the intensity of He^+ is estimated with an absolute maximum lower than 5815 a.u.. So, it can be estimated that the value of He^{**}/He^+ is greater than 10. In such low temperature plasmas, the density of the metastable is about 10^{13} cm^{-3}, which is 10 times higher than that of the excited ones [125]. Thus, the density of He^{**} is only about 10^{12} cm^{-3}. Based on the ratio of He^{**} to He^+, He^+ with a density of 10^{11} cm^{-3} can be estimated. At room temperature and atmospheric pressure, the molecular density of the gas is approximately $2.5*10^{19}$ cm^{-3}. With 3 ppm N_2 molecule in *He* 5.0, which means the maximum density of impact partners for the metastable is $7.5*10^{13}$ cm^{-3}. As a result, the density of N_2^+ produced by metastable (10^{13} cm^{-3}) through Penning ionisation can be estimated to be not greater than 10^{13} cm^{-3}. This reveals that the density of N_2^+ is at most two orders of magnitude higher than the density of He^+. Therefore, N_2^+ can be treated as the key ion that supports plasma propagation in the rising half-phase.

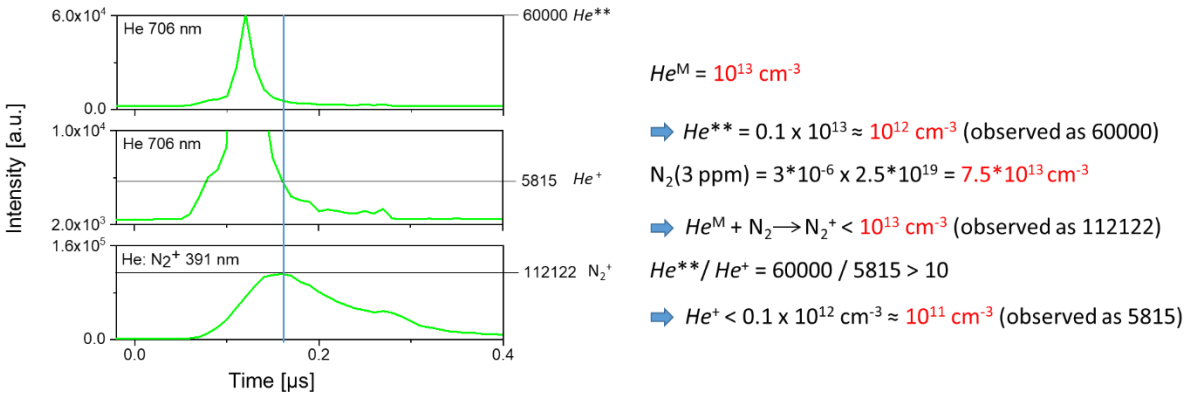

Figure 3.8: Rescaled phoresis plots for emission intensities as a function of time at position x = 1.0 mm during the rising half-phase for He 706 nm and N_2^+ 391 nm measured in He-FµTP.

3.3.3 Position dependent behaviour of *He*-FµTP during the rising half-phase

From the discussion of *He* 706 nm and N_2^+ 391 nm in Figure 3.4, it is shown that excited neutrals and positive ions are generating along the capillary, in which positive ions are responsible for the next round of excited neutral production. This can also be demonstrated by the propagation of the *He* 706 nm signal and the N_2^+ 391 nm signal when their emission intensities are presented as position dependent at different instants of time. It provides a second perspective for analysis, which is shown in Figure 3.9.

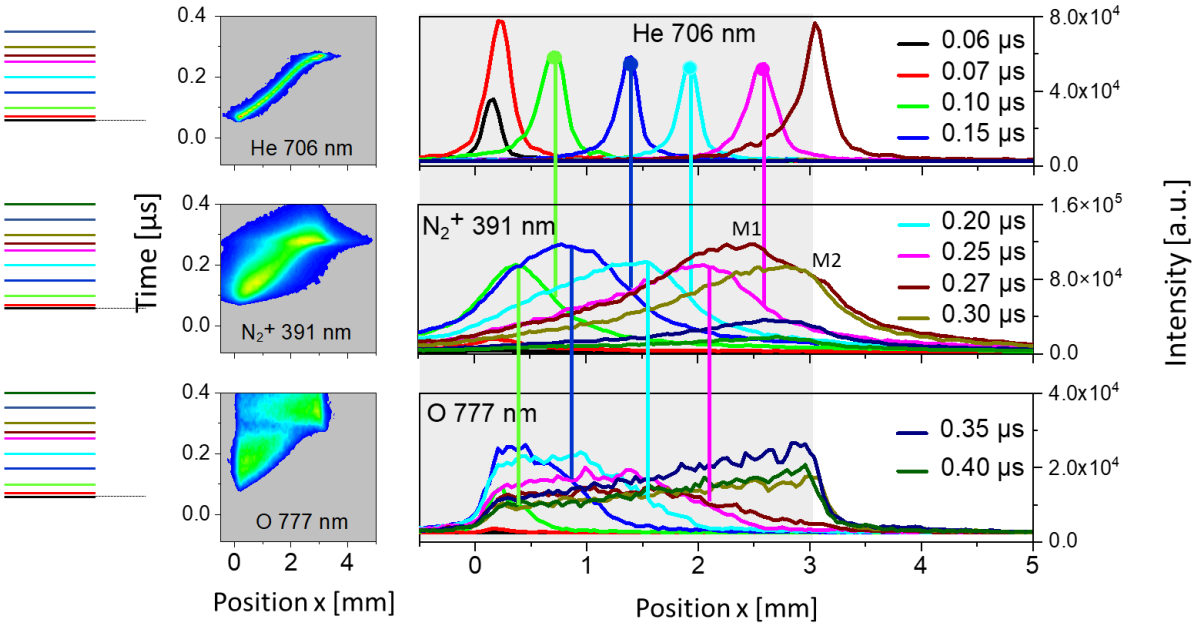

Figure 3.9: Two dimensional colour plots in time and position and the related phoresis plots for the emission intensities as a function of position at different instants of time during the rising half-phase for He 706 nm, N_2^+ 391 nm and O 777 nm measured in He-FμTP with a voltage of 2.5 kV. The lines of different colours on the left represent the process of obtaining values from the corresponding instants over the entire observation range.

From 0.06 μs to 0.07 μs, the emission intensities of *He* 706 nm and N_2^+ 391 nm are increasing. It is known from the measurement of *He* 706 nm that He^M are populated, which collide with the N_2 molecule in the ground state, producing N_2^+ B $^2\Sigma_u^+$ by Penning ionisation. From 0.07 μs to 0.25 μs, each maximum of N_2^+ 391 nm follows that of *He* 706 nm, as illustrated by the vertical colour lines. In this time frame, the maximum of *He* 706 nm decreases slightly with time.

At 0.27 μs, the plasma propagates to the end of the capillary. The maximum of *He* 706 nm is higher than during the previous moments and is even comparable to that at 0.07 μs. It shows a slightly asymmetric shape with a wing on the left side (smaller x) of the peak for each curve and particularly for 0.27 μs. As explained above, excited and ionic *He* species are involved in *He*-FμTP, and they are usually considered to be produced by direct collisions of high-energy electrons with *He* atoms. Due to the fact that the ionisation energy of *He* is higher than the excitation energy, the electrons would have to be accelerated for a longer distance in a certain electric field to meet the required energy. Thus, it is suggested that the wing (on the left side) of each line is contributed by He^+, and the maximum results are obtained from He^{**}.

In case of N_2^+ 391 nm signal, two maxima are observed at 0.27 μs signed with M_1 and M_2 in the plot of N_2^+ 391 nm in Figure 3.9. The first maximum M_1, is even higher than the one measured at 0.25 μs although the previous ones (from 0.15 to 0.25 μs) are decreasing. This increase in measured intensity can be explained as the emission overlap of N_2^+ B $^2\Sigma_u^+$ generated by collisions with He^M and N_2^+ B $^2\Sigma_u^+$ detached from the capillary wall. This is in correlation with the previous result that the intensity of the second maximum for N_2^+ 391 nm is stronger when closer to the capillary end as shown in Figure 3.4. In

addition, no or ignorable *He* 706 nm signal is detected at 0.3 µs, while a strong signal of N_2^+ 391 nm through the capillary is still measured at this moment and even at 0.35 µs. This signal originates from the recombination of N_2^+ which is detached from the glass wall as explained above.

For O 777 nm, there are two parts as shown in its subplot. Up to 0.27 µs, the maximum of O 777 nm follows that of N_2^+ 391 nm as marked by vertical colour lines. From 0.3 µs, the signal of O 777 nm is still detectable through the capillary and the maximum turns towards the capillary end. Comparing the emission shape and distribution with those of *He* 706 nm and N_2^+ 391 nm, it can be seen that O 777 nm is more similar to N_2^+ 391 nm than *He* 706 nm. This is further evidence that the dissociation of O_2 and the subsequent excitation of O to O* is initiated directly by collisions with N_2^+ B $^2\Sigma_u^+$.

Since N_2^+ B $^2\Sigma_u^+$ is produced by collisions of He^M with N_2 X $^1\Sigma_g^+$, and O* is produced by direct collisions of N_2^+ B $^2\Sigma_u^+$ and indirect collisions of He^M with O_2, the decreasing parts of the emission shape of N_2^+ 391 nm and O 777 nm indirectly indicate the presence of He^M. Furthermore, it shows not only the ionisation of N_2 X $^1\Sigma_g^+$ to N_2^+ B $^2\Sigma_u^+$, the dissociation and excitation of O_2 to O*, but also the importance of He^M for the development and propagation of the *He*-plasma.

On the basis of the aforementioned forms of data presentation, i.e. the phoresis plots of related species showing emission intensities as a function of time at different positions and as a function of position at different time instants, it becomes possible to distinguish noble gas ions from their corresponding excited states. Therefore, in this work, a new method of data analysis, Plasma Optical Emission Phoresis Spectroscopy (POEPS), is proposed. This approach allows for a clearer interpretation of the temporal and spatial behaviours of different species.

3.3.4 Emission behaviour of *Ar*-FµTP during the rising half-phase

With the help of POEPS, the discharge mechanism of the *Ar*-plasma is investigated. In case of *Ar*-FµTP, *Ar* 763 nm is chosen as a representative of *Ar* lines, which is emitted by the transition from the Ar^* state to one of the *Ar* metastable states (Ar^M), as illustrated in Figure 3.3. As explained above, due to the fact that the energy level of N_2^+ B $^2\Sigma_u^+$ is higher than that of every excited state of *Ar*, no N_2^+ B $^2\Sigma_u^+$ is observed in *Ar*-FµTP.

The temporal-spatial emission plots and related phoresis plots of *Ar* 763 nm are shown in Figure 3.10. The corresponding positions and instants of time are inserted into the right-hand side of the phoresis plots, separately. A voltage of 3.0 kV is applied to the *Ar*-FµTP to obtain a propagation velocity comparable to that of the *He*-FµTP driven by 2.5 kV. The excitation and ionisation waves reach the end of the capillary (x = 3 mm) at 0.31 µs in *Ar*-FµTP. As shown in Figure 3.10 (a), the shape of *Ar* 763 nm is definitely broader compared to the signal of *He* 706 nm shown in Figure 3.4. Further displays the time dependent emission intensity of *Ar* 763 nm at each position an obvious wing in later time, which leads to their distinctly asymmetric shapes. This means that Ar^* is generated and measured over a continuous

period of time at the same position. In other words, in addition to the Ar^* state produced by collisions of *Ar* atoms with energetic electrons, the higher states of *Ar* capable of decaying to the Ar^* state may also be generated along the capillary.

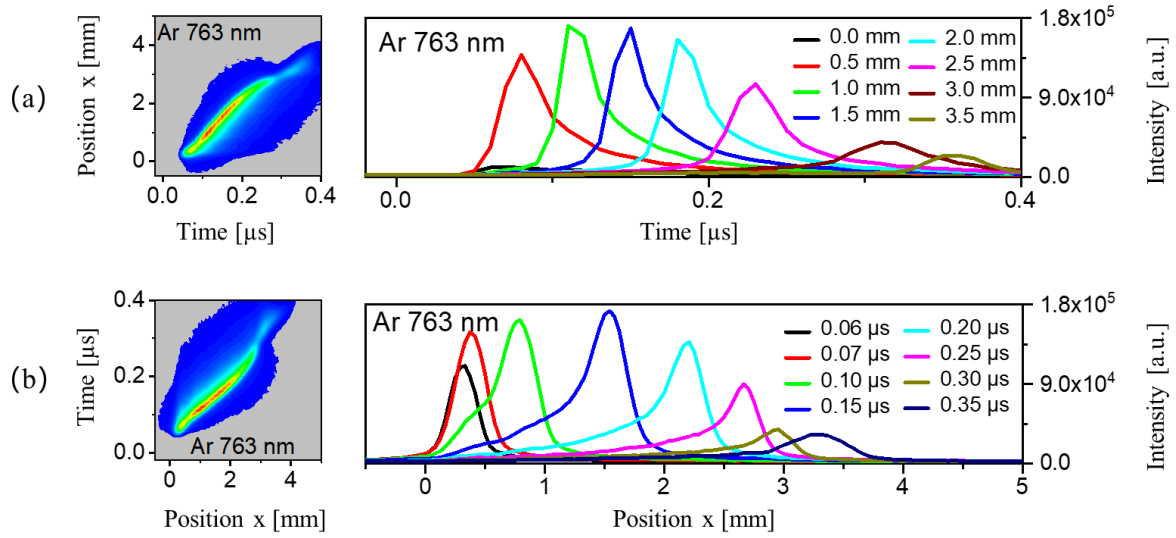

Figure 3.10: Two dimensional colour plots in time and position and the related phoresis plots for the emission intensities as a function of time at different positions (a), as a function of position at different instants of time (b) during the rising half-phase for Ar 763 nm measured in Ar-FμTP at 3.0 kV.

The position dependent phoresis plot of *Ar* 763 nm for each line always has an obvious wing at the left side of the respective maximum, which can be seen in Figure 3.10 (b). This is consistent with the finding that when the emission intensity is plotted in time dependent form at different positions, the wing always appears at later time. The shapes of *Ar* 763 nm resemble those of *He* 706 nm when the contribution of He^+ to *He* 706 nm is enlarged, or to the superposition of *He* 706 nm and N_2^+ 391 nm signals multiplied by different factors. In other words, the wing of *Ar* 763 nm probably can be attributed to the contribution of Ar^+.

As described before, the development of a local potential is necessary for the propagation of excitation and ionisation waves along the capillary. In *He*-FμTP, N_2^+ are the key ions supporting plasma propagation forward. While in *Ar*-FμTP, no N_2 molecules can be Penning ionised by Ar^M to produce N_2^+. Ar^+ is suspected to be generated in *Ar*-FμTP, which plays the same important role in the propagation of excitation and ionisation waves. Similarly to He^+, the signal of Ar^+ can be detected by measuring *Ar* 763 nm because Ar^+ could be depopulated by NIR emission to *Ar** and then to Ar^M, emitting 763 nm. As a result, the shape of *Ar* 763 nm seems to be a composition of *Ar** and Ar^+, with the wing being contributed to Ar^+. Consequently, the role of Ar^+ and N_2^+ X $^2\Sigma_g^+$ in *Ar*-FμTP will be evaluated in the following section.

3.3.5 Emission behaviour of *Ar*-propane-FμTPs during the rising half-phase

Propane was used primarily as an ignition aid, as evidenced by experimental findings that the ignition voltage of *Ar*-plasma can be effectively reduced by incorporating propane into *Ar* [122-124]. In order to verify the presence of Ar^+ and the real key ions responsible for plasma propagation in *Ar*-FμTP, propane was introduced as a major impurity of *Ar* making gas mixtures as discharge gas.

In this study, it can be expected that not only the ignition voltage will be reduced but also the temporal shapes of *Ar* 763 nm will be changed and close to the shapes of *He* 706 nm when the mixtures of propane and *Ar* are used as discharge gases. In other words, the wing of *Ar* 763 nm will become less distinct on the basis that propane ions will replace the role of Ar^+. Unfortunately, there are no known emission wavelengths from the ionised propane state to lower states, hence only the emission behaviour of *Ar* 763 nm is shown. In order to distinguish these plasmas, the plasmas are termed *Ar*-FμTP when the discharge gas is *Ar* 5.0. Instead, it is referred as *Ar*-propane-FμTP if a gaseous mixture of propane with *Ar* is used as discharge gas.

The ionisation energy of propane is 10.9 eV, which is lower than the energy level of Ar^M with 11.5 and 11.7 eV, as illustrated in Figure 3.11. Such gaseous mixture is similar to the case of *He* with the impurity of N_2, where the energy level of N_2^+ B $^2\Sigma_u^+$ with 18.8 eV is lower than He^M with 19.8 and 20.9 eV. Therefore, it is possible for propane molecules to be Penning ionised by Ar^M just as N_2 molecules are ionised by collision with He^M. Similar to N_2^+ in *He*-FμTP, the generated propane ions could create potentials that guide the propagation of excitation and ionisation waves forward.

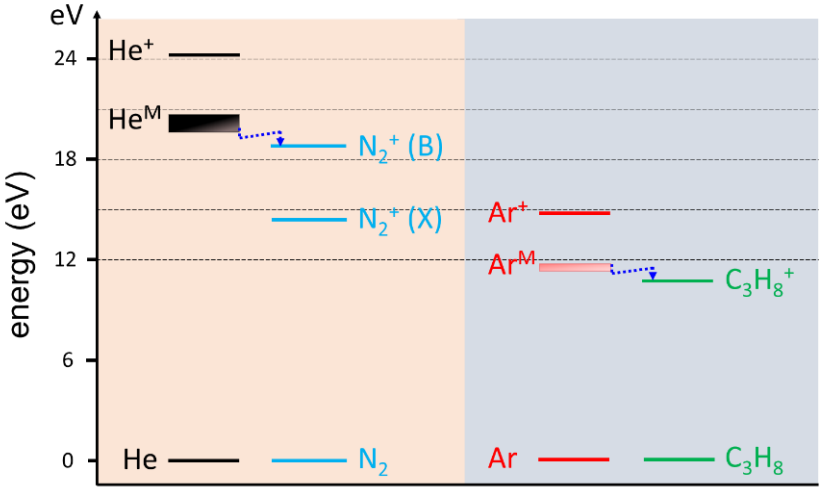

Figure 3.11: Energetic states of N_2 (blue), He (black), Ar (red), and propane (green). The schematic only shows some selected energy levels.

Although the ignition voltage of *Ar*-plasma can be reduced by almost half, for an intuitive comparison, the applied voltage for *Ar*-FμTP is changed from 3.0 kV used previously to 2.8 and 2.9 kV. Besides, *Ar* with different amounts of propane as impurity is used as discharge gases to evaluate their discharge behaviour. The detailed experimental conditions can be found in Table 3.1. Figure 3.12 shows temporal

and spatial colour plots and the position dependent phoresis plots of *Ar* 763 nm measured under different conditions in the rising half-phase. The corresponding discharge gas and applied voltage are listed on the left side of the Figure. The red and blue dots marked on the phoresis plots represent the position at x = 2.5 mm.

As shown in Figure 3.12 (a) and (b), *Ar* 763 nm emission takes approximately 0.35 μs to reach 2.5 mm in both cases of an *Ar*-FμTP driven at 2.8 kV and an *Ar*-propane-FμTP with 2000 ppm propane driven at 2.2 kV (red dots). However, it takes 0.3 μs in both cases of an *Ar*-FμTP driven at 2.9 kV and an *Ar*-propane-FμTP with 4000 ppm of propane driven at 2.2 kV, marked as blue dots in Figure 3.12 (c) and (d). Therefore, it is considered that the average development velocities of the excitation and ionisation waves are comparable in *Ar*-FμTP and the corresponding *Ar*-propane-FμTP. The emission development velocity is related to the propagation of the potential along the capillary. The higher the potential, the stronger the resulting electric field, the faster the electrons are accelerated to a required kinetic energy, and the sooner the excitation and ionisation waves reach a certain position. Therefore, the potential of *Ar*-propane-FμTP with 2000 ppm propane driven at 2.2 kV is equivalent to that of *Ar*-FμTP driven at 2.8 kV, and the potential of *Ar*-propane-FμTP with 4000 ppm propane driven at 2.2 kV is equivalent to that of *Ar*-FμTP driven at 2.9 kV.

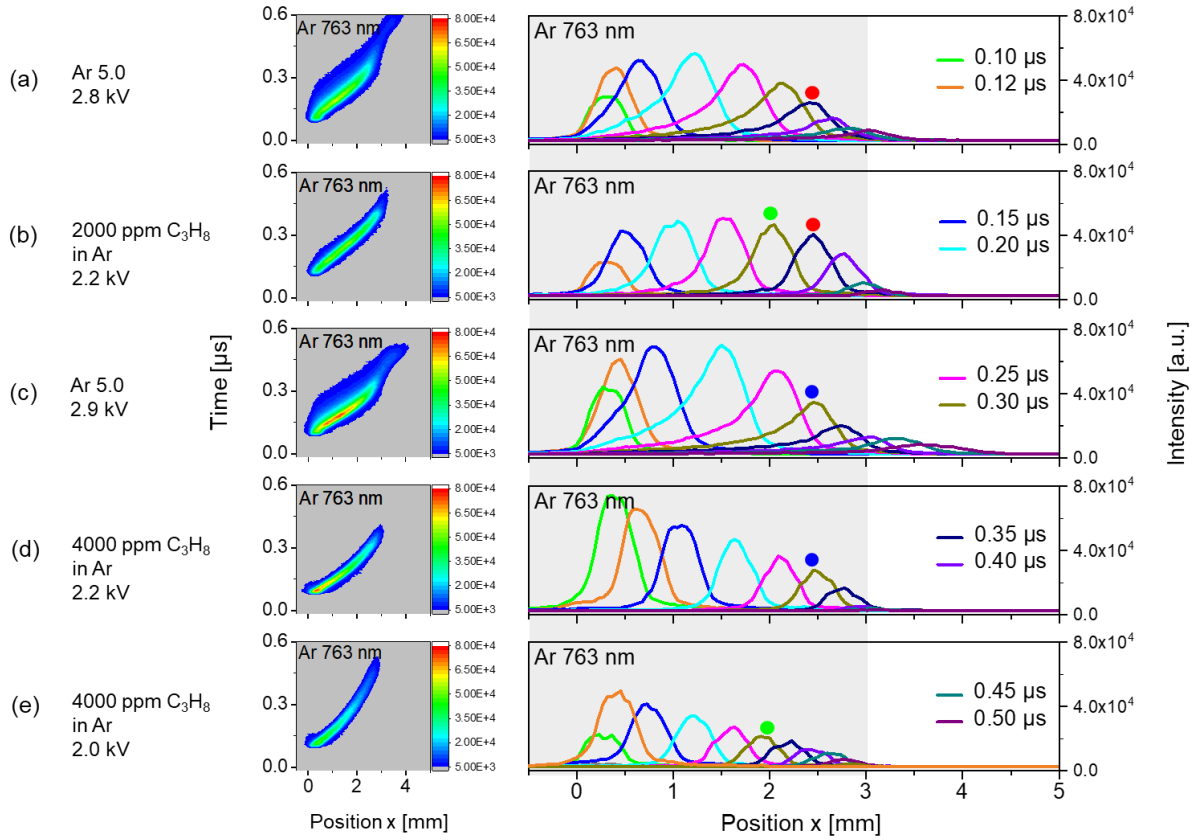

Figure 3.12: Two dimensional colour plots in time and position and the related phoresis plots for the emission intensities as a function of position at different instants of time during the rising half-phase for Ar 763 nm. Ar-FμTPs: (a) at 2.8 kV and (c) at 2.9 kV. Ar-propane-FμTPs: (b) 2000 ppm propane in Ar at 2.2 kV, (d) 4000 ppm propane in Ar at 2.2 kV, (e) 4000 ppm propane in Ar at 2.0 kV.

In the case of *Ar*-FμTP when the applied voltage increases from 2.8 kV (a) to 2.9 kV (c), the required time to reach 2.5 mm is shorten from 0.35 μs to 0.3 μs. The propagation velocity in this case becomes faster. When the applied voltage is constant at 2.2 kV, the time taken is also shorten in the case of *Ar*-propane-FμTP with 4000 ppm propane (d) compared to 2000 ppm propane (b), which means that a higher potential is created in the case of using 4000 ppm. The only difference is that the concentration of propane is higher, implying that more propane ions are generated. These ions contribute to the potential, leading to an increase of the potential and hence a higher development velocity. Due to unknown transitions from the propane ion state to the lower states, propane ions cannot be directly measured by emission spectroscopy. It should be stressed that the wings of *Ar* 763 nm measured in cases of *Ar*-propane-FμTPs are always smaller than those of *Ar*-FμTP. The difference between the areas of the wing surface of *Ar* 763 nm measured in these two types of plasmas is assumed to be the amount of propane ions that contribute to the functional potential. This is illustrated in Appendix A.1.

When the concentration of propane in *Ar* is maintained at 4000 ppm, the propagation of the excitation and ionisation waves slows as expected if the applied voltage is reduced from 2.2 kV to 2.0 kV, which is shown in Figure 3.12 (d) and (e). At 0.3 μs, it only propagates to x = 2.0 mm as marked by a green dot in the case of 2.0 kV, which is similar to the case of *Ar*-propane-FμTP with 2000 ppm propane driven at 2.2 kV (green dot as shown in Figure 3.12 (b)). These results provide further evidence for the role of propane ions in plasma propagation. At the same time, the key role of Ar^+ and the ignorable effect of N_2^+ X $^2\Sigma_g^+$ in *Ar*-FμTP are evident.

3.3.6 Comparison of *Ar*-plasma and *He*-plasma

Compared with the *Ar* 763 nm shapes measured in *Ar*-FμTPs, the *Ar* 763 nm profiles measured in *Ar*-propane-FμTPs are becoming narrower and closer to the *He* 706 nm profiles, but they are still not completely symmetric. This can be explained that although propane ions play an alternative role in the excitation and ionisation development of *Ar*-propane-FμTPs, Ar^+ is still generated simultaneously. Similarly to *He*-FμTP where in addition to the majority of N_2^+ ions, a small amount of He^+ is also generated. The Ar^+ decays to *Ar** and then to Ar^M, thus a 763 nm signal is measured again. Since the ionisation energy of *Ar* is higher than the excitation energy of *Ar**, electrons need a longer distance to be accelerated to a higher energy level to ionise *Ar* atoms than to only excite them. That's why Ar^+ generally locates behind (smaller x) *Ar** along the capillary at the same moment and thus the wings of *Ar* 763 nm are ascribed to Ar^+.

In *Ar*-FμTPs, plasma cannot be ignited when the applied voltage is 2.0 or 2.2 kV. While in the case of *Ar*-propane-FμTPs, due to the presence of propane ions produced by collision of propane molecules with Ar^M, ignition and maintaining-voltage is reduced. This is similar to the case of DBDI in that the ignition voltage is reduced with the addition of propane into *Ar* as the discharge gas [122]. In order to produce and maintain the same amount of Ar^+ in an *Ar*-FμTP as propane ions or Ar^M in an *Ar*-propane-

FμTP, a higher density of electrons with higher energy is required for *Ar*-FμTP. These energetic electrons can be achieved with a higher applied voltage.

Usually, the ignition and sustaining-voltage of an *Ar*-FμTP (~2.4 kV) is higher than that of a *He*-FμTP (~1.5 kV). This seems contradictory to the documented knowledge that since the excitation energy of He^M (19.8 and 20.9 eV) is higher than that of Ar^M (11.5 and 11.7 eV) and even the ionisation energy of Ar^+ (15.8 eV), the energy consumption to ignite *Ar* should be smaller than that of *He*. In *Ar*-FμTPs, no ion states of other species (such as the N_2^+ B $^2\Sigma_u^+$ state in the case of He^M) are below the Ar^M states. Therefore, no sufficient number of ions of other species can be generated to help igniting or sustaining the plasma. In summary, it is identified that *Ar* atoms need to be ionised, but *He* atoms only need to be excited to ignite and sustain the corresponding plasma.

As mentioned before, the lifetimes of metastable states are much longer than those of other excited states and also those of the Ar^+ state. Although the electron energy must be higher in the case of populating He^M than in the case of populating Ar^+, the lifetime of He^M is much longer than that of Ar^+. In order to generate and maintain the same amount of Ar^+ in an *Ar*-plasma as He^M in a *He*-plasma, the *Ar*-plasma needs a higher electron density which is usually fulfilled by increasing the applied voltage. Such high voltages required further confirm that Ar^+ are mainly responsible for the excitation and ionisation in *Ar*-FμTP.

So far, it has been confirmed that Ar^+ are generated in *Ar*-FμTP and mainly drive the plasma develops forward, whereas *He*-FμTP is mainly driven by the generation and presence of N_2^+. Interestingly, the second maximums of both N_2^+ 391 nm and *He* 706 nm at a fixed moment are observed when their emission intensities are presented in the form of time dependent phoresis plots. However, the second maximum of *Ar* 763 nm is not observed even if the corresponding emission intensity is rescaled. In principle, Ar^+ can also attach to the inner wall of the capillary and then be detached by slow electrons or other appropriate species and thereby be measured at one fixed time for all positions along the capillary, but it is not. One possible explanation is that the *Ar* 763 nm emitted in the process of detachment and recombination of Ar^+ attached on the wall is superimposed with the *Ar* 763 nm signal originating from Ar^+ in the gas and is therefore indistinguishable. However, this is not appropriate for *He* 706 nm because He^+ in the case of *He*-FμTP is much less than Ar^+ in the case of *Ar*-FμTP.

The energy level of Ar^M (11.5-11.7 eV) is higher than that of the N_2 C $^3\Pi_u$ states (11.0 eV, as shown in Figure 3.3), which means that Ar^M has an energy high enough to produce N_2 C $^3\Pi_u$ by collision with the ground state of N_2 molecules. This process is called excitation transfer [56]. In addition, energetic electrons can also collide directly with the ground state of N_2 molecules to produce the N_2 C $^3\Pi_u$ states. With the decay of the N_2 C $^3\Pi_u$ state to the N_2 B $^3\Pi_g$ state, the SPS of N_2 can be emitted. In the first case, the emission peaks of *Ar* 763 nm and SPS signal should have a shift in time, while in the latter case, the emission maxima will be reached principally at the same time. In case of *Ar*-FμTP, the emission of N_2

337 nm is the dominant one in SPS as shown in Figure 3.2 (b). Therefore, with the help of the measurement of N_2 337 nm, the information about the *Ar*-plasma will be replenished.

Figure 3.13 shows the temporal-spatial emission plots of both *Ar* 763 nm and N_2 337 nm and their time dependent phoresis plots at different positions measured in *Ar*-FμTP along the capillary during the rising half-phase. It is known that the maximum of *Ar* 763 nm can be attributed to Ar^* (marked as *) and the wing to Ar^+ (marked as +) in the subplot of *Ar* 763 nm, which has been explained above.

Similarly to the signals of N_2^+ 391 nm and O 777 nm measured in *He*-FμTP, two maxima are also observed for each position in the time dependent phoresis plot of N_2 337 nm. The first maxima are shifted in time relative to the corresponding maxima of *Ar* 763 nm, meaning that the N_2 C $^3\Pi_u$ states are generated later than the Ar^* state. In addition, the instant time of the maximum *Ar* 763 nm corresponds to the increase edge of emission intensity of N_2 337 nm as labelled by the colour lines.

However, the highest increase rate moment of N_2 337 nm is not in perfect alignment with the maximum moment of *Ar* 763 nm, but with a slight offset. This is different from the case of *He* 706 nm with N_2^+ 391 nm, it might be caused by the cumulative contribution of Ar^+ and Ar^* to the signal of *Ar* 763 nm in this case. The produced Ar^M will collide with N_2 molecules, resulting in emission of N_2 337 nm, and thus offset is observed. Based on the explanation above, the collision of Ar^M with N_2 X $^1\Sigma_g^+$ is the main process to generate the N_2 C $^3\Pi_u$ states.

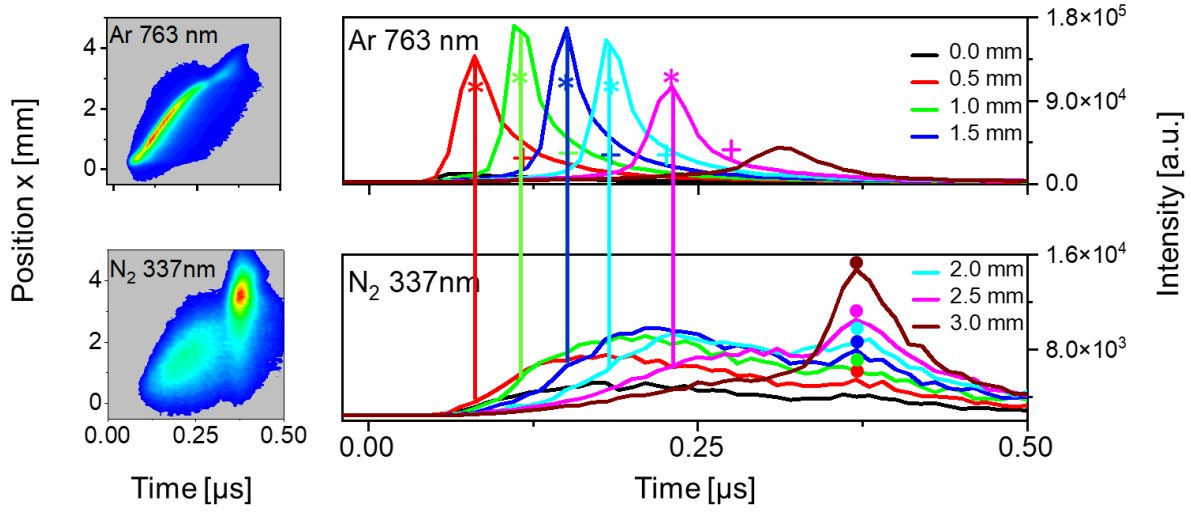

Figure 3.13: Two dimensional colour plots in time and position and the related phoresis plots for the emission intensities as a function of time at different positions during the rising half-phase for Ar 763 nm and N_2 337 nm in Ar-plasma. The applied voltage is 3.0 kV.

The second maximum of N_2 337 nm is observed at 0.37 μs for all positions in the capillary as indicated by the colour dots, which is later than the instant of time at which the development of the excitation and ionisation waves reach the capillary end (3.0 mm) at 0.31 μs. Additionally, the intensity of the second maximum is increasing along the capillary. This phenomenon is similar to the second maximum of O 777 nm and N_2^+ 391 nm measured in a *He*-FμTP in the rising half-phase, where the O 777 nm signal

results from the collection of O_2 by the N_2^+ B $^2\Sigma_u^+$ attached on the inner wall. The possibility that such a second maximum of N_2 337 nm originates from the recombination of N_2^+ B $^2\Sigma_u^+$ or collection of N_2 by N_2^+ attached on the inner wall is ruled out due to the fact that no N_2^+ B $^2\Sigma_u^+$ and negligible N_2^+ X $^2\Sigma_g^+$ is involved in *Ar*-FμTP as explained above. After the excitation and ionisation waves reach the capillary end, the electric field inside the capillary becomes weak, and thereby the low energy electrons are not able to generate the N_2 C $^3\Pi_u$ states by direct collisions with N_2 molecules.

One possible interpretation is that these maxima of N_2 337 nm emission arise from collisions between Ar^M and N_2 X $^1\Sigma_g^+$, where Ar^M is populated by NIR emission from Ar^+ to Ar^* and then to Ar^M. Thus, it is a hint that some Ar^+ is attached to the glass surface during propagation forward along the capillary and detached from the surface by slow electrons and N_2 molecules when the emission reaches the end of the capillary. It should be noted that the emission intensity of N_2 337 nm is related not only to the density of Ar^M but also to the concentration of N_2 in the local gaseous mixture. A higher concentration of N_2 can be expected at the end of the capillary due to air diffusion, so that the emission intensity of N_2 337 nm at 3 mm is higher than other positions can be accepted.

3.3.7 Plasma propagation during the falling half-phase

The preceding sections already demonstrated and discussed the plasma behaviours during the rising half-phase, the present section will focus on the falling half-phase. Figure 3.14 shows the plasma evolution during the falling half-phase measured in *He*-FμTP. The two dimension colour plots and position dependent phoresis plots of *He* 706 nm, N_2^+ 391 nm, and O 777 nm are shown in Figure 3.14 a, b and c, respectively. Compared to the signal obtained in the rising half-phase, the shapes of these are completely different. The shapes of *He* 706 nm show more than one peak and have a six times broader position-full width at half maximum (p-FWHM) than in the rising half-phase. There are at least two peaks (curves at 25.08 and 25.09 μs) and three peaks (curves between 25.10 and 25.14 μs), which means that the decay from He^{**} to He^* takes place at two or three positions at the same moment. In other words, He^{**} is populated at different positions at the same time.

Due to the higher electron density and energy in the vicinity of the electrode resulting from the secondary electron emission in the falling half-phase, it is suspected that not only He^{**} was generated but *He* atoms can also be ionised to He^+. In comparison with the rising half-phase, there is a considerable increase in the number of species, which results in a clear enhancement of emission intensity. He^{**} can be populated through the recombination of He^+. He^* state is then populated by the transition from He^{**}, and thus the 706 nm is measured again. As a result of the overlap of contributions of both He^+ and He^{**} to 706 nm, the emission intensity of *He* 706 nm in this half-phase is about two times higher than that in the rising half-phase.

He^+ and He^{**} possess disparate prerequisites for generation, that is, the different requirements for the acceleration of electrons along the capillary, which results in their detection as 706 nm at varying

positions at the same instant of time. The peak corresponding to He^{+} (marked as +) moves towards the end of the capillary following the peak of He^{**} (marked as *), which is noticeable between 25.10 µs and 25.14 µs. In addition, as a result of the recombination of He^{+}, a peak can always be observed around the electrode tip (marked as •).

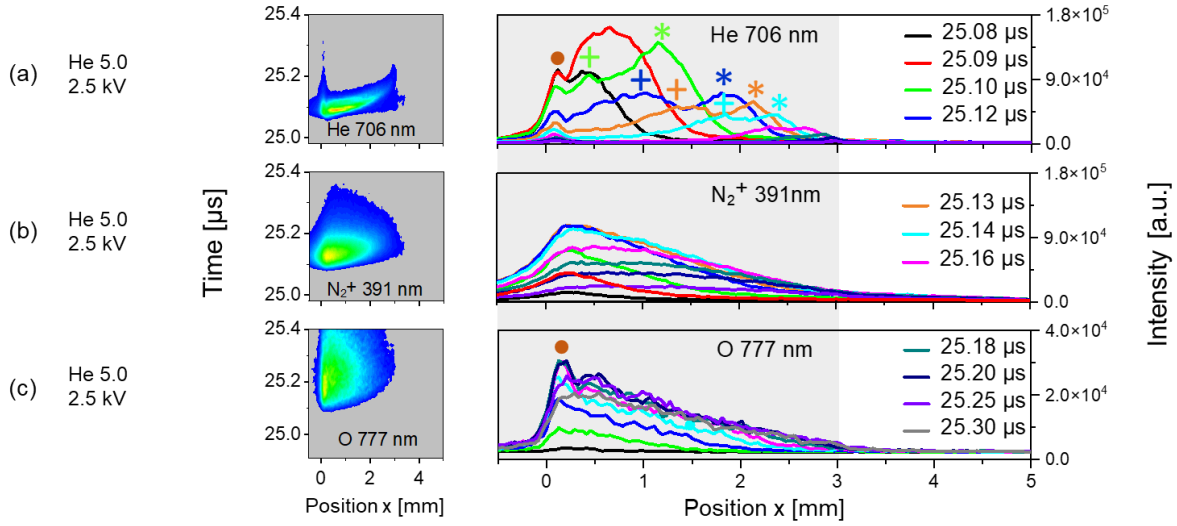

Figure 3.14: Two dimensional colour plots in time and position and the related phoresis plots for the emission intensities as a function of position at different instants of time during the falling half-phase for (a) He 706 nm, (b) N_2^+ 391 nm, (c) O 777 nm measured in He-FµTP at 2.5 kV.

Compared to that in the rising half-phase, the emission of N_2^+ 391 nm shows a slightly lower maximum and a sharp decrease in intensity along the capillary in this half-phase. The signal peaks of N_2^+ 391 nm do not move forward, but rather appear in the vicinity of the electrode tip at every moment due to the attraction of negative electrode. The maximum of *He* 706 nm is reached at 25.09 µs and then decreases to zero at 25.18 µs, whereas the signal of N_2^+ 391 nm at this moment is still present with an intensity half of the highest maximum at 25.12 µs. In addition, the N_2^+ 391 nm signal is still detectable at a later time. However, the *He* 706 nm peak reaches the capillary exit at 25.18 µs, which means the electric field over the whole capillary becomes much weaker after this moment. Therefore, electrons are unable to obtain enough energy to generate N_2^+ by direct collisions with N_2 molecules after 25.18 µs. So, this is evidence that N_2^+ also attached to the inner wall of the capillary in the falling half-phase, and these N_2^+ ions mainly concentrate in the vicinity of the electrode tip. While in the rising half-phase, they are distributed more in the vicinity of capillary exit.

In principle, the change in emission intensity of N_2^+ 391 nm follows the change of *He* 706 nm. In other words, it should be higher in the falling half-phase than that in the rising half-phase like *He* 706 nm. Because most of N_2^+ B $^2\Sigma_u^+$ is produced by He^M through Penning ionisation, but it is not. One possible explanation is that N_2^+ B $^2\Sigma_u^+$ is attracted by the negative electrode, part of N_2^+ B $^2\Sigma_u^+$ is neutralised directly by slow electrons, and the remaining N_2^+ B $^2\Sigma_u^+$ is measured by emitting 391 nm. It can be imaged that in the falling half-phase, the N_2^+ in the gas near the negative electrode will congregate and form a positive ion cloud.

As shown in Figure 3.14 (c), the emission intensity of O 777 nm in this half-phase is comparable to that in the rising half-phase. According to the emission intensity of *He* 706 nm and N_2^+ 391 nm in both half-phases described in the previous part, the ratios of emission intensities of *He* 706 nm to O 777 nm in two half-phases differ, while the ratios of emission intensities of N_2^+ 391 nm to O 777 in two half-phases are close. In addition, the shape of O 777 nm is similar to that of N_2^+ 391 nm to some extent, where there is no obvious peak movement towards the end of the capillary. Instead, the peaks for each time appear to gather in the vicinity of the electrode tip. They are observed at the same position (marked as a dot), which is located between the electrode tip and the maximum of N_2^+ 391 nm.

Similarly to the first peak of *He* 706 nm attributed to He^+ as marked with a dot, it does not move forward with time runs. Between 25.08 μs and 25.18 μs, the emission intensity of *He* 706 nm is decreasing, while O 777 nm is increasing in time at this position. It can be interpreted that this peak originates primarily from the collision of He^M with O_2 accompanied by the generation of O* and the consumption of He^+. According to these clues, it can be seen that the generation of O 777 nm can be attributed to N_2^+ B $^2\Sigma_u^+$ and He^M to different degrees depending on the exact position. Therefore, it can be concluded that the initiation of O 777 nm along the capillary is produced more by collisions with N_2^+ B $^2\Sigma_u^+$ than by collisions with He^M in both half-phases. But for the falling half-phase, only in the vicinity of the electrode tip, the collisions of He^M with O_2 dominate.

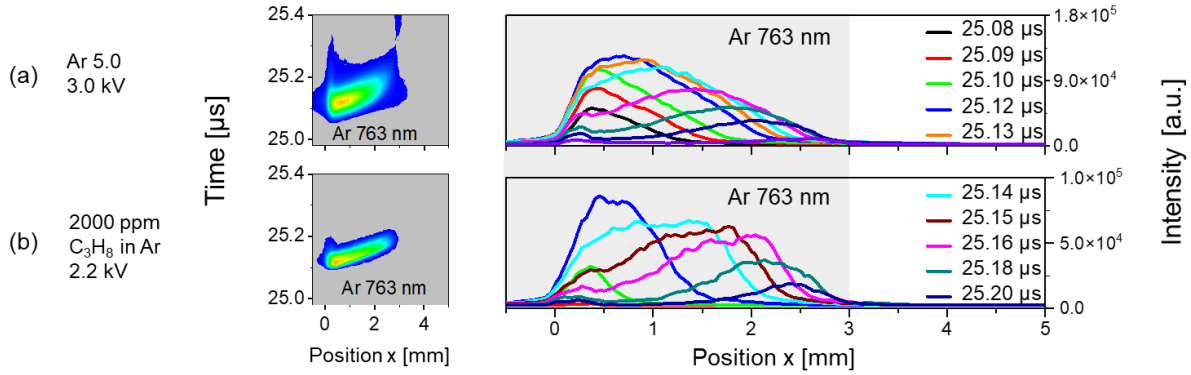

Figure 3.15: Two dimensional colour plots in time and position and the related phoresis plots for the emission intensities as a function of position at different instants of time during the falling half-phase for (a) Ar 763 nm measured in Ar-FμTP at 3.0 kV, (b) Ar 763 nm measured in Ar-propane-FμTP, the concentration of propane is 2000 ppm, and the applied voltage is 2.2 kV.

The temporal-spatial emission plots and the position dependent phoresis plots of *Ar* 763 nm measured in *Ar*-FμTP at 3.0 kV is shown in Figure 3.15 (a). The shapes are quite different from the ones measured in the rising half-phase, which are also similar to the superposition of *He* 706 nm and N_2^+ 391 nm multiplied by different factors. The emission intensity in this case is lower than that in the rising half-phase. As explained in the rising half-phase, Ar^+ is generated, which mainly guides the excitation and ionisation along the capillary. Both Ar^+ and Ar^* contribute to the shape and intensity of 763 nm. In the falling half-phase, due to the secondary electron emission with high energy, the number of Ar^+ is

definitely higher than that in the rising half-phase, leading to the increased contribution from Ar^+ to *Ar* 763 nm and thus the blunter peak of *Ar* 763 nm.

When the falling half-phase starts, a negative potential is introduced to the electrode. The electrons coming from the secondary electron emission will collide with *Ar* atoms, resulting in the formation of Ar^+. These Ar^+ are attracted by the negative electrode and accumulate in the vicinity of the electrode tip, forming an ion transient cloud that is similar to the N_2^+ ion cloud that provides a local potential in *He*-FμTP. These transient ion clouds with positive potential will act as a "virtual positive electrode" [24] and further shield the effect on front positions (larger x value) from the negative electrode. Electrons will be attracted from another side and move towards the electrode and then participate in subsequent excitation and ionisation reactions along the capillary. That's why the emission developments in both half-phases have the same propagation direction despite the polarity of the applied voltage. The later process is different from it that happened in the initial stage in the falling half-phase but close to it that happened in the whole rising half-phase, which has already been explained before. During the later process, it is predictable that some Ar^+ is repelled from this ion cloud and moved towards the capillary end. Therefore, the decay of these Ar^+ during movement also overlaps with the decay of Ar^*.

As expected, due to the participation of propane ions in the case of *Ar*-propane-FμTP, the shapes of *Ar* 763 nm measured in *Ar*-propane-FμTP with 2000 ppm propane at 2.2 kV as shown in Figure 3.15 (b) are close to those of *He* 706 nm. In addition, the emission intensity of *Ar* 763 nm obtained in this half-phase is also higher than that in the rising half-phase. These results further demonstrate that propane ions in *Ar*-propane-FμTP play the same role as N_2^+ in *He*-FμTP. While in the case of *Ar*-FμTP, Ar^+ are the main functional ions. Throughout the peaks displayed above, it can be clearly seen that neither ions nor excited species could extend beyond the end of the capillary but were confined to the inside of the capillary. Even though a higher energy dissipation takes place in the falling half-phase, each reaction occurs only inside the capillary. Therefore, it can be concluded that the plasma in the falling half-phase is not involved in the protonation processes outside the capillary.

3.4 Conclusions

In this chapter, the discharge mechanisms of *He*-FμTP and *Ar*-FμTP inside the capillary are investigated and compared by means of temporally and spatially resolved OES. The results show that the discharge behaviour of FμTP with *He* and *Ar* as discharge gas in the same configuration differs.

In case of *He*-FμTP, with the help of time- and position-dependent phoresis plots of *He* 706 nm, He^+ is identified in both half-phases. In addition to He^{**}, He^+ is also responsible for the appearance of a slight wing in the *He* 706 nm curves. However, the estimated density of He^+ is two orders of magnitude lower than that of He^M. Both He^+ and He^{**} eventually decay to the He^M state, which is a good collision partner with N_2 molecules to generate N_2^+ B $^2\Sigma_u^+$. With the transition from N_2^+ B $^2\Sigma_u^+$ to N_2^+ X $^2\Sigma_g^+$, N_2^+ 391 nm is emitted and measured. Part of N_2^+ B $^2\Sigma_u^+$ will attach to the glass wall during plasma propagation and

then detach by collecting slow electrons as well as O_2. After collisions between N_2^+ B $^2\Sigma_u^+$ with O_2 molecules, O_2 is dissociated into two O atoms. Then, the atom is excited to the O^* state, and O 777 nm is measured as the result of transition. Based on the behaviours of these three species, it is considered that the production of O 777 nm is more attributed to collisions of O_2 with N_2^+ B $^2\Sigma_u^+$ than with He^M. In addition, N_2^+ is found to be primarily responsible for excitation and ionisation, and only a small amount of He^+ is produced in a *He*-FμTP.

In case of *Ar*-FμTP, a distinct wing is observed in *Ar* 763 nm curves in both forms of time- and position-dependent phoresis plots. When propane is added into *Ar* and the mixture is used as a discharge gas, propane will be ionised by Penning ionisation. These propane ions play the same role as N_2^+ B $^2\Sigma_u^+$ in *He*-FμTP and compensate for the absence of N_2^+ in *Ar*-FμTP. As a result, the shape of *Ar* 763 nm becomes narrower and close to that of *He* 706 nm, meanwhile the ignition and maintenance voltage is obviously reduced. Therefore, Ar^+ is demonstrated to be generated in *Ar*-FμTP, which is the key ion to support plasma propagation. Since the lifetime of Ar^+ is much shorter than that of Ar^M and He^M, this effectively explains why *Ar* 5.0 is harder to ignite than *He* 5.0, even though the energy levels of all excited and ionised *Ar* states are lower than those of He^M. Because the production of N_2^+ X $^2\Sigma_g^+$ by Ar^+ is very small, its effect in *Ar*-FμTP is negligible.

In this work, a new data analysis method called Plasma Optical Emission Phoresis Spectroscopy (POEPS) is proposed that can be used to distinguish noble gas ions from excited species. It is introduced on the fact that the resulting signal consists of a symmetrical peak from the excited species and a wing due to the ionised ones. This is the first time that the element ions can be distinguished only by means of emission spectroscopy in weakly ionised plasmas. This approach makes it easier to observe the subtle details that are always obscured and lost in the commonly used 2D colour plots, assists in elucidating the mechanisms underlying plasma discharge. With the help of POEPS, it is confirmed that both ions and excited species do not propagate beyond the capillary exit during the falling half-phase, resulting in a negligible contribution for protonation.

In summary, it was demonstrated that N_2^+ is the protagonist responsible for plasma maintenance in the case of *He*-FμTP, while Ar^+ is the key ion for *Ar*-FμTP, the transition between these two discharge modes is also confirmed in *neon*-FμTP [27]. Furthermore, the attachment of ions to the capillary surface is confirmed and also the subsequent detachment by electrons as well as N_2 and O_2. Overall, the generation and propagation mechanisms of *He*-FμTP and *Ar*-FμTP within the capillary have been more understood so far, providing physical knowledge and further insight into the plasma discharge mechanism.

CHAPTER 4

Influence of a metallic target on FμTPs

Cold atmospheric plasma can extend as an effluent into the ambient air, making it more adaptable to the morphology and size of the treated objects [112]. Its applications are based on the reactive species contained in the plasma to a significant extent, and the production of these active substances is determined by the plasma behaviours. FμTP provides a promising technology for generating a cold plasma under atmospheric pressure in a miniaturised, economical, and flexible configuration, so it is more suitable for applications in certain special scenarios [7].

However, the stability of FμTPs was found to be very sensitive to the variation of the local electric field. During the laboratory measurement operation, it was noticed that the presence of a conductor close to plasma has a non-negligible impact on the discharge process. In other words, the conductor may greatly affect the performance of the plasma in specific situations. In practical application scenarios, plasma typically tends to be close to or even in direct contact with the conductive targets. For example, when coupled to the MS as an ionisation source, the MS inlet may affect the final detection efficiency of the analyte. To control these disturbances, it is urgent to have a deep understanding of the effect of the conductor on discharge processes to use FμTP industrially.

In FμTP, the electrons are periodically accelerated and maintain the excitation and ionisation waves through collisions. If free charges cannot be fully redistributed before the electric field reverses, some charges will remain trapped on the capillary surface. The remaining negative and positive charges have been shown to play an essential role in discharge evolution [130]. In order to better understand and regulate plasma discharge behaviour in front of a target, especially in small distances, it is crucial to investigate and elucidate the intricate mechanisms involved in the FμTP-target system. This chapter will experimentally simulate the discharge conditions in actual applications using artificially added metallic targets in front of FμTP. To study the spatial and temporal characteristics of FμTP and the influence of

the target on the discharge behaviour, not only will the polarity of the applied voltage be investigated but also the target distance will be discussed in detail.

This work is of great significance for both fundamental and application research, especially when coupled with MS and IMS as a soft ionisation source. In such instances, the existence of conductors with great interference to the plasma is difficult to avoid. Therefore, this experiment serves as a considerable guide for realistic application scenarios of FμTPs. In addition, it also has reference values for other plasma based ionisation sources to get better performance.

4.1 Experimental arrangement

The experimental arrangement is shown in Figure 4.1, this is similar to the setup before. However, FμTP with a discharge volume in length of 10 mm was used for the measurements. The FμTP was driven by a square wave voltage of V_{pp} in 2.0 kV, whose polarity can be switched through specific bias circuits. *He* with a purity of 99.999% was supplied as discharge gas, the other information has been completely described and shown in Section 2.1.3.

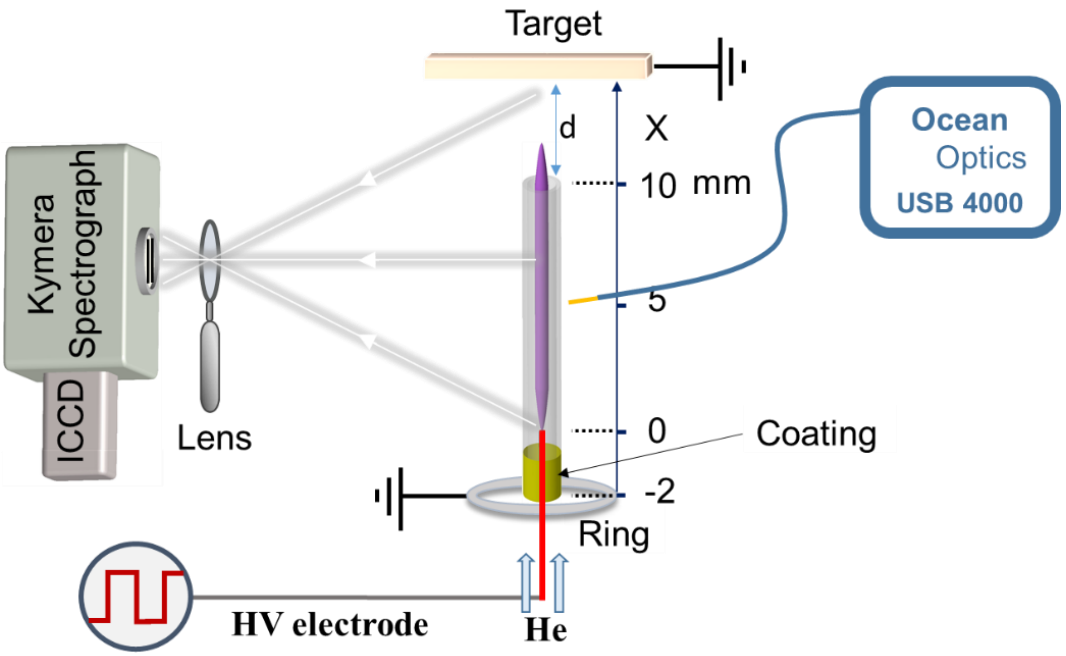

Figure 4.1: Schematic of the experimental arrangement.

As demonstrated in Figure 4.1, the distance from the tip of the HV electrode to the end of the capillary is 10 mm. In order to explore the influence of a metallic target on the plasma, the mainly used special equipment here comprises a grounded cuboid brass target (40*10*2.5 mm), which was placed in front of the FμTP. The distance between the target and the capillary end is able to adjust. Besides, a grounded brass ring (ID-10 mm, OD-20 mm, thickness-2 mm) was placed 2 mm behind the HV electrode tip only for promoting the plasma ignition. The other detailed experimental condition has already been

introduced in Section 3.1, here only the key instruments utilised in this work are presented in the illustration.

The USB 4000 spectrometer was used for general recognising the characteristic emission lines of reactive species present in these plasmas through an optical fibre. The fibre is perpendicular to the longitudinal axis of the capillary in a distance of 1 mm. The ICCD system captures the temporally and spatially resolved spectra of the plasma through a convex lens. The gate width and step width are both set as 10 ns for 706 nm and 391 nm emission in this chapter.

4.2 Integrated emission spectra

To investigate the potential value of the polarity switch for the applications of FμTP, as well as the influence of conductor on these plasmas, voltages in three polarities were employed to drive the plasma. The voltage waveforms of these three square wave voltages are captured by a digital oscilloscope and are shown in Figure 4.2 (a). Correspondingly, the plasmas driven by these three polarity voltages are defined as the P-, NP- and N-plasmas, which will be used many times in the following text.

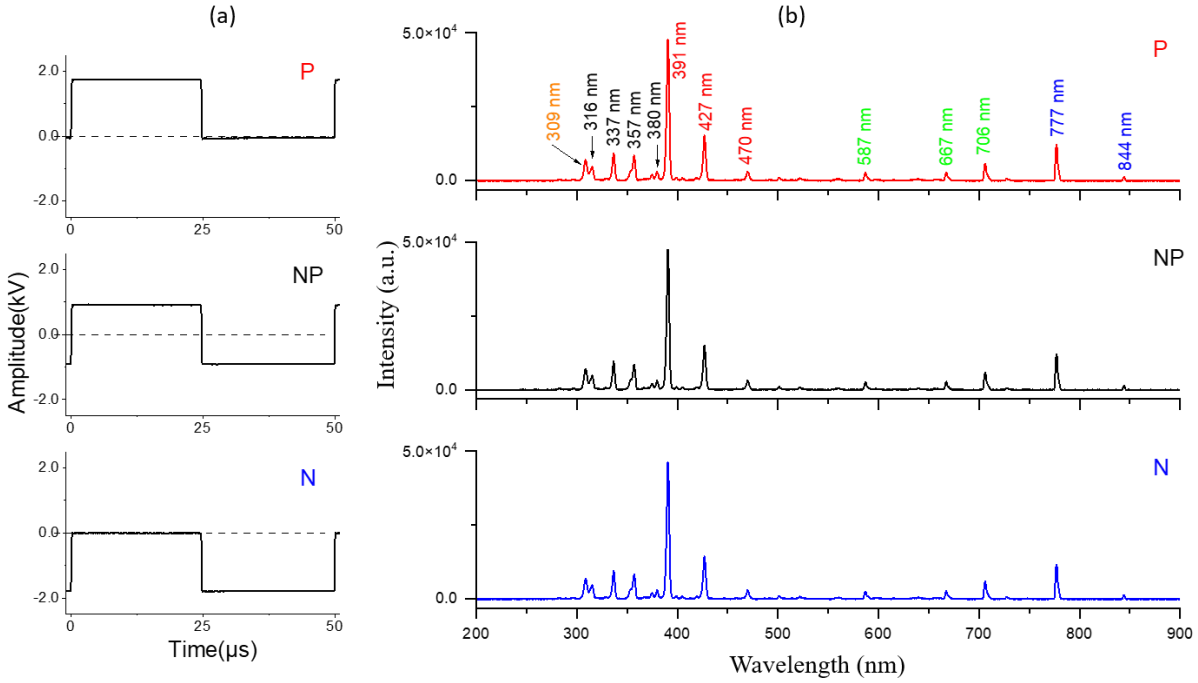

Figure 4.2: (a) Voltage waveform of the applied three polarity square wave voltages with a Vpp of 2.0 kV captured by a digital oscilloscope, the black dashed lines represent 0 kV; (b) Integrated emission spectra recorded with an integration time of 50 ms in He-FμTP driven by three polarity voltages without target.

Firstly, the optical fibre connected to a spectrometer was placed perpendicular to the capillary axis to measure the emission spectrum in *He*-FμTP without a target. Figure 4.2 (b) shows the spectra recorded at the middle position (x = 5 mm) between the HV electrode tip and the capillary exit of three kinds of FμTP. The results obtained demonstrate completely the same integrated emission spectra at this position in every plasma, the polarity switch of the driven voltage seems to do nothing.

Therefore, the major spectral lines are labelled only in P-plasma as a representative. There are mainly emission lines of OH (309 nm, orange text), N_2 (316, 337, 357 and 380 nm, black text), N_2^+ (391, 427 and 470 nm, red text), *He* (587, 667 and 706 nm, green text), and O (777 and 844 nm, blue text). In order to facilitate data collection and subsequent analysis, a good signal-to-noise ratio is essential. Therefore, the evolution of the most intensive emission lines of the plasma is investigated. Here, *He* emission at 706 nm and the first negative band system of N_2^+ 391 nm are chosen as concern and set as centre wavelengths to scrape data about their spatial-temporal distribution behaviours.

4.3 Spatial and temporal evolution of emission spectra

4.3.1 Free plasmas

In the absence of a target introduced into the proximity of the capillary nozzle, the plasma generated along the capillary is designated as "free plasma". For FμTP, the evolution of free plasmas is first investigated for three polarity voltages. The results indicate that their spatial and temporal evolution behaviours are also almost identical among the three polarities. In this manner, only the case of NP-plasma is displayed in Figure 4.3 as a representative, the other two can be found in Appendices B.1 and B.2.

4.3.1.1 Evolution behaviour of the NP-plasma

In the typical case of NP, from 0.16 μs to 0.57 μs, the position of each maximum of N_2^+ 391 nm always follows that of *He* 706 nm, as illustrated by the vertical colour lines in Figure 4.3. This is due to the fact that N_2^+ B $^2\Sigma_u^+$ (measured by 391 nm) is populated by collisions of He^M (measured by 706 nm) with the N_2 molecule through Penning ionisation. In this time frame, the maximum of *He* 706 nm decreases slightly with time to 0.46 μs, but increases at 0.57 μs when the plasma arrives at the end of the capillary. After reaching x = 10 mm, the maximum of *He* 706 nm is higher than the previous moments. However, the emission intensity of N_2^+ 391 nm decreases apparently until 0.57 μs and slightly increases at 0.60 μs around the capillary exit.

It is necessary to point out that, unlike the phenomenon that a slightly asymmetric shape with a wing to the left hand side (smaller x) of the peak shows in each 706 nm curve, as described in Section 3.3.3, it is hard to distinguish such a wing or asymmetric shape here. As explained above, the excited and ionic *He* species are involved in *He*-FμTP, the wing for each line is contributed by He^+ and the maximum results from He^{**}. Therefore, this inconsistency could probably be explained by the lower voltage used here (2.0 kV compared to 2.5 kV in Section 3.3.3), thus leading to a lower production of He^+. In the same way, due to the higher electron density and energy that resulted from the secondary electron emission during the falling half-phase, not only more He^{**} but also more He^+ were generated. As a result, the emission intensity of *He* 706 nm in this half-phase is about two times higher than that in the rising

half-phase. In addition, due to the recombination of He^+, a peak can always be observed around the electrode tip, as shown in Figure 4.3 (c).

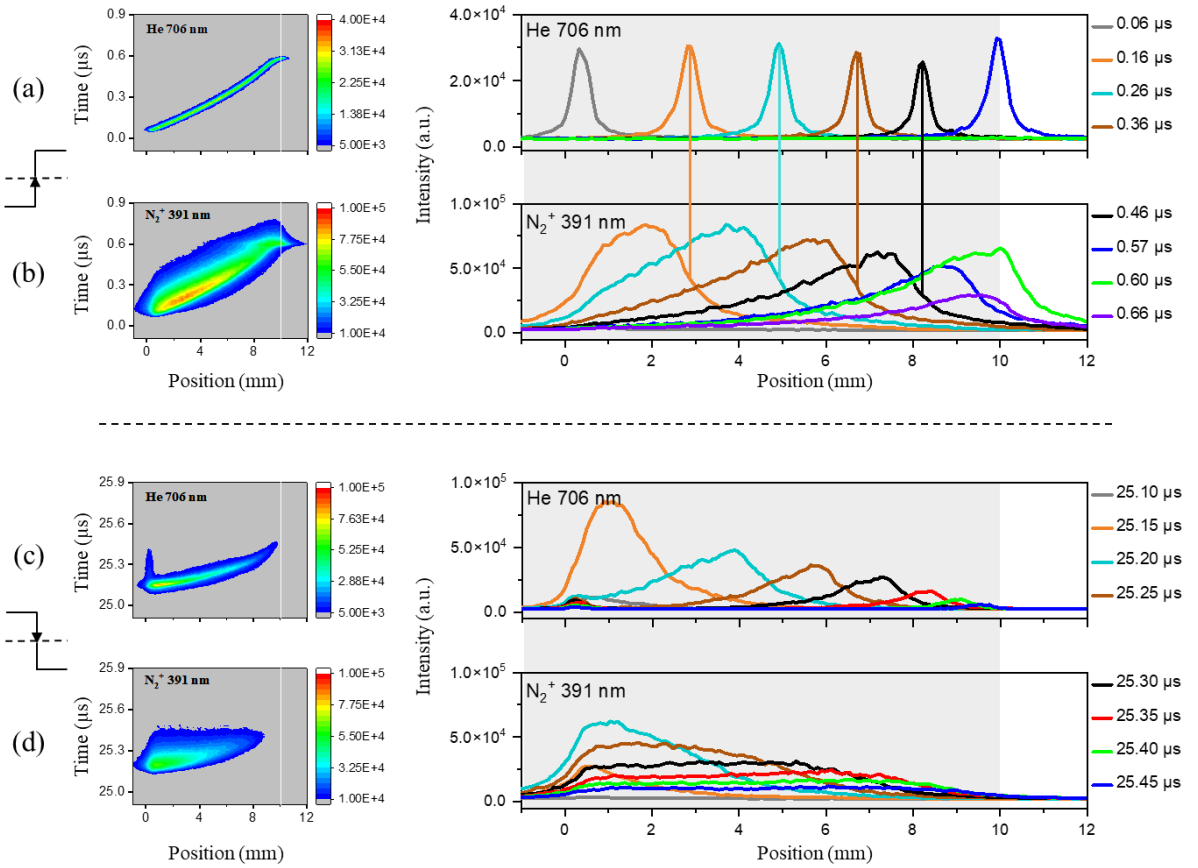

Figure 4.3: Two dimensional contour plots in time and position and the related phoresis plots for the emission intensities as a function of position at different time during the rising and the falling half-phases for He 706 and N_2^+ 391 nm measured from the free NP-plasma, respectively. The white vertical line in the left four plots at 10 mm represents the exit of the capillary (x = 10 mm).

Compared to that in the rising half-phase, the emission of N_2^+ 391 nm shows a slightly lower maximum and a sharp decrease in intensity along the capillary in the falling half-phase. In Figure 4.3 (d), the peaks of N_2^+ 391 nm do not move forward, but rather appear in the vicinity of the electrode tip at every moment. This is caused by the attraction of the negative electrode to the positive N_2^+ B $^2\Sigma_u^+$ ions. Moreover, the emission intensity of N_2^+ 391 nm in the falling half-phase is not higher than that in the rising half-phase, like the *He* 706 nm signal. This can be attributed to the fact that part of N_2^+ B $^2\Sigma_u^+$ are neutralised. Besides, a very narrow shape for 706 nm but a wide shape for 391 nm in both half-phases were observed. This is related to their different generation mechanisms. These phenomena are similar to those observed in Section 3.3.3, suggesting that the plasma has a similar evolution mechanism after the capillary length changed from 3 mm to 10 mm. During both half-phases, the excitation and ionisation waves move forward on the basis of the repetitive initiation of new transient potential until the local potential is not sufficient to sustain the next round of excitation.

When a positive- or negative-biassed voltage is applied to the electrode, something should not be forgotten. As shown in Figure 4.2 (a), the applied voltage amplitude introduced in the P-plasma was two

times higher of that in the NP-plasma during the rising half-phase, the applied voltage amplitude introduced in the N-plasma was two times higher of that in the NP-plasma during the falling half-phase. In addition, according to common perception, the applied voltage amplitude is 0 kV in the P-plasma during the falling half-phase, and the applied voltage amplitude is 0 kV in the N-plasma during the rising half-phase. Therefore, no plasma should be generated in both cases. However, compared to those displayed in Figure 4.3, similar shapes and comparable intensities are observed for both emissions of 706 nm and 391 nm for the P- and N-plasmas in both half-phases. It reveals that the applied DC bias seems to have done nothing for plasma emission along the capillary. This similar phenomenon suggests that the P-plasma and the N-plasma both have an evolution mechanism similar to that of the NP-plasma even though a positive and a negative DC bias voltage was additionally implemented.

4.3.1.2 Comparison of plasmas among polarities

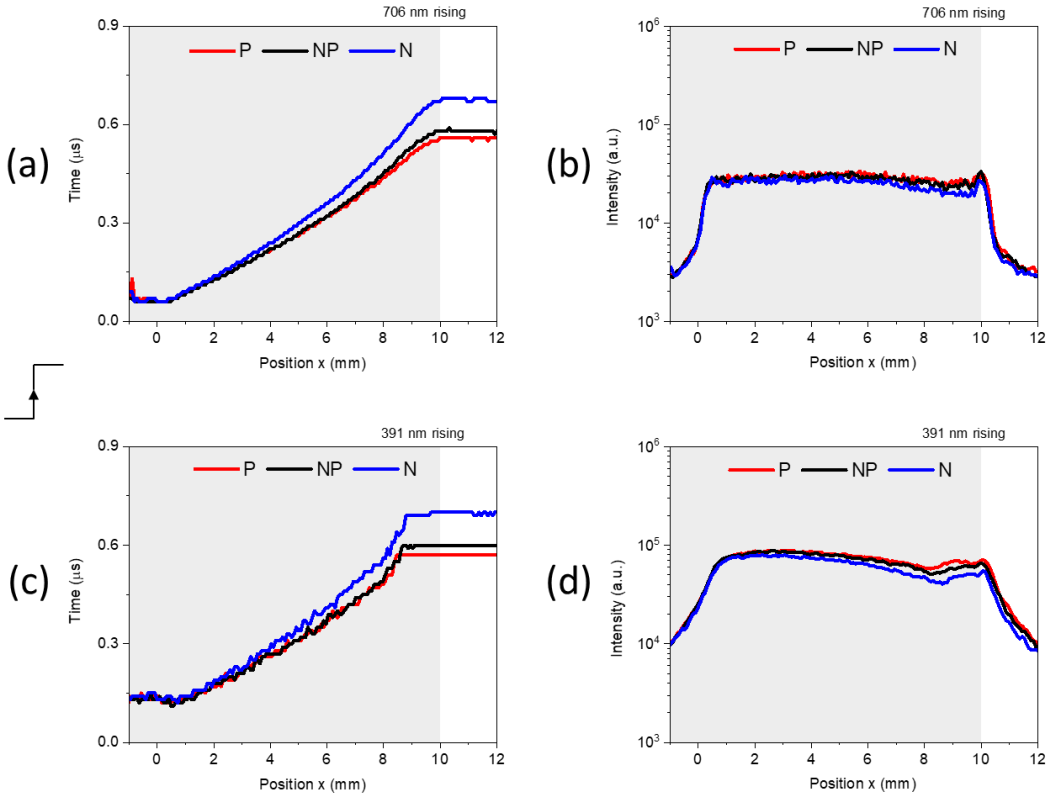

Figure 4.4: The plots for the time and intensities of emission maximum as a function of position during the rising half-phase for He 706 and N_2^+ 391 nm measured from the free plasmas in three polarities, respectively.

As illustrated in Figure 4.4, a comparison is made between the evolution velocity and emission intensity of three polarity plasmas during the rising half-phase. The maximum emission intensity of a specific specie is extracted at each position along the capillary. The ignition times of 706 nm in the rising half-phase are at the same moment in each measurement, seems independent of the polarity of the applied voltage, but the time when the emission arrives at the exit of the capillary differs. It is earliest in P, a little later in NP, and latest in N. This also suits for the 391 nm emission in the rising half-phase, which are shown in Figure 4.4 (a) and (c). This indicates that the propagation speed of the P-plasma is the

fastest, followed by that of the NP-plasma, and that of the N-plasma is the slowest. And a relatively uniform intensity along the entire capillary of 706 and 391 nm emission during the rising half-phase can be observed regardless of the polarity in Figure 4.4 (b) and (d). Besides, a slight intensity relationship of P > NP > N between these three polarity plasmas can also be discovered. These results may be related to the resistance-capacitance characteristics of the bias circuit, which produces a phase shift that results in the lag or advance of plasma development.

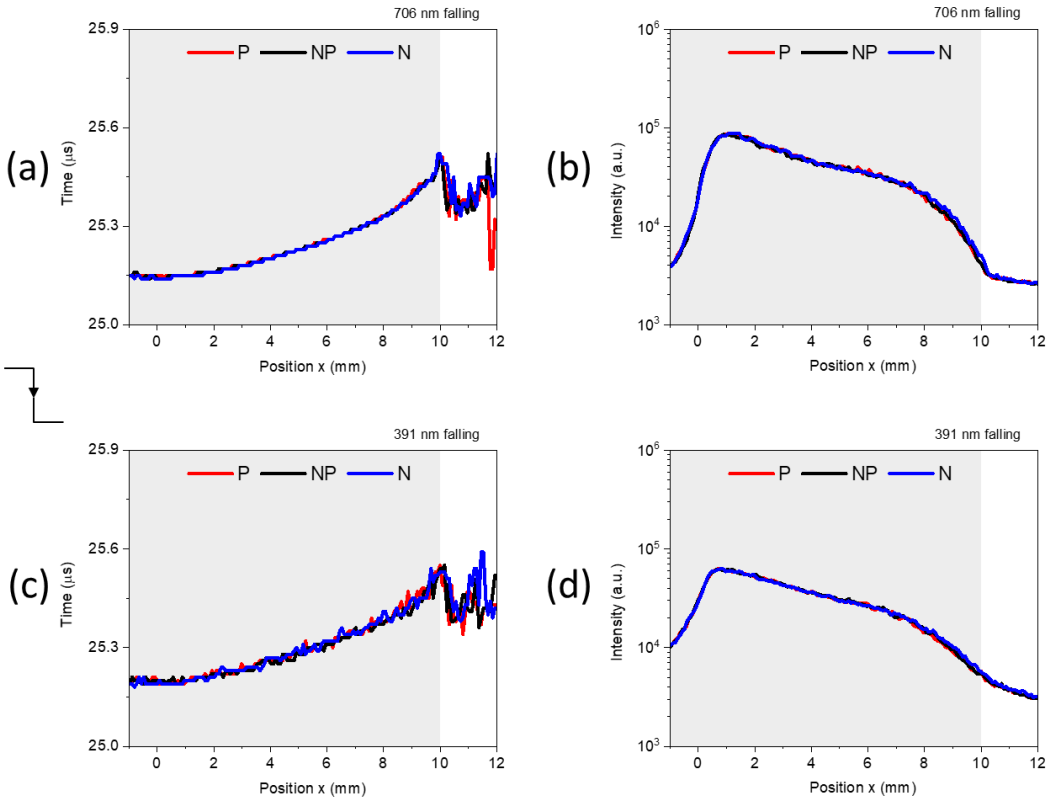

Figure 4.5: The plots for the time and intensities of emission maximum as a function of position during the falling half-phase for He 706 and N_2^+ 391 nm measured from the free plasmas in three polarities, respectively.

As illustrated in Figure 4.5, a comparison is made between the evolution velocity and emission intensity of three polarity plasmas during the falling half-phase. It is evident that the curves are almost overlapping, indicating that both the 706 and 391 nm have equivalent behaviours across the three polarities. In other words, they initiate concurrently, require an equivalent duration to reach the same position, and exhibit comparable intensity at each position along the capillary.

When the falling half-phase starts, the initial local electric field is established by both the remaining charges from the rising half-phase and the applied HV. All three plasmas have the same electric field direction, which is from the capillary wall (attached surface charges) towards the HV electrode. So, the electrons (e.g., emitted from the HV electrode) will be accelerated, collide with other neutral particles, and launch the preliminary plasma. Certainly, positive ions are also produced, and they will be attracted by the negative electrode. As shown in Figure 4.5 (d), the maximum of N_2^+ 391 nm preferred to be closer to the HV electrode.

As explained previously, it is expected that these positive ions will form an ion cloud near the electrode tip. At this time, the direction of the local electric field will be altered, which is from the positive ion cloud to the capillary wall. Then, the electrons are accelerated and undergo subsequent collisions that result in further reactions, generating a new ion cloud at another position. The later process is similar to that that occurred in the rising half-phase, but negative charges will attach to the wall during this process. As a result, the attached positive charges on the glass wall will gradually be neutralised and might be substituted by negative charges until a potential comparable to that of the applied HV is reached.

Here, the emission also extinguishes at the old position. However, as the plasma propagates forward, new emissions appear at new positions with larger x values. Moreover, there are amounts of electrons emitted from the electrode tip during the initial stage of the falling half-phase. In the subsequent process, the electrons and negative ions will attach to the capillary wall due to the mutual repulsion and neutralise the positive charges that accumulated at the wall. This diminishing process takes less time because of the higher density of the initial electrons, which move much faster than ions. This is why all three plasmas have a higher propagation speed during the falling half-phase than during the rising half-phase, as shown in Figure 4.4 and Figure 4.5. When there is no target, it can be seen that the plasma evolution has more or less the same emission images among three polarities especially in the falling half-phase.

It is declared that, since the plasma jet system is equivalent to a capacitor [85], the bias DC voltage might be filtered out and does not work directly in the discharge process [131]. Due to the fact that only one electrode exists in the discharge configuration used in this section, it may also suit here. The consistent and rapid change in the AC voltage of P-, NP-, and N-plasmas, occurring at the onset of each half-phase, may underpin the observed phenomenon. As described in Section 2.2, an alternating voltage will lead to repetitive polarisation of the dielectric barrier. This is caused by the dislocation of the electron cloud of the Si-O bond inside the dielectric layer along the electric field, and the resulting instantaneous dipole moment will generate an inverse electric field to the applied electric field [47]. Therefore, this kind of rapid fluctuation will lead to the same repeatedly polarisation process of the capillary material. As a result, an identical surface charge accumulation process will occur on the inner surface of the capillary, which is proposed to be the main reason for guiding plasma propagation in FμTP [24]. Due to the irrelevance of DC bias in respect to the charges attached at the capillary wall of the free plasmas, the plasmas have almost the same evolution behaviour among the three polarities regardless of the bias voltage. However, this explanation still needs to be further confirmed.

It should be emphasised that, whether in the rising or falling half-phase, the responsible positive ion cloud should not be regarded as its own forward movement. Because plasma is always accompanied by the production of equal numbers of positive and negative charged particles, the so-called ion cloud cannot exist stably for a long time on μs scale and move forward. Instead, it should be understood as the repeated alternation of the continuous consumption and formation process along the capillary of a series

of positive ion clouds. In other words, the electric field is, thus, what propagates with fast excitation and ionisation waves, not the produced particles [83].

Once the potential gradient between the glass wall and the HV electrode falls below a certain threshold (breakdown voltage of the discharge gas), the optical emission ceases. Near the electrode tip, the emission of 706 nm in all cases during the falling half-phase has an evident tail which can be attributed to the second electron emission from the electrode tip. As it only exists a short time that extinguishes a little bit earlier before the plasma front arrives at the exit, this might be an indication that the attached charges reach a potential comparable to that of the applied HV on the inner electrode. Therefore, it shields the potential gradient and hinders the bombardment of positive ions.

4.3.1.3 Diagnosis plasma ignition

In view of the fact that the free plasmas are identical between different polarities in previous sections, it can be suspected that the transient local potential at the exit of the capillary is also identical. To verify this conjecture, a diagnosis tube placed vertically below the outlet of the FμTP capillary was used to transport *He* gas to replace surrounding air in the vicinity of the orifice. *Ar*-FμTPs are driven by a square wave voltage (V_{pp} = 3.2 kV) in three polarities with *Ar* as discharge gas.

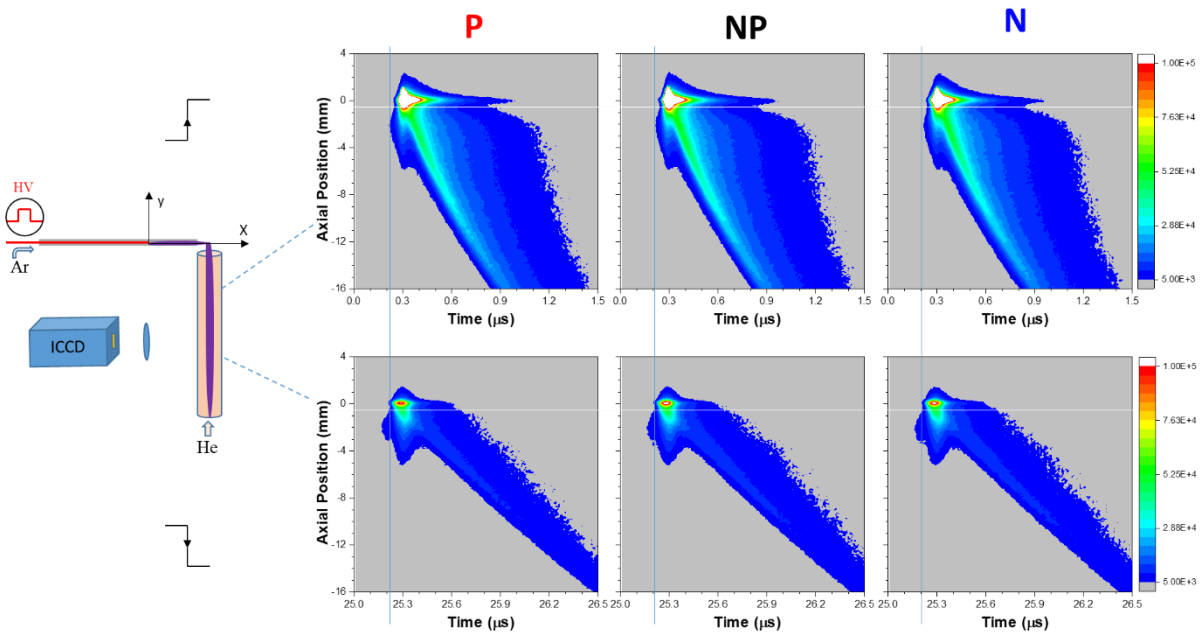

Figure 4.6: Spatial and temporal evolution of the whole emission intensities observed from He-diagnosis plasmas in front of Ar-FμTP free plasmas driven by a HV in three polarities during the rising and falling half-phases, respectively. The white horizontal line at y = -0.5 mm represents the exit of the diagnosis tube.

The horizontal distance between the diagnosis tube axis and the discharge capillary end is 0.5 mm, and the perpendicular distance between the diagnosis tube end and the discharge capillary axis is also exactly 0.5 mm. The ICCD system focusses on the diagnosis plasmas, which are formed after the diagnosis gas is ignited by *Ar*-FμTPs. The evolutionary behaviour of the diagnosis plasmas is recorded in the y direction and the corresponding results are demonstrated in Figure 4.6. It can be seen that all of the diagnosis plasmas are activated from the intersection (0 mm) of the discharge capillary and the diagnosis

tube at almost the same moment (marked by blue vertical lines) during both the rising and the falling half-phases. They also exhibit a comparable propagation speed between three polarities during the rising and falling half-phases, separately. Furthermore, the emission shapes and intensities are all comparable across the three polarities.

In summary, the present study has demonstrated that these diagnosis plasmas, activated by free plasmas in three polarities, are indistinguishable in terms of their evolution behaviour. This indicates that the "transient local potential" or "ion cloud" at the capillary orifice proposed in Chapter 3 is truly the same among the three polarity free plasmas. In addition, the intensity of such potential actually depends on the plasma behaviour within the capillary. It can thus be seen that, in this experiment, the additional DC bias seems to have been isolated and also plays no role in both P- and N-plasmas.

It can also be concluded that in free plasmas, i.e., when there is no interference, almost the same reaction process occurs inside and outside the capillary of FμTP driven by three polarities. Otherwise, there should be some discernible change in emission intensity, shape, or propagation speed, etc. However, this does not correspond to the differentiation of MS signals between the three polarities observed in the laboratory, as displayed in Figure 4.7.

4.3.1.4 Comparison of MS detection

MS is a powerful analytical technique that has been widely applied in many fields. MS detection is based on the mass-to-charge (m/z) ratio of the ions to be analysed. After the neutral analytes were ionised, the resulting ions are accelerated into the MS to be detected. As a soft ionisation source with good analytical performance, FμTP attracted increasing attention for analytical application. The MS signal height usually depends on many external factors, such as the discharge features of the plasma-based ionisation source and the position of the ionisation source relative to the MS inlet. From previous measurements, it is known that the voltage polarity switch seems to make no sense for free plasmas in terms of discharge features. Therefore, now the question arises whether it is also the same in MS analysis.

In this case, the MS inlet acts as a metallic target. As one of the important factors, the polarity switch is expected to make a difference for the MS signal. As shown in Figure 4.7 (a), a *He*-FμTP driven by a square wave voltage (V_{pp} = 2.0 kV) in three polarities is placed in front of a Finnigan LTQ mass spectrometer (Waltham, USA) inlet with 4 mm distance. In this case, no sample was added, the surrounding air components will be ionised by the FμTP ionisation sources and then detected by the MS. The sampling capillary temperature, voltage and tube lens voltage were set to 200 °C, 11 V and 35 V for the positive ion mode, 260 °C, 2.6 V and -30 V for the negative ion mode, respectively. Those parameters were chosen after separately tuning the $H_3O^+(H_2O)$ signal at m/z 37 and the NO_3^- signal at m/z 62 in two modes [9]. In view of the relatively high signal intensity, two MS peaks obtained under positive and negative ion modes are chosen as representatives: the signals at m/z 37 and 55 corresponding to $H_3O^+(H_2O)$ and $H_3O^+(H_2O)_2$, while the signals at m/z 32 and 62 corresponding to O_2^- and NO_3^- [20, 132, 133]. The data obtained and displayed here are an average of 1 min of full scan mode.

Therefore, the discrepancy between the two half-phases of the plasma source is eliminated or averaged in MS detection.

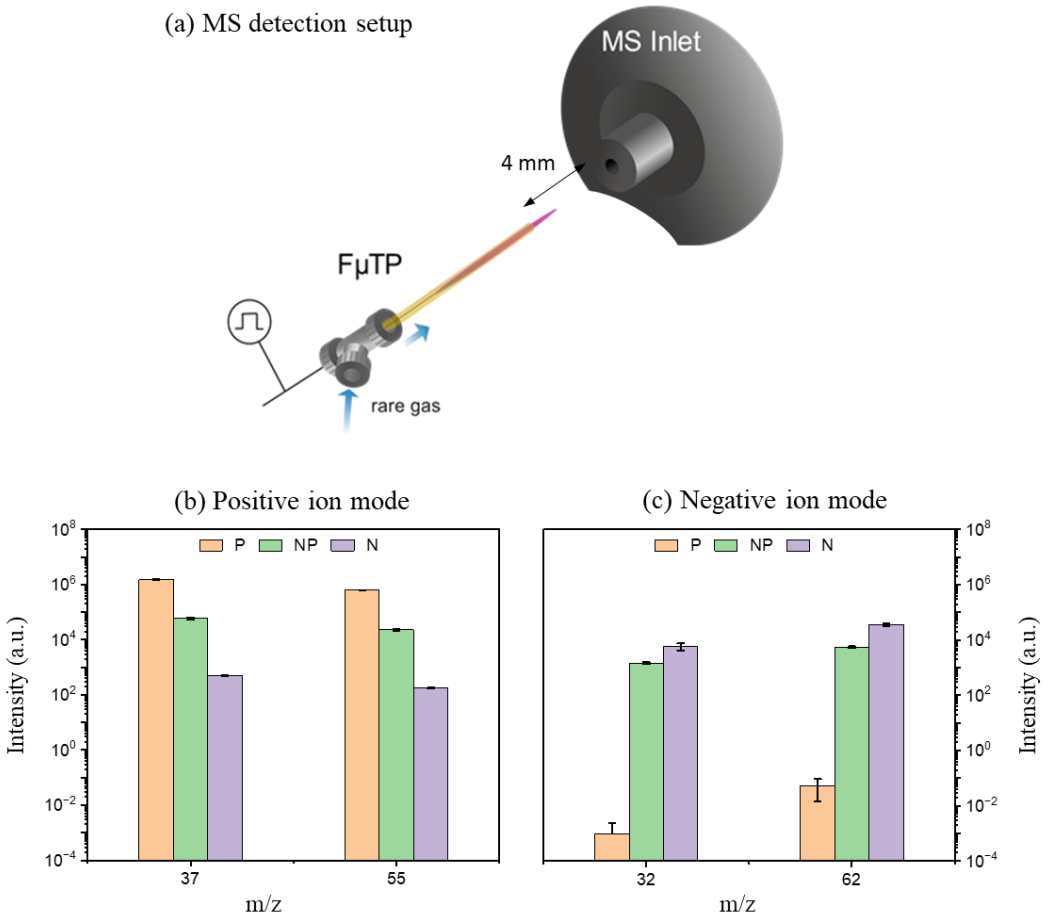

Figure 4.7: (a) Setup for MS detection in front of FμTP with a distance of 4 mm to the MS inlet. The MS signal intensities obtained of representative ions in front of three polarity He-FμTPs under (b) positive and (c) negative ion modes, respectively (the ordinate is on the log10 scale).

Figure 4.7 (b) and (c) illustrate the intensities of several representative ions under two ion detection modes, separately. The signal intensities obtained with the P-plasma are more than 25 times higher than those with the NP-plasma under positive ion mode, while the signal intensities obtained with the N-plasma are at least 4 times higher than those with the NP-plasma under negative ion mode. This means that distinct ionisation performances between these three plasmas with different polarities exist for MS detection. It is noteworthy that plasma sources with polarity antithetical to the MS operation mode are still effective in this instance, i.e., the P-plasma under negative ion mode and the N-plasma under positive ion mode. This can be attributed to the fact that the excitation and ionisation waves outside the capillary are capable of propagating against the direction of the electric field and reaching the MS inlet. Consequently, ions are generated near the entrance, enter the vacuum chamber, and then are detected. Moreover, the NP-plasma exhibits good performance in both ion modes, demonstrating its mode compatibility. In other words, the NP-plasma can be used for MS detection in both ion modes without any intervention.

When FμTP is used as an ionisation source, the ionisation rate of neutral substances is closely correlated with the transient potential in front of the capillary orifice. Previous observations have revealed that both FμTPs and ignited diagnosis plasmas exhibit virtually identical evolutionary behaviours across the three polarities, irrespective of the bias voltage. Nevertheless, quite different MS signal intensities of water cluster are obtained between the three polarities when coupling to the MS instrument in 4 mm distance. In this sense, it suggests that at least the transient potential around the capillary exit was significantly affected by the presence of the MS inlet. This local potential is formed by the ionised air components located outside the capillary, which consequently establishes a substantial electric field. This local field assumes a dual role, functioning not only as a chemical reactor for further ionisation but also accelerating the respective ions towards the MS. In turn, the electrical field and therewith the transmission efficiency of the respective ions is inseparable from the process of surface charge accumulation within the capillary. Therefore, it is reasonable to suspect that dramatic variations in terms of inside plasma reactions also exist because of the MS inlet.

According to the description in Section 2.2.2, some charges will accumulate on the capillary surface because of the delayed redistribution of charges as the AC electric field reversal. As a result, an analogous electrostatic field will be generated by these residual charges, which is called “extra potential bias”. It should be pointed out that, unlike the DC bias introduced by external specific bias circuits, this “extra potential bias” is generated by the discharge system itself. This extra potential bias has a destructive effect on plasma evolution. It may not be very noticeable in the case of the free plasmas, but when external conductors or grounded targets are present and close, this destructive effect would become particularly significant.

As a consequence, one possible explanation is that the MS inlet significantly altered this extra potential bias, distorting the electric field distribution, thereby affecting the plasma development. This differentiated local potential around the capillary exit leads to varied ion efficiencies between three polarity FμTPs, which ultimately results in their different MS performance. To clarify the possible reasons for the differences, it was necessary to explore how exactly the target affects the plasma behaviour. Therefore, a subsequent experiment was scheduled in which a metallic target was introduced to replace the role of a MS inlet at various distances from the capillary nozzle.

4.3.2 FμTP with a target in various distances

Given that the consistency of plasma evolution shown in Figure 4.6 does not match the differentiation of MS signals among the three polarities observed in Figure 4.7, it is essential to verify the influence of MS inlet on the discharge behaviour of FμTP and further clarify the implications on MS analysis and related applications. Therefore, a metallic target was intentionally placed in front of the FμTP. This section will investigate how a metallic target at various distances from the capillary exit affects the

plasma behaviours under three polarity voltages. The results will be exhibited and introduced separately according to the half-phase of the driven voltage.

4.3.2.1 The rising half-phase

When the target distance is 3, 5 and 9 mm, the 706 nm propagation speed of the N-plasma was always the slowest and the P-plasma the fastest, as shown in Figure 4.8. It also can be seen that the emission slope of 706 nm in the rising half-phase is getting bigger with the distance decreasing from 9 to 3 mm in the P-plasma but opposite in the NP- and N-plasmas. This means that the plasma propagation is gradually accelerated with distance decreasing in the P-plasma but decelerated in the NP- and N-plasmas. This can be explained by the enhancement and weakness effect of another electric field formed between the target and the capillary wall.

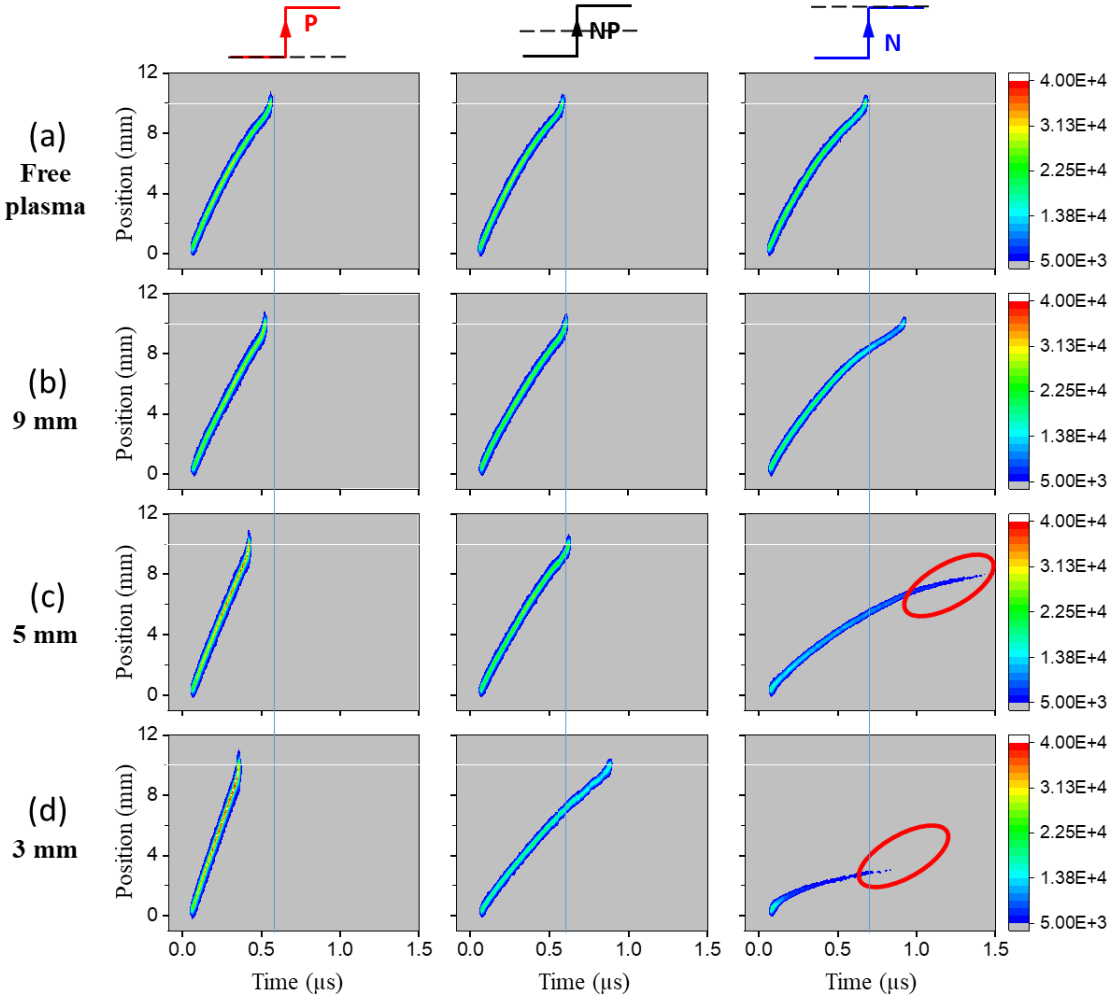

Figure 4.8: Spatial and temporal evolution of the emission intensities of He 706 nm line observed from plasma with a target in 3, 5 and 9 mm driven by the HV in P, NP and N polarity during the rising half-phase, respectively. The white line at 10 mm represents the exit of the capillary (x = 10 mm).

It has been reported that, in AC-corona discharge confined within a plastic tube, alternating wall charging by positive ions during the positive period and by electrons during the negative period occurs [67]. Therefore, it is assumed that in the case of NP-plasma, the remaining attached charges on the glass wall are negative at the beginning of the rising half-phase and then progressively replaced by positive

charges at the end of the rising half-phase. Immediately after that, the remaining attached positive charges on the glass wall at the beginning of the falling half-phase will progressively be replaced by negative charges once again at the end of the falling half-phase. Taking the situation of NP-plasma in front of the grounded target as an example, its schematic diagram of the dynamics electric field in 10 scenarios throughout the cycle along the capillary are shown in Figure 4.9. It can also be used as a reference for understanding the process in the cases of P- and N-plasmas, there are only a few nuances which will be explained later.

However, in the case of P-plasma, the remaining attached charges on the glass wall are positive at the beginning of the rising half-phase and even more positive charges attach to the surface progressively at the end of this half-phase. Then, these positive surface charges will progressively be neutralised by negative charges but not completely at the end of the falling half-phase. In the case of N-plasma, on contrast, the remaining attached charges on the glass wall are negative at the beginning of the rising half-phase, and the partial surface charges will be neutralised gradually but the overall polarity is still negative at the end of this half-phase. Subsequently, more negative charges will attach to the capillary wall at the end of the falling half-phase. The above assumptions will be supported and discussed in detail in Section 6.2.

In the initial stage of the P-plasma, an incipient electric field (E_0, symbolised by red arrows as shown in Figure 4.9 (1)) was built pointing from the HV electrode to the capillary wall. In this case, electrons are attracted by the electrode and collide with other species such as *He* atoms. Then, the positive ions produced, such as N_2^+, will move in the electric field, and some will progressively attach to the glass wall until the end of the capillary as the plasma propagates forward. Synchronously, some of the positive ions will gather to form a space ion cloud. It will in turn further attract free electrons that are in front of itself, thereby cause further collision occurring, and then a new ion cloud is created at a further position. For free plasmas, this is the crucial reason that guides the plasma propagating along the capillary to the exit step by step [24].

After the formation of an ion cloud, the same local electric field (E_1, symbolised by black arrows in Figure 4.9) is established in three polarity plasmas: during the rising half-phase, it is directed towards the surface charge in front of it ((2), (3), (4)); whereas during the falling half-phase, it is directed towards the surface charge behind it ((7), (8), (9)). When a grounded metallic target was placed in front of the plasmas, there is no doubt that another electric field (E_2, symbolised by yellow arrows in Figure 4.9) is created between the capillary wall and the grounded target and increases gradually as the distance decreases. In short, these two electric fields (E_1 and E_2) are in the same direction for the P-plasma, and they all contribute to the movement of the ionisation wave towards the grounded target. Therefore, as the target distance decreases, the plasma propagation gets faster and the emission intensity also increases.

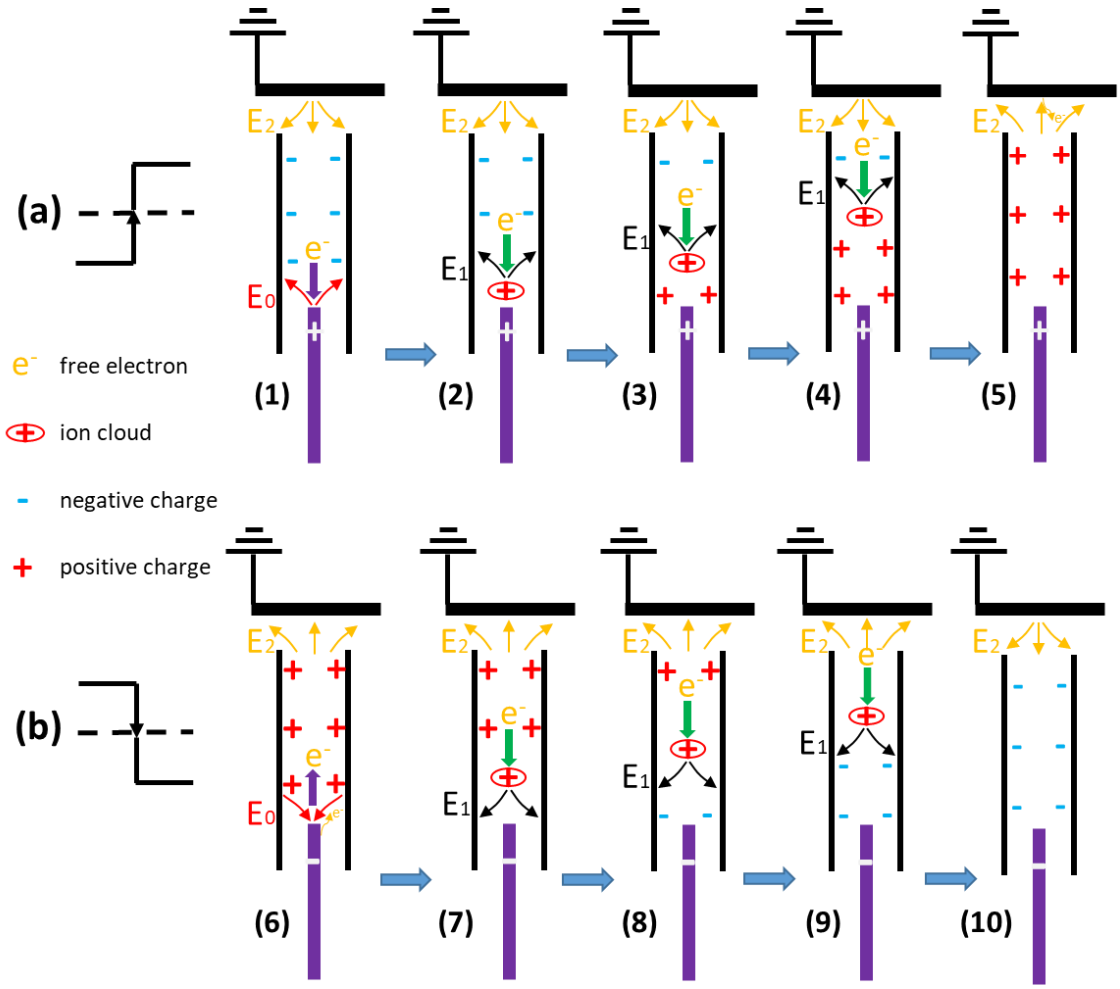

Figure 4.9: Schematic diagram of the dynamics electric field along the capillary for NP-plasma in front of grounded target during (a) the rising and (b) the falling half-phases, separately. The bottom purple line represents the HV electrode, the two black thin lines represent the capillary sidewalls, and the upper black line represents the grounded target.

It should be emphasised that the green arrows in the figure indicate the direction in which the space ion cloud attracts the electron motion. The purple arrows represent the attraction effect only during the early stage of the rising half-phase and the repulsion effect only during the early stage of the falling half-phase on electrons by the HV electrode. Due to the polarity change of the surface charge, the direction of E_2 has a reversion for the NP-plasma when the plasma wave arrives at the capillary exit. However, this is not the case for P- and N-plasmas because no such surface charge polarity change happens.

In contrast to the P-plasma that the capillary wall is filled with positive charges at the beginning of the rising half-phase, the NP- and N-plasmas are conjectured to contain mainly attached negative charges. This is a result of the applied negative amplitude that imposes the polarity of the discharge front reaching the capillary surface [134]. Therefore, the electric field (E_2) between the target and the capillary wall is not towards the target like in the P-plasma but towards the capillary wall in the NP- and N-plasma as shown in Figure 4.9 (a). Given that all these plasmas have the same electric field (E_1) direction, the superposed electric field ($E_1 + E_2$) is enhanced in the P-plasma but weakened in both the NP- and N-plasmas. In this manner, the movement of excitation and ionisation waves will be accelerated in the P-

plasma but decelerated in the NP- and N-plasmas because of the presence of the target. These effects become more and more intensive as the target distance is shortening.

In N-plasma, once the target distance is reduced to 3 or 5 mm, the 706 nm cannot even reach the capillary exit anymore, as shown in Figure 4.8 (c) and (d) marked with red circles. When the distance decreases to 5 mm, the emission seems to stop at x = 8 mm, which means that these two opposite electric fields (E_1 and E_2) are comparable and offset each other at this position. Thus, the discharge in this area will gradually be suppressed and eventually quenched. Furthermore, after the distance decreases to 3 mm, the plasma can even only propagate to x = 3 mm. An increasingly obvious weakness of the intensity along the capillary can be observed as the target distance decreases in the N-plasma. The 391 nm emission has similar behaviour which can be seen in Figure 4.10 (c) and (d). The electric field from the inner HV electrode to the grounded target has been neglected here because of the long distance and the shielding effect of attached charges on the glass wall.

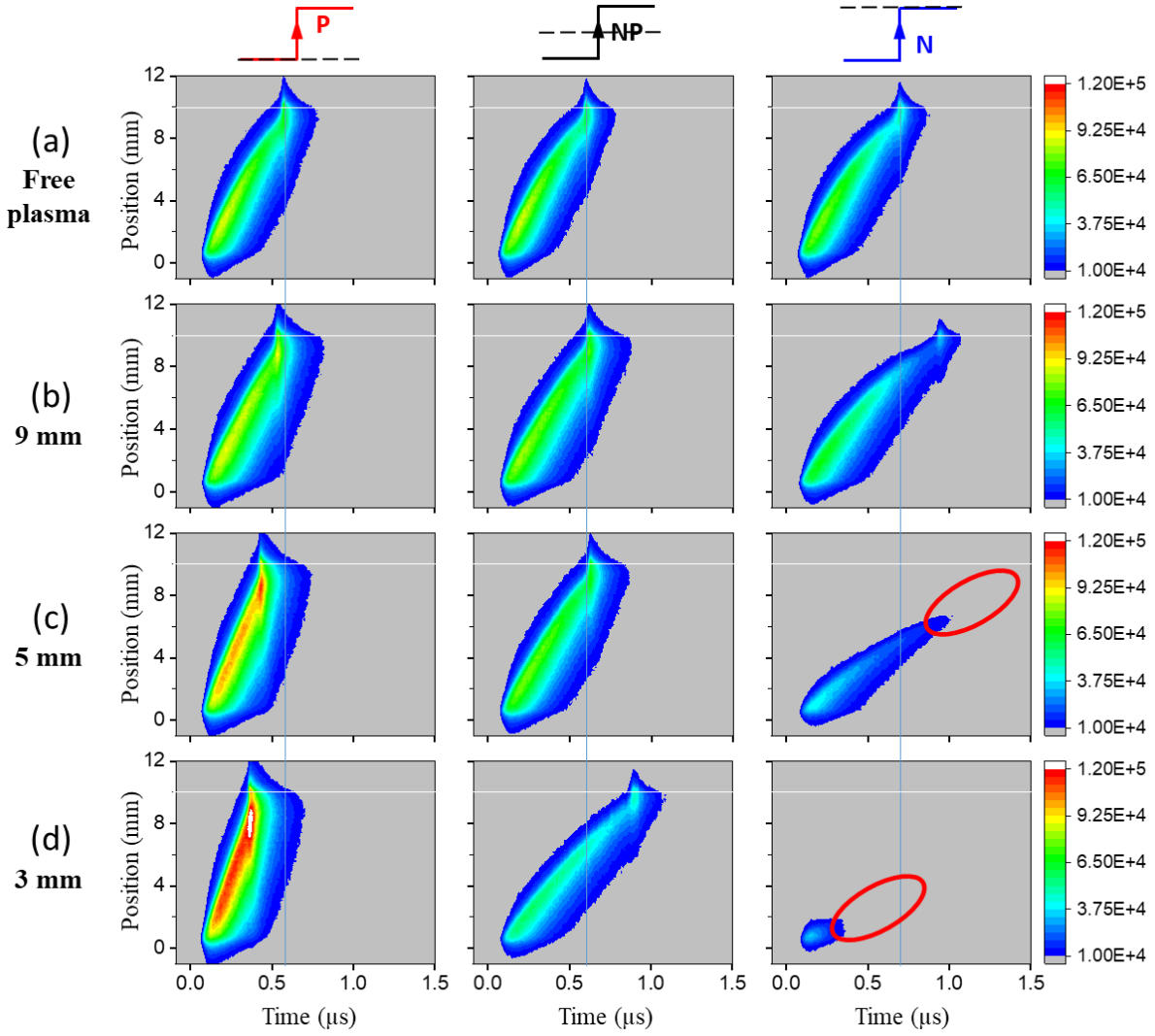

Figure 4.10: Spatial and temporal evolution of the emission intensities of N_2^+ 391 nm line observed from plasma with a target in 3, 5 and 9 mm driven by P, NP and N polarity HV during the rising half-phase, respectively. The white line at 10 mm represents the exit of the capillary (x = 10 mm).

As shown in Figure 4.10 in comparison to Figure 4.8, the 391 nm emission during the rising half-phase has a very similar behaviour to the 706 nm emission between different polarities under various target distances. When comparing the change trend of emission intensity of the *He* 706 nm line with that of the N_2^+ 391 nm line in the rising half-phase under decreased target distances, it can be found that both the intensity of *He* 706 and N_2^+ 391 nm increases in the P-plasma. This could be attributed to the fact that more N_2^+ B $^2\Sigma_u^+$ with a high energetic level were generated due to the stronger electric field. However, due to the two electric fields (E_1 and E_2) both towards the capillary wall inhibit each other, the intensity of *He* 706 and N_2^+ 391 nm are decreasing in the N- and NP-plasmas as target distance shortening especially in the N-plasma. In addition, the slope of the N_2^+ 391 nm emission in the rising half-phase decreases with decreasing electrode distance in the NP- and N-plasmas, but increases in the P-plasma. This similar behaviour can be explained in the same way as described above for *He* 706 nm.

As the plasma propagates forward during the rising half-phase, some positive charged particles will attach to the capillary wall and neutralise the negative charges that attached on the capillary wall during the falling half-phase. In turn, positive charges might attach to the glass wall as a replacement at the end of the rising half-phase. During the falling half-phase, vice versa. According to the peak propagation of N_2^+ 391 nm, it can be deduced that some of the positive ions, such as N_2^+ will move and deposit on the grounded target and then are guided away. However, it did not occur for the N-plasma with a target at 5 or 3 mm away above the capillary exit according to Figure 4.10 (c) and (d). Similar to *He* 706 nm, the emission of N_2^+ 391 nm also stops at the positions closer and closer to the inner HV electrode with shortening distance. This implies that the positive ion clouds are not able to be generated at positions beyond the stop point (x = 7 or 2 mm), it can be attributed to the mutual inhibition at this point between E_1 and E_2.

Inevitably, both attached positive and negative charges near the target will be guided by the electric field, move to the target, and then are guided away consecutively. This release process will become more and more intense as the target distance decreases and will lead to a smaller number of ions remaining on the capillary wall. However, for the P-plasma, the increase in ions resulting from the higher electric field generated by the shorter distance always outweighs the guide loss through the grounded target.

4.3.2.2 The falling half-phase

As it can be seen from Figure 4.11, the P-, NP- and N-plasmas have comparable emission intensities and similar shapes of the 706 nm emission in the falling half-phase. The propagation seems to keep the same as the distance varies. However, there is an enhancement of the emission around the capillary exit in the N-plasma, particularly when the distance was 5 and 3 mm, as shown in Figure 4.11 (c) and (d), marked with yellow circles. This can be explained by the superposition of two electric fields (E_1 and E_2) pointing in the same direction, which is similar to the mechanism described in the P-plasma during the rising half-phase.

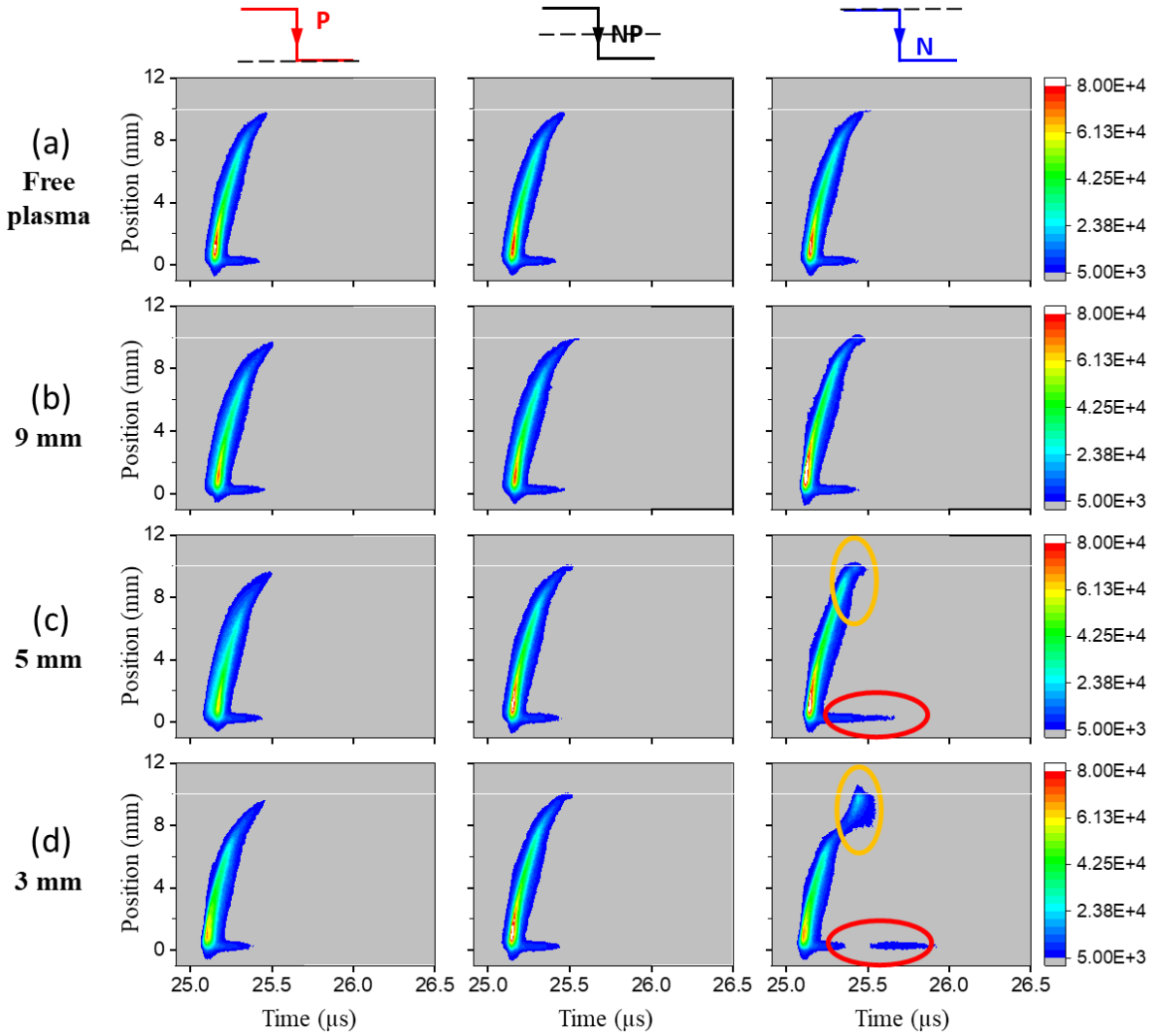

Figure 4.11: Spatial and temporal evolution of the emission intensities of He 706 nm line observed from plasma with a target in 3, 5 and 9 mm driven by HV in P, NP and N polarity during the falling half-phase, respectively. The white line at 10 mm represents the exit of the capillary (x = 10 mm).

In contrast to the rising half-phase, the 706 nm in N-plasma can always reach the exit of the capillary in the falling half-phase even when the target distance is smaller than 5 mm. It should be mentioned that, when the distance is 3 or 5 mm, the tailing phenomenon (marked with red cycles) near the HV electrode tip becomes much longer in N-plasma and still exists after the plasma front arrives at the exit. This seems to be related to the abnormal phenomenon of the N-plasma that it cannot reach the exit during the rising half-phase. One possible reason is that the charge attachment process requires more time than the P- and NP-plasma to reach the same potential.

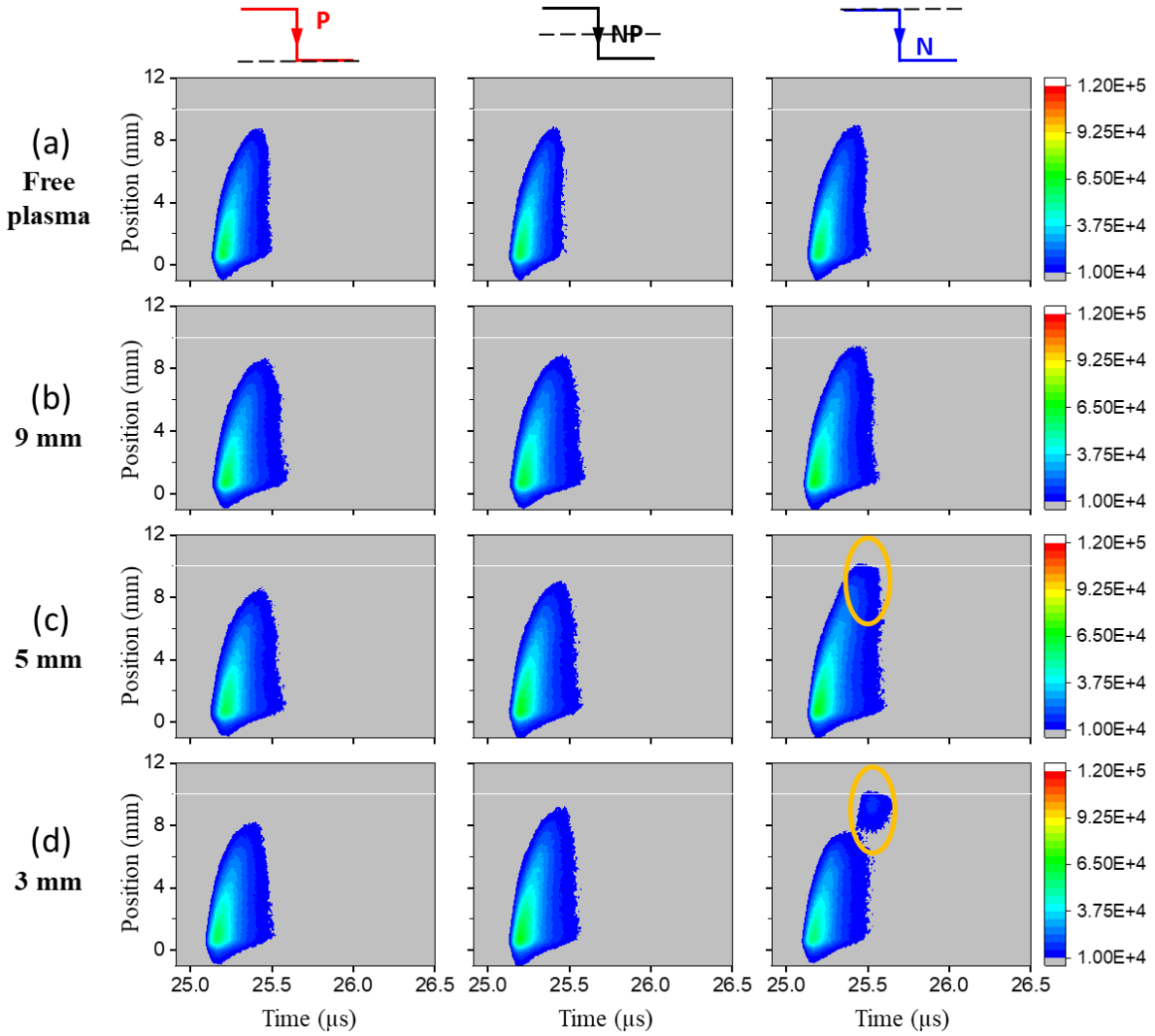

Figure 4.12: Spatial and temporal evolution of the emission intensities of N_2^+ 391 nm line observed from plasma with a target in 3, 5 and 9 mm driven by HV in P, NP and N polarity during the falling half-phase, respectively. The white line at 10 mm represents the exit of the capillary (x = 10 mm).

Just like 706 nm, the P- and NP-plasmas also have comparable intensities and similar shapes regarding the 391 nm emission in the falling half-phase which can be seen in Figure 4.12. Similar with 706 nm, there is an obvious emission enhancement of N_2^+ 391 nm around the capillary exit in the N-plasma. It is particularly obvious when the distance was 3 mm as shown in Figure 4.12 (d), also marked with yellow circles. It is worth mentioning that the N-plasma can arrive the exit of the capillary but the P- and NP-plasmas could not if the target distance decrease to 3 or 5 mm, which is exactly opposite to their behaviours during the rising half-phase. This 391 nm mutation in the N-plasma might be the result of the aforementioned enhancement of the 706 nm emission.

For both 706 and 391 nm, the igniting times are nearly the same in both the rising and falling half-phases, no matter what target distance and polarity voltage was used. All of the plasmas have comparable travel speeds and intensity in the falling half-phase with respect to the free plasmas. A comparison of the emission distribution during the falling half-phase with that during the rising half-phase reveals that the

emission intensities of the lines 706 and 391 nm are preferable to be comparable along the whole capillary (between x = 0 and 10 mm) during the rising half-phase. However, a huge decline always appears during the falling half-phase, regardless of the polarity of the driven voltage.

This reveals that a comparable number of charges are distributed along the capillary until the capillary end during the rising half-phase, but a hugely decreased number of charges attach to the capillary wall along the length during the falling half-phase. This could result from the repulsion and attraction effects of the HV electrode and the attached charges on the glass wall. In other words, a uniform distribution of charges is built up along the capillary during the rising half-phase, whereas a more concentrated charge distribution is built up close to the HV electrode during the falling half-phase. Therefore, it means that the local electric field during the falling half-phase is insensitive to the presence of the grounded target unless the gap is small enough. This is supported by the more and more obvious enhancement around the exit in the N-plasma with the shortening of the target distance, which is demonstrated in Figure 4.11 and Figure 4.12. However, due to the higher number of charges distributed around the exit, the plasmas during the rising half-phase are more sensitive to the presence of the target than those during the falling half-phase under the same distances.

4.3.3 FμTP with a target in 2 mm distance

In this section, a further investigation on the FμTP driven by three polarity voltages with a target in a distance of 2 mm from the capillary exit will be focused and compared with the free plasmas. The results will also be displayed and introduced separately according to each half-phase of the driven voltage. Besides, the individual special evolutionary behaviours will be discussed in detail.

4.3.3.1 The rising half-phase

In comparison with a bigger target distance shown before, the propagation of the plasma is further accelerated in the P-plasma with stronger emission but further decelerated in both NP- and N-plasmas with weaker emission or shorter length. The P-plasma is found to start reaching the target surface after the distance is reduced to 2 mm, which means that the emission appears at the position of x = 12 mm. However, the N-plasma becomes shorter as shown in Figure 4.13 marked with red circles.

After the target distance is decreased to 2 mm, the plasma re-ignition like process occurred in the P-plasma, which represents an additional second plasma propagation as shown in Figure 4.13 marked with yellow circles. This phenomenon was never seen before the target distance was small enough, which can be observed in both 706 and 391 nm emission. In this case, it was initiated after the primary plasma reaches the target. This behaviour has been reported and characterised in various studies [135-138], clearly illustrates a similar emission evolution process. Like a reflection, the restrike could actually return from the target surface back into the capillary along the fully conductive ionised channel. This channel is formed after the first plasma propagation and connects to the HV electrode.

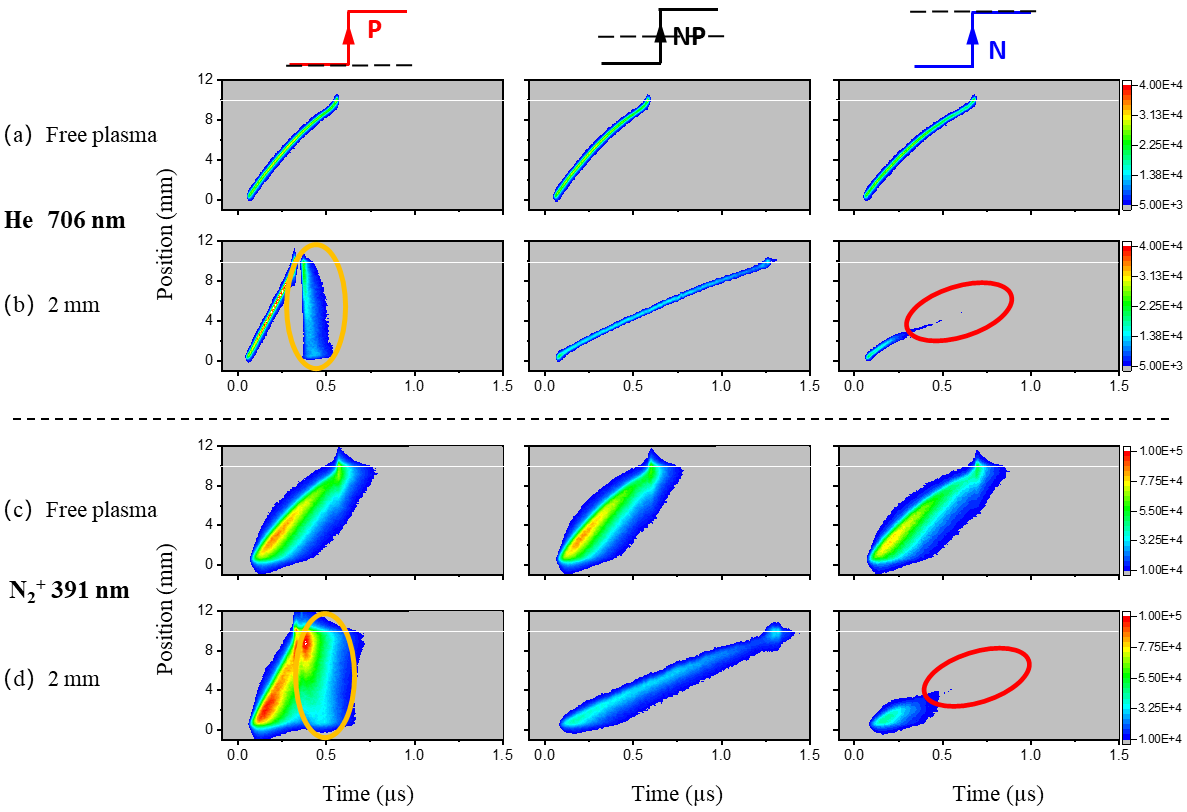

Figure 4.13: Spatial and temporal evolution of the emission intensities of He 706 and N_2^+ 391 nm lines observed from plasma with a target in 2 mm distance compare to the free plasmas driven by HV in P, NP and N polarity during the rising half-phase, respectively (a, b and c, d). The upper subplots (a) and (c) represent those measured in the free plasmas. The white line at 10 mm represents the exit of the capillary (x = 10 mm).

This special behaviour is similar to that observed in a pin-ring configured discharge system, such as LTP and iLTP [104], in which it was named coincident plasma. This coincident plasma generally has a relatively much stronger emission and thus is not conductive to soft ionisation [103]. The so-called coincident plasma can be interpreted similarly. As the streamer head propagates through the capillary, it leaves behind a quasi-neutral channel containing positive and negative charged particles. This channel effectively behaves as a conductive path extending from the HV electrode, which becomes short-circuited once the excitation and ionisation waves reach the grounded electrode, resulting in a sudden re-acceleration of charged species in the opposite direction [139].

For easier observation and analogy, this is marked with black dashed arrows in Figure 4.14 (a) and (b). In LTP, the plasma directly contacts the inner ground electrode, which plays a similar role to the metallic target in this case. While in iLTP, the plasma reaches the dielectric ring electrode. Nevertheless, this kind of re-ignition like process appears in both configurations regardless of whether the plasma reaches a direct ground electrode or a dielectric grounded electrode. As displayed in detail in Figure 4.14 (d), the counter propagation of the secondary plasma launches almost immediately after the primary plasma impact on the target surface, but with a disruption period (between two red dashed lines) about 30 ns. The secondary plasma consequently propagates in the remnant ionised channel of the primary plasma, in a speed of 166.7 km/s (black dashed arrow: 0.36 - 0.42 us corresponding to 10 - 0 mm), which is

almost five times faster compared to the primary plasma in a speed of 35.7 km/s (blue dashed arrow: 0.05 - 0.33 us corresponding to 0 - 10 mm). This anomaly will be discussed further in the following text.

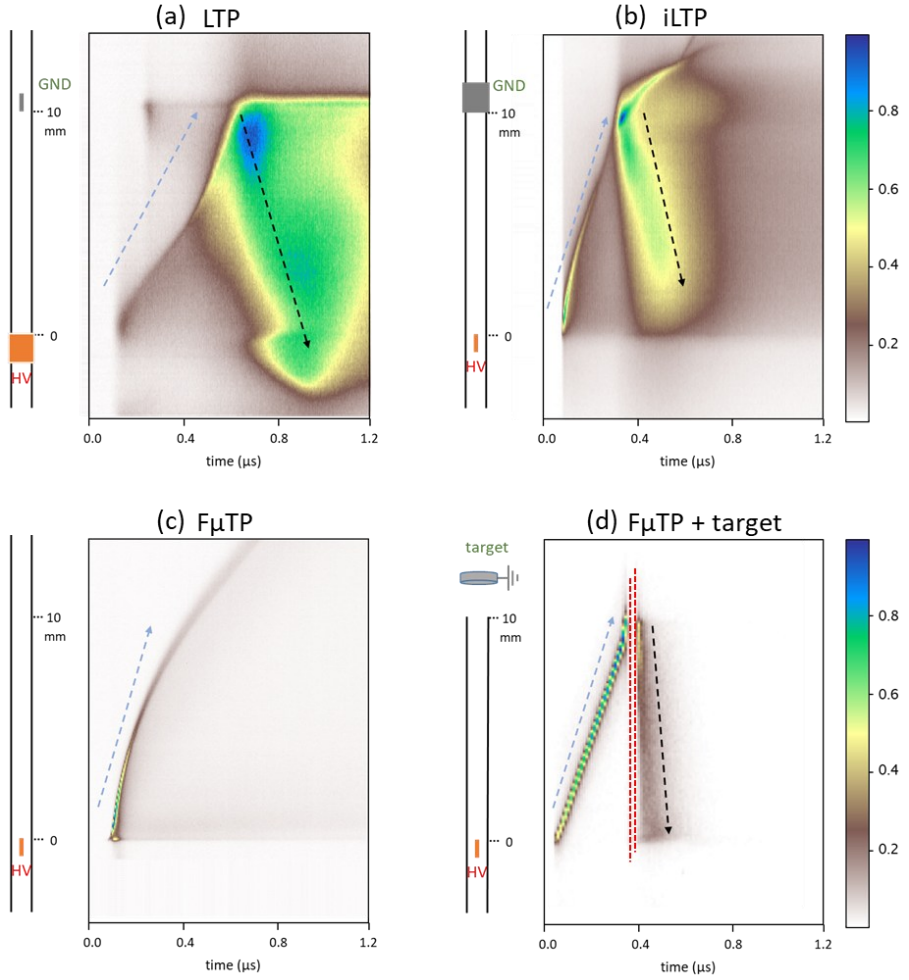

Figure 4.14: Spatiotemporal integrated emission observed from (a) LTP, (b) iLTP, and (c) FμTP without target during the rising half-phase [104]. (d) Spatiotemporal evolution of the emission intensities of 706 nm observed from FμTP driven by positive-biassed HV at a distance of 2 mm from the target during the rising half-phase. The relative intensities are normalised to their highest reached intensity. The discharge configurations are shown as sketches on the left side of the graphics to further illustrate the imaged dimensions. The dotted arrows visualise the successive stages of plasma development and indicate its propagation direction.

It can be clearly seen in Figure 4.14 (d), the first plasma propagates along the capillary from the HV electrode to the target while the second one propagates in the opposite direction. Nevertheless, the emission intensity peaks are both observed in the vicinity of the capillary exit for these two plasmas. As explained in Section 4.3.2.1, the enhancement of the first plasma can be attributed to the addition of the two electric fields (E_1 and E_2) pointing in the same direction and thus increasing the final field strength. As the distance to the target decreases, the gain effect brought about by the target will become more and more obvious, especially at the position close to the target. So, the first plasma has an obviously gradual increase as the excitation and ionisation waves approach the target, this is shown in Figure 4.14 (d). In contrast, it is not that clear but can still be distinguished in Figure 4.8, especially when the distance decreases to 3 mm.

This reflection illustrates the discharge mode transition that happened in FμTP, which can be explained as follows. Once the first plasma front reaches the metallic target, the plasma column that electrically connects the inner HV electrode to the target was established. The conductive channel acts as a transient transmission line between these two electrodes, and positive ions are transiently and partially transferred to the metallic target with subsequent bombardments. Therefore, it is no doubt that more energetic electrons are emitted through the second electron emission of the target and then be accelerated, thereby more positive ions will be populated. During these processes, the positive space charges will congregate and form an ion cloud near the target during the mentioned disruption period.

What cannot be ignored is that as the plasma propagates forward, the initial positive charges attached on the glass wall will be partially and gradually detached and neutralised. Since the attached charges that are closer to the HV electrode experience a longer time, the loss will inevitably be greater. In the end, the direction of the potential gradient will reverse after a certain accumulation time, which was previously described as a disruption period. Subsequently, the electrons will be reaccelerated toward the positive space charge cloud resulting in the ignition of the secondary plasma front, hereafter the generation of further ions starts in the direction back to the inner HV electrode.

As the initiation of the reflected second plasma, a local electric field (E_3) is formed from the positive ion cloud towards the capillary wall. So, the electrons are attracted, and collisions will happen producing more positive ions, the attached positive charges on the glass wall are supplied and then reach a potential comparable to that of a cloud. However, at the same time, a new ion cloud is already generated at new positions (smaller x values), thus this plasma propagates versus the HV electrode step by step. With the emission closer to the HV electrode, the influence of another electric field (E_4) that has an opposite direction will become more and more powerful. This electric field is from the HV electrode towards the glass wall and is formed by the detachment of the attached charges on the glass wall as mentioned before. Therefore, the secondary plasma front is progressively damped, with a continuous drop in intensity from the capillary end to the HV electrode during its propagation inside the channel. Another possible explanation is the decrease of conductivity in the streamer channel caused by various electron loss processes [107].

In addition, it can be observed that an intermittent (uneven) shape appears only in the primary plasma but not in the secondary plasma. This interruption in the primary plasma corresponds to the gradual build-up of the local potentials, whereas this does not appear to be the case in the secondary plasma. It strongly hints at a different mechanism. Due to the fact that the conductive channel was already built by the primary plasma, the high residual conductivity prevented the second streamer from propagating through the existing channels [107]. This is likely to be the result of the high conductivity in the channel, which rapidly shields the local electric field and thus suppresses the development of a new ionisation front [107]. As a result, the reversed local potential establishment process of the secondary plasma is difficult and is thereby not that drastic and identifiable. Since the reversed electric field in the channel

is rather weak but more conductive, the reversed discharge emission looks quite less intensive but lasts for a shorter time interval. However, this is not suitable for LTP and iLTP, which might be attributed to the isolating effect of the glass tubes between the two electrodes.

This reflection phenomenon is drastically contingent upon parameters such as target distance and discharge voltage polarity, which affect whether the potential gradient is reversed. The decrease in emission intensity between the capillary exit and the target can be attributed to the diffusion of surrounding air, resulting in a low density of rare gas atoms in this area and thus weaker reactions. Due to the small target distance, the ion cloud could attract electrons and thereby produce a new ion cloud before being quenched by air components. From the perspective of fluid dynamics, air diffusion has also been weakened because of the blocking effect of the target. This also further explains why this reflection phenomenon does not occur at a gap over 2 mm. However, such reflection is undesirable for analytical applications as it may lead to energy waste, loss of reactive species and analyte ions, and even damage to the internal electrode. Consequently, it is imperative to implement specific measures to circumvent this reflection in its practical applications.

4.3.3.2 The falling half-phase

The comparison of spatial and temporal evolution of the 706 and 391 nm lines during the falling half-phase is shown in Figure 4.15. It should be mentioned that the tailing phenomenon of 706 nm near the

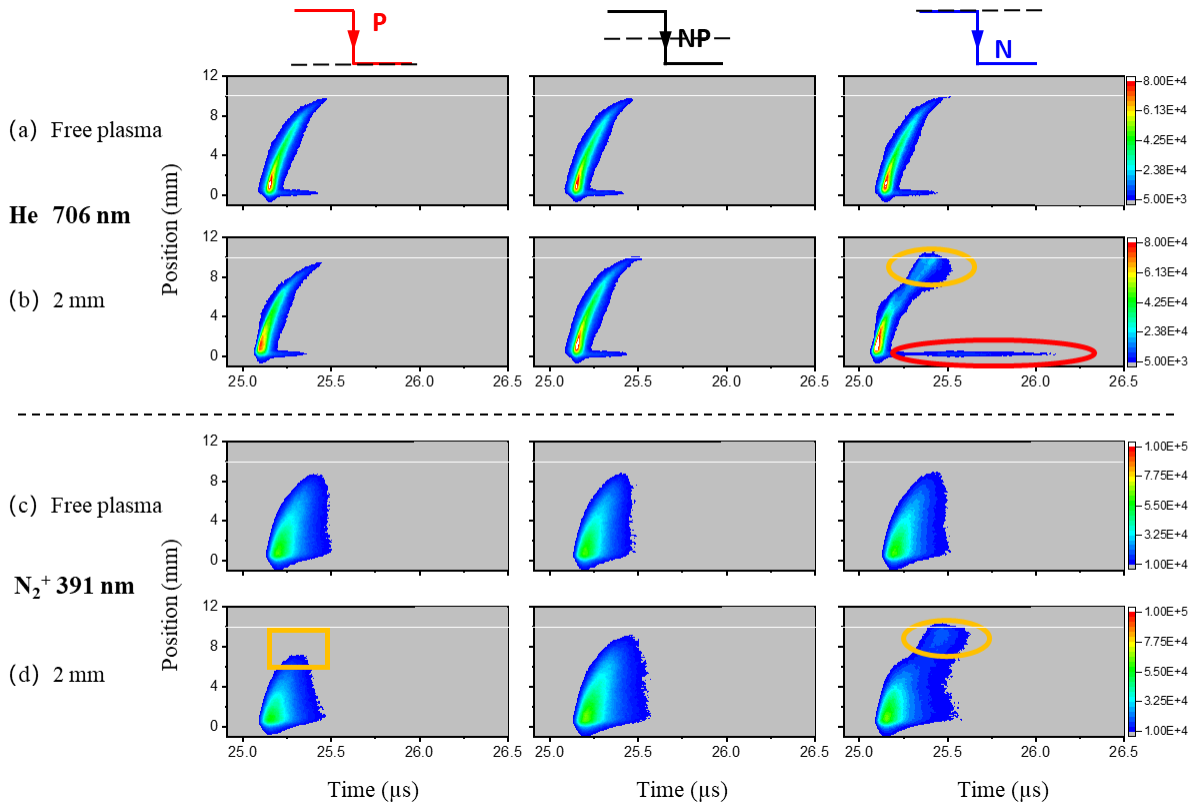

Figure 4.15: Spatial and temporal evolution of the emission intensities of He 706 and N_2^+ 391 nm lines observed from plasma with a target in 2 mm distance compare to the free plasmas driven by HV in P, NP and N polarity during the falling half-phase, respectively (a, b and c, d). The upper subplots (a) and (c) represent those measured in the free plasmas. The white line at 10 mm represents the exit of the capillary (x = 10 mm).

HV electrode tip sustains an even longer time than before in the case of the N-plasma with a distance of 2 mm, also marked with a red circle in Figure 4.15 (b). In addition, an even stronger emission enhancement of both 706 and 391 nm around exit still exists, which are marked with yellow circles, as shown in Figure 4.15 (b) and (d). It demonstrates the presence of a further strengthened local electric field near the capillary end and the target in the falling half-phase. Once the target distance was too small, the charge carrier in the conductive channel will grow significantly and even exceed the breakdown limit. This is a warning sign for applications and the corresponding prevention and control measures must be taken. The responsible local electrical field enhancement can be attributed to the effect of the target on the accumulated surface charges, which will be further discussed in Chapter 6.

It is worth noticing that a slight reduction of 391 nm emission during the falling half-phase of the P-plasma (marked with yellow rectangle) is found in Figure 4.15 (d), which could be considered as the sequelae of its reflection during the rising half-phase. This is because no indication of this type of emission reduction was found before the distance was reduced to 2 mm, just as the reflection phenomenon does not occur at a distance of more than 2 mm.

4.4 Conclusions

In this chapter, the discharge processes of three polarity FμTPs on the background of the influence of a metallic target under several distances have been investigated and discussed. The observed special behaviours are not readily accounted for by the existing literature. Nevertheless, available hints suggest a combined influence of the target and surface charge deposition. Accordingly, several hypotheses are proposed to explain these phenomena, particularly concerning the interplay between emission evolution and local electric field variations. The introduction of an influence of target to the accumulated charges on the glass surface for distorting the local effective electric field allows the results to qualitatively correspond to the experimental data.

For free plasmas, FμTPs exhibit very similar emission behaviours in both half-phases, regardless of the voltage polarity. It was suspected that the consistent repeatedly polarisation of the capillary can be used to explain this, which can be attributed to the applied voltage undergoing the same rapid change process at the initial stage of each half-phase. It seems that the bias DC voltage is filtered out and does not work directly in the discharge process. So, almost the same number of surface charges accumulate on the glass wall and dominate the subsequent behaviour.

When a metallic target is introduced in front of FμTP, polarity-dependent electric field distributions give rise to quite different plasma behaviours at various target distances. When a bipolar voltage was applied, the NP-plasma decelerates during the rising half-phase as the target approaches. When a positive voltage was applied, the P-plasma accelerates during the rising half-phase as the target approaches, which is opposite to the NP-plasma. At a target distance of 2 mm, another discharge mode appears, which looks like a reflection. It is believed that the enhanced electric field on the propagation pathway of the P-

plasma and the subsequent potential gradient reversion near the target results in the re-ignition of the secondary plasma front. When a negative voltage was applied, the N-plasma also decelerates during the rising half-phase as the target approaches, which is similar to that of the NP-plasma. When the target distance is equal or smaller than 5 mm, the plasma even cannot reach the capillary exit during the rising half-phase but capable during the falling half-phase. Both the P- and NP-plasmas demonstrate comparable behaviour during the falling half-phase across all measured target distances. In contrast, the N-plasma exhibits a pronounced enhancement of the 706 and 391 nm emissions near the capillary exit during the falling half-phase. This indicates the presence of a significant electric field enhancement, suggesting a potential hazard in application scenarios where a small distance exists. Therefore, the N-FμTP should be avoided from coupling with MS inlet at distances below 3 mm.

The onset of discharge mode alteration in the P-plasma at 2 mm and the distortion in the N-plasma below 5 mm are both not desirable for practical applications. However, the NP-plasma shows a smoother change tendency and more predictable behaviour over a range of distances, which suggests enhanced controllability. In general, from the perspective of minimising the risk of reflection and distortion, NP-plasma is argued still a priority option for applications in small distances. Based on the comparison between diagnosis plasma ignition and MS detection experiments, the significant impact of a nearby conductor on FμTP was further indicated. The compatibility of NP-plasma for MS detection in both positive and negative ion modes was also evidenced. Moreover, it was convinced that the polarity switching of FμTP provides considerable benefits to the ionisation application when it is coupled with MS at a distance of 4 mm. This information is fundamental for any attempt to improve the performance of plasma-target systems.

Overall, these insights gained into the influence of a conductive target on plasmas driven by three polarity voltages under varying distance conditions contributed to the performance optimisation of FμTP for applications.

CHAPTER 5

Characterisation of corona discharge

The classical corona discharge was named due to its luminescence phenomenon which is like a halo of the moon in the dark, this is also in accordance with the cognition that the corona discharge is a local region discharge around the electrode edge [42]. Typically, a corona discharge only yields a very small plasma (~ mm scale). In contrast, FμTP has the capacity to generate a long plasma column (~ cm scale) and can even produce a plasma jet that exceeds the capillary length. From this point of view, FμTP seems to offer more applications prospects than corona discharge in numerous other fields, in addition to its utilisation as an ionisation source.

Both DC and AC voltages can be used for initiating corona discharge. Recent studies have revealed that AC-corona discharge is superior to DC-corona discharge as a soft ionisation source [68, 71]. The realisation of analyte ionisation by AC-corona discharge bears a resemblance to traditional APCI through the so-called "CI" process. "CI" was first proposed refers narrowly to a technique that uses reagent gas ions (produced by chemical reactions) to undergo ion-molecule reactions (mainly gas-phase proton transfer) with neutral sample molecules rather than conventional directly electron impact to achieve soft ionisation [140]. Compared to the configuration of corona discharge, FμTP is frequently treated as just a variant of corona discharge. Someone may ask whether the discharge in FμTP is also a corona discharge, even though the discharge properties in FμTP have already been deeply investigated [9, 10, 23-27].

In the case of bipolar square wave voltage typically applied in FμTP, each cycle consists of two distinct half-phases with voltages in opposite polarity. During these phases, nearly constant positive or negative amplitudes are considered to be applied, with the exception of the sharp rising and falling edges of the waveform. In order to better understand and distinguish FμTP from corona discharge, it is valuable to

further explore and compare their discharge characteristic from multiple perspectives. In hope of ascertaining the similarities and differences between DC-, AC-corona discharges, and FμTP, this chapter will discuss the subject carefully.

5.1 Experimental arrangement and data processing

The basic experimental arrangement used in this chapter is shown in Figure 5.1, where a needle electrode is connected to a HV power generator (DC or AC). In particular, a copper ring (ID-10 mm, OD-20 mm, thickness-2 mm) was used as an electrical potential detector. It was placed coaxially with the HV electrode and can be moved along the needle axis through a translation stage. The real-time ring potential waveform is monitored by a 70 MHz digital storage oscilloscope (Agilent DSO-X 2002A, USA) in combination with a single-ended HV passive probe (Tektronix P6015, USA). The setup enables the investigation of potential around the plasma under defined conditions.

The same optical instruments (Ocean Optics and ICCD system) are also utilised to obtain integrated as well as temporal-spatial resolved emission spectra. Other detailed experimental conditions, such as the applied voltages or special equipment used in the individual measurements, will be introduced in the corresponding sections.

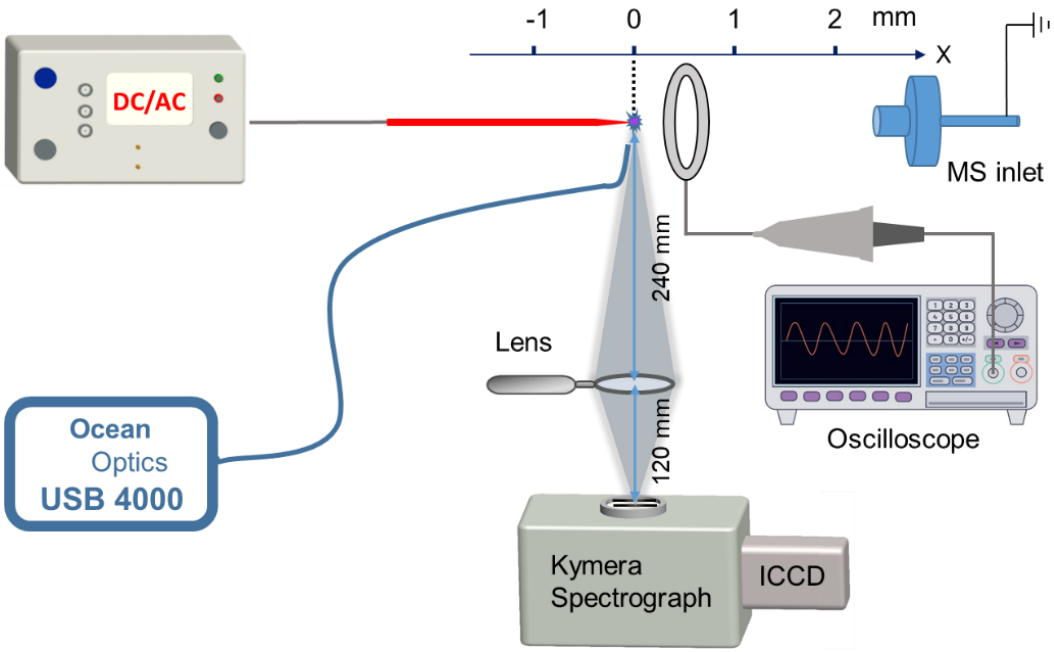

Figure 5.1: Schematic diagram of the experimental setup.

In this instance, both DC- and AC-corona discharges are initiated in ambient air. In order to eliminate the influence of electromagnetic radiation from the HV generator on the detected signal, two times measurements were performed: one time using the oscilloscope in DC coupling mode (detect both DC and AC components) and one time using the oscilloscope in AC coupling mode (only detect AC component), but all measuring when plasma is ignited. Then the data processing method utilised here

for the analysis is achieved by calculating the difference between these signals obtained under two coupling modes. After this method was employed for corona discharges, a constant static potential waveform (or DC component potential) was observed at each position for these plasmas.

In principle, because of no electrical connexion, the DC component coming from the HV power generator itself could not be transferred to the ring detector when a DC voltage or a biassed AC voltage is applied to the electrode. In addition, the AC coupling mode has filtration to the DC component. Therefore, the final DC component obtained after subtraction should be considered as a masterpiece of plasma.

5.2 From DC- to AC-corona discharge

Corona discharge is also known as a type of localised emission resulting from transient gaseous ionisation when the voltage gradient exceeds a critical value. Until now, no distinction has been made between positive and negative DC-corona discharges in terms of optical shape. Furthermore, there is no direct report on their more subtle emission images or on whether they can be distinguished from each other. Fortunately, quite different shapes and colours in a macro photography perspective between positive and negative DC-corona discharges were found for the first time using a camera equipped with a macro lens.

5.2.1 Macroscopic photos of DC-corona discharges

Corona discharge can be visible in the form of light and is typically regarded as a violet glow spot around the needle tip in the dark room. To understand more about DC-corona discharge, a commercial APCI needle (tip diameter ~100 μm) was applied as the HV electrode and a MS inlet (not shown in the photos) was used as counter electrode with an 8 mm distance. A digital camera (Fujifilm X-T5, Japan) paired with a macro lens was employed to shoot photos in an exposure time of 30 s. A series of subtle photos of DC-corona plasmas driven by positive and negative voltages with various amplitudes are displayed in Figure 5.2, respectively. The location of the needle tip is marked by the white horizontal lines. Without the help of micro focus camera, these photos are hard to be recognised directly by human eyes.

As demonstrated in Figure 5.2 (a), the application of a positive DC voltage to the needle resulted in the observation of a more and more apparent “hat”-shaped plasma in a colour of blue-purple packs the electrode surface as the applied amplitude increasing. It seems that no high-energy-level species depart from the electrode surface and move outward. The higher the applied voltage, the gradually longer the emission length from the tip towards the back of the electrode can be seen, and a more and more bright emission at the electrode tip is observed. As shown in Figure 5.2 (b), when a negative DC voltage was applied to the needle, a “fan-spray” plasma (sector-shaped plasma) is observed in red-purple colour towards the ambient air. However, nearly no emission is found in the rear part of the electrode tip. The

higher the applied voltage, the brighter the image in the same colour can be seen especially in front of the electrode tip. It seems that the high-energy-level species always depart from the electrode tip and prefer to disperse in a forward rather than a backward direction.

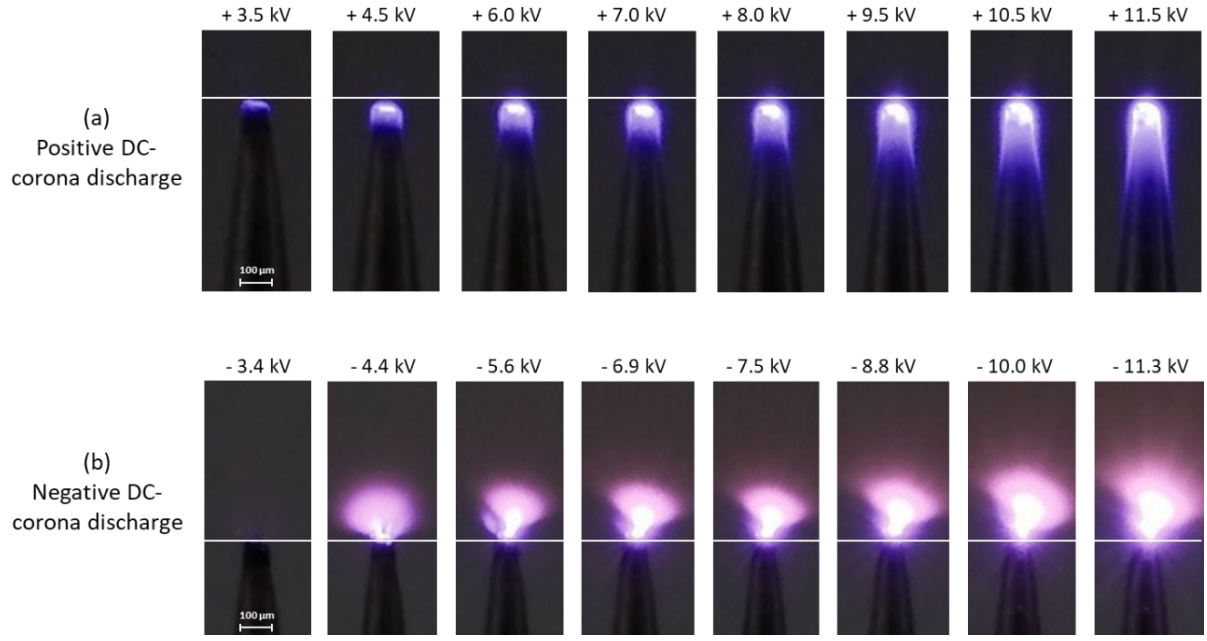

Figure 5.2: Macroscopic photos of (a) positive and (b) negative DC-corona plasmas under various voltages taken by a digital micro focus camera, the specific value of applied voltages are shown on the top of each photo, the white horizontal lines mark the location of the needle tip.

As the voltage amplitudes increase, these photos reveal that both DC-corona plasmas present an expansive image, not only a point-like image anymore. The positive DC-corona discharge manifests itself as a uniform plasma packs the needle tip part. The negative DC-corona discharge manifests itself as a non-uniform plasma, which appears as tufts of the emission from the needle tip injecting into ambient air [141]. Besides, the colour also differs between these two kinds of corona discharge. In comparison to the positive DC-corona discharge, the negative one appears to be more red. In short, the positive DC-corona discharge is strikingly different from the negative one, no matter in colour or shape.

These photos were taken in an exposure time of 30 s, which is a hugely long time compared to the typical nanosecond time scale of the discharge process. So, these photos can be treated as the integration of many transient photos during this time period. In order to obtain high-speed information with higher resolution, it is meaningful to capture their transient emission distribution images.

5.2.2 Transient images of DC-corona discharges

The entrance slit of the spectrograph was placed parallel to the axis of needle electrode, its width was set to 2500 µm. Even though there is no trigger edge in the applied DC voltage, high-speed optical emission measurements are still possible to be implemented. In this case, the ICCD system was still triggered by a synchronous signal generator. The transient images in almost an instant (during 20 ns of

the gate width) are shown in Figure 5.3. With the help of these kinds of images, a deeper insight into the reaction emission region of the discharge process at one moment becomes reality.

Since corona discharge produces an extremely thin plasma with feeble emission intensity, background interference (e.g., scattered or stray light) requires careful control. It should also be noted that the utilised ICCD system incorporates built-in signal amplification and noise suppression capabilities. If plasma emission is too weak, it may fall below the system's noise threshold and be filtered out. In such cases, the background noise intensity approaches that of the plasma emission, and the plasma signal may be misidentified as background, preventing the capture of transient images. To obtain clear images at such a short exposure time, it is essential to minimise background light noise. Therefore, all potential light sources present in the room, including indicator lights, were masked during the data acquisition process.

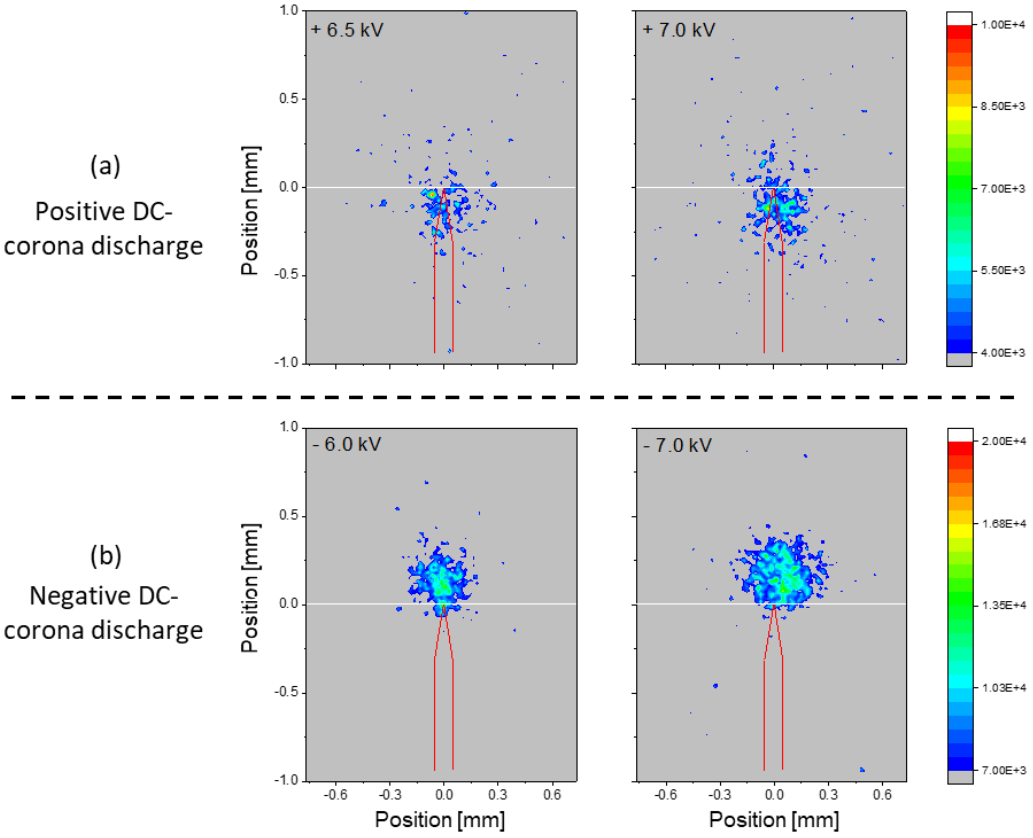

Figure 5.3: Instant whole emission images of DC-corona discharge driven by (a) positive (+6.5 and +7.0 kV) and (b) negative (-6.0 and -7.0 kV) DC voltages. The red curves represent the contour of the needle electrode, and the white horizontal lines at 0 mm represent the position of the needle tip.

As demonstrated in Figure 5.3, the emission images obtained from the positive and negative DC-corona discharges exhibit a similar morphology to that observed in Figure 5.2. An emission that surrounding the needle tip primarily below position 0 mm is observed in positive DC-corona discharge. Conversely, a cloud of emission in negative DC-corona discharge exists in the vicinity of the needle tip, but mainly upon position 0 mm. The distinct emission images and the evident position shift along the needle axis between these two kinds of corona discharges can be attributed to the distinctively opposite electric field directions and, consequently, the different reaction mechanisms.

The specific principles of their formation process have been well discussed. Both positive and negative DC-corona discharges have been established to be reliant upon a chain reaction process known as the electron avalanche [50, 142]. Their step-by-step electron-impact reaction process is not the main point of this thesis, thus no further elaboration is given here but only a brief statement and comparison. The greatest distinction between positive and negative DC-corona discharges with respect to the generation of secondary electron avalanches pertains to the origin of these secondary electrons [42]. In a positive DC-corona discharge, they are initiated by the gas surrounding the plasma, with these new secondary electrons travelling inward. Conversely, in a negative DC-corona discharge, they are emitted from the electrode tip, with these new secondary electrons travelling forward. Their distinguishable morphologies relate to the distinct micro-discharge process.

In a positive DC-corona discharge, free electrons are attracted and accelerated inward, moving towards the surface of the HV electrode. Consequently, the highest-energy electrons are generated in the vicinity of the HV electrode surface. In this region of high potential gradient, the electron density exhibits a precipitous decline in proximity to the needle surface. These high-energy electrons collide with N_2 molecules to excite or ionise them, resulting in predominantly blue-violet light emission, as shown in Figure 5.2 (a). Due to the homogeneous source of secondary avalanche electrons, the emission of positive DC-corona discharge is uniform. Since the entire curved needle electrode is at high potential but with the smallest radius of curvature at the end, this results in the strongest electric field at the electrode tip. Therefore, at a voltage of 3.5 kV as shown in Figure 5.2 (a), the excitation and ionisation of N_2 occurs only at the tip. As the applied voltage is increased in a gradual manner, the electric field strength at an increasing number of locations breaks through the threshold value, and thus more and more photon emission appears along the electrode surface. As a consequence, its emission image gradually extends posterior to the electrode tip, thereby undergoing a gradual transition in shape from a point to a hat. In addition, positive ions are repelled outwards.

In a negative DC-corona discharge, a substantial number of electrons are repelled and scattered in a fan shape, accelerated outward, and collide with N_2. Due to electrons are allowed to drift a long path, the discharge continues some distance beyond the needle tip. So, many high-energy electrons are located in the outer, low-field regions due to the repulsion effect [141]. This results in a diffusive and slightly larger visible region in the case of negative DC-corona discharge than the corresponding positive DC-corona discharge, which is displayed in Figure 5.2 and Figure 5.3. In addition, positive ions are attracted inward by the negative electrode. As a result, the ensuing neutralisation of partial N_2^+ leads to much less remaining of N_2^+, measured by the relatively lower emission of the 391 nm line in the negative DC-corona discharge. As the applied voltage increases, more and more energetic electrons are scattered, so more and more intense excitation and ionisation of N_2 occurs in front of the tip. So, increasingly strong light emission is observed, but with little change in shape and colour, as shown in Figure 5.2 (b).

The sketches of positive and negative DC-corona discharges are shown in Figure 5.4, the red needles at the bottom represent the HV electrodes. The red dashed ellipses show the plasma regions, where the electron-impact reaction mainly occurs, and thereby the approximate area of light emissions. Besides, the large arrows at the top near the grounded plate indicate the movement directions of the unipolar charges in the ion drift region [42]. This means that outside the plasma region, nearly pure positive charged particles in positive DC-corona discharge and pure negative charged particles in negative DC-corona discharge are pushed by the respective electric force and move forward. It should be noted that, in the ion drift region, the field generated by the space charge causes a significant distortion to the external electric field [72].

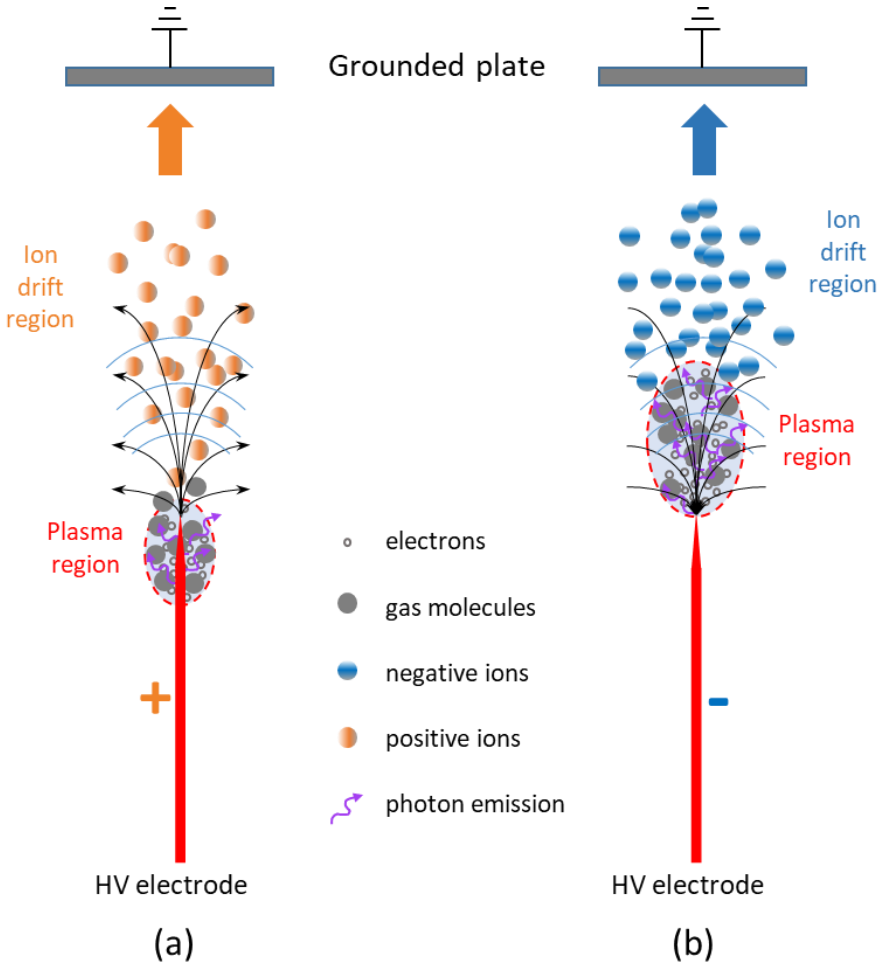

Figure 5.4: Sketches of (a) positive and (b) negative DC-corona discharges in a point-to-plate geometry, the positive and negative ions are not depicted in the plasma regions.

With the help of a numerical model, the number density of electrons in the negative DC-corona discharge was found to be nearly four orders of magnitude greater than that in the positive DC-corona discharge [72, 141, 143]. As a result, the negative DC-corona plasma appears thicker than the positive plasma, and this variation in plasma thickness is discernible through photon emission. This also explains the experimental finding that the ignition voltage of negative DC-corona discharge is lower than that of positive DC-corona discharge [144]. This might also be the reason why the higher amount of N_2 is

excited in the negative DC-corona discharge than in the positive DC-corona discharge, which will be discussed later.

Both the positive and negative DC-corona discharges rely on the impact reactions of energetic electrons. However, these space electrons are rapidly consumed by massive neutralisation through the rapid quenching action of the surrounding air components. Only in the plasma regions, this quenching action is weaker than the electron generation. It is the competition between these two processes that causes both positive and negative DC-corona discharges to be limited to locally sustaining the discharge reaction and presenting the small optical images.

In summary, in positive DC-corona discharge, the electric field strength is greatest at the edge of the electrode (needle surface), so the electrons get highest energy near the edge, thus the light emission seems to be located mainly near the electrode surface, like a hat wrapped around the needle electrode. In negative DC-corona discharge, the electrons emitted from electrode tip are scattered forward and accelerated, so that the collision reactions can occur at a relatively distant location.

5.2.3 Ocean Optics spectra of DC-corona discharges

The previous photos of positive and negative DC-corona discharges exhibit a similar purple-blue colour, mainly due to the emission of N_2 (SPS) and N_2^+ (FNS) in the range of 380 ~ 500 nm, as shown in Figure 5.5. However, it was also found that the negative DC-corona discharge always has a more red colour

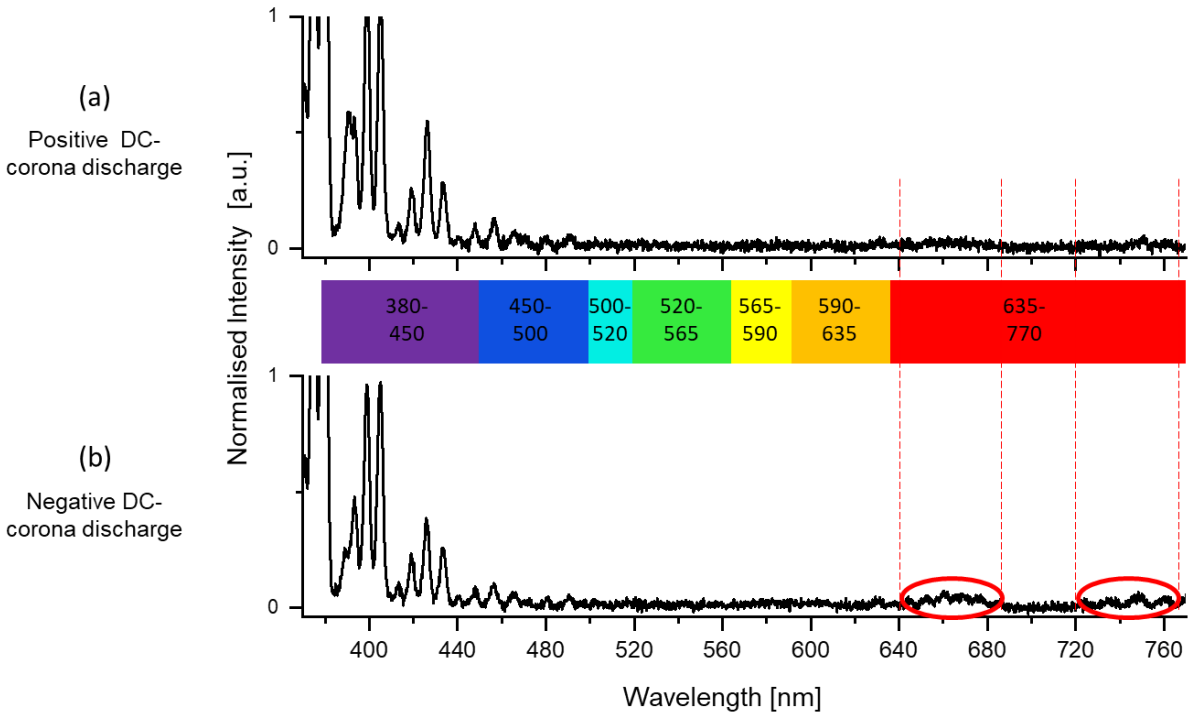

Figure 5.5: Normalised integrated emission spectra of (a) positive (+13.0 kV) and (b) negative (-12.5 kV) DC-corona discharges with a MS inlet as counter electrode.

than the positive DC-corona discharge. It is worth noting that, according to Figure 5.2 and Figure 5.3, the negative DC-corona discharge always has a relatively stronger emission intensity than the positive one. Similarly to FμTP in the falling half-phase, it can be attributed to the secondary electron emission from the electrode caused by the positive ion bombardment.

Their integrated spectra are obtained by Ocean Optics, both are normalised to their maximum intensities, and are displayed in Figure 5.5. In the range of 380 ~ 770 nm which corresponds to the range of visible light [59], if the highest peaks are scaled, almost the same peaks for these two spectra can be seen in the range of 380 ~ 565 nm. Various emission lines are observed in visible range, the detailed transition system band of these species are listed in Table 5.1 [145].

Table 5.1: Spectroscopic features of species observed by OES from ambient air plasma in visible range

Species	***λ (nm)***	***Transition system band (v', v'')***	***Species***	***λ (nm)***	***Transition system band (v', v'')***
N_2	380.5	$C^3\Pi_u$ —— $B^3\Pi_g$ (0, 2)	N_2	590.6	$B^3\Pi_g$ ——$A^3\Sigma_u^+$ (9, 5)
$\mathbf{N_2^+}$	391.4	$B^2\Sigma_u^+$ —— $X^2\Sigma_g^+$ (0, 0)	N_2	595.9	$B^3\Pi_g$ ——$A^3\Sigma_u^+$ (8, 4)
N_2	394.3	$C^3\Pi_u$ —— $B^3\Pi_g$ (2, 5)	N_2	601.4	$B^3\Pi_g$ ——$A^3\Sigma_u^+$ (7, 3)
N_2	399.8	$C^3\Pi_u$ —— $B^3\Pi_g$ (1, 4)	N_2	607.0	$B^3\Pi_g$ ——$A^3\Sigma_u^+$ (6, 2)
N_2	405.9	$C^3\Pi_u$ —— $B^3\Pi_g$ (0, 3)	N_2	632.3	$B^3\Pi_g$ ——$A^3\Sigma_u^+$ (10, 7)
N_2	420.1	$C^3\Pi_u$ —— $B^3\Pi_g$ (2, 6)	N_2	639.5	$B^3\Pi_g$ ——$A^3\Sigma_u^+$ (9, 6)
N_2	427.0	$C^3\Pi_u$ —— $B^3\Pi_g$ (1, 5)	N_2	646.9	$B^3\Pi_g$ ——$A^3\Sigma_u^+$ (8, 5)
N_2	434.4	$C^3\Pi_u$ —— $B^3\Pi_g$ (0, 4)	N_2	654.5	$B^3\Pi_g$ ——$A^3\Sigma_u^+$ (7, 4)
N_2	457.4	$C^3\Pi_u$ —— $B^3\Pi_g$ (1, 6)	N_2	662.4	$B^3\Pi_g$ ——$A^3\Sigma_u^+$ (6, 3)
N_2	575.5	$B^3\Pi_g$ ——$A^3\Sigma_u^+$ (12, 8)	N_2	670.5	$B^3\Pi_g$ ——$A^3\Sigma_u^+$ (5, 2)
N_2	580.4	$B^3\Pi_g$ ——$A^3\Sigma_u^+$ (11, 7)	N_2	750.4	$B^3\Pi_g$ ——$A^3\Sigma_u^+$ (4, 2)
N_2	585.4	$B^3\Pi_g$ ——$A^3\Sigma_u^+$ (10, 6)	N_2	762.6	$B^3\Pi_g$ ——$A^3\Sigma_u^+$ (3, 1)

Concurrently, some discernible peaks can be observed within the yellow and orange ranges, but salient peaks can be seen particularly in the red range (marked as red circles) as shown in Figure 5.5. These emission lines are also marked as red text in Table 5.1. Corresponding to the range of 565 ~ 770 nm, which are observed in the negative DC-corona discharge but nearly none in the positive DC-corona

discharge. These emission lines come from the N_2 first positive system FPS (N_2 (B) → N_2 (A)), which is demonstrated to have a higher population rate in the negative DC-corona discharge. This might be owing to the much higher electron number density in the negative DC-corona discharge, which is related to their different origins of secondary electrons, as described before.

When emissions in the purple and blue ranges have comparable intensities for these two kinds of corona discharges, the negative DC-corona discharge with a relatively stronger emission in the red-range is more sensitive to human eyes [59]. That is why the negative DC-corona discharge seems to look more red than the positive one.

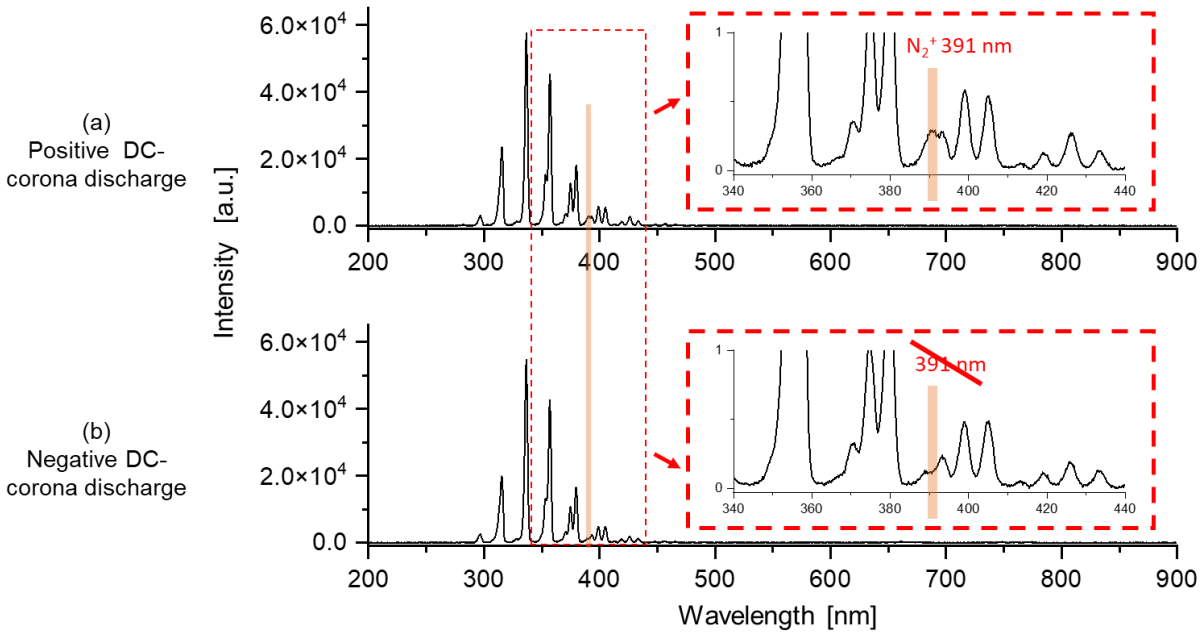

Figure 5.6: Integrated emission spectra and normalised zoomed images of (a) positive +13.0 kV and (b) negative -12.5 kV driven DC-corona discharges with a MS inlet as counter electrode, the integration time was 500 ms and 50 ms, respectively.

Despite the fact that the integration time of the negative DC-corona discharge is 10 times shorter, the corresponding emission intensity is equivalent to that of the positive DC-corona discharge. This indicates that the absolute emission intensity of the negative DC-corona discharge is significantly stronger than that of the positive one.

To concern the possible difference of the N_2^+ 391 nm emission between the positive and negative DC-corona discharges, the spectra were normalised and zoomed in the range of 340 ~ 440 nm. It can be observed that the relative emission of N_2^+ 391 nm in the positive DC-corona discharge is obviously stronger than in the negative DC-corona discharge, which is marked by an orange column in Figure 5.6. This is similar to that described in Section 3.3.7 for FμTP, the emission of N_2^+ 391 nm in the falling half-phase shows a lower maximum of intensity compared to that in the rising half-phase. As described before, for corona discharge, this can also be attributed to the attraction effect on positive ions by the negative electrode.

5.2.4 Potential measured with a ring around the DC-corona discharges

To gain an intuitive insight into the electric potential around plasma, a ring detector was introduced as described in Section 5.1 and moved along the electrode axis in two directions with a step of 2 mm. The potential results measured in DC-corona discharges are displayed in Figure 5.7, with a configuration of two opposing needles used. In this system, the red needle is connected to a DC power generator and the black needle is directly grounded. The distance between electrodes is 8 mm and the origin point (0 mm) is located at the HV electrode tip, so the ground electrode tip is located at 8 mm.

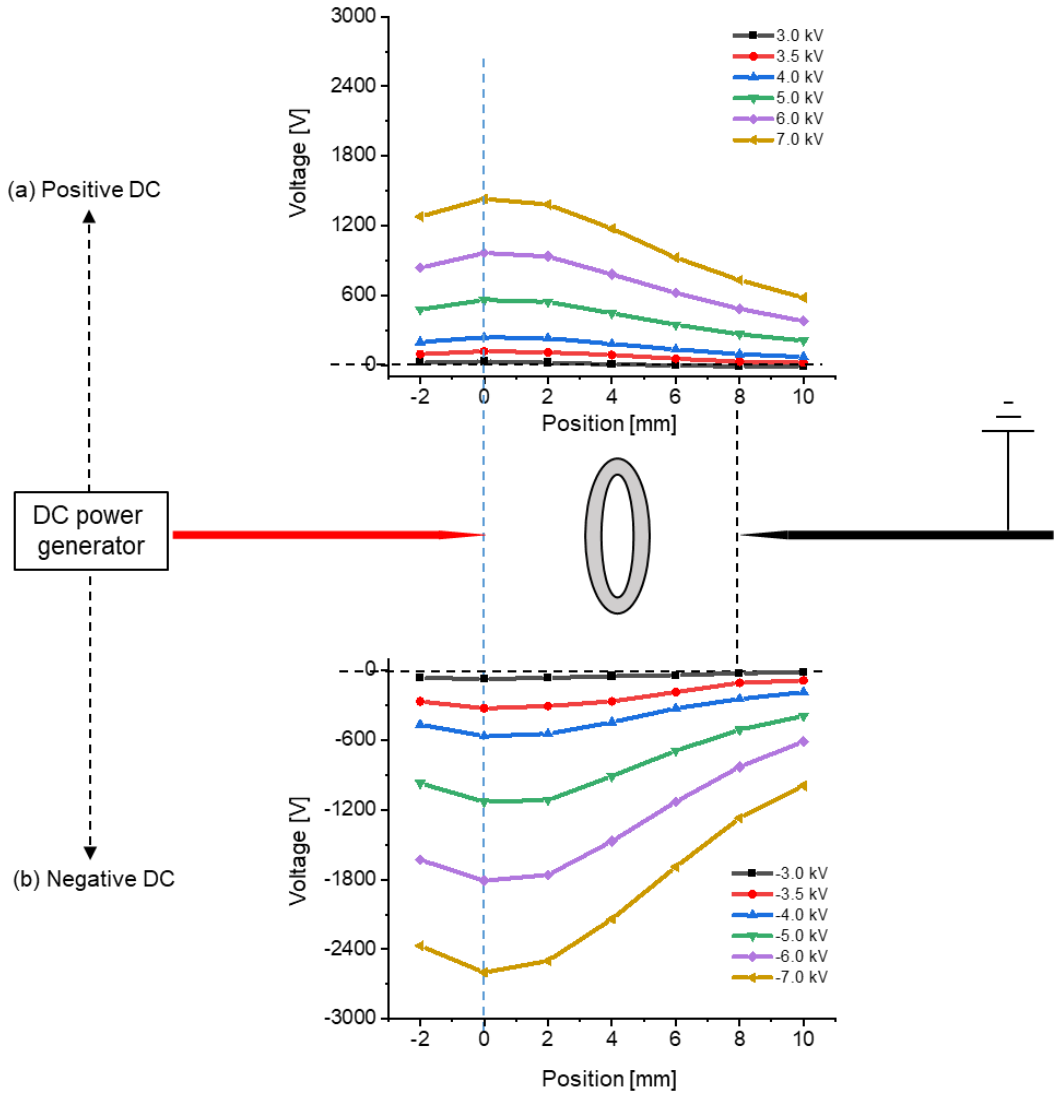

Figure 5.7: Ring potential values around corona discharge as a function of position in a pin-to-pin geometry discharge system driven by (a) positive and (b) negative DC generator with various amplitudes.

In case of positive DC-corona discharge, positive values are always obtained at various positions, as shown in Figure 5.7 (a). While negative values are always measured at various positions in the negative DC-corona discharge as shown in Figure 5.7 (b). In other words, the polarity of the ring potential remains constant and is congruent with the polarity of the applied voltage on the electrode.

When a sufficiently high DC voltage is applied to the HV electrode, ambient air is broken down. Reactive species including positive ions, negative ions, electrons, and excited species are generated. The free charges will build the electrical connexion between the ring detector and the ion drift region of the corona discharge that is shown in Figure 5.4. When a positive voltage is applied, the predominance of positive charges in the ion drift region will result in the formation of a positive potential. Therefore, the oscilloscope detects a positive potential through the principle of resistor voltage division. Similarly, when a negative voltage is applied, a negative potential is measured.

In both the positive and negative DC-corona discharges, the potential amplitudes have a highest value at the tip of the powered needle (marked by a vertical blue dashed line). From this point, it gradually decreases in two directions. This is related to the equivalent resistance change of the plasma channel. It is found that when the applied amplitude on the HV electrode increases, the higher ring potential amplitude can be measured at each position in both types of DC-corona discharges. This is caused by the more severe discharge reactions, and therefore more charged particles in the ion drift region will be generated, thus a higher potential will be generated. On the other hand, a higher charge density also represents a smaller channel resistance.

When the applied amplitudes on the HV electrode are the same, the ring potential amplitudes measured at the same positions in the case of negative DC-corona discharge are always higher than that in the positive one. On the one hand, negative DC-corona discharge is commonly stronger than positive DC-corona discharge under comparable discharge conditions, as demonstrated in Figure 5.2 and Figure 5.3, which means a larger number of charged species are produced. On the other hand, lots of negative ions are produced by electron capture due to the high mobility and high density of electrons [42]. As a consequence, negative DC-corona discharge has a higher negative potential but a lower channel resistance compared to positive DC-corona discharge. Finally, the ring potential in the negative DC-corona discharge is greatly higher than that in the positive DC-corona discharge.

These results identify that a DC potential exists in DC-corona discharge, regardless of what polarity and amplitude is used. In summary, positive charged particles are the main reacting species in the ion drift region for positive DC-corona discharge, while negative charged particles dominate in the negative DC-corona discharge. Now, the question arises of what happens when an AC voltage is applied.

DC-corona discharge can reach its quasi-steady state, although the negative DC-corona discharge may occur in a pulsed mode (the so-called Trichel pulses due to the space charge effect) [42, 62, 142], the applied electric field direction is constant. In an AC-corona discharge, the direction of the electric field is constantly reversing. This leads to the ongoing alternation of different collision reactions, so it is difficult to form a similar stable form. In this work, a disposable stainless steel acupuncture needle with a tip diameter of 700 nm [70, 71] was used to initiate AC-corona discharge. It is evident that the needle tip is excessively sharp, thus appearing to be extremely fragile. Once the AC-corona discharge is ignited, it is very easy to switch to an arc discharge, and the tip is quickly destroyed by ion bombardment.

Therefore, it becomes very difficult to sustain the plasma for long periods of time, as this is typically accompanied by continuous electrode erosion. On the other hand, AC-corona discharge is even smaller in dimension and even faster in evolution compared to DC-corona discharge. Therefore, the ICCD resolution is too low to acquire distinguishable images of AC-corona discharge.

As was the case for positive DC-corona discharge, the relatively low net space charge density in the plasma region for negative DC-corona discharge does not disturb the Laplacian distribution of the electric field [141]. However, the residual space charge aggregated near the electrode tip in the AC-corona discharge greatly affects its local electric field distribution. Therefore, AC-corona discharge is not just a simple alternation of positive and negative DC-corona discharges. It is different from what would be expected if positive and negative DC-corona discharges operated separately [72]. A similar effect also exists in FμTP, and it is even more significant, which will be discussed further.

5.2.5 Diagnosis plasma ignition by AC-corona discharges

In view of the limitations described above, direct characterisation of an AC-corona discharge is difficult. Based on the experience in Chapter 4, a nearby conductor affects plasma behaviour a lot. In terms of MS analysis, the influence of a MS inlet on AC-corona discharge also could not be ignored. So, it should be taken into account when AC-corona discharges are used as ionisation sources. Therefore, in the following section, diagnosis plasma was employed again for the investigation of AC-corona discharge. The main concern here is the difference in the evolution behaviour of diagnosis plasma ignited by three polarity AC-corona discharges between with and without MS inlet.

The diagnosis tube was placed 0.5 mm under the APCI needle and its axis coincides just with the electrode tip. *He* was transmitted by the vertical diagnosis tube as the diagnosis gas. For comparison, a MS inlet was introduced with a distance of 3 mm from the electrode tip. A square wave voltage was utilised to sustain AC-corona discharge and then ignite the diagnosis plasma for all cases. Because of the enhancement effect of the MS inlet on the discharge reactions, a much lower driven voltage is required to get a comparable emission intensity under the same collection parameters. Therefore, 2.4 kV was utilised for the case with MS inlet, while 3.2 kV was employed for the case without MS inlet. Their temporally and spatially resolved optical emission spectra under the three polarity conditions (P, NP, and N) were collected by the same ICCD system.

As displayed in Figure 5.8 (a), not only the emission intensity but also the propagation velocity are almost the same when no MS inlet exists. This means that, with the absence of the MS inlet, the same diagnosis plasmas were ignited during the rising half-phase by AC-corona discharges in three polarities. However, the three diagnosis plasmas became visibly different when a MS inlet was introduced, as shown in Figure 5.8 (b). Compared with the intensity observed in the NP-plasma, the case in the N-plasma was weakened but enhanced in the P-plasma. Besides, the P-plasma has the highest propagation speed, the NP-plasma has a lower speed, and the N-plasma has the lowest speed.

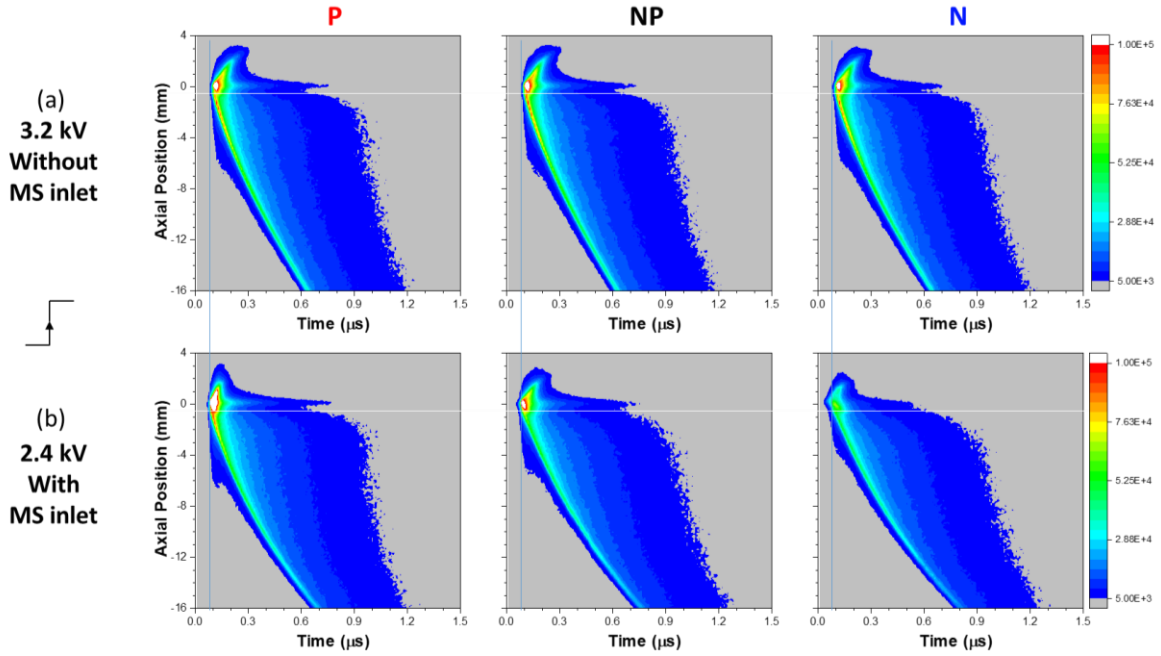

Figure 5.8: Whole emission evolution behaviours of diagnosis plasmas ignited by three polarity AC-corona discharges during the rising half-phase (a) without MS inlet and (b) with MS inlet in 3 mm distance, respectively. The white horizontal line at -0.5 mm represents the exit of the diagnosis tube.

As displayed in Figure 5.9 (a), the spectra are also almost the same in both shapes and intensities. This means that, with the absence of the MS inlet, the same diagnosis plasmas were also ignited during the falling half-phase by AC-corona discharges in three polarities. However, when a MS inlet was introduced, the three diagnosis plasmas differ slightly, as shown in Figure 5.9 (b). Compared with the intensity observed in the NP-plasma, the emission in the N-plasma case was enhanced but remained

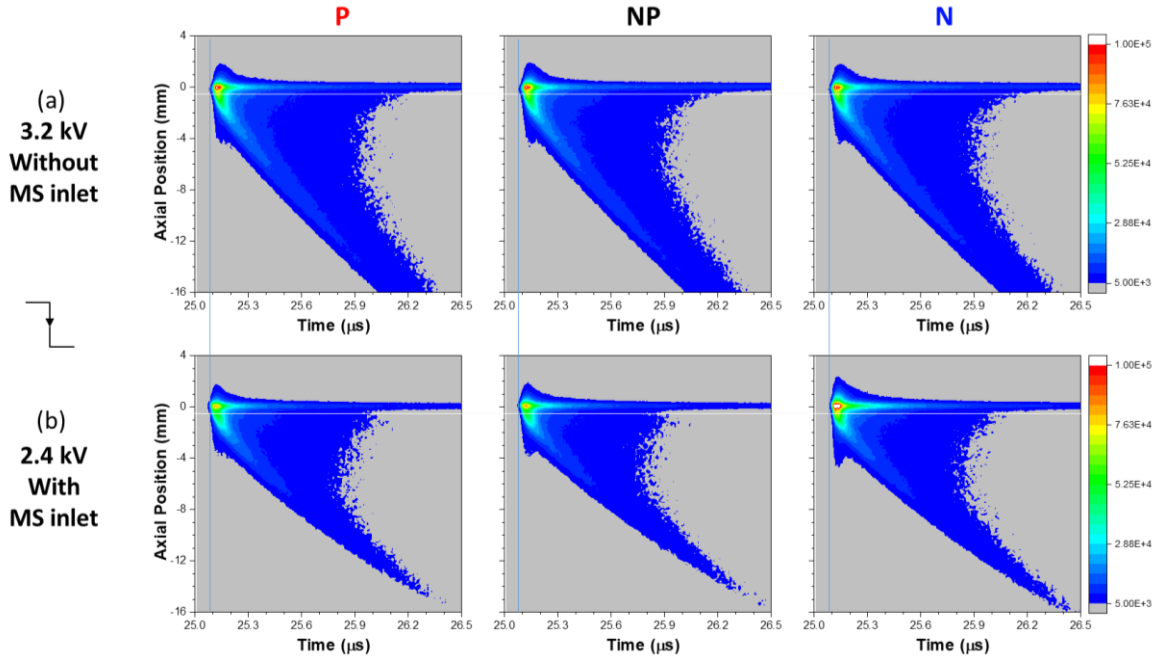

Figure 5.9: Whole emission evolution behaviours of diagnosis plasmas ignited by three polarity AC-corona discharges during the falling half-phase (a) without MS inlet and (b) with MS inlet in 3 mm distance, respectively. The white horizontal line at -0.5 mm represents the exit of the diagnosis tube.

comparable in the case of the P-plasma. Besides, all of them have very close propagation speeds. In addition, with the presence of MS inlet, all diagnosis plasmas are ignited simultaneously by a much lower voltage and propagate obviously slower than free plasmas.

In short, for AC-corona discharge without MS inlet, the ignited diagnosis plasmas are almost identical across three polarities, with no visible difference. This indicates that the diagnosis gas is excited and ionised in the same manner. However, the introduction of an MS inlet causes the diagnosis plasmas to become clearly different in both half-phase stages. This basically resembles the case of FμTP with a metallic target shown in Section 4.3, which once again confirms the huge impact of a MS inlet on plasma (AC-corona discharge and FμTP). This influence is also found to depend on the driven voltage polarity, which means a different effect on their transient potentials. Therefore, in the following section, the same ring detector was employed to detect the DC potentials around the AC-corona discharge.

5.2.6 Potential measured with a ring around the AC-corona discharges

The potential results measured around AC-corona discharges driven by three polarity voltages are displayed in Figure 5.10. In this case, only a sterile acupuncture needle (0.25 * 40 mm, Suzhou Huanqiu Acupuncture Medical Appliance Co., Ltd) but no counter electrode is used. In this system, the needle is directly connected to an AC power generator. The polarity of square wave voltage can similarly be switched by adding a DC bias, and the output is also named a biassed AC voltage. The origin point (distance = 0 mm) in this case is considered to be located at the electrode tip. The ring detector is also moving along the needle axis in two directions with a step of 2 mm.

Figure 5.10 (a) shows the waveform schematic diagram of the applied voltage in the positive-biassed (P), bipolar (NP) and negative-biassed (N) cases. Ring potentials at various positions along the needle axis are measured under three polarity voltages. The results are represented by three coloured curves, as shown in Figure 5.10 (b). It demonstrates that all three potential curves have the highest amplitudes in the vicinity of the needle tip marked by a dashed vertical magenta line. All of them decrease in two directions with a further distance from the tip.

Due to the same resistor voltage divider effect, a strongest absolute potential in the N-corona discharge, a weaker absolute potential in the P-corona discharge, and a weakest absolute potential in the NP-corona discharge were measured at each position. It reveals a largest amount of remnant charge agglomerates around the electrode tip in the N-corona discharge, a smaller amount in the P-corona discharge, and a lowest amount in the NP-corona discharge. This is highly consistent with the ignition difficulty of AC-corona discharge driving by different polarity voltages in the same configuration. N-corona discharge is the easiest one, P-corona discharge is harder and NP-corona discharge is the most difficult one. This provides indirect evidence for the speculation of remnant space charge effect in AC-corona discharge.

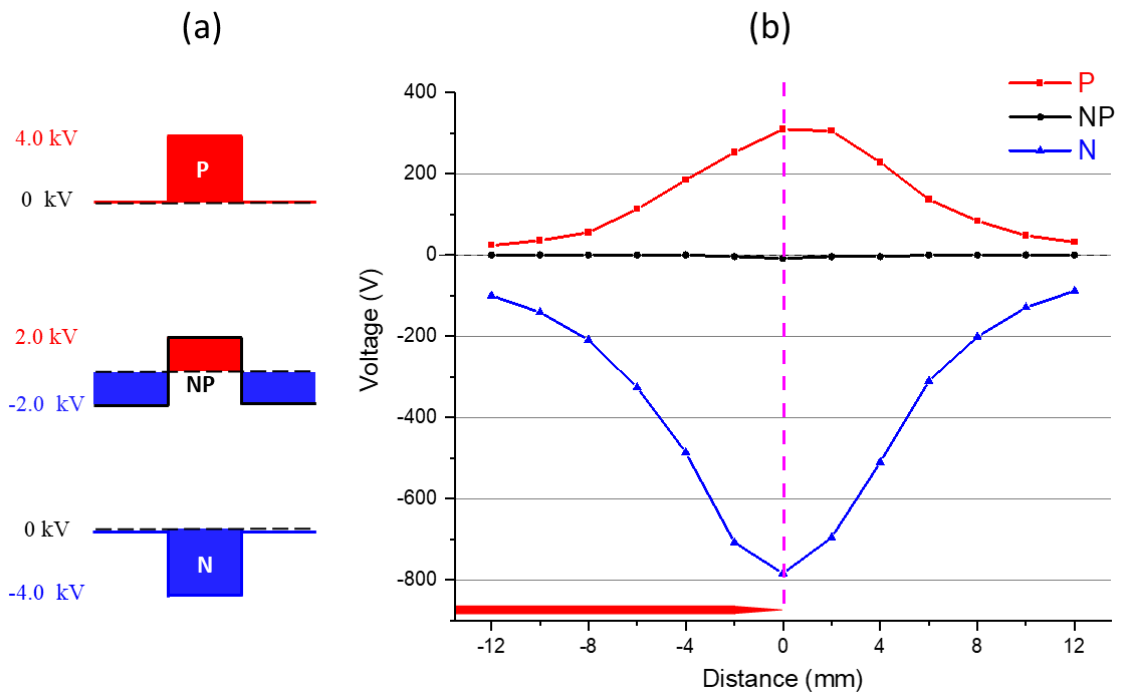

Figure 5.10: (a) Voltage waveform schematic diagram of the applied three polarity square wave voltages, the black dashed lines represent 0 kV; (b) Ring potential values as a function of position along the axis of AC-corona discharges driven by a V_{pp} of 4.0 kV. The red needle at the bottom represents the HV electrode.

The interesting thing is that there is always a negative potential in the N-corona discharge and a positive potential exists in the P-corona discharge, but a very small and nearly zero negative potential is present in the NP-corona discharge. The results of the P- and N-corona discharges in Figure 5.10 are consistent with those of the positive and negative DC-corona discharges shown in Figure 5.7. The previous explanations also apply here, the enhanced potential value of the N-corona discharge can be attributed to the secondary electron emission which produces more charged particles and in turn greatly reduces the resistance of the conductive channel. Besides, it might also be related to the low mobility of positive ions and the high mobility of electrons, thus a different height of local potential.

When a bipolar AC voltage was applied, that means the same amplitudes but in different polarities during two half-phases, as shown in Figure 5.10 (a). The NP-corona plasma can be simply treated as the combination of modes that appear with a positive DC-corona discharge during the rising half-phase and a negative DC-corona discharge during the falling half-phase [29]. As described above, under the same discharge conditions, the negative corona discharge is stronger than the positive corona discharge. It causes more charged particles to be produced during the falling half-phase than during the rising half-phase. Besides, the difference in mobility should not be neglected. As the potential polarity on the electrode is constantly switching, the charged particles may keep oscillating back and forth. Consequently, the space charges are largely neutralised in one cycle. Taking into account all of these factors, only a small amount of charges gather in the vicinity of the electrode tip in the air and can be successfully measured by the ring detector. As a result, the final net potential of NP-corona discharge has a weak but negative value.

In the former section, the diagnosis plasmas ignited by the free plasmas in three polarities are nearly identical. This suggests that the transient potentials of the free plasmas in different polarities should also be identical for AC-corona discharge. Therefore, the charged particles produced by air ionisation are also identical. However, the presence of a MS inlet affects plasma behaviour and therewith their ionisation properties to varying degrees for three polarities. Moreover, significantly different ring potential values are detected here, indicating various electric fields responsible for accelerating the respective ions to the MS entrance. Accordingly, it can be inferred that the three polarity AC-corona discharges exhibit different ionisation and transport efficiencies when disturbed by a close MS inlet. Consequently, the resulting MS signals will exhibit great differences, but this requires further experimental verification.

5.3 Conclusions

By capturing subtle images using a micro-focus camera, this work reveals for the first time the distinct colours and optical shapes of positive and negative DC-corona discharges. The positive DC-corona discharge is manifested with a “hat” shape that wraps the needle tip part, while the negative DC-corona discharge is manifested with a “fan-spray” shape leaving the needle tip. These specific forms are further evidenced through time-resolved emission spectra obtained with an ICCD, indicating that their appearances are not limited to the classic “corona” shape.

Their different shapes are supposed to be related to the microscopic mechanisms: in positive DC-corona discharge, the electric field strength is greatest at the edge of the electrode (needle surface), so electrons get highest energy near the edge, and thus the light emission seems to be located mainly near the electrode surface; in negative DC-corona discharge, the electrons emitted from electrode tip are scattered forward and accelerated, so that the collision reactions can occur at a relatively distant location. The more red colour of negative DC-corona discharge than positive one is confirmed owing to the relatively stronger emission in the red-range, and these emission lines come from the N_2 first positive system. Besides, the significantly stronger emission of N_2^+ 391 nm in positive DC-corona discharge than in negative one is also verified.

Additionally, when there is no interference, the diagnosis plasma ignition experiments show that the diagnosis gas is excited and ionised in the same manner across three polarity AC-corona discharges. However, the introduction of a MS inlet causes the diagnosis plasmas to obviously differ. This once again confirms the huge impact of a conductor such as the MS inlet on plasma, and this effect strongly depends on the driven voltage polarity.

With the help of an electrical connexion built by charged particles around a plasma in the air, a DC component potential was measured through a ring detector in both DC- and AC-corona discharges. Always, a positive potential was obtained for both the positive DC-corona discharge and the P-corona discharge, and a negative potential was always detected for both the negative DC-corona discharge and

the N-corona discharge. Interesting, a very weak negative potential was measured in the NP-corona discharge. Anyway, it was discovered that all of these plasmas have a biggest DC component potential value in the vicinity of the needle tip. The superior ionisation efficiency of the AC-corona discharge in comparison to the DC-corona discharge seems to be related to the remnant space charges, so the relationship of ring potential between these two kinds of corona discharges needs to be experimentally explored.

CHAPTER 6

Differences between FμTP and corona discharge

In consideration of the similar sharp pin electrode configuration, FμTP is frequently perceived as a mere AC-driven corona discharge. The greatest configuration discrepancy is evident in the presence of an additional capillary containing a specific discharge gas within FμTP. A corona discharge is usually equipped with a counter electrode in a suitable distance, and thus it is treated as a fake single-electrode discharge. In contrast, such counter electrode is not required at all in FμTP which is initiated in a real single-electrode configuration. In addition, published measurements [9, 10, 23-29] show quite different emission behaviours between FμTP and corona discharge. It strongly implies their different discharge mechanisms and ionisation performances. This is suspected to be strongly related to the significant role of this additional capillary in FμTP.

In FμTP, it has been proven that neither Penning ionisation nor charge transfer between plasma gas species and ambient air are responsible for the protonation of analytes outside the capillary [26]. Instead, a transient local potential at the capillary exit was proposed to play a major role. Such potential is independent of the discharge gas type but depends solely on the local charge density. It could create a high temporal electric field in which chemical reactions occur to produce excited and ionised species in the environment. On the one hand, these ions might gather in groups and attract free electrons to be accelerated and then collide with other species, which supports the further excitation and ionisation. On the other hand, due to the very small distance (~ nm scale) between the particles, a hugely stronger electric field than the applied external electric field will be built which can effectively ionise the sample molecules. The produced target ions can be transferred to the MS entrance by the propagation of the

excitation and ionisation waves. It reveals that FμTP is capable of ionising samples without the help of an extra electric field.

In an AC-corona discharge, the generated positive and negative ions are subsequently neutralised by the following opposite voltage. This leads to a decrease in the conductivity of the discharge gap, which suppresses the occurrence of arcing much more than in DC-corona discharges [68]. Similarly, in conjunction with the continuously reversing electric field and the accumulated charges on the dielectric surface, FμTP would also have a low possibility of arc discharge [85].

The soft ionisation of APCI is dependent on the "CI" reactions between the reagent ions and the analyte molecules, whereas AC-corona discharge was revealed to have a relatively better ionisation performance. As discussed in former chapter, the transient potential is suspected to be responsible for this, and these potentials have already been detected. Therefore, it is valuable to also detect the existence of such potential in FμTP and then compare it to the corona discharge case. This study is essential to better understand the discharge properties of FμTP from an electrical perspective, which is also expected to provide some corroboration to compare their ionisation performance.

6.1 Experimental arrangement

In order to directly detect this potential around FμTPs, the same ring detector in suitable dimensions was employed for the investigation. This method is complementary to the diagnostic technique that focusses on the OES characterisation of a plasma. Figure 6.1 illustrates the experimental arrangement employed in this chapter.

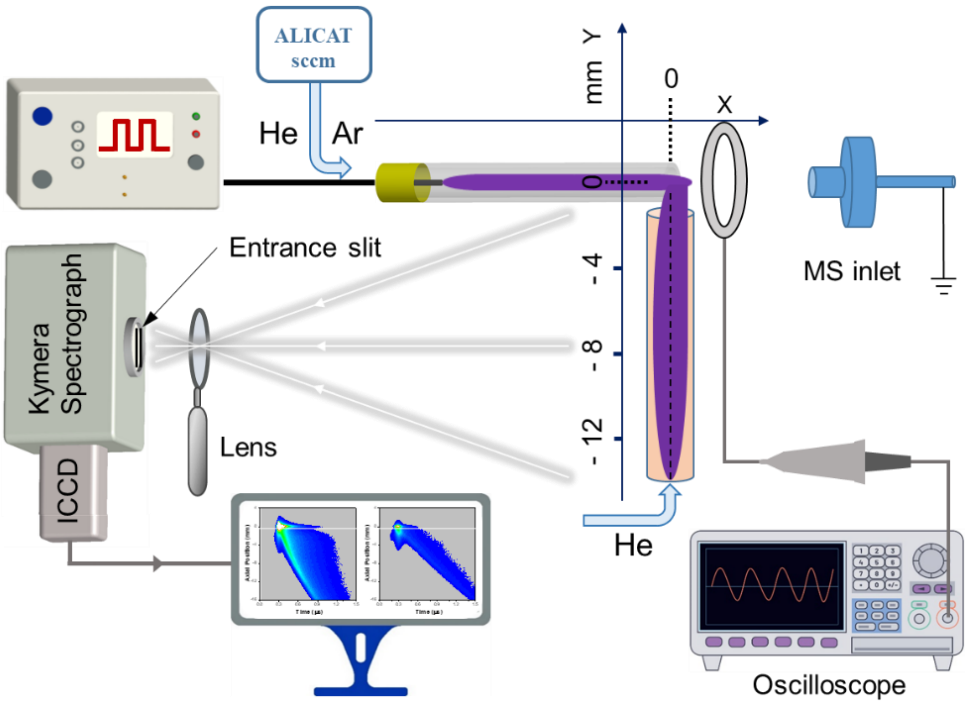

Figure 6.1: Schematic diagram of the experimental setup.

This simple setup is a good auxiliary characterisation method for providing distinct information, as no other tool more suitable for electrical characterisation can be adopted without disrupting the single-electrode discharge system of FμTP. In addition, a vertically placed diagnosis tube was utilised for comparison. To eliminate the influence of electromagnetic radiation on potential measurements, the same signal deal strategy as that implemented in corona discharge was used for FμTP. Then, a similar constant static potential waveform (DC component potential) can be obtained at each position for FμTPs. Due to the same reason, such potential should also be regarded as a consequence of plasma.

6.2 Potential measured with a ring around the FμTP

As already demonstrated in the previous chapter, the transient potential formed by accumulated charges on the capillary wall is responsible for plasma propagation. It is also inferred that N_2^+ and H_2O^+ can be produced in the electric field created by the transient potential in the open air and then participate in the protonation process [26]. In the investigation of excitation and ionisation outside the discharge capillary by introducing a diagnosis gas as a substitute for ambient air, it experimentally confirmed that a temporally and spatially limited potential plays a significant role in the generation of reactant ions responsible for protonation in the surrounding air [9, 10, 26]. However, these results are only indirect evidence for the presence of this kind of potential.

Because of the single electrode configuration of FμTP, classic electrical characteristics (such as I-V curves) are not able to be measured. In order to enrich the characterisation data dimensionality for studying, a ring detector was also taken for the electric potential measurements. The same operation was implemented for FμTP with *He* used as discharge gas, and the results obtained are exhibited in Figure 6.2. The same AC power generator was employed and connected to the inner electrode, which is 3 mm away from the capillary end. The AC voltage polarity can also be switched by the same method as

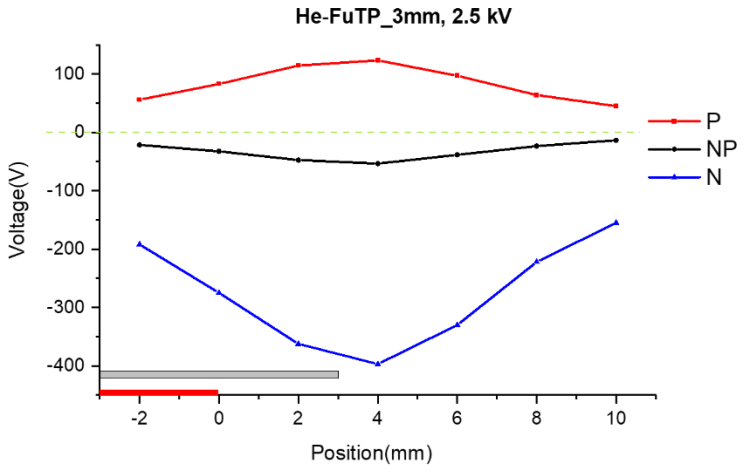

Figure 6.2: Ring potential values as a function of position along the axis of a 3 mm long He-FμTP driven by a square wave voltage (V_{pp} = 2.5 kV) in three polarities. The horizontal red and grey columns at the bottom of the figure represent the inner HV electrode and the capillary glass wall, respectively.

described above. The origin point (0 mm) in this case is also considered to be located at the electrode tip. The ring detector moves along the capillary axis in two directions with a step of 2 mm.

In Figure 6.2, the static potentials measured in three polarity plasmas are represented by three coloured curves, respectively. Similar results between different polarities compared to AC-corona discharge are observed here. The potential alters with the position of the ring, a biggest negative amplitude in the N-FμTP and a smaller positive amplitude in the P-FμTP, but a smallest negative amplitude in the NP-FμTP can be observed at each position. This result directly evidenced the existence of previously proposed transient potential, further certifying the suspicion. Besides, it also reveals the rationale behind the propensity for shortcut damage to occur in the N-FμTP compared to the P- and NP-FμTPs. In the event that N-FμTP is utilised as an ionisation source in front of the MS, a shortcut can readily occur between the MS inlet and the HV electrode. This dangerous phenomenon has already been observed in the laboratory and poses a risk of damaging the MS instrument.

Even though the dielectric capillary separates the plasma from the ring detector, charged particles can still successfully build the connexion path. It confirms that the presence of capillary did not significantly disturb the establishment of the electrical connexion through free charges. Similarly to the explanation given for AC-corona discharge, the weak negative potential value in NP-FμTP may be due to the mechanism proposed in Figure 4.9. As the positive and negative charged particles alternately adhere to the capillary wall following the continually reversal of the applied electric field, the accumulated surface charges are largely neutralised in one cycle.

It is important to emphasise that an obvious difference appears here. All of these potential curves have the highest absolute value in the vicinity of the capillary exit instead of at the electrode tip despite the polarities of the applied voltage. This can be explained by the assumption that a temporally and spatially limited ion cloud is generated at the capillary end in the ambient air [9, 10, 26]. As a result, even though the HV electrode did not contact the air components, the surrounding air can still be effectively ionised. To figure out the effect of the capillary on plasma, a longer capillary with a distance of 10 mm to the inner electrode tip was used. In this case, the plasma can still reach the capillary end as in the upper case in Figure 6.2. The positions beyond the capillary outlet are not measured due to the limitation of the effective stroke of the translation stage, the results are drawn in Figure 6.3.

Similarly to that displayed in Figure 6.2, under the same driven voltage, the potential value around the capillary exit of the P-FμTP is close to 100 V and the N-FμTP close to -400 V while the NP-FμTP is close to -50 V. The measured DC potential can also be attributed to the resistor voltage division effect. Once the connexion path between glass wall and ring detector was built by the charged particles, the electric potential formed by these accumulated charges can be detected by the oscilloscope. Therefore, in terms of surface charge accumulation on the inner capillary wall, it is reasonable to suspect the polarity situation of these attached charges for the P-, NP- and N-FμTPs as proposed in Section 4.3.2.

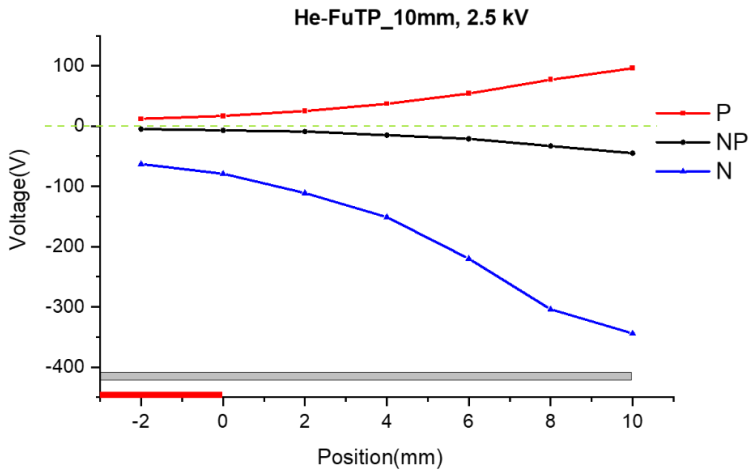

Figure 6.3: Ring potential values as a function of position along the axis of a 10 mm long He-FμTP driven by a square wave voltage (V_{pp} = 2.5 kV) in three polarities. The horizontal red and grey columns at the bottom of the figure represent the inner HV electrode and the capillary glass wall, respectively.

These results demonstrate that the DC bias is relevant with respect to the charges attached on the capillary wall, which are responsible for plasma propagation within the capillary. In fact, the accumulated surface charges produce an extra electric field which is superimposed on the applied electric field and alters the final local fields of the three polarity FμTPs to be comparable. In other words, it is the surface charges that indeed shield the applied DC bias [90]. Because these effective local fields are almost identical, the three free plasmas have consistent evolution behaviours regardless of the DC bias voltage, as observed in Section 4.3.1.

Although nearly the same results are obtained here, the maximum position is shifted to 10 mm following the shift of the capillary exit from 3 mm to 10 mm. This further confirms the key role of the capillary in expanding the plasma length and effectively transferring the chemical reactor from the electrode tip to the capillary exit. It has also been confirmed by a series of analytical experiments with FμTPs in different discharge volume lengths [7-21]. Therefore, in the ionisation applications of FμTP, the distance from the electrode tip to the capillary end is not the key, as possible weakening can be compensated for through parameter adjustment. In reality, the real key is the distance from the capillary end to the target sample to be detected. It implies that the discharge volume length of FμTP seems to not decide the amount of surface charge accumulation and thus the transient potential at the capillary end. In summary, the ionisation performance is not diminished by an increase in the discharge volume length, thus substantiating its capacity for long-distance and flexible applications.

Due to the instability and weakness of *Ar*-FμTP at 2.5 kV, a higher voltage of 3.0 kV was used here. Figure 6.3 and Figure 6.4 demonstrate that *He*- and *Ar*-FμTPs have a similar trend of ring potential between three polarities along the capillary. Besides, potentials measured around a *He*-FμTP driven by 3.0 kV also exhibit close values compared to *Ar*-FμTP, which can be seen in Appendix C.1. This is consistent with their comparable ionisation efficiency as an ionisation source. Besides, FμTPs operated with krypton and xenon as discharge gases also obtained comparable ionisation efficiencies in MS

measurements [9, 10]. Accordingly, it can be concluded that, no matter what polarity of voltage, discharge gas type, and discharge volume distance are used for FuTP, the ring potentials all have a similar performance. They always reach maximums near the capillary outlet, and then gradually weaken with bigger distance from the capillary exit.

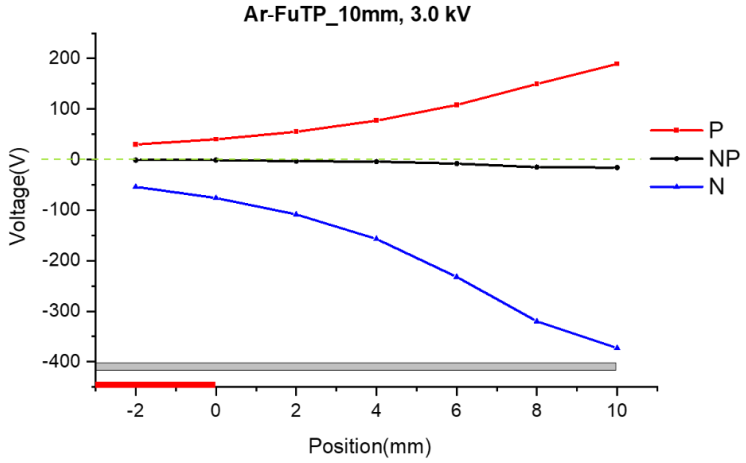

Figure 6.4: Ring potential values as a function of position along the axis of a 10 mm long Ar-FμTP driven by a square wave voltage (V_{pp} = 3.0 kV) in three polarities. The horizontal red and grey columns at the bottom of the figure represent the inner HV electrode and the capillary glass wall, respectively.

Previous experiments have indicated that the transient potentials of the three polarity plasmas are the same in the case of free plasmas. However, as the polarity of the driven voltage switches, significantly different ring potentials are detected. It suggests that the polarity of the driven voltage is indeed the source of this difference. Nevertheless, the comprehensive local electric field in the case of P and N remains comparable with the case of NP. This is counterbalanced by the superposition of the transient potentials with the applied bias voltages. As a result, free plasmas exhibit the same emission behaviours among the three polarities. In other words, the presence of the MS inlet/metallic target rather than the ring detector significantly alters the plasma behaviour. This means that the ring potential data displayed here are measured under a negligible influence, so it is reliable for intuitively feeling the electric potential around plasma. Furthermore, this ring potential can be treated as a representative of the formed DC potential, which accelerates the respective ions into the MS entrance. Their differing values cause the ions concerned to be efficiently transmitted to varying degrees, resulting in the measurement of differing intensities of the MS signal (as shown in Section 4.3.1.4).

Regardless of the discharge gas (*He* or *Ar*) and the discharge volume length (3 mm or 10 mm), the relationship among the detected ring potentials for the three polarities remains consistent and also aligns well with the observed MS signal heights under each condition. This means that the P-FμTP with the strongest positive ring potential obtains the strongest MS signal intensity in the positive ion mode. Conversely, the N-FμTP with the strongest negative ring potential obtains the strongest MS signal intensity in negative ion mode. Based on the above understanding, it is reasonable to suspect that the corona discharge is also like this.

6.3 Comparison of the ring potential intensity

Since similar ring potentials are detected in corona discharge and FμTP, the strongest potentials under three polarities are quantitatively compared between FμTP and the AC-corona discharge driven by the same applied voltage. This means that the DC component potential values that are measured at the capillary exit for FμTPs and at the needle tip for corona discharges, the results are shown in Figure 6.5. The data measured at the needle tip of positive and negative DC-corona discharges are also drawn here as references. AC-corona discharge was found to have a stronger potential than DC-corona discharge for both positive and negative cases. It also reveals that, under the same applied voltage amplitudes, FμTP always has the strongest potential, while AC-corona discharge has a weaker value no matter which polarity voltage is applied.

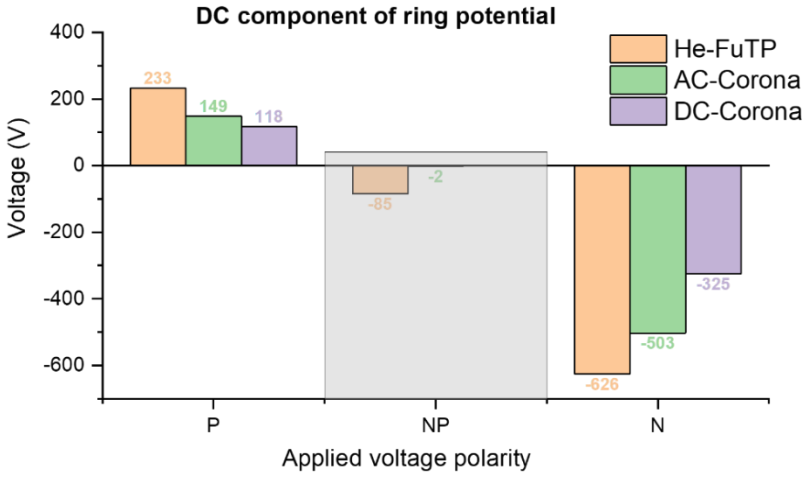

Figure 6.5: DC component ring potential values measured at the capillary exit of a 10 mm long He-FμTP and at the needle tip of AC-corona discharge both driven by a square wave voltage (V_{pp} = 3.5 kV) in three polarities. Data measured at the needle tip of DC-corona discharges driven by DC voltages of ± 3.5 kV are also shown.

As explained before, the detected DC component potentials must be related to the plasma rather than to the HV generator. All can be considered as the result of a resistor voltage divider which is realised through the connexion path to the ring detector. This conductive path was established by the charged particles, making it possible to directly measure these potentials by oscilloscope. It is worthy to discuss this ring potential because it is actually responsible for accelerating the formed ions into the MS inlet. In the case of a corona discharge, the charges responsible for electrical connexion all come from the ionisation of air substances. Although there is a specific noble gas in addition to air in the case of a FμTP, no noble gas ions can propagate beyond the capillary [25, 26], let alone reach the MS. Thus, these charges and the MS ions detected in FμTP also come completely from the ionisation of air species. According to the results presented in Figure 6.5, it is reasonable in some sense to suspect that FμTP would be more efficient than both AC- and DC-corona discharges as an ionisation source.

For corona discharge, the plasma starts from the electrode tip and cannot develop forward but was limited around the tip due to the fast quenching of charges in ambient air. It can be concluded that FμTP

is initiated as a corona discharge at the tip of the inner electrode. Subsequently, the discharge develops and propagates along the capillary to the outlet under further guidance. In turn, the plasma propagation process results in surface charge accumulation and local potential transients. Ring potentials measured in FμTP as well as corona discharges reveal that ambient air compositions can be effectively excited and ionised in these cases. All function particles come from ionisation reactions, but there is an apparent difference between corona discharge and FμTP. The electric field around the electrode tip generated by the applied voltage on the needle is responsible for these reactions in corona discharge, while the temporally and spatially limited ion cloud generated at the capillary outlet rather than the electrode tip plays the key role in FμTP. These ion clouds are formed after plasma injects into surrounding air, and the accumulated surface charges, especially near the capillary exit, make a significant contribution.

Based on the previously described FμTP development mechanism, it is conceivable that this ring potential might originate from both the attached surface charges and the ion clouds. However, the detected potential waveform is a constant horizontal curve without any cyclic fluctuation, even though a periodic change in the driving voltage exists. What is certain is that the ring potential can be detected only in the presence of a plasma, but the attachment and detachment processes of the surface charges on the capillary wall seem to have no influence on this ring potential. This can be explained by the long-term retention of charges on the surface in time constants up to a second scale [49]. Besides, due to its extremely fast speed (< ns scale), the generation and neutralisation process of space charged particles in the plasma column is also not relevant. Therefore, it is confirmed that this ring potential precisely comes from the local potential generated by the quasi-static accumulated surface charges but especially the part around the capillary exit. Moreover, the height of this potential signal depends on the number of surface charges. This means that, with the introduction of a DC bias to the applied voltage, the amount of surface charges is essentially different and disturbed by the external conductor as well. So, after introducing the grounded target as in Chapter 4, the three polarity plasmas themselves become different. Whether the target changes surface charge accumulation by affecting polarisation or by affecting the electric field, or both, it ultimately leads to a different transient potential, which in turn causes different ion efficiencies.

It is imperative to emphasise that due to the local potential differs between three polarities along the entire capillary length, the final MS signals detected exhibit a significant disparity. It follows that as far as the ionisation is concerned, the local potential plays a dominant role. The measured DC component potential can be regarded as a representative of the local potential around plasma. Therefore, the intensity of measured potential can be regarded as an evaluation indicator for an electrical field that drives the ions to the MS inlet. This ring potential has also been found to increase with increasing applied voltage amplitude of FμTP, which is expected and also consistent with their improved performance [8]. In summary, it is certain that the localised transient potential should be regarded equivalent to the propagation of the excitation and ionisation waves, but the exact reaction processes are not clear yet. According to the explanation and comparison above, it is foreseeable that the AC-corona discharge would have a relatively lower ion efficiency than FμTP due to the absence of a charge storage container.

6.4 MS performance of FμTP with DC bias

To confirm the relationship between the ring potential and the corresponding MS signal height under different operating voltage properties, various DC bias voltages were introduced into the bipolar voltage (NP) to gradually shift its polarity. A *He*-FμTP was placed 4 mm in front of the MS inlet, then the ring potential was measured at the capillary exit. For MS detection, the same parameters as described in Section 4.3.1.4 were set here. The correspondence between ring potentials and specific peak intensity values is shown in Figure 6.6.

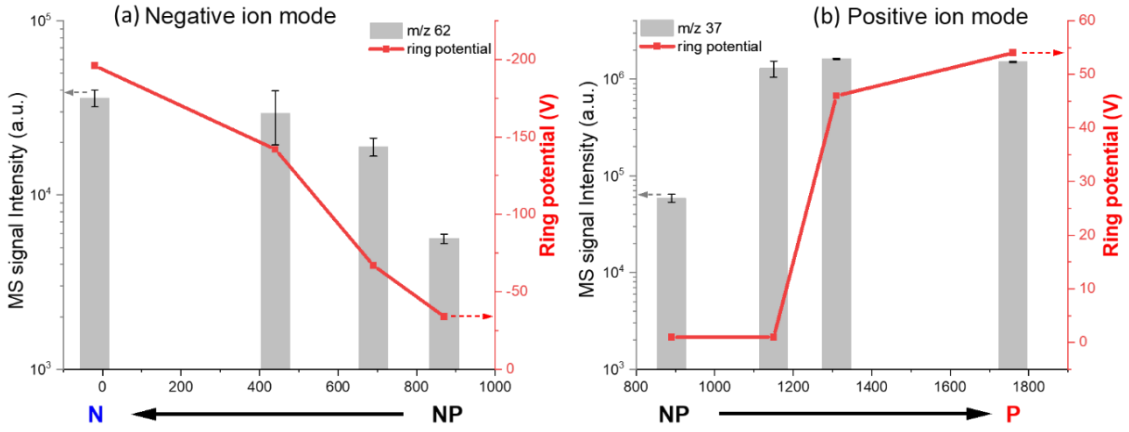

Figure 6.6: (red curves) DC component ring potentials measured at the capillary exit of a He-FμTP driven by a square wave voltage (V_{pp} = 2.0 kV) with various bias voltages in front of the MS inlet with a distance of 4 mm; (grey columns) The obtained MS signal intensities of represent ions in front of a He-FμTP with a distance of 4 mm to the MS inlet under (a) negative and (b) positive ion modes, respectively (the left ordinate is on the log10 scale). The horizontal axis is the upper voltage amplitude (V) of the driven square wave voltage.

No additional sample was added in this experiment, and thus the surrounding air substances were ionised and detected. Two MS peaks obtained under the negative and the positive ion modes are chosen as representative, respectively. The signal at m/z 62 corresponds to the NO_3^-, while the signal at m/z 37 corresponds to the $H_3O^+(H_2O)$. This figure reflects that, when the polarity of the driven voltage gradually switched from NP to N (as shown in (a), from right to left), both the ring potential and the MS signal intensity became stronger. The same applies when the polarity of the driving voltage is gradually switched from NP to P (as shown in (b), from left to right). Besides, the MS experiment with 2-Butanone (C_4H_8O) as an analyte also exhibits a similar relationship, which can be found in Appendix C.2. Thus, a consistent change trend is demonstrated to exist between the ring potential and the corresponding MS signal strength with varying bias voltages. In other words, the detected ring potential qualitatively represents the MS signal height, and thus the ring potential experiment can be analogised to the results of MS detection. Therefore, ring potential performance has proven to be appropriate to describe the resulting MS signal height to a certain extent.

Based on what was demonstrated in Figure 6.5 and Figure 6.6, a higher MS signal intensity of the water cluster can be expected by FμTP than by corona discharge. Due to the fact that these water clusters provide H^+ for the production of protonated analyte molecules $[M+H]^+$, it is reasonable to suspect that

FμTP could achieve a higher MS signal intensity. In short, these evidences are good clues for arguing that FμTP is more efficient than both AC-corona discharge and APCI for ionisation. It is essential to note that the data set demonstrates the beneficial effect of bias voltage on MS analysis. Specifically, polarity deflection substantially improves signal intensity. However, these experimental conditions do not represent optimal coupling parameters for MS analysis. This experiment was conducted solely to demonstrate the strong positive correlation between the ring potential and the ion efficiency of FμTP, which may also suit other AC driven plasma-based ionisation sources.

Generally speaking, for analytical chemistry applications, the coupling conditions (including a lot of factors, such as voltage, gas flow, and distance) with MS are typically optimised through a series of adjustments before being finalised to achieve optimal sensitivity and signal-to-noise ratio, etc. For instance, under typical conditions, *He*-FμTP was driven by a 2.5 kV voltage with the capillary positioned coaxially and the end approximately 3 mm from the MS inlet. From experience, this typical configuration usually yields optimal MS signals. However, since MS signal values approach saturation, the distinction becomes negligible (as shown in Appendix C.3). For practical FμTP ionisation applications, scenarios at a distance of more than 3 mm in various angles to the MS inlet are sometimes unavoidable. Consequently, in these cases, the DC bias will offer a considerable gain effect.

Commercial APCI (DC-corona discharge) is accepted to be based on the "CI" mechanism to achieve ionisation, so contact between plasma and species is required, otherwise no ionisation reaction happens. As reported, AC-corona discharge has been attempted for chemical ionisation similar to the APCI and is experimentally proven capable of giving ion signal intensities comparable to or even stronger than those of the DC-corona discharge. Even softer ionisation was found to be achieved with AC-corona discharge than with DC-corona discharge [67, 69, 71]. In addition, with the help of MS, the radial distribution of negative ions in AC-corona discharge was shown to be significantly broader than those of positive ions, owing to the substantially higher mobility of electrons compared to that of ions.

The ionisation efficiency of AC-corona discharge was revealed to be higher than that of DC-corona discharge for both positive and negative ion modes of operation. This is attributed to the generation of remnant electrons and positive ions in the rising and falling half-phases of the AC-corona discharge, respectively [68]. In further, the superior analytical performance of AC-corona discharge in comparison to DC-corona discharge can be reasonably suspected to be related to the improved ionisation and transportation efficiency. In other words, the local transient potential and the higher DC ring potential contribute to optimised ionisation and transmission. It ultimately leads to a combined improvement of the MS signal with AC-corona discharge. From the results of the MS signal reported [67, 68, 71], it is shown that residual space charges play an important role that cannot be neglected.

It is worth emphasising that neither DC-corona discharge nor AC-corona discharge can ignite a diagnosis plasma if there exists isolation (such as glass), which has been experimentally verified. Although a transient potential exists in AC-corona discharge, it is not high enough to ignite a diagnosis

plasma when they are separated. However, some experiments showed that such transient potential in FμTP is high enough to successfully ignite a diagnosis plasma even beyond a glass wall [9, 26]. In this case, the diagnosis gas is separated from the discharge plasma by a dielectric glass. So, the prerequisite required for the occurrence of CI does not exist. It suggests that, for FμTP, the CI process induced by the applied voltage does not dominate the excitation and ionisation processes of other substances. In fact, the protonation mechanism of FμTP is reported to be based primarily on a transient local potential at the capillary exit [26]. The minor role of the photo-ionisation effect has already been verified through relevant comparative MS experiments [10]. It was also found that when FμTP was blocked by a completely opaque medium (e.g., a notebook), the diagnosis plasma behind the medium could still be ignited successfully. This further confirms that the dominant role of photo-ionisation could be ruled out.

In summary, the DC component potentials mentioned above in AC-corona discharge and FμTP both derive from the residual charge effect brought about by plasma. In addition to the CI process, the transient local potential due to the residual space charge effect in AC-corona discharge also contributes to the ionisation process. This is one of the most possible reasons that AC-corona discharge outperforms DC-corona discharge, another one can be suspect to the higher electrical field that is responsible for ion transport. However, the exact principle is unclear, which may require in-depth study. Similarly, it is reasonable to consider that FμTP further outperforms AC-corona discharge due to the enlarged residual surface charge effect. In addition, FμTP experimentally exhibited better MS performance than APCI for pesticide analysis in both positive and negative ion detection modes [19, 146].

Overall, it can be concluded that the protonation mechanism of FμTP is dominated by the transient local potential at the tube exit. It realises analyte ionisation and sampling actually through the propagation of the excitation and ionisation waves in ambient air to the MS entrance. Benefiting from the enrichment of charges by the capillary, the residual charge effect is amplified, enabling FμTP to achieve a higher MS signal than the AC-corona discharge. However, at the same time, the contribution of the regular CI process induced by the applied voltage in FμTP should not be overlooked.

6.5 Comparison through diagnosis plasma

The plasma propagation behaviour that progressively develops with time in FμTP during two half-phases, respectively, has been demonstrated a lot. Due to the single electrode discharge system, the plasma does not develop almost instantaneously as in AC-corona discharge but develops and propagates gradually on μs-level time scale. Besides, the AC-corona discharge confined in a plastic tube has been found to be milder than the DC-corona discharge because of the wall charging effect [67]. All of these seems to imply that, as an ionisation source, FμTP is even milder than AC-corona discharge. In this section, this will be further explored with the help of the diagnosis plasma.

For the free plasma configuration, similar to the case of FμTP (shown in Figure 4.8), the diagnosis plasmas in front of AC-corona discharge also have completely the same evolution behaviours between

three polarities (shown in Figure 5.8 and Figure 5.9). Accordingly, when there is no conductor interference, almost the same transient potentials among three polarities can also be regarded to exist around the needle tip of AC-corona discharge. For these two types of plasmas, the diagnosis plasmas show nearly no difference between the three polarities. In order to explore the hardness and softness of the ionisation process, the evolution behaviours of the diagnosis plasmas ignited separately by FμTP and AC-corona discharge are recorded and compared. However, the comparison is performed only between the two, not between different polarities (already discussed before). Therefore, only the case of the NP-plasma is used as a representative for comparison here.

As shown in Figure 6.7, the diagnosis tubes were vertically placed in the vicinity of the electrode tip for AC-corona discharge (a) and around the capillary exit for FμTP (d), respectively. *He* in 500 sccm transmitted by a diagnosis tube was used as a diagnosis gas. The vertical distances from the diagnosis

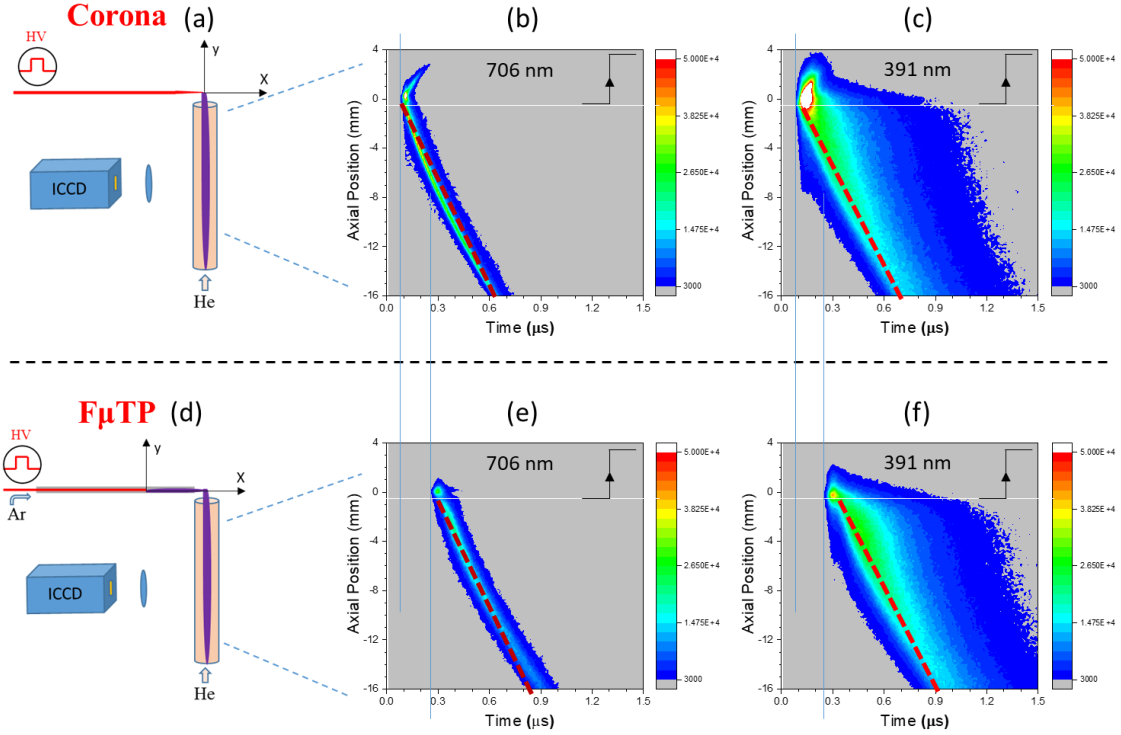

Figure 6.7: Spatial and temporal evolution of He 706 nm and N_2^+ 391 nm observed from He-diagnosis plasmas during the rising half-phase in front of AC-corona discharge and Ar-FμTP, respectively. The white horizontal line at y = -0.5 mm represents the exit of the diagnosis tube.

tube end to the electrode tip of the AC-corona discharge and to the capillary axis of FμTP are 0.5 mm. The discharge gap between the HV electrode tip and the capillary exit in the *Ar*-FμTP is 3 mm. Besides, the same driven voltage of a bipolar square wave with a V_{pp} of 3.2 kV was applied for both of them. The same system composed of Kymera Spectrograph and ICCD was utilised, with the focus being exclusively directed towards the diagnosis plasma region to ascertain its specific evolutionary process.

To be specific, as shown in Figure 6.7, both emission of 706 and 391 nm ignites later during the rising half-phase in FμTP than in AC-corona discharge. On the one hand, due to the capillary, the plasma can be guided until the capillary end, thus ionising analytes. On the other hand, excitation and ionisation

waves or transient potentials in FμTP require a certain amount of time to travel from the HV electrode tip to the capillary outlet and then ignite the diagnosis plasma. Therefore, the ignition time of the diagnosis plasma is always delayed for FμTP compared to AC-corona discharge.

It can be seen that the diagnosis plasma always has a comparable emission intensity and travel speed in front of FμTP and AC-corona discharge during the rising half-phase. This is not perfectly consistent with the relationship between the DC component potentials shown in Figure 6.5, which might be due to differences in the discharge volume length and the discharge gas type used in FμTP. The diagnosis gas can be considered as a substitute for the surrounding air under this condition, so the emission of the diagnosis plasma can be treated equivalent to the excitation and ionisation of air. In other words, without interference, AC-corona discharge and FμTP have comparable ionisation efficiencies.

FμTP has been reported to consist of a dielectrically guided discharge during the rising half-phase, followed by a combination of a dielectrically guided discharge and a negative glow discharge during the falling half-phase [24]. The negative glow discharge can be attributed to the secondary electron emission from the negative electrode, which is out of the range of the slit and thus is not detectable at here. This kind of phenomenon also happened in the AC-corona discharge during the falling half-phase, so an ongoing emission always appears near the electrode tip, as shown in Figure 6.8 (b) and (c).

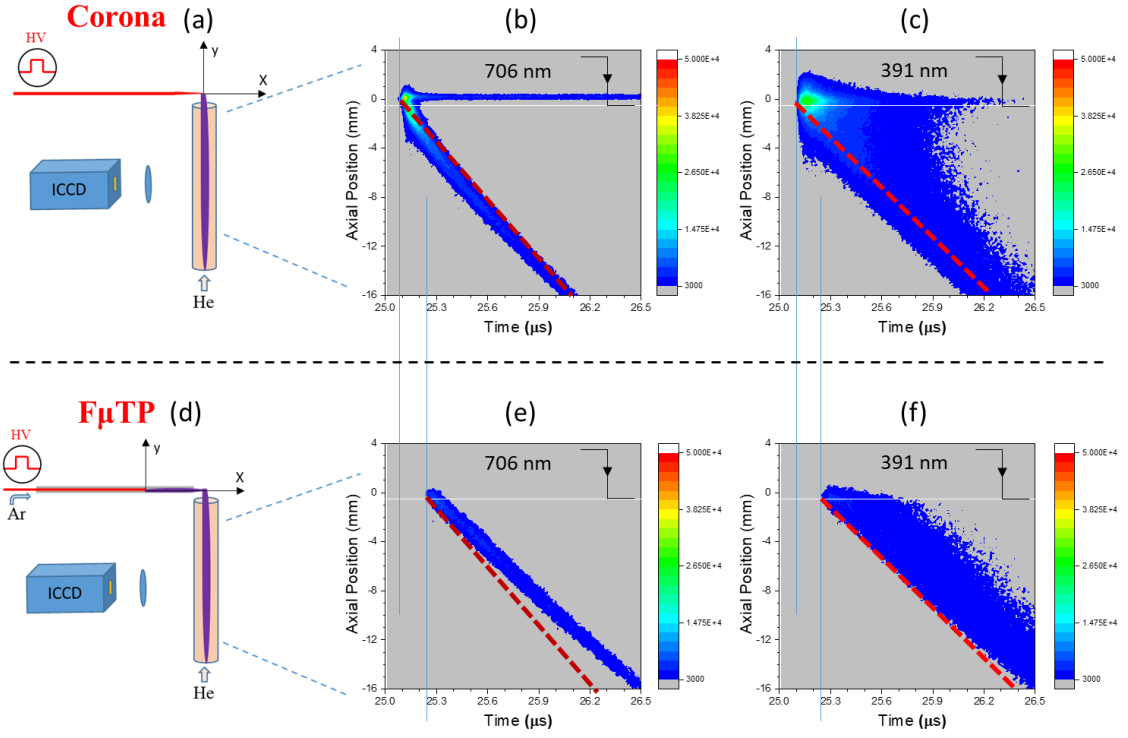

Figure 6.8: Spatial and temporal evolution of the He 706 nm and N_2^+ 391 nm observed from He-diagnosis plasmas during the falling half-phase in front of the AC-corona discharge and Ar-FμTP, respectively. The white horizontal line at y = -0.5 mm represents the exit of the diagnosis tube.

Similarly to the rising half-phase, as displayed in Figure 6.8, these two emission lines igniting later in FμTP compared to that in AC-corona discharge. As mentioned above, this delay can be explained by the time-consuming nature of plasma propagation within the capillary. Unlike the rising half-phase,

these two emission lines have slower propagation speeds and slightly weaker intensities in FμTP than in AC-corona discharge. This can be attributed to the contribution of secondary electron emission in AC-corona discharge, which thus leads to more severe reactions and more emissions.

A very significant and continuous emission of 706 and 391 nm in the vicinity of the axial position at position 0 mm can be seen in AC-corona discharge but not in FμTP, which can be attributed to the spatial distance of FμTP between the HV electrode and the diagnosis gas in the horizontal direction. So, even though secondary electron emission also happens in FμTP, the energetic electrons emitted are not able to do anything directly for diagnosis plasma. Therefore, no such long-tail emission is observed in the case of FμTP. Due to the distance between the HV electrode and the capillary end, the emitted high-energy electrons from the HV electrode do not participate in the ionisation reactions.

These results demonstrate that even in the absence of conductor-induced interferences and despite partial energy dissipation during propagation to the capillary exit, FμTP maintains a transient localised potential or ionisation capacity comparable to that of an AC-corona discharge. Due to the capillary configuration, FμTP features a spatial isolation effect for high-energy electrons. These electrons originate from secondary electron emission and are subsequently accelerated by the external field. As a result, they are effectively excluded from participating in ionisation processes. Thus, ionisation in FμTP is predominantly governed by the secondary electric field formed at the capillary exit, rather than by the primary voltage applied to the electrode. It hints that this mechanism effectively suppresses analyte fragmentation, which constitutes a significant advantage for sensitive and selective analytical applications.

In summary, it is confirmed that energetic electrons are involved in the ionisation of analytes during the falling half-phase in the AC-corona discharge but not in FμTP. However, the analytes are easy to fragment by these high-energy electrons. Due to additional capillary, this does not appear to be a problem in FμTP. In short, FμTP is implied to be softer than AC-corona discharge when used for ionisation. This will require further confirmation through MS analysis on various types of analytes.

6.6 The function of capillary in FμTP

The typical physical configurations of corona discharge and FμTP have already been described before, the other detailed information can be found in Section 2.1. Corona discharges usually are formed in high curvature areas of electrode, such as sharp corners, protrusions, edges of metal surfaces or small diameter wires. It is evident that, owing to the high potential gradients present at these specific locations, the breakdown process will occur first in these areas, thereby forming a plasma. Corona discharge occurs only when the electric field surrounding a conductor surpasses the dielectric strength of air, usually it needs 3 kV/mm [60]. Corona discharge requires a specially manufactured sharp electrode tip or edge to generate a local high electric field. In addition, a counter electrode (such as a grounded plate) is usually required. However, FμTP does not have such a strict requirement and can easily be ignited without

special treatment at the blunt end of the electrode. The prerequisite is a sufficiently thin tungsten wire (typical diameter of 100 μm) used as a HV electrode, with no demand for any counter electrode but with the ion cloud acting as a virtual counter electrode. Even though corona discharge can also be ignited in a single electrode configuration, a much higher driven voltage is usually required. In instances where APCI is employed for MS analysis, the MS inlet actually functions as the counter electrode, thereby greatly facilitating the discharge process.

For FμTP, an additional glass capillary is essential as a channel for discharge gas transfer, thus forming a local controlled gas composition environment for plasma generation and propagation. Usually, FμTP is sustained in a special discharge gas, which is transmitted through this capillary to replace atmospheric air. For FμTP, this thin capillary is the key role responsible for the formation of the long plasma column and even the plasma jet. It is confirmed that a transient potential created by surface charges on the glass wall leads to the propagation of excitation and ionisation waves within the capillary and the excitation of a noble gas outside the capillary [26]. Furthermore, this additional capillary separates the air from the HV electrode and is replaced with a specific discharge gas.

If the same sharp electrode is used, the only differentiation as for the discharge configuration between DC-corona discharge and AC-corona discharge seems to be the driven voltage. DC-corona discharge can generate a basically monopolar positive or negative ion swarm, while AC-corona discharge can alternately produce positive and negative ion swarms in two half-phases [71]. This is also the same case for FμTP, which is typically driven by a bipolar voltage. It was found that a FμTP can be ignited in various gas composition and even in ambient air [7], if ignoring the difference at the end of the electrodes, the only difference as for the discharge configuration between AC-corona discharge and FμTP seems to be the additional capillary.

In contrast to the light emission shapes of positive and negative DC-corona discharges displayed in Section 5.2, which correspond to the rising and falling half-phases of a square wave cycle, no similar phenomenon is observed in FμTP. However, the transient images of FμTP exhibit similar point-like light emission patterns, with the positions of these points gradually moving along the capillary over time [24]. It seems that the corona discharge at the electrode tip is moving along the capillary, but in reality, the ion cloud within the capillary acts as a virtual electrode. The movement of this ion cloud is actually the result of the development and propagation of excitation and ionisation waves, known as dielectric guided discharge [24]. This indicates that the residual charge plays a decisive role in the formation process of FμTP. This is somewhat similar to the guiding effect caused by a self-organising charge distribution reported in many investigations regarding the interplay between charged particles and the insulating capillary [93, 147, 148]. It should be emphasised that in FμTP, due to the special effect of capillary, the plasma originating from the electrode tip is able to overcome the limitations of localised discharge reactions. Instead, the plasma arises from the electrode tip in both half-phases and gradually develops into a plasma column and even forms a plasma jet. This is due to the effective isolation of air

by the capillary wall, which suppresses its quenching effect on the inside species. Once the plasma leaves the capillary end into the surrounding ambient air, the quenching effect causes the plasma to rapidly extinguish and terminate at a certain position in front of the tube exit.

It was found that the required ignition voltage amplitude of AC-corona discharge is apparently lower than the DC-corona discharge under the same conditions. Studies have shown that it is probably because the space charge effects of respective remanent charges around the needle tip devote to each half-phase of AC-corona discharge [28]. These residual charges greatly promote discharge reactions, which shows their powerful effect that cannot be ignored. As described in Section 2.2, the fused silica capillary utilised in FμTP is a good dielectric material with a large relative dielectric constant, so it can be effectively polarised. In each half-phase, a large number of charged particles accumulate on the capillary wall, generating a strong local electric field. Therefore, it can be suspected that the presence of capillary hugely increases the number of residual charges, further amplifying the effect of the residual charge on the discharge behaviour. Such charge effect in FμTP has been discussed in the previous part and will be carefully considered in the following sections.

6.6.1 Dynamic discharge configuration

Research has shown that due to the rapid change of the electric field, the charged particles generated by AC-corona discharge within each half-phase do not have enough time to be completely eliminated. Instead, the residual charge at the end of the previous half-phase promotes the occurrence of discharge reactions in the next half-phase. This effect has been discussed and confirmed in multiple publications [29, 68, 71]. In AC-corona discharge, the local electric field around the needle tip is significantly distorted by the residual space charges from the previous half-phase. To a great extent, it is precisely the hysteresis effect of charge relative to the periodic reversal of the electric field direction that determines many characteristics that distinguish it from DC-corona discharge. If there is a way to enhance this residual charge effect, a novel optimised plasma can be achieved. In FμTP, the capillary plays exactly this role. In further detail, it is the residual charges accumulated on the inner wall of the capillary that are at work. This point has been discussed repeatedly in previous chapters and in other publications [24-26]. The quartz capillary acts as a good storage device for residual charges, allowing a large number of free charges to accumulate. These surface charges can effectively alter the local electric field, which can ultimately and completely change the behaviour of the discharge plasma.

This assertion is also supported by recent research that demonstrates that a substantial improvement in overall MS performance was realised through optimisation of the dielectric material in DBDI [149]. Specifically, the use of dielectric materials with higher dielectric constants can enhance discharge reactions, thereby achieving more effective ionisation and expanding the mass range of detectable ions. This indicates the critical role of the dielectric constant in the DBDI source. The higher the dielectric constant, the more charge the material can store, resulting in a stronger electric field. This stronger

electric field promotes the more efficient ionisation of molecules, including those that are difficult to ionise using materials with lower dielectric constants.

In Section 4.3.1.3 and some publications [9, 26], the diagnosis gas placed perpendicular to the discharge plasma was ignited and a long plasma column similar to that in the discharge capillary was generated inside the diagnosis tube. This indicates that a surface charge accumulation process similar to that in the discharge capillary must occur on the inner wall of the diagnosis tube. However, it is worth noting that, due to the mutually perpendicular directions, the charged particles find it extremely hard to enter the diagnosis tube. As explained before, dielectric polarisation and charge accumulation are two separate mechanisms that may interact but are not the premise of each other. Therefore, there is reason to suspect that the polarisation of the diagnosis tube significantly promotes the accumulation of free charges on its inner surface, thereby guiding the formation of a long diagnosis plasma column. The Coulomb force between the two opposite charges, the polarised charge and the surface charge, should be considered.

This has also been confirmed in experiments where DC- and AC-corona discharges are used to ignite diagnosis plasma. As shown in Figure 6.9, the same diagnosis tube filled with *He* as diagnosis gas was placed below the electrode tip. It was found that *He* inside the diagnosis tube can only be initiated by AC-corona discharge and forms a long plasma column marked by the red dashed box in Figure 6.9 (c).

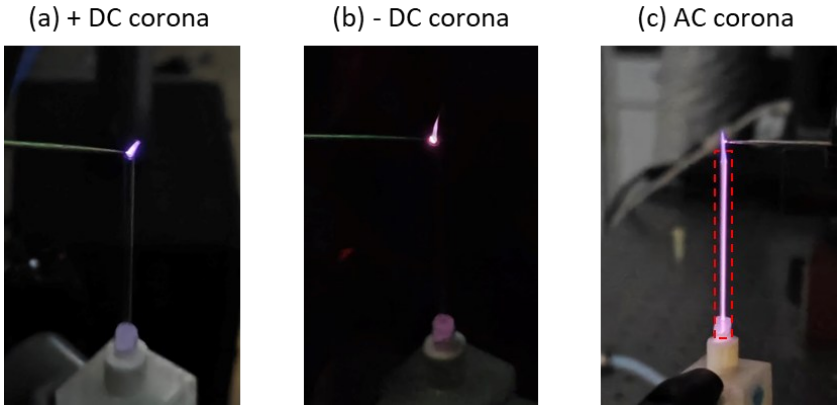

Figure 6.9: Photos of diagnosis gas (He in 500 sccm) ignited by (a) positive DC-corona discharge driven by a voltage of +12 kV, (b) negative DC-corona discharge driven by a voltage of -12 kV and (c) AC-corona discharge driven by a bipolar square wave voltage with V_{pp} = 3.5 kV, respectively.

For DC-corona discharge, due to the absence of depolarisation effect, charged particles find it extremely difficult to repeatedly adhere to the surface of the diagnosis tube to initiate an excitation and ionisation wave, let alone accumulate to a sufficient extent to alter the local electric field. In contrast, for AC-corona discharge, the diagnosis tube undergoes an ongoing polarisation and depolarisation process, resulting in the periodic attachment of surface charges. Eventually, a considerable number of charges accumulated on the glass wall generating a quasi-static local potential. In other words, the long diagnosis plasma column is the result of the synergistic action of glass polarisation and charge accumulation. Therefore, unlike that in AC-corona discharge scenario, the gas inside the diagnosis tube is difficult to be ignited by DC-corona discharge and thus cannot form a long diagnosis plasma column.

Since glass polarisation interacts with charge accumulation, and the impact of conductors such as a MS inlet on the local electric field is certain, this necessarily implies an effect on capillary polarisation and even surface charge accumulation. Of course, the primary cause of this effect is not a change in the intrinsic polarisation mechanism of the fused quartz. The "electronic polarisation" of the material itself is not altered, what is altered are the boundary conditions of both the local electric field and the surface/space charges that drive it. A nearby metal can alter these boundary conditions around the plasma, thereby significantly influencing the overall polarisation behaviour of the capillary. This includes variations in the local total electric field at the quartz surface/near-surface region, surface charge accumulation, and the slow charge distribution generated by the plasma. Therefore, the impact mechanism of an external metal to plasma is confirmed, especially to FμTP, which is acting through the influence to dielectric polarisation or charge accumulation and thus change the local electric field.

In FμTP and in corona discharge, all electric fields achieve plasma ignition through the electron avalanche mechanism at atmospheric pressure [42]. However, the presence of capillary in FμTP allows significant free charges to adhere and accumulate on the inner surface, resulting in a plasma behaviour significantly different from corona discharge after ignition. Arguably, after the first ignition, these memory charges soon dominate the behaviour of FμTP. The initial discharge forms an ion cloud, which acts as a virtual counter electrode in the subsequent plasma column formation process, and this electrode gradually moves towards the tube exit over time.

6.6.2 Charge accumulation and its effect

This section will describe the accumulation mechanism of free charges on the capillary inner surface, quantitative analysis of the accumulated charges, and its effect on the discharge dynamics of FμTP are also included. During the two half-phases of the applied square wave voltage, electrons and ions produced by the ionisation of gas during the discharge process migrate toward the electrodes or the outlet under the influence of the electric field. At the same time, some charged particles migrate onto the dielectric surface. Here, the quartz glass used as the dielectric barrier layer has extremely low conductivity ($\sigma \approx 10^{-16}$ S/m), so charged particles cannot be rapidly dissipated through bulk or surface conduction, but can only deposit on its surface. Although positive ions (such as N_2^+) driven by the electric field can impact the dielectric surface and recombine with deposited electrons/negative ions, or vice versa, the accumulated charge on the capillary wall still remains due to the insufficient recombination efficiency.

The surface charge density $\sigma_{surface}$ after a single discharge can be estimated from the relationship between the electric field and the dielectric capacitance: $\sigma_{surface} = \varepsilon_0 \varepsilon_r E_{gas}$ [150], ε_0 is the dielectric constant of vacuum (~8.85×10^{-12} F/m), ε_r is the dielectric constant of quartz glass (~3.8) and the electric field in the gas gap under 2.5 kV is $E_{gas} \approx 3.5\times10^7$ V/m [23], then:

$$\sigma_{surface} = (8.85\times10^{-12})\times3.8\times3.5\times10^7 \approx 1.18\times10^{-3}\ \text{C/m}^2$$

The surface electric field strength corresponding to this charge density is:

$$E_{surface} = \sigma/\varepsilon_0 = (1.18\times10^{-3})/(8.85\times10^{-12}) \approx 1.33\times10^{8}\ \text{V/m}$$

This reverse electric field will superimpose on the applied electric field, significantly altering the net electric field of the discharge gap. Therefore, the accumulated charges can regulate discharge dynamics, such as triggering the self-quenching effect. During the plateau period of the square wave voltage (i.e., the voltage holding stage), the accumulated surface charges form a reverse electric field ($E_{surface}$) that is opposite to the direction of the applied electric field ($E_{applied}$). The net electric field is: $E_{net} = E_{applied} - E_{surface}$, when $E_{net} < E_{breakdown}$ (gas breakdown threshold), the discharge reaction rapidly stops, achieving self-quenching [49, 52]. However, until the next half-phase begins, a considerable number of surface charges may still remain on the capillary wall. The self-quenching time depends on the charge accumulation rate and the electric field cancellation efficiency. Typical values are close to 100 ns, which is comparable to the duration of the plasma emission spectra observed in experiments.

At the rising or falling edge of a square wave function, the direction of the applied electric field rapidly reverses, but the surface charge cannot be dissipated quickly. It is important to note that the surface charge referred to here is the free charge deposited on the inner surface of the capillary (i.e., the interface between the plasma and the dielectric) rather than the polarised charge within the dielectric material. It is precisely due to this mismatch that the net electric field (E_{net}) is further enhanced after polarity reversal. At this point, a brief reverse discharge may occur, but the net electric field is quickly suppressed, resulting in a symmetric self-quenching process.

The electronic polarisation relaxation time of quartz glass ($\tau_{electronic} \sim10^{-16}$ s) is much shorter than the edge time of square wave (~100 ns [23]) and the discharge timescale. Thus, the polarisation response can be regarded as instantaneous, with no delay contribution to the discharge dynamics. Polarised charges are generated by the displacement of the electron cloud within the dielectric, its value is small ($\sigma_{polarisation} \approx \varepsilon_0(\varepsilon_r-1)E$ [78]$\sim10^{-4}$ C/m^2) and its effect on the net electric field can be ignored. The surface charges are dominated by the real charges injected by plasma, with a density as high as 10^{-3} C/m^2, which is the main factor in electric field regulation. From above, due to the extremely fast relaxation of the electronic polarisation, the delay can be neglected because of the ultra-fast response of quartz glass. Furthermore, the polarised charge is one order of magnitude lower than the surface charge. Therefore, the core contradiction lies in the “retention” of surface charge rather than the “delay” of polarisation. In other words, in low-conductivity dielectric materials like quartz glass, the accumulation of surface charge is the core regulatory factor for plasma discharge dynamics.

6.7 Conclusions

Based on the results and discussions presented above, the conclusions are obtained as follows. Although FμTP shares many similarities with corona discharge, such as analogous physical configurations and

transient optical images, it features a purely single-electrode design and an additional quartz capillary. The accumulation of surface charges plays a key role in the regulation of plasma discharge dynamics, particularly in effects such as self-quenching. As a consequence, one major distinction between FμTP and APCI is that the plasma in FμTP repeatedly extinguishes and reignites, making it an intermittent plasma source similar to AC-corona discharge [68]. Concurrently, the charging of the capillary wall partially shields the voltage applied on the HV electrode, effectively reducing the risk of direct discharge.

Another major difference in the discharge mechanism between APCI and FμTP lies in the dynamic discharge configuration of the latter. In FμTP, the moving ion cloud within the capillary acts as a transient counter-electrode, guiding the plasma propagates forward. This mechanism allows FμTP to overcome the spatial limitations of localised discharge, such as those in corona discharge, thus improving both its flexibility and operational safety. It has already been demonstrated that there is a mutually reinforcing relationship between the local transient potential and the plasma propagation along the capillary. Without the capillary, new local potentials cannot form and the plasma cannot be guided forward to develop into an extended plasma column. This highlights the critical role of the capillary in the formation of FμTP, showing that the process is not limited to the region near the electrode tip. Accordingly, it is evident that FμTP is not a traditional corona discharge, but a guided discharge that can even produce a plasma jet.

With the assistance of charged particles in the surrounding air, an electrical connexion is also established. As a result, a DC component potential was measured using a ring detector. Furthermore, a strong correlation between the ion efficiency and the ring potential has been identified from the experiments. This makes the ring potential a useful indicator for evaluating the MS performance of different ionisation sources. Although APCI and AC-corona discharge achieve ionisation mainly through traditional “CI” processes induced by the applied voltage, FμTP is revealed to rely primarily on secondary transient potentials. The combined analysis of these experiments suggests that FμTP is promising in achieving softer ionisation in a higher ion efficiency than both DC- and AC-corona discharges. This can be attributed to the presence of capillary, which isolates secondary electron emission and amplifies the residual charge effect as well. To clarify this, further research is essential.

In summary, the distinct characteristics and advantages of FμTP that separate it from traditional corona discharges should not be overlooked. Therefore, FμTP should not be simply classified as a corona discharge. Rather, a completely new type of plasma can be considered, which initiates as a corona discharge at the electrode tip and is then guided to form an extended plasma column. Due to the benefits provided by the capillary, FμTP is expected to surpass conventional corona discharges not only in terms of plasma form but also in analytical capability. From an analytical perspective, the results obtained hint that FμTP outperforms both AC- and DC-corona discharges when used as an ionisation source. In addition, FμTP also shows broader applications prospects for safe and flexible operation.

CHAPTER 7

Summary and outlook

This thesis presents a systematic investigation of the discharge mechanism and propagation dynamics in *He*- and *Ar*-FμTPs, with an emphasis on identifying the dominant ions that guide plasma evolution within the capillary. Based on these findings, the influence of a nearby metallic target in front of the *He*-FμTP driven by three polarity voltages under varying distance conditions was then examined. It provides information on conductor–plasma interactions and their implications for MS applications. Besides, it helps improve the performance of FμTP and provides inspiration for the optimisation of other plasma-based applications. Furthermore, comparative studies with corona discharges were conducted to better understand and distinguish FμTP from classical corona discharge. Moreover, it contributes to clarifying the distinct discharge characteristics and advantages of FμTPs as plasma-based ionisation sources. In summary, the measurements presented provide essential guidance in achieving the transfer of FμTP technology from the invention prototype to practical application. Therefore, a comprehensive analysis of optical emission, electrostatic potential, and the corresponding MS signal provides a more profound, universal, and robust means to characterise, quantify, and predict plasma-based performance for analytical applications.

7.1 Summary

The background of electrical breakdown and plasma generation was first introduced in the second chapter, including corona discharge and FμTP. It also dealt with the basic process of dielectric polarisation as well as the charge accumulation on the dielectric surface. The simple introduction to the principles of the OES diagnostic method for plasma characterisation was also included.

In the third chapter, *He* and *Ar* were employed as discharge gases to explore plasma behaviours in both half-phases of the AC cycle. Using time- and position-resolved phoresis plots, a new data analysis

method (POEPS) was proposed, enabling the differentiation of noble gas ions from excited states. The results indicate that in a *He*-FμTP, N_2^+ dominates the excitation and ionisation process and only a small amount of He^+ is produced. However, Ar^+ has been found to play a similar leading role in supporting plasma propagation forward in *Ar*-FμTP. However, when propane was added as trace impurity into *Ar* and the mixture used as discharge gas, propane was proven to be ionised by Penning ionisation. These propane ions play the same role as N_2^+ in *He*-FμTP and compensate for the absence of N_2^+ in *Ar*-FμTP. In addition, ions and excited species were found not to propagate beyond the capillary exit during the falling half-phase, implying a limited contribution to protonation processes.

The fourth chapter revealed that the FμTP behaviour is highly sensitive to nearby conductors. Experiments demonstrated that different target distances and applied voltage polarities significantly alter plasma evolution due to changes in the electric field distribution. Because the local electric field dominates the subsequent behaviour of plasma, the influence of a target on the accumulated surface charges, thereby distorting the local electric field, was introduced for interpretation. In addition, plasmas with positive-biassed (P), negative-biassed (N), and bipolar (NP) voltages exhibited distinct discharge behaviours. NP-plasma showing the smoothest change tendency of evolution, which suggests enhanced controllability. From the perspective of discharge, this makes NP the most favourable mode for analytical applications. Moreover, the significant impact of a nearby conductor on FμTP was indicated. The mode compatibility of NP-plasma for detection in both ion modes was evidenced. These findings highlight the strong coupling between surface charge accumulation, local electric field distortion, and plasma propagation. The benefits of polarity switching in enhancing ion efficiency when FμTP couples with MS at a distance that exceeds 3 mm was also confirmed.

In the fifth chapter, both DC- and AC-corona discharges were carefully surveyed. Both high-resolution imaging and space-resolved emission spectra revealed, for the first time, distinct optical morphologies (in colour and shape) for positive and negative DC-corona discharges. Besides, their appearances are not only limited to the classic “corona” shape. Spatial potential mapping further demonstrated that the measured electrostatic potential always shared the same polarity of the driven voltage in both DC- and AC-corona discharges. Moreover, a very weak negative potential also appeared in bipolar AC-corona discharge. In all cases, the strongest potential was consistently discovered in the vicinity of the needle tip, which further indicated a strong localised electric field at this location. It was reasoned that the superior ionisation efficiency of AC-corona discharge compared to that of DC-corona discharge is related to the residual space charges, which manifest as the ring potential measured here.

In the sixth chapter, comparative studies showed that FμTPs produce stronger potentials than corona discharges under identical applied voltages. A clear correlation between ion efficiency and local potential was established from MS experiments of FμTP with varying DC bias. This is an important part of the evidence to show that FμTP is more efficient than corona discharge as ionisation source. Additionally, a softer ionisation characteristic of FμTP than corona discharge was also hinted through

the diagnosis plasma experiments. This is attributed to their different ionisation mechanisms. Nevertheless, both of these findings need to be further verified through more direct evidence. The distinct characteristics confirm that FμTP is not just a modified corona discharge but rather an extended discharge that initiates as a corona discharge near the electrode tip and is subsequently guided through the capillary into a stable plasma column or jet. Besides, it demonstrated that FμTP primarily achieve ionisation through secondary transient potentials rather than conventional CI processes induced by the applied voltage. In short, the function of capillary has been revealed to be guiding plasma propagation, reducing the risk of direct discharge, amplifying the residual charge effect, and isolating secondary electron emission. As a result, FμTP is able to achieve more flexible application forms, showing great potential for higher ion efficiency and softer ionisation compared to both DC- and AC-corona discharges.

Overall, the present thesis provides new insight into the mechanisms governing FμTP formation, propagation, and ion efficiency. Factors such as discharge gas composition, electrode configuration, additional DC bias in the driven voltage, and nearby conductors, especially the MS inlet when coupling to the plasma, were shown to play critical roles. The findings offer valuable theoretical and experimental guidance to further enhance the analytical performance and versatility of FμTP and related plasma-based technologies.

7.2 Outlook

Despite the advances achieved in this work, several aspects of FμTP and related plasma-based ionisation sources require further investigation and optimisation. The types, abundances, and transport efficiencies of the interest ions remain key factors that influence the overall performance. A combined analysis on the interaction of these variables will facilitate a deeper understanding of ion species generation pathways, spatial transport mechanisms, and recombination dynamics. Finally, it will contribute to improving both analytical sensitivity and source stability. Besides, the correlation between the electrical and optical discharge characteristics of the plasma also warrants further exploration. A systematic evaluation and comparison of DC-, AC-corona discharge and FμTP in terms of MS performance under both positive and negative ion modes, particularly at varying distances to the MS inlet, need to be carried out. It will offer direct insights into their ionisation efficiencies and softness. Meanwhile, effective measures must be developed and implemented to mitigate the risk of electrical shortcut in plasma–MS configurations. Moreover, the relationship between electrostatic potentials and corresponding MS signals obtained at various distances should be thoroughly clarified. It will establish a theoretical basis for improving the efficiency of ion transport and collection.

From a discharge perspective, the behaviour of practical noble gas plasmas remains an open question. While ionisation of noble gas atoms is generally regarded as the foundation for plasma formation, experimental observations reveal sustain voltages that deviate significantly from theoretical predictions based on ionisation energies. This discrepancy is likely caused by trace impurities (typically on the order

of several ppm) present even in high-purity gases. Systematic investigations into the contribution of such impurities are therefore essential to clarify the real major cause that is responsible for such contradiction, to identify the dominant ionisation pathways, and to reconcile theoretical models with experimental results. Furthermore, investigation on the lowest self-sustaining voltage after ignition of FμTP has revealed a viable approach to efficiently reduce the required voltage. This is achieved by the introduction of an appropriate amount of helping gas into the discharge gas, such as trace hydrocarbon additives. For instance, the lowest self-sustaining voltage of an *Ar*-FμTP was substantially lowered from 2.4 kV to 1.2 kV by adding 1000 ppm acetylene. Such findings provide a promising strategy for effectively reducing power supply requirements and improving the energy efficiency of plasma systems in practical applications.

In summary, a combined analysis of electrical, optical discharge characteristics, and plasma–MS coupling detection will further deepen the theoretical understanding of plasma behaviour and promote the development of more efficient and reliable plasma-based ionisation sources. Continued interdisciplinary research along these lines will advance both the scientific foundation and the engineering applications of FμTP and related plasma technologies.

Bibliography

1. Dole, M.; Mack, L. L.; Hines, R. L.; Mobley, R. C.; Ferguson, L. D.; Alice, M. B., Molecular Beams of Macroions. *The Journal of Chemical Physics* **1968,** *49* (5), 2240-2249.
2. Fenn, J. B.; Mann, M.; Meng, C. K.; Wong, S. F.; Whitehouse, C. M., Electrospray ionization for mass spectrometry of large biomolecules. *Science* **1989,** *246* (4926), 64-71.
3. Horning, E. C.; Horning, M. G.; Carroll, D. I.; Dzidic, I.; Stillwell, R. N., New picogram detection system based on a mass spectrometer with an external ionization source at atmospheric pressure. *Anal Chem* **1973,** *45*(6), 936-943.
4. Cody, R. B.; Laramée, J. A.; Durst, H. D., Versatile New Ion Source for the Analysis of Materials in Open Air under Ambient Conditions. *Anal Chem* **2005,** *77*(8), 2297-2302.
5. Ding, X.; Duan, Y., Plasma-based ambient mass spectrometry techniques: The current status and future prospective. *Mass Spectrom Rev* **2015,** *34* (4), 449-73.
6. Yue, H.; He, F.; Zhao, Z.; Duan, Y., Plasma-based ambient mass spectrometry: Recent progress and applications. *Mass Spectrom Rev* **2023,** *42* (1), 95-130.
7. Brandt, S.; Klute, F. D.; Schutz, A.; Marggraf, U.; Drees, C.; Vogel, P.; Vautz, W.; Franzke, J., Flexible Microtube Plasma (FμTP) as an Embedded Ionization Source for a Microchip Mass Spectrometer Interface. *Anal Chem* **2018,** *90* (17), 10111-10116.
8. Drees, C.; Schutz, A.; Niu, G.; Franzke, J.; Vautz, W.; Brandt, S., Stepwise optimization of a Flexible Microtube Plasma (FmicroTP) as an ionization source for Ion Mobility Spectrometry. *Anal Chim Acta* **2020,** *1127*, 89-97.
9. Speicher, L.; Song, H.; Ahlmann, N.; Foest, D.; Hoving, S.; Brandt, S.; Niu, G.; Franzke, J.; Tian, C., Soft ionization mechanisms in flexible micro-tube plasma-from FμTP to closed micro-tube plasma. *Anal Bioanal Chem* **2024,** *416* (22), 4919-4927.
10. Tian, C.; Song, H.; Ahlmann, N.; Brandt, S.; Foest, D.; Niu, G.; Franzke, J.; Speicher, L., Soft ionization mechanisms in flexible micro-tube plasma-elucidation of He-, Ar-, Kr-, and Xe-FmicroTP. *Anal Bioanal Chem* **2024,** *416* (22), 4907-4918.
11. Vogel, P.; Lazarou, C.; Gazeli, O.; Brandt, S.; Franzke, J.; Moreno-Gonzalez, D., Study of Controlled Atmosphere Flexible Microtube Plasma Soft Ionization Mass Spectrometry for Detection of Volatile Organic Compounds as Potential Biomarkers in Saliva for Cancer. *Anal Chem* **2020,** *92* (14), 9722-9729.
12. Foest, D.; Knodel, A.; Ahrends, R.; Coman, C.; Franzke, J.; Brandt, S., Flexible Microtube Plasma for the Consecutive-Ionization of Cholesterol in Nano-Electrospray Mass Spectrometry. *Anal Chem* **2023,** *95* (22), 8423-8432.
13. Knodel, A.; Foest, D.; Brandt, S.; Ahlmann, N.; Marggraf, U.; Gilbert-Lopez, B.; Franzke, J., Detection and Evaluation of Lipid Classes and Other Hydrophobic Compounds Using a Laser Desorption/Plasma Ionization Interface. *Anal Chem* **2020,** *92* (22), 15212-15220.

14. Foest, D.; Franzke, J.; Brandt, S., Quasi-Simultaneous Identification of Polar and Neutral Lipids in Mass Spectrometry by kHz Switching of Electrospray and Plasma Ionization. *Anal Chem* **2025,** *97* (4), 2011-2018.

15. Foest, D.; Knodel, A.; Brandt, S.; Franzke, J., Coupling paper spray ionization with the flexible microtube plasma for the determination of low polar biomarkers in mass spectrometry. *Anal Chim Acta* **2022,** *1201*, 339619

16. Knodel, A.; Marggraf, U.; Ahlmann, N.; Brandt, S.; Foest, D.; Gilbert-Lopez, B.; Franzke, J., Standardization of Sandwich-Structured Cu-Glass Substrates Embedded in a Flexible Diode Laser-Plasma Interface for the Detection of Cholesterol. *Anal Chem* **2020,** *92* (6), 4663-4671.

17. Bouza, M.; Ahlmann, N.; Garcia-Reyes, J. F.; Franzke, J., Solvent-Assisted Laser Desorption Flexible Microtube Plasma Mass Spectrometry for Direct Analysis of Dried Samples on Paper. *Anal Chem* **2023,** *95* (50), 18370-18378.

18. Moreno-Gonzalez, D.; Castilla-Fernandez, D.; Vogel, P.; Niu, G.; Brandt, S.; Drees, C.; Garcia-Reyes, J. F.; Molina-Diaz, A.; Franzke, J., Evaluation of a novel controlled-atmosphere flexible microtube plasma soft ionization source for the determination of BTEX in olive oil by headspace-gas chromatography/mass spectrometry. *Anal Chim Acta* **2021,** *1179*, 338835.

19. Garcia-Martinez, J.; Cano-Carrillo, I.; Gilbert-Lopez, B.; Bouza, M.; Beneito-Cambra, M.; Franzke, J.; Molina-Diaz, A.; Garcia-Reyes, J. F., Miniaturized flexible micro-tube plasma ionization source for the effective ionization of non-easily ionizable pesticides in food with liquid chromatography/mass spectrometry. *Talanta* **2024,** *274*, 126011.

20. Tian, C.; Speicher, L.; Xue, D.; Moreno-Gonzalez, D.; Marggraf, U.; Ahlmann, N.; Brandt, S.; Franzke, J.; Niu, G., Ionization of semi-fluorinated n-alkanes in controlled atmosphere using flexible micro-tube plasma (FuTP) ionization source with square- and sine-wave voltage. *Talanta* **2022,** *249*, 123662.

21. Foest, D.; Knodel, A.; Ahrends, R.; Coman, C.; Franzke, J.; Brandt, S.; The Flexible Microtube Plasma as Post-Ionization Source for Cholesterol in nano-Electrospray Mass Spectrometry. *Anal Chem* **2023,** *95*.

22. Fechner, A.; Drees, C.; Vautz, W.; Sielemann, S.; Telgheder, U.; Franzke, J.; Brandt, S., Seamless analysis of liquid samples by coupling a thermal desorption chip with ion mobility spectrometry. *Anal Bioanal Chem* **2025,** *417* (22), 5037-5046.

23. Gazeli, O.; Lazarou, C.; Niu, G.; Anastassiou, C.; Georghiou, G. E.; Franzke, J., Propagation dynamics of a helium micro-tube plasma: Experiments and numerical modeling. *Spectrochimica Acta Part B: Atomic Spectroscopy* **2021,** *182*.

24. Tian, C.; Ahlmann, N.; Brandt, S.; Franzke, J.; Niu, G., Optical characterization of miniature flexible micro-tube plasma (FμTP) ionization source: A dielectric guided discharge. *Spectrochimica Acta Part B: Atomic Spectroscopy* **2021,** *181*.

25. Song, H.; Tian, C.; Speicher, L.; Ahlmann, N.; Brandt, S.; Niu, G.; Franzke, J., Elucidation of discharge mechanisms in He- and Ar-flexible μ-tube plasmas by temporally and spatially resolved plasma optical emission phoresis spectroscopy. *Spectrochimica Acta Part B: Atomic Spectroscopy* **2024,** *219*.

26. Song, H.; Tian, C.; Speicher, L.; Ahlmann, N.; Foest, D.; Höving, S.; Brandt, S.; Niu, G.; Franzke, J., Excitation and ionization of a diagnosis gas in front of the flexible μ tube plasma and in a diagnosis tube. *Spectrochimica Acta Part B: Atomic Spectroscopy* **2024,** *221*.

27. Tian, C.; Speicher, L.; Song, H.; Ahlmann, N.; Brandt, S.; Niu, G.; Franzke, J., Study of the discharge mode transition in a Ne-flexible micro-tube plasma (FμTP). *Spectrochimica Acta Part B: Atomic Spectroscopy* **2025,** *228*.

28. Zhang, C. H.; MacAlpine, J. M. K., A phase-related investigation of AC corona in air. *IEEE Transactions on Dielectrics and Electrical Insulation* **2003,** *10* (2), 312-319.

29. El-Koramy, R. A.; Yehia, A.; Omer, M., Development of ac corona discharge modes at atmospheric pressure. *Physics of Plasmas* **2011,** *18* (2).

30. Chen, Z.; Wirz, R. E., Cold atmospheric plasma (CAP) technology and applications. *Springer Cham*: **2021**.

31. Lin, S. P.; Khumsupan, D.; Chou, Y. J.; Hsieh, K. C.; Hsu, H. Y.; Ting, Y.; Cheng, K. C., Applications of atmospheric cold plasma in agricultural, medical, and bioprocessing industries. *Appl Microbiol Biotechnol* **2022,** *106* (23), 7737-7750.

32. Burm, K. T. A. L., Plasma: The Fourth State of Matter. *Plasma Chemistry and Plasma Processing* **2012,** *32* (2), 401-407.

33. Eliezer, Y.; Eliezer, S., The Fourth State of Matter: An Introduction to the Physics of Plasma. *Adam Hilger*: **1989**.

34. Bittencourt, J. A., Fundamentals of Plasma Physics. *Springer New York*: **2004**.

35. Hazeltine, R. D.; Waelbroeck, F.L., The Framework of Plasma Physics. *Westview*: **2004**.

36. Morozov, A. I., Introduction to Plasma Dynamics. *CRC Press*: **2012**.

37. Bruggeman, P.; Brandenburg, R., Atmospheric pressure discharge filaments and microplasmas: physics, chemistry and diagnostics. *Journal of Physics D: Applied Physics* **2013,** *46* (46), 464001.

38. Kanazawa, S.; Kogoma, M.; Moriwaki, T; Okazaki, S., Stable glow plasma at atmospheric pressure. *Journal of Physics D: Applied Physics* **1988,** *21* (5), 838-840.

39. RAY, S., An Introduction to High Voltage Engineering. *PHI Learning*: **2013**.

40. Paschen, F., Ueber die zum Funkenübergang in Luft, Wasserstoff und Kohlensäure bei verschiedenen Drucken erforderliche Potentialdifferenz. *Annalen der Physik* **1889,** *273*, 69-96.

41. Lieberman, M. A.; Lichtenberg, A. J., Principles of Plasma Discharges and Materials Processing. *John Wiley & Sons*: **2024**.

42. Bruggeman, P. J.; Iza, F.; Brandenburg, R., Foundations of atmospheric pressure non-equilibrium plasmas. *Plasma Sources Science and Technology* **2017,** *26* (12), 123002.

43. Wadhwa, C. L., High Voltage Engineering. *New Age International*: **2007**.

44. Cai, R.; Kulmala, M., Opinion: Influence of the mean free path of air on atmospheric particle growth. *Aerosol Research* **2025,** *3* (1), 231-235.

45. Kogelschatz, U., Filamentary, patterned, and diffuse barrier discharges. *IEEE Transactions on Plasma Science* **2002,** *30* (4), 1400-1408.

46. Wagner, H. E.; Brandenburg, R.; Kozlov, K. V.; Sonnenfeld, A.; Michel, P.; Behnke, J. F., The barrier discharge: basic properties and applications to surface treatment. *Vacuum* **2003,** *71* (3), 417-436.

47. Niu, G.; Knodel, A.; Burhenn, S.; Brandt, S.; Franzke, J., Review: Miniature dielectric barrier discharge (DBD) in analytical atomic spectrometry. *Anal Chim Acta* **2021,** *1147*, 211-239.

48. Iranshahi, K.; Defraeye, T.; Rossi, R. M.; Müller, U. C., Electrohydrodynamics and its applications: Recent advances and future perspectives. *International Journal of Heat and Mass Transfer* **2024,** *232*, 125895.

49. Nijdam, S.; Van Veldhuizen, E.; Bruggeman, P.; Ebert, U., An Introduction to Nonequilibrium Plasmas at Atmospheric Pressure. *Plasma chemistry and catalysis in gases and liquids* **2012**, 1-44.

50. Raizer, Y. P.; Allen, J. E., Gas discharge physics. *Berlin: Springer*: **1997**.

51. Wang, Y.; Ma, X.; Hu, L.; Zhou, X.; Wang, Z.; Zhang, X., Ionization wave propagation characteristics under different polarity of pulse waveforms in micro-DBD device driven by bipolar nanosecond pulse waveform. *Physics of Plasmas* **2019,** *26* (11).

52. Waskoenig, J., O'Connell, D., Schulz-Von Der Gathen, V., Winter, J., Park, S. J., Eden, J. G., Spatial dynamics of the light emission from a microplasma array. *Appl. Phys. Lett.* **2008,** *92* (10).

53. Leal-Quirós, E., Plasma processing of municipal solid waste. *Brazilian Journal of Physics* **2004,** *34*, 1587-1593.

54. Bradshaw, S. J.; Raymond, J., Collisional and Radiative Processes in Optically Thin Plasmas **2013,** Space Science Reviews, *178* (2), 271-306.

55. Hodgman, S. S.; Dall, R. G.; Byron, L. J.; Baldwin, K. G.; Buckman, S. J.; Truscott, A. G., Metastable helium: a new determination of the longest atomic excited-state lifetime. *Phys Rev Lett* **2009,** *103* (5), 053002.

56. Miller, W. H.; Morgner, H., A unified treatment of Penning ionization and excitation transfer. *The Journal of Chemical Physics* **1977,** *67* (11), 4923-4930.

57. Penning, F. M., Über Ionisation durch metastabile Atome. *Naturwissenschaften* **1927,** *15* (40), 818-818.

58. Marton, L.; Marton, C., Advances in Electronics and Electron Physics. *Academic Press*: **1980**.

59. Fantz, U., Basics of plasma spectroscopy. *Plasma Sources Science and Technology* **2006,** *15* (4), S137-S147.

60. Kaiser, K. L., *Electrostatic discharge*. CRC press: **2005**.

61. Lüttgens, G.; Lüttgens, S.; Schubert, W., Static electricity: understanding, controlling, applying. *John Wiley & Sons*: **2017**.

62. Akishev, Y. S.; Dem'yanov, A. V.; Karal'nik, V. B.; Monich, A. E.; Trushkin, N. I., Comparison of the AC barrier corona with DC positive and negative coronas and barrier discharge. *Plasma Physics Reports* **2003,** *29* (1), 82-91.

63. Chen, H. W.; Lai, J. H.; Zhou, Y. F.; Huan, Y. F.; Li, J. Q.; Xie, Z.; Wang, Z. C.; Luo, M. B., Instrumentation and Characterization of Surface Desorption Atmospheric Pressure Chemical Ionization Mass Spectrometry. *Chinese Journal of Analytical Chemistry* **2007,** *35* (8), 1233-1240.

64. Carroll, D. I.; Dzidic, I.; Stillwell, R. N.; Horning, M. G.; Horning, E. C., Subpicogram detection system for gas phase analysis based upon atmospheric pressure ionization (API) mass spectrometry. *Analytical Chemistry* **1974,** *46* (6), 706-710.

65. Brandenburg, R.; Navrátil, Z.; Jánský, J.; St'ahel, P.; Trunec, D.; Wagner, H. E., The transition between different modes of barrier discharges at atmospheric pressure. *Journal of Physics D: Applied Physics* **2009,** *42* (8), 085208.

66. Destrieux, A.; Laurent, M.; Naudé, N.; Profili, J.; Laroche, G., On the modification of the dielectric barrier discharge electrical properties over one-hour operation using measurements without discharge. *Physica Scripta* **2025,** *100* (9), 095606.

67. Rankin-Turner, S.; Ninomiya, S.; Shimada, H.; Kinoshita, K.; Hiraoka, K., Miniature APCI ion source using AC corona discharge in a PFA tube: its application to the analysis of low-volatility compounds coupled with heat pulse desorption mass spectrometry (HPD/MS). *International Journal of Mass Spectrometry* **2025,** *514*, 117461.

68. Hiraoka, K.; Shimada, H.; Kinoshita, K.; Rankin-Turner, S.; Ninomiya, S., What is the advantage of alternative current (AC) corona discharge for APCI mass spectrometry? *International Journal of Mass Spectrometry* **2024,** *504*, 117299.

69. Hiraoka, K.; Rankin-Turner, S.; Ninomiya, S.; Shimada, H.; Kinoshita, K.; Yamabe, S., Corona Discharge and Field Electron Emission in Ambient Air Using a Sharp Metal Needle: Formation and Reactivity of CO(3) (-*) and O(2) (-*). *Mass Spectrom (Tokyo)* **2021,** *10* (1), A0100.

70. Usmanov, D. T.; Chen, L. C.; Yu, Z.; Yamabe, S.; Sakaki, S.; Hiraoka, K., Atmospheric pressure chemical ionization of explosives using alternating current corona discharge ion source. *J Mass Spectrom* **2015,** *50* (4), 651-61.

71. Habib, A.; Usmanov, D.; Ninomiya, S.; Chen, L. C.; Hiraoka, K., Alternating current corona discharge/atmospheric pressure chemical ionization for mass spectrometry. *Rapid Commun Mass Spectrom* **2013,** *27* (24), 2760-6.

72. Tian, Y.; Liu, C.; Huang, X.; Tian, W.; Cao, W.; Zhu, Y.; Zhao, L., The propagation of the Ion-Flow Near the AC Transmission Lines. *IEEE Access* **2020,** *8*, 146498-146509.

73. Davidson, J. H., Electron Density and Energy Distributions in the Positive DC Corona: Interpretation for Corona-Enhanced Chemical Reactions. *Plasma Chemistry and Plasma Processing* **2002**, *23* (1), 183.

74. Yang, M.; Yuan, Y.; Li, Y.; Sun, X.; Wang, S.; Liang, L.; Ning, Y.; Li, J.; Yin, W.; Che, R.; Li, Y., Dramatically enhanced electromagnetic wave absorption of hierarchical CNT/Co/C fiber derived from cotton and metal-organic-framework. *Carbon* **2020,** *161*, 517-527.

75. Lu, R.; Wang, J.; Duan, T.; Hu, T. Y.; Hu, G.; Liu, Y.; Fu, W.; Han, Q.; Lu, Y.; Lu, L.; Cheng, S. D.; Dai, Y.; Hu, D.; Shen, Z.; Jia, C. L.; Ma, C.; Liu, M., Metadielectrics for high-temperature energy storage capacitors. *Nat Commun* **2024,** *15* (1), 6596.

76. Zhou, Y.; Wang, Q., Advanced polymer dielectrics for high temperature capacitive energy storage. *Journal of Applied Physics* **2020,** *127* (24).

77. Wei, W.; Gu, Z., Electrification of particulate entrained fluid flows—Mechanisms, applications, and numerical methodology. *Physics Reports* **2015,** *600*, 1-53.

78. Liu, H., Dielectrics under Electric Field. *Electric Field*, **2018,** 322.

79. Ozerov, R. P.; Vorobyev, A. A., Physics for chemists. *Elsevier*: **2007**.

80. Feng, W.; Liu, Y.; Bi, Y.; Su, X.; Lu, C.; Han, X.; Ma, Y.; Feng, C.; Ma, M., Recent advancement of magnetic MOF composites in microwave absorption. *Synthetic Metals* **2023,** *294*, 117307.

81. Qin, M.; Zhang, L.; Wu, H., Dielectric Loss Mechanism in Electromagnetic Wave Absorbing Materials. *Advanced Science* **2022,** *9* (10), 2105553.

82. Čápek, V.; Silinsh, E. A., Dynamics of electronic polarization in molecular crystals. *Chemical Physics* **1995,** *200* (3), 309-318.

83. Sobota, A.; Guaitella, O.; Sretenović, G. B.; Kovačević, V. V.; Slikboer, E.; Krstić, I. B.; Obradović, B. M.; Kuraica, M. M., Plasma-surface interaction: dielectric and metallic targets and their influence on the electric field profile in a kHz AC-driven He plasma jet. *Plasma Sources Science and Technology* **2019,** *28* (4), 045003.

84. Stańczyk, B.; Wiśniewski, M., The Promising Potential of Cold Atmospheric Plasma Therapies. *Plasma* **2024,** *7* (2), 465-497.

85. Deepak, G. D.; Anne, G.; Bhat, S. K., Modeling and optimization of argon-based floating helix electrode cold plasma. *Sci Rep* **2025,** *15* (1), 33422.

86. Viegas, P.; Slikboer, E.; Bonaventura, Z.; Garcia-Caurel, E.; Guaitella, O.; Sobota, A.; Bourdon, A., Quantification of surface charging memory effect in ionization wave dynamics. *Sci Rep* **2022,** *12* (1), 1181.

87. Li, T.; Yan, H. J.; Yu, S. Q.; Wang, Y. Y.; Li, J. Q.; Song, J.; Zhang, Q. Z., Measurements of surface charge dynamics and surface-breakdown characteristics of surface dielectric barrier discharges. *Journal of Applied Physics* **2022,** *132* (15).

88. Zhu, Y.; Takada, T., Sakai, K., Tu, D., The dynamic measurement of surface charge distribution deposited from partial discharge in air by Pockels effect technique. *Journal of physics D: applied physics* **1996**, *29* (11), 2892.

89. Zogning, C.; Lobry, J.; Moiny, F., Numerical Simulation of Corona Discharge Plasma Affecting the Surface Behavior of Polymer Insulators. *Energies* **2024,** *17* (17), 4247.

90. Opaits D. F.; Shneider, M. N.; Miles, R. B.; Likhanskii, A. V.; Macheret, S. O., Surface charge in dielectric barrier discharge plasma actuators. *Physics of Plasmas* **2008**, *15* (7).

91. Cristofolini, A.; Borghi, C. A.; Neretti, G., Charge distribution on the surface of a dielectric barrier discharge actuator for the fluid-dynamic control. *Journal of Applied Physics* **2013,** *113* (14).

92. Liu, F.; Zhou, W.; Wang, Z.; Zhou, X.; Fang, Z., Effect of pulse width and repetition frequency on the uniformity and accumulation effect of atmospheric-pressure nanosecond pulsed DBD. *Physica Scripta* **2025,** *100* (10), 105608.

93. Lemell, C.; Burgdörfer, J.; Aumayr, F., Interaction of charged particles with insulating capillary targets – The guiding effect. *Progress in Surface Science* **2013,** *88* (3), 237-278.

94. Liu, Q.; Chen, Y.; Wang, J.; You, M.; Guo, Z.; Hu, M.; Wu, S., Optimizing the Electrical Performance of Polytetrafluoroethylene (PTFE) via Dielectric Barrier Discharge Plasma Treatment. *IEEE Transactions on Dielectrics and Electrical Insulation* **2025**.

95. Lindgren, E. B., Charge-Induced Polarization in Dielectric Particle Systems: A Geometry-Dependent Effect. *J Chem Theory Comput* **2025,** *21* (12), 6135-6150.

96. Ali, S.; Masood, W.; Singh, K.; Jahangir, R., Test charge driven response of a dusty plasma with polarization force. *Frontiers in Astronomy and Space Sciences* **2022,** *9*, 987561.

97. Yambe, K.; Nizam, A. I. B. K.; Sato, T., Suppression of Plasma Current by Insulator in Atmospheric Pressure Plasma Jet. *IEEE Transactions on Plasma Science* **2025**.

98. Lu, X.; Xiong, Q.; Xiong, Z.; Hu, J.; Zhou, F.; Gong, W.; Xian, Y.; Zou, C.; Tang, Z.; Jiang, Z.; Pan, Y., Propagation of an atmospheric pressure plasma plume. *Journal of Applied Physics* **2009**, *105* (4), 043304.

99. Pechereau, F.; Bonaventura, Z.; Bourdon, A., Influence of surface emission processes on a fast-pulsed dielectric barrier discharge in air at atmospheric pressure. *Plasma Sources Science and Technology* **2016,** *25* (4), 044004.

100. Chua, Z. Q.; Prabhu, G. R. D.; Wang, Y. W.; Raju, C. M.; Buchowiecki, K.; Ochirov, O.; Elpa, D. P.; Urban, P. L., Moderate Signal Enhancement in Electrospray Ionization Mass Spectrometry by Focusing Electrospray Plume with a Dielectric Layer around the Mass Spectrometer's Orifice. *Molecules* **2024,** *29* (2), 316.

101. Massines, F.; Rabehi, A.; Decomps, P.; Gadri, R. B.; Ségur, P.; Mayoux, C., Experimental and theoretical study of a glow discharge at atmospheric pressure controlled by dielectric barrier. *Journal of Applied Physics* **1998,** *83* (6), 2950-2957.

102. Zhao, Z.; Li, J., Repetitively pulsed gas discharges: memory effect and discharge mode transition. *High Voltage* **2020,** *5* (5), 569-582.

103. Klute, F. D.; Michels, A.; Schutz, A.; Vadla, C.; Horvatic, V.; Franzke, J., Capillary Dielectric Barrier Discharge: Transition from Soft Ionization to Dissociative Plasma. *Anal Chem* **2016,** *88* (9), 4701-4705.

104. Klute, F. D.; Brandt, S.; Franzke, J., Spatiotemporal characterization of different dielectric barrier discharges designed for soft ionization. *Spectrochimica Acta Part B: Atomic Spectroscopy* **2021,** *176*, 106037.

105. Klute, F. D.; Schütz, A.; Brandt, S.; Burhenn, S.; Vogel, P.; Franzke, J., Characterization of dielectric barrier discharges for analytical chemistry. *Journal of Physics D: Applied Physics* **2018,** *51* (31), 314003.

106. Horvatic, V.; Vadla, C.; Franzke, J., Discussion of fundamental processes in dielectric barrier discharges used for soft ionization. *Spectrochimica Acta Part B: Atomic Spectroscopy* **2014,** *100*, 52-61.

107. Nijdam, S.; Takahashi, E.; Markosyan, A. H.; Ebert, U., Investigation of positive streamers by double-pulse experiments, effects of repetition rate and gas mixture. *Plasma Sources Science and Technology* **2014,** *23* (2), 025008.

108. Martínez-Calderón, A. A.; Sant'Anna, M. M.; Hinojosa, G., Electron-detachment cross sections for O−+ N 2 near the free-collision-model velocity threshold. *Physical Review A* **2024,** *109* (3), 032806.

109. Bailey, T. L.; Mahadevan, P., Electron Transfer and Detachment in Collisions of Low-Energy Negative Ions with O2. *The Journal of Chemical Physics* **1970,** *52* (1), 179-190.

110. Ning, C.; Lu, Y., Electron Affinities of Atoms and Structures of Atomic Negative Ions. *Journal of Physical and Chemical Reference Data* **2022,** *51* (2).

111. Boerner, H., The Role of Free Electrons in Ball Lightning Creation. *Plasma Physics* **2023**.

112. Zaplotnik, R.; Primc, G.; Vesel, A., Optical Emission Spectroscopy as a Diagnostic Tool for Characterization of Atmospheric Plasma Jets. *Applied Sciences* **2021,** *11* (5), 2275.

113. Rachdi, L.; Sushkov, V.; Hofmann, M., Optical emission spectroscopy diagnostics for plasma parameters investigation in a Duo-Plasmaline surface-wave sustained discharge. *Spectrochimica Acta Part B: Atomic Spectroscopy* **2022,** *194*, 106432.

114. Rajasekaran, P.; Ruhrmann, C.; Bibinov, N.; Awakowicz, P., Space-resolved characterization of high frequency atmospheric-pressure plasma in nitrogen applying optical emission

spectroscopy and numerical simulation. *Journal of Physics D: Applied Physics* **2011***, 44* (48), 485205.

115. Chen, F. F.; Chang, J. P., Optical Emission Spectroscopy. Lecture notes on principles of plasma processing, *Springer Science & Business Media*: **2003**.

116. Parigger, C. G.; Helstern, C. M.; Gautam, G., Temporally and spatially resolved emission spectroscopy of hydrogen, cyanide and carbon in laser-induced plasma. *Atoms* **2019,** *7* (3), 74.

117. Sobelman, I. I., Atomic spectra and radiative transitions. *Springer Science & Business Media*: **2012**.

118. Docenko, D.; Sunyaev, R. A., Optical and near-infrared recombination lines of oxygen ions from Cassiopeia A knots. *Astronomy & Astrophysics* **2008,** *484* (3), 755-771.

119. Ye, R.; Zheng, W., Temporal-spatial-resolved spectroscopic study on the formation of an atmospheric pressure microplasma jet. *Appl. Phys. Lett.* **2008,** *93* (7).

120. Ayala-Cabrera, J. F.; Turkowski, J.; Uteschil, F.; Schmitz, O. J., Development of a Tube Plasma Ion Source for Gas Chromatography-Mass Spectrometry Analysis and Comparison with Other Atmospheric Pressure Ionization Techniques. *Anal Chem* **2022,** *94* (27), 9595-9602.

121. Ayala-Cabrera, J. F.; Montero, L.; Meckelmann, S. W.; Uteschil, F.; Schmitz, O. J., Review on atmospheric pressure ionization sources for gas chromatography-mass spectrometry. Part II: Current applications. *Anal Chim Acta* **2023,** *1238*, 340379.

122. Schutz, A.; Lara-Ortega, F. J.; Klute, F. D.; Brandt, S.; Schilling, M.; Michels, A.; Veza, D.; Horvatic, V.; Garcia-Reyes, J. F.; Franzke, J., Soft Argon-Propane Dielectric Barrier Discharge Ionization. *Anal Chem* **2018,** *90* (5), 3537-3542.

123. Heylen, A. E. D., Ionization coefficients and sparking voltages in argon-methane and argon-propane mixtures†. *International Journal of Electronics* **1968,** *24* (2), 165-175.

124. Klute, F. D.; Schutz, A.; Michels, A.; Vadla, C.; Veza, D.; Horvatic, V.; Franzke, J., An experimental study on the influence of trace impurities on ionization of atmospheric noble gas dielectric barrier discharges. *Analyst* **2016,** *141* (20), 5842-5848.

125. Horvatic, V.; Muller, S.; Veza, D.; Vadla, C.; Franzke, J., Atmospheric helium capillary dielectric barrier discharge for soft ionization: determination of atom number densities in the lowest excited and metastable states. *Anal Chem* **2014,** *86* (1), 857-864.

126. Gherardi, M.; Puač, N.; Marić, D.; Stancampiano, A.; Malović, G.; Colombo, V.; Petrović, Z. L., Practical and theoretical considerations on the use of ICCD imaging for the characterization of non-equilibrium plasmas. *Plasma Sources Science and Technology* **2015,** *24* (6), 064004.

127. Pinchuk, M.; Nikiforov, A.; Snetov, V.; Chen, Z.; Leys, C.; Stepanova, O., Role of charge accumulation in guided streamer evolution in helium DBD plasma jets. *Scientific Reports* **2021,** *11* (1), 17286.

128. Robert, E.; Sarron, V.; Ries, D.; Dozias, S.; Vandamme, M.; Pouvesle, J. M., Characterization of pulsed atmospheric-pressure plasma streams (PAPS) generated by a plasma gun. *Plasma Sources Science and Technology* **2012,** *21* (3), 034017.

129. Xiong, Z.; Kushner, M. J., Atmospheric pressure ionization waves propagating through a flexible high aspect ratio capillary channel and impinging upon a target. *Plasma Sources Science and Technology* **2012,** *21* (3), 034001.

130. Babaeva, N. Y.; Naidis, G.; Tarasenko, V.; Sorokin, D.; Zhang, C.; Shao, T., Evolution of ionization waves in a multi-pulsed plasma jet: the role of memory charges. *Plasma Science and Technology* **2023,** *25* (3), 035406.

131. Gong, W.; Yue, Y.; Ma, F.; Yu, F.; Wan, J.; Nie, L.; Bazaka, K.; Xian, Y.; Lu, X.; Ostrikov, K., Control of radial propagation and polarity in a plasma jet in surrounding Ar. *Physics of Plasmas* **2018,** *25* (1).

132. Dryahina, K.; Polášek, M.; Jašík, J.; Sovová, K.; Španěl, P., Ion Chemistry in Dielectric Barrier Discharge Ionization: Recent Advances in Direct Gas Phase Analyses. *Mass Spectrometry Reviews* **2024**.

133. Gyr, L.; Wolf, J.-C.; Franzke, J.; Zenobi, R., Mechanistic Understanding Leads to Increased Ionization Efficiency and Selectivity in Dielectric Barrier Discharge Ionization Mass Spectrometry: A Case Study with Perfluorinated Compounds. *Analytical Chemistry* **2018,** *90* (4), 2725-2731.

134. Slikboer, E.; Guaitella, O.; Garcia-Caurel, E.; Sobota, A., Towards plasma jet controlled charging of a dielectric target at grounded, biased, and floating potential. *Sci Rep* **2022,** *12* (1), 1157.

135. Darny, T.; Pouvesle, J. M.; Puech, V.; Douat, C.; Dozias, S.; Robert, E., Analysis of conductive target influence in plasma jet experiments through helium metastable and electric field measurements. *Plasma Sources Science and Technology* **2017,** *26* (4), 045008.

136. Norberg, S. A.; Johnsen, E.; Kushner, M. J., Helium atmospheric pressure plasma jets touching dielectric and metal surfaces. *Journal of Applied Physics* **2015,** *118* (1).

137. Klarenaar, B.; Guaitella, O.; Engeln, R.; Sobota, A., How dielectric, metallic and liquid targets influence the evolution of electron properties in a pulsed He jet measured by Thomson and Raman scattering. *Plasma Sources Science and Technology* **2018,** *27* (8), 085004.

138. Babaeva, N. Y.; Naidis, G. V.; Panov, V. A.; Wang, R.; Zhang, S.; Zhang, C.; Shao, T., Plasma bullet propagation and reflection from metallic and dielectric targets. *Plasma Sources Science and Technology* **2019,** *28* (9), 095006.

139. Klute, F. D., Characterization of dielectric barrier discharges for analytical applications. *Doctoral dissertation, Dissertation, Dortmund, Technische Universität*: **2019**.

140. Munson, M. S. B.; Field, F. H., Chemical ionization mass spectrometry. I. General introduction. *Journal of the American Chemical society* **1966**, *88* (12), 2621-2630.

141. Chen, J.; Davidson, J. H., Model of the Negative DC Corona Plasma: Comparison to the Positive DC Corona Plasma. *Plasma chemistry and plasma processing* **2003**, *23* (1), 83-102.

142. Loeb, L. B., Electrical coronas: their basic physical mechanisms. *Univ of California Press*: **2022**.

143. Asipuela, A.; Iváncsy, T., Study and Numerical Simulation of Negative and Positive Corona Discharge: A Review. *Periodica Polytechnica Electrical Engineering and Computer Science* **2022,** *66* (3), 294-300.

144. Tabrizchi, M.; Khayamian, T.; Taj, N., Design and optimization of a corona discharge ionization source for ion mobility spectrometry. *Review of Scientific Instruments* **2000,** *71* (6), 2321-2328.

145. Lofthus, A.; Krupenie, P. H., The spectrum of molecular nitrogen. *Journal of physical and chemical reference Data* **1977,** *6* (1), 113-307.

146. Cano-Carrillo, I.; Gilbert-Lopez, B.; Moreno-Gonzalez, D.; Franzke, J.; Garcia-Reyes, J. F., Efficient and Wide Chemical-Space Ionization of Organic Contaminants Using LC-MS with a Miniaturized Plasma Source Applying Different Discharge Gases. *Anal Chem* **2025,** *97* (38), 20962-20972.

147. Stolterfoht, N.; Yamazaki, Y., Guiding of charged particles through capillaries in insulating materials. *Physics Reports* **2016,** *629*, 1-107.

148. Kojima, T. M., Ion guiding in macro-size insulating capillaries: straight, tapered, and curved shapes. *Journal of Physics B: Atomic, Molecular and Optical Physics* **2018,** *51* (4), 042001.

149. Guan, X.; Wei, C.; Yan, X.; Zenobi, R., Optimization of Dielectric Material Improves Ionization Capability and Mass Range of Dielectric Barrier Discharge Ionization Mass Spectrometry. *Journal of the American Society for Mass Spectrometry* **2025,** *36* (8), 1812-1820.

150. Fan, J.; Xu, X., Method for Measuring Surface Charge on Insulating Materials Based on the Vibrating Capacitor Method. *Applied Sciences* **2024,** *14* (8), 3141.

Appendix

A. Investigation of the discharge mechanisms in *He*- and *Ar*-FμTPs

A.1 The overlap of different origins for *Ar* 763 nm emission

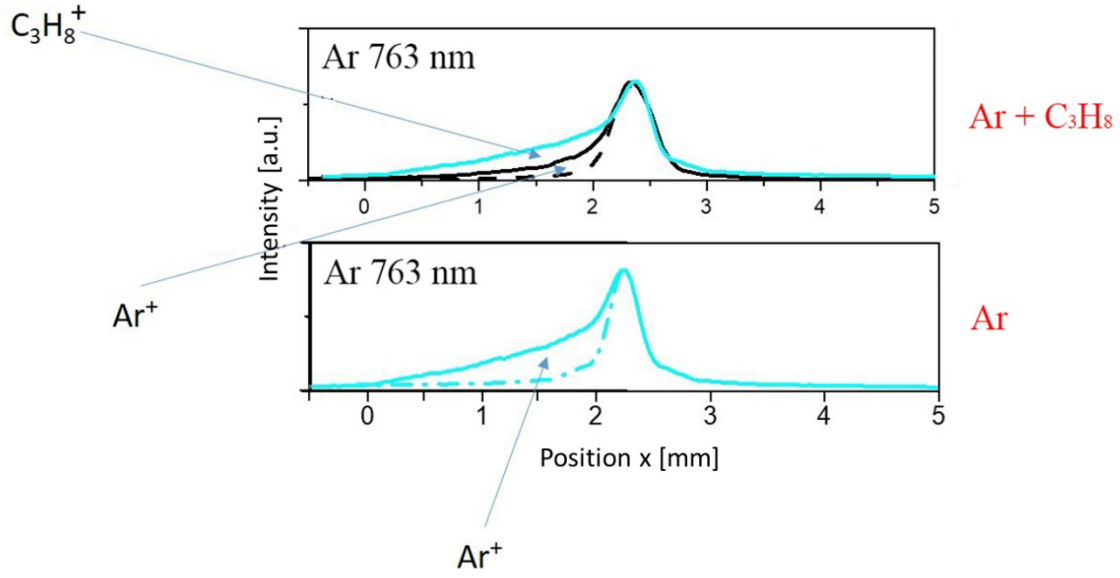

Figure A.1: Schematic of the overlap of different origins for Ar 763 nm emission in the phoresis plots. It shows the emission intensities as a function of position at one instant of time during the rising half-phases for Ar 763 nm measured from Ar-FμTP and Ar-propane-FμTP. Since propane ions partially replace the role of Ar^+, the wing becomes less obvious.

B. Influence of a metallic target on FµTPs

B.1 Evolution behaviour of the P-plasma

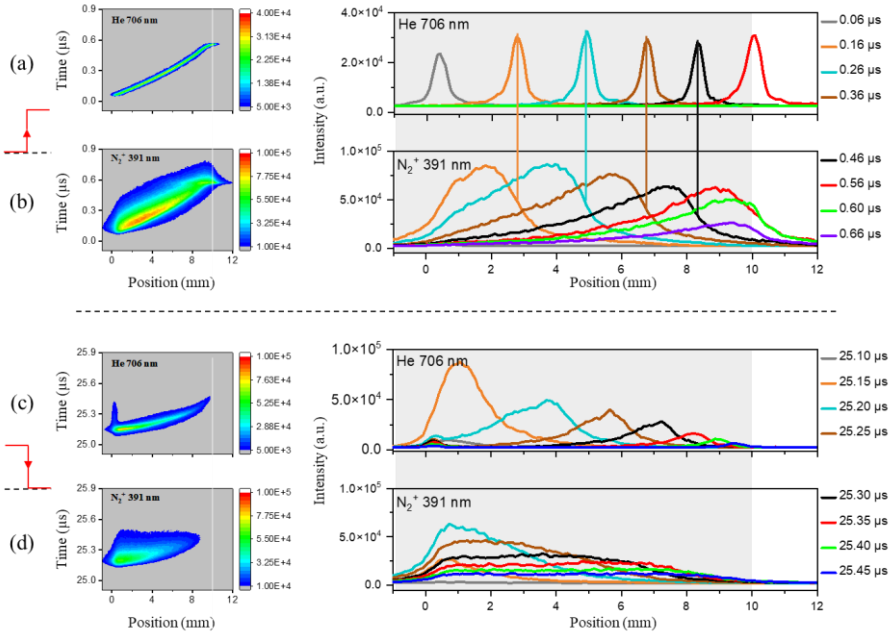

Figure B.1: Two dimensional contour plots in time and position and the related phoresis plots for the emission intensities as a function of position at different time during the rising and the falling half-phases for He 706 and N_2^+ 391 nm measured from the free P-plasma, respectively.

B.2 Evolution behaviour of the N-plasma

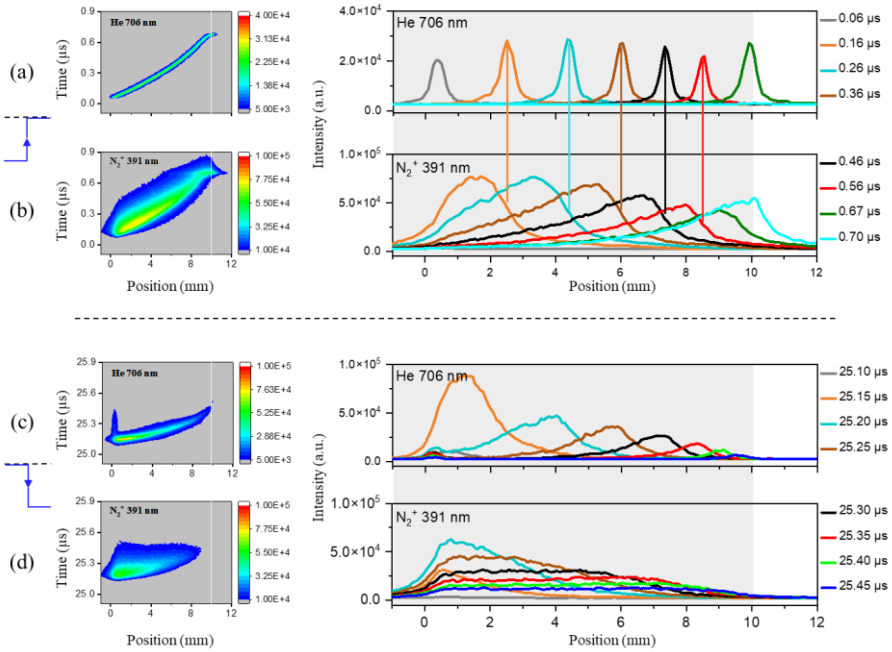

Figure B.2: Two dimensional contour plots in time and position and the related phoresis plots for the emission intensities as a function of position at different time during the rising and the falling half-phases for He 706 and N_2^+ 391 nm measured from the free N-plasma, respectively.

C. Differences between FμTP and corona discharge

C.1 Potential measured around a 10 mm long *He*-FμTP driven by 3.0 kV

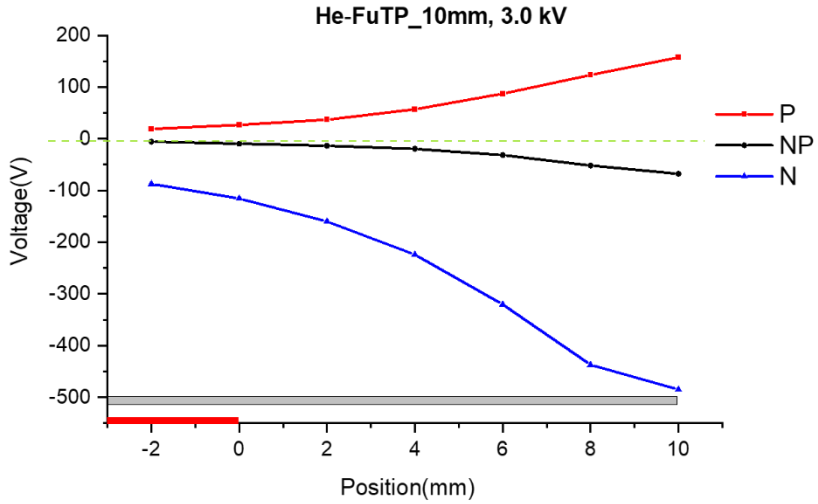

Figure C.1: Ring potential values as a function of position along the axis of a 10 mm long He-FμTP driven by a square wave voltage (V_{pp} = 3.0 kV) in three polarities. The horizontal red and grey columns at the bottom of the figure represent the inner HV electrode and the capillary glass wall, respectively.

C.2 MS detection of 2-Butanone with FμTP

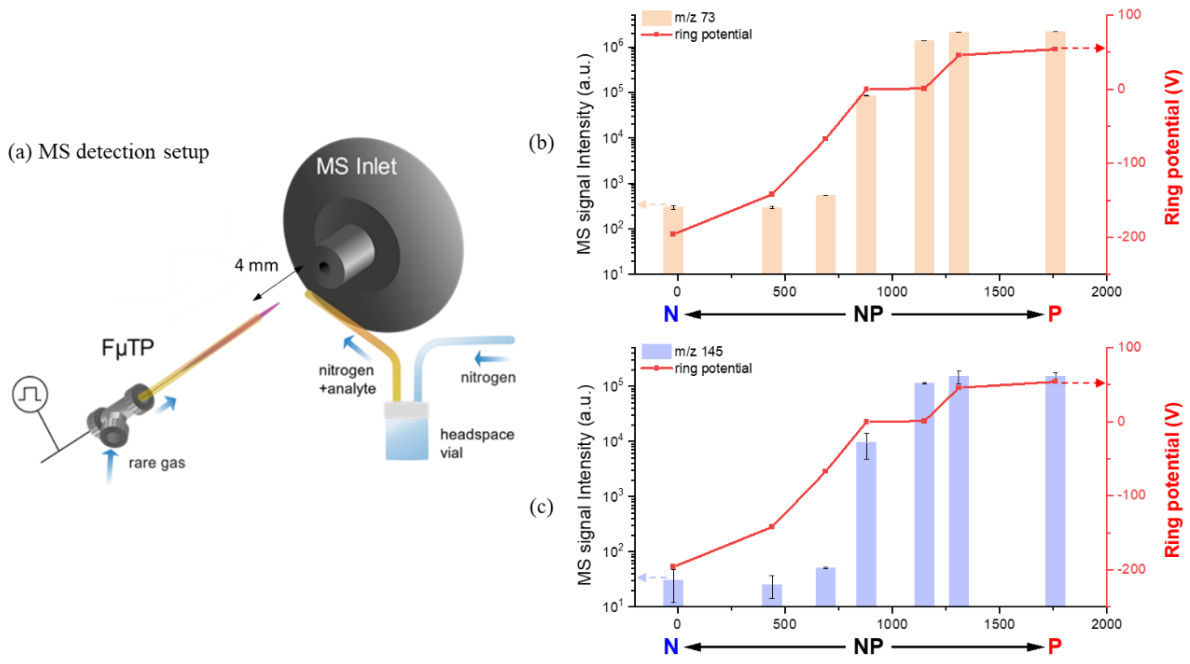

Figure C.2: (a) The setup for MS detection in front of a FμTP with a distance of 4 mm to the MS inlet, nitrogen was used as the carrier gas at a flow rate of 100 sccm for sampling, 2-Butanone (C_4H_8O, m/z 72) was used as analyte. The obtained MS signal intensities of (b) m/z 73 and (c) m/z 145 ions in front of the He-FμTPs (driven by V_{pp} = 2.0 kV) with various DC biases under positive ion mode, respectively (the left ordinate is on the log10 scale). The red curves represent the ring potentials measured at the capillary exit of He-FμTP in front of the MS inlet. The horizontal axis is the upper voltage amplitude (V) of the driven square wave voltage.

C.3 MS detection of FμTP with various DC bias voltages

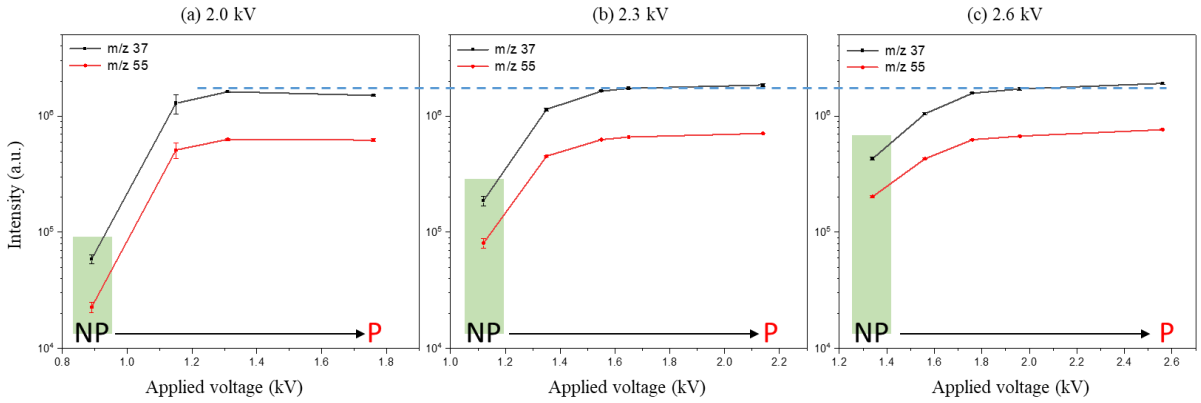

Figure C.3: The obtained MS signal intensities of m/z 37 and m/z 55 ions with a distance of 4 mm in front of the He-FμTPs driven by V_{pp} of (a) 2.0 kV, (b) 2.3 kV and (c) 2.6 kV with various DC biases under positive ion mode, respectively (the left ordinate is on the log10 scale). The horizontal axis is the upper voltage amplitude of the driven square wave voltage. The green bars represent the cases of bipolar (NP) voltages without DC bias, and the corresponding MS signal height greatly increases as the applied amplitude increases. Since the MS signal values approach saturation, the distinction becomes increasingly negligible, particularly in P cases. The horizontal dashed line represents the saturated maximum height of the MS signals.

List of Publications and Presentations

Peer-reviewed Articles (relevant for this work)

P1 **Hao Song**, Caiyan Tian, Luisa Speicher, Norman Ahlmann, Sebastian Brandt, Guanghui Niu, Joachim Franzke*

Elucidation of discharge mechanisms in *He*- and *Ar*-flexible µ-tube plasmas by temporally and spatially resolved plasma optical emission phoresis spectroscopy

Spectrochimica Acta Part B: Atomic Spectroscopy, **2024,**

DOI: 10.1016/j.sab.2024.107014

P2 **Hao Song**[1], Caiyan Tian[1], Luisa Speicher, Norman Ahlmann, Daniel Foest, Simon Höving, Sebastian Brandt, Guanghui Niu, Joachim Franzke*

Excitation and ionisation of a diagnosis gas in front of the flexible µ tube plasma and in a diagnosis tube

Spectrochimica Acta Part B: Atomic Spectroscopy, **2024**,

DOI: 10.1016/j.sab.2024.107052

P3 Luisa Speicher, **Hao Song**, Norman Ahlmann, Daniel Foest, Simon Höving, Sebastian Brandt, Guanghui Niu, Joachim Franzke***,** Caiyan Tian*

Soft ionisation mechanisms in flexible µ-tube plasma—from FµTP to closed µ-tube plasma

Analytical and Bioanalytical Chemistry, **2024**,

DOI: 10.1007/s00216-024-05420-8

P4 Caiyan Tian, **Hao Song**, Norman Ahlmann, Sebastian Brandt, Daniel Foest, Guanghui Niu, Joachim Franzke*, Luisa Speicher*

Soft ionisation mechanisms in flexible µ-tube plasma—elucidation of *He*-, *Ar*-, *Kr*-, and *Xe*-FµTP

Analytical and Bioanalytical Chemistry, **2024**,

DOI: 10.1007/s00216-024-05419-1

P5 Caiyan Tian, Luisa Speicher, **Hao Song**, Norman Ahlmann, Sebastian Brandt, Guanghui Niu, Joachim Franzke*

Study of the discharge mode transition in a *Ne*-Flexible µ-Tube Plasma

Spectrochimica Acta Part B: Atomic Spectroscopy, **2025,**

DOI: 10.1016/j.sab.2025.107180

Further Peer-reviewed Article

- Simon Höving*, **Hao Song**, Luisa Speicher, Arthur Schiller, Joachim Franzke

  Compact Plasma Ionization for Ion Mobility Spectrometry Using a 4.3 MHz Miniature Tesla Coil
  Journal of the American Society for Mass Spectrometry, **2024**,
  DOI: 10.1021/jasms.4c00360

Presentations

- **Hao Song**, Caiyan Tian, Luisa Speicher, Norman Ahlmann, Daniel Foest, Simon Höving, Sebastian Brandt, Guanghui Niu, Joachim Franzke
  Excitation and ionization of a diagnosis gas in front of the Flexible μ-Tube Plasma and in a diagnosis capillary
  The 5th International Symposium on Frontiers of Plasma and Energy Conversion
  Nanjing, China, 27. Oct. 2023 - 29. Oct. 2023
- **Hao Song**, Caiyan Tian, Luisa Speicher, Norman Ahlmann, Daniel Foest, Simon Höving, Sebastian Brandt, Guanghui Niu, Joachim Franzke
  Excitation and ionization of a diagnosis gas in front of the Flexible μ-Tube Plasma
  The 33rd International Conference on Ion Mobility Spectrometry
  Miami Beach, USA, 20. Jul. 2024 - 26. Jul. 2024

Declaration of Pre-Published Contents

Parts of this thesis were already published by the author in articles (P1-P5) and presentations. Experimental data, results and part of methodology are based on the manuscript. This thesis contains the following reproductions:

Chapter 3	content partly published in	P1, P2, P4, P5
3.1	content partly published in	P1, P5
3.2	content partly published in	P1, P4
3.3	content partly published in	P1, P2, P4
3.4	content partly published in	P1, P2, P5
Chapter 4	content partly published in	P1 – P4
4.1		
4.2		
4.3	content partly published in	P1 – P4
4.4	content partly published in	P1 – P4
Chapter 5		
5.1		
5.2		
5.3		
Chapter 6	content partly published in	P1 – P5
6.1	content partly published in	P1 – P5
6.2		
6.3		
6.4	content partly published in	P1 – P4
6.5	content partly published in	P2 – P4
6.6	content partly published in	P1 – P5
6.7	content partly published in	P1 – P5

Acknowledgments

Herewith I would like to express my gratitude and appreciate to the people who made this thesis possible. The present work was carried out at the *Leibniz-Institut für Analytische Wissenschaften-ISAS e.V.* in Dortmund, and was funded by *ISAS* and the China Scholarship Council (*CSC*, grant no. 202208080127).

I am very grateful to PD Dr. Joachim Franzke for giving me the opportunity to undertake my PhD work under his supervision. I appreciate for all the affirmation and encouragement he has given me over the years. I will always remember his words that interest, questioning, and patience are the best teachers. I would also like to thank him for the many fruitful discussions and suggestions regarding the experimental work and data evaluation, and for his corrections and guidelines when writing my thesis.

I would like to thank Prof. Dr. Dr. h. c. Oliver Kayser, Prof. Dr.-Ing. Norbert Kockmann and PD Dr. Frank Katzenberg for reviewing and examining this thesis, and for their valuable suggestions given on this work. Many thanks are directed to Norman Ahlmann, for his efficient assistance in the construction of the experimental platform as well as for his technical support in the production of plasma sources and many other setups.

My sincere appreciation goes to Dr. Guanghui Niu for helping me apply for the CSC programme and for his invaluable suggestions regarding my research direction. I would also like to thank my colleagues who first guided my steps in the laboratory: Dr. Alexander Knodel, Dr. Sebastian Brandt and Ulrich Marggraf. Many thanks go to the Miniaturisation group at ISAS for the pleasant working atmosphere, collaboration, discussions, and fun, as well as for their patience and the help in improving my English language skill.

I am thankful to Dr. Luisa Speicher for her useful holiday advice, and for the collaboration on writing our publications. I am very thankful to Dr. Daniel Foest for carefully reading my thesis and making corrections, as well as for the photo shoots. Special thanks go to Dr. Simon Höving and Arthur Schiller for helping me deal with personal issues and solve technical problems with 3D printing. Thank you to Dr. Annika Fechner for organising the Christmas party and many other events. Thank Christopher Borg for so many kind conversations and helps. I will never forget the friendly discussions over coffee and delicious cake.

I also express my gratitude to other colleagues and friends I have had the pleasure of meeting during this period, for their kindness and support. Last but not least, I am deeply indebted to my family, especially to my wife, Dr. Caiyan Tian, for her encouragement and support.